

# **Thermophoretic Transport in Dispersions of Asymmetric Colloids and Microchannels**

Inaugural-Dissertation

zur

Erlangung des Doktorgrades  
der Mathematisch-Naturwissenschaftlichen Fakultät  
der Universität zu Köln  
vorgelegt von

Zihan Tan  
aus Lianyuan, China

Berichterstatter: **Prof. Dr. Gerhard Gompper**  
(Gutachter) **Prof. Dr. Simone Wiegand**  
**Dr. Marisol Ripoll**

Tag der mündlichen Prüfung: der 12. April 2018

*“Nature uses only the longest threads to weave her patterns, so that each small piece of her fabric reveals the organization of the entire tapestry.”*

Richard Feynman



# Abstract

Temperature gradients triggered force on colloid (or fluid) is referred to as *thermophoretic* (*thermoosmotic*) *force*. This driven mechanism offers rich transport phenomena out of thermodynamic equilibrium. With a mesoscale hydrodynamic simulations method, this thesis focuses on thermophoretic response of colloids with geometric and compositional asymmetries, and their resulting net flows, from both fundamental mechanism and application viewpoints.

Firstly, combined analytical theory and simulation, we study thermophoretic / diffusio-phoretic flows and forces, and related finite size effects for spherical colloids. Local quantities such as slip flow and associated local pressure at the solid-liquid boundary layer are obtained which explicitly explain the microscopic mechanisms of thermophoresis. Then, we exploit how the particle shape influences thermophoresis. The elongated colloids exhibit an orientation dependent thermophoretic response, i.e. the *anisotropic thermophoresis*. We introduce a linear decomposition scheme to show and understand this anisotropic phenomenon. Quite contradictory from anisotropic friction, we realize that the thermophoretic force of a rod oriented with the temperature gradient can be larger or smaller than when oriented perpendicular to it. This transition depends not only on the geometric details of the surface, also on the colloid-solvent interaction. Then the dependence on the rod aspect ratio is studied. Later, we move our attention to the heterodimer composed of two beads with different thermophoretic properties. The resulting alignment is linearly dependent on temperature gradient, and strongly relies on the size ratio. Additionally, the interacting heterodimers in a confined slit with walls are investigated in the presence of a temperature gradient. The colloids first align to the gradient due to thermophoretic torques, then accumulate at the wall. We observed the exponential decay of both positional and orientation order as the distance to the accumulation walls increases. This is reminiscent of "*sedimentation-diffusion equilibrium*" phenomenon. Hydrodynamic interaction in the case of phoretic heterodimers seems to be of importance when colloids are close to the wall.

With an application perspective, we propose two types of micropumps which use thermophoresis as surface forcing mechanism, but with different symmetry breaking by incorporating obstacles at the middle of the microchannel. In the first micropump, the temperature gradient is applied perpendicular to the channel walls; and elongated obstacles are fixed and tilted to the gradient. This geometric asymmetry and thermophoresis enable fluid to flow along the channel. The resulting flow patterns, the magnitude and direction of the net flux density rely on the channel geometric parameters. The flow strength, path and direction can be tuned by the length, rugosity, and thermophobic/thermophilic

properties of the obstacles. The net flow flux for obstacles with various interfacial properties can be captured by anisotropic thermophoresis. The second micropump uses fixed, metallic / non-metallic compositional obstacles aligned with the channel walls. By laser illumination, temperature gradient can be established due to the higher heat absorption in the metallic composition, which consequently leads to a net flow flux. The resultant far field flow resembles *Poiseuille* flow. Its pumping capability strongly depends on the length of the non-metallic part as well as the inter-separation distance of the obstacles, but is only slightly dependent on the channel width. Finally, a comparison of the pumping capability between different phoretic pumps is made.

# Kurzzusammenfassung

Eine Kraft, welche durch einen Temperaturgradienten auf ein Kolloid oder eine Flüssigkeit ausgeübt wird, bezeichnet man als *thermophoretische* (*thermoosmotische*) Kraft. Dieser getriebene Mechanismus bietet vielfältige Transportphänomene im thermodynamischen Nichtgleichgewicht. Diese Arbeit verwendet mesoskalige hydrodynamische Simulationen, um dieses Phänomen zu studieren. Der Fokus der Arbeit liegt auf der thermophoretischen Reaktion des Kolloids, dessen Asymmetrie und Struktur systematisch verändert wird. Der resultierende Nettofluss, der zugrundeliegende Mechanismus und dessen Anwendungen werden diskutiert.

Zunächst untersuchen wir sowohl mittels analytischer Theorien als auch mit Simulationen thermophoretische/diffusiophoretische Flüsse und Kräfte sowie Auswirkungen für sphärische Kolloide und bestimmen den Einfluss der endlichen Abmessungen der untersuchten Systeme. Lokale Größen wie der Schlupffluss und der zugehörige lokale Druck an der Festkörper-Flüssigkeits-Grenzschicht werden berechnet und verwendet, um den mikroskopischen Mechanismus der Thermophorese explizit zu erklären. Darauffolgend bestimmen wir den Einfluss der Teilchenform auf die Thermophorese. Die gestreckten Kolloide zeigen eine orientierungsabhängige thermophoretische Reaktion, welche als *anisotrope Thermophorese* bezeichnet wird. Wir führen ein lineares Zerlegungsschema ein, um das anisotrope Phänomen zu illustrieren und zu verstehen. Im Gegensatz zur anisotropen Reibung, erkennen wir, dass die thermophoretische Kraft eines in Richtung des Temperaturgradienten orientierten Stabes größer oder kleiner sein kann als die der senkrechten Orientierung. Dieser Übergang hängt nicht nur von den geometrischen Details der Oberfläche ab, sondern ebenfalls von der Kolloid-Lösungsmittel Wechselwirkung. Danach wird die Abhängigkeit des Längen- zu Dicken-Verhältnisses erforscht. Später wenden wir unsere Aufmerksamkeit den Hetero-Dimeren zu. Diese sind aus zwei Monomeren mit unterschiedlichen thermophoretischen Eigenschaften zusammengesetzt. Die resultierende Ausrichtung ist linear abhängig vom Temperaturgradienten und wird stark durch das Größenverhältnis beeinflusst. Im Weiteren werden wechselwirkenden Heterodimere in einem Spalt in der Anwesenheit eines Temperaturgradienten untersucht. Die Kolloide richten sich zuerst aufgrund des thermophoretischen Drehmomentes zum Gradienten aus und lagern sich dann an einer Wand des Spaltes an. Wir beobachteten den exponentiellen Abfall der Positions- und Orientierungsordnung mit zunehmendem Abstand zu dieser Wand. Dies erinnert an ein Sedimentation-Diffusionsgleichgewicht. Hydrodynamische Wechselwirkungen scheinen eine große Bedeutung für die phoretischen Heterodimere zu haben, wenn die Kolloide sich in der Nähe von Wänden befinden.

In Hinblick auf mögliche Anwendungen schlagen wir zwei Typen von Mikropumpen vor, die Thermophorese als den Oberflächen als Antriebsmechanismus nutzen. Hierzu werden verschiedene die Symmetrie brechende Hindernisse in der Mitte des Kanals positioniert. Bei der ersten Mikropumpe wird der Temperaturgradient senkrecht zu den Kanalwänden angelegt und gestreckte Hindernisse werden lokal fixiert und zum Gradienten geneigt. Diese geometrische Asymmetrie und die Thermophorese ermöglichen es der Flüssigkeit am Kanal entlang zu fließen. Die resultierenden Strömungsmuster, die Stärke und die Richtung der Nettostromdichte hängen von den geometrischen Kanalparametern ab. Die Stromflussstärke, der Strompfad und die Stromrichtung können durch die Länge, Rauheit und die thermophobischen/thermophilen Eigenschaften der Hindernisse angepasst werden. Der Nettostromfluss für Hindernisse mit verschiedenen Grenzflächeneigenschaften kann durch die anisotrope Thermophorese bestimmt werden. Die zweite Mikropumpe verwendet räumlich fixierte Metall-Nichtmetall Verbindungen als Hindernisse, welche zu den Kanalwänden ausgerichtet sind. Durch Laserbeleuchtung entsteht ein Temperaturgradient aufgrund der höheren Wärmeabsorption des metallischen Endes der heterogenen Verbindungen, der zu einem Nettostromfluss führt. Der resultierende Fernfeldfluss ähnelt dem *Poiseuille*-Fluss. Die Pumpleistung hängt stark von der Länge der nicht - metallischen Anteile sowie dem Abstand zwischen den Hindernissen ab - jedoch nur geringfügig von der Kanalbreite. Zum Abschluss stellen wir eine genauere Übersicht und den Vergleich der Pumpleistungen zwischen den verschiedenen phoretischen Pumpen vor.

# Acknowledgements

*"One falling leaf is indicative of the coming of autumn."* “一叶知秋。”

Huai-nan Tzu[1], An Liu 《淮南子》, 刘安

Doing a PhD is indeed a beautiful and mysterious endeavour after all, although at the beginning can be frustrating. Being part of the quest for new development of thermophoresis from both fundamental and application sides has been challenging and exciting. My happiness obtained from my PhD research can be viewed in many aspects. I can be excited by learning new algorithms, or by some moments when I found a nice explanation for my simulation results, or enjoying some conference talks. I also enjoyed working in the environment of white noise rendered by the strangers in the airport or train station during traveling. It is also fascinating, that many of the complex phenomena occurring in nature follow thermodynamic and mechanical laws which can be formulated in either simple mathematical forms, or several lines of computer programming code. This procedure of learning, observing, perceiving and achieving, has been a colorful journey in my life. However, all of these happiness can not be real without the help and support from other people around me.

First and foremost, thanks beyond thanks to my supervisor Dr. Marisol Ripoll who hosted and has guided me as her PhD student since three years ago. Marisol, without whom I would have never had chances to grow to be a scientist and physicist. Marisol, you always forgive my stupidities and stubbornness, and being open to listen to my naive and wild theories. Thanks a lot for your incredible patience, and for your time on our discussions and correcting my papers and thesis. Moreover, you've given me a lot degrees of freedom on my research projects and such that I have never got bored of my work. It was also very nice of you for supporting my attendances in many conferences, in which I've learned soft matter in general from different perspectives and found inspirations for my own work.

Also I sincerely thank my promoter Prof. Dr. Gerhard Gompper for providing this research opportunity and making this PhD project possible, especially when I was in trouble. I thank him for bring a lot of academic events related to Active Matter and Biophysics into the big group of ICS-2. In such an "active" academic atmosphere, all the members discuss our research "lively". I am also grateful to Prof. Dr. Simone Wiegand as my second examiner who

has spent her precious time on proofreading and examining my thesis, and providing insightful and constructive comments on my work during conferences.

Then, my debt to a number of colleagues and friends is enormous. I would like to mention first Dr. Adam Woyssocki and Prof. Dr. Jinglei Hu (胡晶磊) who helped me on the study of MPC methods and programming, on the writing of restart binary files, when I just started the PhD program. Especially Adam, you taught me “simple” physics. By which I mean you explained me intricate physics effortlessly in popular and easy-to-understand language, during our casual chatting and lunch conversations. I am still impressed that you demonstrated the break-down of Galilean invariance in SRD solvent by moving a cup of coffee. I also appreciated the time I spent with Dr. Chien-Cheng Huang (黄建成) and his family in Düsseldorf. I am much indebted to my co-author Prof. Dr. Mingcheng Yang (杨明成), with whom we had a lot of amazing detailed discussions regarding our research. His rich experience on simulation of thermophoresis, helped me very much on calculation of the local pressure inside the solid-liquid boundary layer under temperature gradient. I also thank Martin Wagner, my officemate. During the past three years, we’ve had a lot stimulating and interesting chatting on our own research problems and results, and also shared some numerical tricks, few lines of code, and sometimes musics. I also want to thank Christian Philipps for helping me on the German abstract, I was so impressed by his quick action.

The PhD in Jülich has not only be pleasant for the above mentioned reasons but also because of the nice connections between other colleagues and friends, sometimes beyond institutes. Here I specially want to thank Mrs. Helga Paffen and Mrs. Meike Kleinen, our secretaries who helped me on administration side, and Mrs. Dorothea Henkel, who solved my problems on computer facility part in an very efficient way. I would also like to thank all my lovely colleagues and friends from ICS-2 and ICS-3, with whom I spent a lot of happy recreation time on such as playing basketball or football, hiking, swimming, partying and eating etc..

Moreover, I would like to acknowledge the major financial support by China Scholarship Council (CSC), and by the Bavarian Ministry of Economic Affairs and Media, Energy and Technology within the joint projects in the framework of the Helmholtz Institute Erlangen-Nürnberg for Renewable Energy (IEK-11) of Forschungszentrum Jülich. EU-COST action MP1305 "Flowing

Matter" is kindly acknowledged for supporting my expenses in several conferences. I also gratefully thank the computing time granted on the super-computer JURECA at Jülich Supercomputing Centre (JSC).

Furthermore, I would like to offer my special thanks to two persons in special ways. I am indebted to Prof. Dr. Jan Dhont, who actually didn't know any of my research until the end of my PhD. I enjoyed the short but stimulative discussion on my research with him. But what has helped me a lot is THE famous book (*An Introduction to Dynamics of Colloids*) he wrote, which has become my favorite book during my PhD. The physics of colloids in this book is well written and explained. It is always a inspiring reading material either I was a layman or has become more sophisticated in the field of colloidal physics. Moreover, I have also enjoyed the lectures by him in IFF spring school and IHRS-BioSoft. Besides, I am really grateful to Prof. Dr. Ran Ni (倪冉), who offered his strongest supporting during the anxious summer in 2014. Ran, you has acted as a mentor in my academic career part so far, every internet or face-to-face conversation with you inspired me to think further and deeper. I admire that you can always point out the crucial factors of the problems straightforwardly. I enjoyed our time in Amsterdam and Porto. I am sure we will meet in the future more often.

Finally, I am deeply grateful for tremendous supporting from my family, which has formed my robust and fundamental inner fuel since I was born. 最后，我想感谢我的家人们，他们对我无穷无尽的支持是我在学术路上一直前进的原动力。 Even though I do have struggled very much to explain you what is soft matter, colloids, thermophoresis and so on. Especially, I would like to dedicate this thesis to my grandmother, Fengzhen Liang (梁凤贞), and grandfather, Xianzhang Tan (谭显章). I owe my ardent and deepest gratitude to you and your incredible and cordial love and support, I wish you both a healthy and happy life forever. 感激你们对我的养育之恩，以及这么多年对我的关爱，支持和理解。我祝你们健康长寿，平安快乐，幸福美满。



# Contents

<b>Abstract</b>	<b>v</b>
<b>Kurzzusammenfassung</b>	<b>vii</b>
<b>Acknowledgements</b>	<b>ix</b>
<b>1 Background: asymmetry, soft matter and thermophoresis</b>	<b>1</b>
1.1 Asymmetry and soft matter . . . . .	1
1.1.1 Symmetry in nature . . . . .	1
1.1.2 Asymmetry in soft matter . . . . .	3
1.2 Thermophoresis: beating Brownian dance by temperature gradient . . . . .	4
1.2.1 Brownian motion . . . . .	4
Short time Brownian motion . . . . .	6
1.2.2 Transport effects induced by temperature gradient . . . . .	6
Thermal diffusion in liquid mixtures . . . . .	6
Thermally driven motion in gases . . . . .	7
Colloidal thermophoresis . . . . .	9
1.2.3 Low Reynolds number hydrodynamics . . . . .	10
1.3 Applications: separation, synthetic swimmers and microfluidics	12
1.3.1 Separation techniques . . . . .	12
1.3.2 Synthetic microswimmers . . . . .	12
1.3.3 Micromachines and micropumps . . . . .	13
1.4 The structure of this thesis . . . . .	13
<b>2 Multi-Particle Collision Dynamics</b>	<b>15</b>
2.1 Motivation . . . . .	15
2.2 Multi-particle collision dynamics and its coupling . . . . .	16
2.2.1 Algorithm . . . . .	16
2.2.2 Temperature gradient . . . . .	17
2.2.3 Hybrid coarse grained methods . . . . .	17
Molecular dynamics . . . . .	18

	MPC-MD coupling . . . . .	19
2.2.4	Simulation parameters in this thesis . . . . .	20
2.3	Transport properties of MPC fluid . . . . .	21
2.3.1	Self diffusivity . . . . .	21
2.3.2	From Poiseuille flow to shear viscosity . . . . .	22
2.3.3	Study on Brownian motion at short time scales . . . . .	23
2.3.4	Hydrodynamical dimensionless numbers . . . . .	24
2.4	MPC simulation of thermophoresis . . . . .	26
2.4.1	Thermophoretic force measurement . . . . .	26
2.5	Color coding in flow stream line patterns . . . . .	27
<b>3</b>	<b>Thermophoresis of spherical colloids</b>	<b>29</b>
3.1	Introduction . . . . .	29
3.2	Phoretic mechanisms: theory . . . . .	30
3.2.1	Macroscopic linear transport . . . . .	31
3.2.2	General solutions of slip velocities for phoresis . . . . .	32
3.3	Simulation studies on macroscopic phoresis . . . . .	34
3.3.1	Simulation implementation . . . . .	35
3.3.2	Results . . . . .	35
3.3.3	Far field flow around phoretic colloids . . . . .	37
3.4	Microscopic mechanism of thermophoretic simulation . . . . .	39
3.4.1	Inhomogeneous pressure . . . . .	39
	Local pressure computation around spherical colloid . . . . .	43
3.4.2	Near field flow maps induced by phoretic forces . . . . .	45
3.5	Hydrodynamic origin of finite size effects . . . . .	46
3.5.1	Analytical evaluation of FSEs factor . . . . .	47
3.5.2	Flow field: simulation vs. analytical theory . . . . .	48
3.5.3	Finite system size scaling . . . . .	49
3.6	Conclusions . . . . .	50
<b>4</b>	<b>Anisotropic thermophoresis</b>	<b>53</b>
4.1	Introduction . . . . .	53
4.2	Model of rods . . . . .	55
4.3	Results . . . . .	56
4.3.1	Linear decomposition of the thermophoretic force . . . . .	56
4.3.2	Does thermophoretic anisotropy induce orientation? . . . . .	59
4.3.3	Aspect ratio effect . . . . .	61
4.3.4	Surface effects . . . . .	63
4.3.5	Thermophoretic anisotropy factor . . . . .	66

4.4	Conclusions . . . . .	68
<b>5</b>	<b>Microfluidic pump driven by anisotropic thermophoresis</b>	<b>71</b>
5.1	Introduction . . . . .	71
5.2	Model and methods . . . . .	73
5.2.1	Device setup . . . . .	73
5.2.2	Simulation setups and parameters . . . . .	73
5.3	Results . . . . .	75
5.3.1	Flow pattern and flow flux . . . . .	75
5.3.2	Influence of PBCs . . . . .	77
5.3.3	Mechanism: anisotropic thermophoresis . . . . .	77
5.3.4	Channel geometrical properties . . . . .	78
	Transverse direction: effect of channel width . . . . .	79
	Longitudinal direction: the role of the separation between obstacles . . . . .	82
5.3.5	Interfacial properties . . . . .	86
	Relating thermophoretic anisotropy factor to flux density	86
	The role of the obstacle aspect ratio . . . . .	87
	Rugosity dependence: flow direction variation . . . . .	90
	Thermophilic or thermophobic: flow path alternation .	92
5.4	Conclusions . . . . .	93
<b>6</b>	<b>Pumping fluid by partially heated pillars</b>	<b>95</b>
6.1	Introduction . . . . .	95
6.2	Model and method . . . . .	97
6.2.1	Composition of the device . . . . .	97
6.2.2	Simulation implementation . . . . .	97
6.3	Discussion . . . . .	98
6.3.1	Influences of aspect ratio . . . . .	98
	Temperature field . . . . .	98
	Flow fields and velocity quantification . . . . .	100
	Flux density . . . . .	101
6.3.2	Channel geometrical effects . . . . .	105
	The role of channel width . . . . .	105
	Dependence of the obstacle interseparation . . . . .	106
6.3.3	Comparison with other thermophoretic micropumps .	107
	Pumping capability . . . . .	108
	Comparison of microfluidic pumping to physical parameters . . . . .	110

6.4	Summary . . . . .	111
<b>7</b>	<b>Thermophoretic orientation of heterodimers</b>	<b>113</b>
7.1	Introduction . . . . .	113
7.2	Alignment . . . . .	114
7.2.1	Linear response theory . . . . .	114
7.2.2	Simulation vs. linear response theory . . . . .	119
7.3	Size ratio effect . . . . .	121
7.4	Isotropic thermal diffusion factor of heterorod . . . . .	123
7.5	Phoretic motion of heterodimeric dispersions in confinement . . . . .	124
7.5.1	Concentration and orientation order . . . . .	125
7.5.2	Confirming the effects of hydrodynamic interaction . . . . .	130
7.5.3	Relaxation time of position and orientation . . . . .	130
7.5.4	Aggregation for different dimer densities . . . . .	132
7.6	Conclusions and outlook . . . . .	135
<b>8</b>	<b>Epilogue</b>	<b>137</b>
8.1	Synopsis . . . . .	137
8.2	Outlook . . . . .	139
<b>A</b>	<b>Analytical calculation for thermophoretic force</b>	<b>141</b>
A.1	The slip flow solution . . . . .	141
A.2	Local pressure gradient solution . . . . .	142
A.3	Force balance solution: summing all the potential interacting forces . . . . .	142
<b>B</b>	<b>Analytical flow field for different boundary conditions</b>	<b>143</b>
B.1	Thermophoretic flow field of fixed colloid confined between walls . . . . .	143
B.2	Thermophoretic flow field of fixed colloid in open PBCs . . . . .	146
<b>C</b>	<b>Further discussion on the rugosity dependence of <math>\alpha_T</math></b>	<b>149</b>
C.1	Geometric effects on $\alpha_{T,\perp}$ and $\alpha_{T,\parallel}$ . . . . .	150
C.1.1	The perpendicular factor $\alpha_{T,\perp}$ . . . . .	150
C.1.2	The parallel factor $\alpha_{T,\parallel}$ . . . . .	151
C.2	Non-geometric effects on $\alpha_{T,\perp}$ and $\alpha_{T,\parallel}$ . . . . .	153
	<b>Bibliography</b>	<b>155</b>
	<b>Eigenhändigkeitserklärung</b>	<b>167</b>

**Curriculum Vitae**



# List of Figures

1.1	Nature exhibits the beauty of symmetry everywhere . . . . .	2
1.2	Phase transitions in liquid crystals . . . . .	3
1.3	Particle suspended in a gas under a temperature gradient $\nabla T$ . . . . .	8
2.1	Self-diffusion coefficient $D$ of a simple solvent simulated with MPC . . . . .	21
2.2	The study of Poiseuille flow and shear viscosity in MPC fluid. . . . .	23
2.3	Hydrodynamic memory effect . . . . .	24
3.1	Spherical particle in an applied gradient $\nabla Y_\infty$ . . . . .	32
3.2	Concentration profiles with different reaction rates . . . . .	36
3.3	Phoretic forces $F_{ph}$ as a function of external gradient $\nabla Y$ . . . . .	36
3.4	Flow field representations of phoretic colloids in simulations. . . . .	38
3.5	Flow velocity profiles as a function of relative distance to colloid center. . . . .	39
3.6	Schematic diagram of local quantity measurements. . . . .	40
3.7	A simplified model for thermophoresis in simulation. . . . .	40
3.8	Local pressure profile . . . . .	42
3.9	Pressure field . . . . .	43
3.10	Pressure averaged at the surface as a function of polar angle $\theta$ . . . . .	44
3.11	Flow inside boundary layer. . . . .	45
3.12	Flow field of colloid confined between walls. . . . .	48
3.13	Flow field induced by twin colloids in periodic temperature gradient. . . . .	49
3.14	Finite size effects of thermal diffusion factor. . . . .	50
4.1	Sketch of the model of rod . . . . .	55
4.2	Sketch of the thermophoretic force of a colloidal rod fixed with different orientations . . . . .	57
4.3	Thermophoretic force obtained from simulations as a time average for a fixed smooth rod . . . . .	58
4.4	Thermophoretic force for fixed rods with different orientations . . . . .	58

4.5	Normalized diffusion coefficient for a freely rotating rod . . . . .	60
4.6	Normalized thermodiffusion factors for rods of fixed diameter $d$ and varying length $L$ . . . . .	61
4.7	Thermodiffusion factors for rods of fixed surface area $S$ . . . . .	63
4.8	Parallel and perpendicular thermodiffusion factors for rods with $L/d = 3.7$ with various interaction potentials. . . . .	64
4.9	Thermodiffusion factors for rods with $L/d = 3.7$ as a function of the rugosity parameter $l/d$ . . . . .	65
4.10	Sketch illustrating the decrease of the thermophoretic force along an indented surface. . . . .	66
4.11	Anisotropic thermophoretic factor $\chi_T$ for different types of rods. . . . .	67
5.1	Schematic representations of the model of micropump and obstacles with various rugosities. . . . .	74
5.2	The flow stream lines and the corresponding flux density. . . . .	76
5.3	Normalized flux density $J_\rho/J_\rho^0$ calculated with different number of obstacles. . . . .	77
5.4	The flow field as a function of varying channel width $H$ . . . . .	79
5.5	The channel width dependence of the flux and stagnation angle . . . . .	80
5.6	Velocity profiles $v_x$ at different cross sections for various channel widths. . . . .	80
5.7	The flow patterns vary with changing of obstacle separation $D$ . . . . .	84
5.8	Flux and stagnation angle/distance vary with separation distance . . . . .	85
5.9	Velocity profiles at different cross sections for various channel width $D$ . . . . .	85
5.10	$J_\rho/\nabla T$ as a function calculated with different $\chi_T$ . . . . .	87
5.11	Flow stream lines in microchannels with obstacles of varying aspect ratio $W/d$ . . . . .	88
5.12	The effects of aspect ratio on flux, stagnation angle and flow profiles. . . . .	89
5.13	Directing the flow via changing the rugosity of obstacles. . . . .	90
5.14	Alternating the flow path via changing colloid-solvent interactions. . . . .	92
6.1	Different types of JPs. . . . .	97
6.2	Schematic representations of micropump and partially metal coated obstacle. . . . .	98

6.3	Temperature fields of different sizes of pillars in the same microchannel. . . . .	102
6.4	Temperature profiles along different axes for different $W/d$ . . .	103
6.5	Maps of flow stream lines for pillars with different aspect ratios.	103
6.6	Flow velocity profiles $v_x$ along different axes for different aspect ratios. . . . .	104
6.7	Flow flux density calculated at different $W/d$ . . . . .	104
6.8	Temperature profiles for different channel width $H$ in axis $A_1 - A_2$ . . . . .	105
6.9	Flow velocities profiles and flux with different channel width $H$ . . . . .	105
6.10	Temperature profiles in $A_1 - A_2$ axes for different $D$ . . . . .	107
6.11	The inter-pillar separation $D$ dependencies of flow velocity profiles and flux densities. . . . .	107
6.12	Flow flux density of two types of micropumps as a function of channel positions. . . . .	108
7.1	Schematic representation of a heterodimer in temperature gradient. . . . .	115
7.2	The alignment of heterodimers in different temperature gradient. . . . .	120
7.3	Size ratio dependence of orientation . . . . .	122
7.4	Thermophoretic forces of a heterorod as a function of temperature gradient . . . . .	124
7.5	Snapshots of simulations with $a48 - r6$ heterodimers . . . . .	126
7.6	The local concentration and orientation. . . . .	128
7.7	The hydrodynamic attraction effect . . . . .	129
7.8	Temporal average of concentration and orientation . . . . .	131
7.9	Snapshot of 10 heterodimers aggregate at the wall . . . . .	132
7.10	Snapshot of 20 heterodimers aggregate at the wall . . . . .	133
7.11	Snapshot of 50 heterodimers aggregate at the wall . . . . .	134
B.1	Schematic diagrams for fixed colloid in temperature gradient confined between walls and by PBCs . . . . .	144
B.2	Analytical calculation of flow velocity with consideration of PBCs and confined walls . . . . .	145
B.3	The flow decay of the Stokes term and the Source dipole term	146
C.1	Schematic diagrams of thermophoretic surface forces on rods	149

C.2	The flow velocity fields of rod perpendicular to $\nabla T$ in different cross sections . . . . .	150
C.3	The magnitudes of the averaged slip flow in different cross sections . . . . .	151
C.4	The local temperature gradient along the long axis . . . . .	152
C.5	The flow velocity fields of rod parallel to $\nabla T$ with different rugosities . . . . .	152
C.6	Schemes of overlapping interacting area of rough and smooth rods with different potentials. . . . .	153

# List of Tables

2.1	Units associated with MPC algorithm. . . . .	21
2.2	Typical values (or order of magnitudes) of dimensionless numbers in this thesis . . . . .	25
5.1	$\chi_T$ and corresponding rescaled flow flux $J_\rho/\nabla T$ of micropump with different interfacial properties . . . . .	86
6.1	Pumping capability of three types of micropumps. . . . .	110



# List of Abbreviations

<b>AP</b>	<b>Anisotropic Thermophoretic Micropump</b>
<b>DPD</b>	<b>Dissipative Particle Dynamics</b>
<b>FEM</b>	<b>Finite Element Method</b>
<b>FSEs</b>	<b>Finite Size Effects</b>
<b>LBM</b>	<b>Lattice Boltzmann Method</b>
<b>LET</b>	<b>Local Equilibrium Thermodynamics</b>
<b>MPC</b>	<b>Multi-Particle Collision Dynamics</b>
<b>MD</b>	<b>Molecular Dynamics</b>
<b>PBCs</b>	<b>Periodic Boundary Conditions</b>
<b>PP</b>	<b>Partially Heated Thermophoretic Micropump</b>
<b>RP</b>	<b>Ratchet Thermophoretic Micropump</b>
<b>TFFF</b>	<b>Thermal Field-flow Fractionation</b>
<b>TP</b>	<b>Thermophoretic Micropump</b>
<b>WCA</b>	<b>Weeks-Chandler-Anderson (potential)</b>



# List of Symbols

$\Omega$	Angular frequency
$l$	Bead-bead distance
$d$	Bead diameter
$\delta$	Boundary layer thickness
$\tau_D$	Brownian or diffusive timescale
$c$	Concentration
$U_{cs}$	Colloid-solvent potential
$U_{cc}$	Colloid-colloid potential
$r_c$	Cutoff radius
$\hat{u}_x, y, z$	Components of orientation unit vector
$H$	Channel width
$\rho$	Density
$\Delta$	Displacement of potential
$D_{DP}$	Diffusiophoretic mobility
$f$	Frequency
$J$	Flux, or angular momentum
$J_\rho$	Flux density
$\mathbf{T}$	Fluctuating torque
$\Psi_{th}$	Fluctuating torque of heterocolloids
$L_D$	Heterodimer bond length
$\tau_{\gamma,trans}$	Inertial (translational) timescale
$\tau_{\gamma,rot}$	Inertial (rotational) timescale
$D$	Inter pillar separation
$Kn$	Knudsen number
$M, m$	Mass
$\mathfrak{R}$	MPC rotation axis
$a$	MPC collision cell size
$h$	MPC collision time, mean free path
$\alpha$	MPC collision angle
$\Delta t$	MD time step
$Mc$	Mach number

$\mathbf{p}$	Momentum
$I_d$	Momentum of inertia
$v_B$	Maximum of the slip velocity
$J_\rho^*$	Normalized flux density
$\hat{\mathbf{u}}$	Orientation unit vector
$\hat{\mathfrak{R}}$	Orientalional operator
$W$	Obstacle length of a pillar in a channel
$\mathbf{r}$	Particle position
$U$	Potential
$\varepsilon$	Potential intensity
$n$	Potential stiffness, or normal unit
$Pe$	Péclet number
$Pr$	Prandtl number
$P$	Pressure (tensor)
$P_\infty$	Pressure at the bulk
$p$	Probability
$\mathbf{f}$	Random force or force density of the fluid
$R$	Radius
$Re$	Reynolds number
$D_r$	Rotational self diffusion coefficient
$\gamma_r$	Rotational friction coefficient
$L$	Rod length
$\zeta$	Reaction rate
$S_T$	Soret coefficient
$v_s$	Slip velocity
$Sc$	Schmidt number
$\varphi$	Stagnation angle
$S_d$	Stagnation distance
$\mathfrak{R}_r$	Size ratio of a heterodimer
$L_x, L_y, L_z$	Simulation box sizes
$T$	Temperature
$\mathbf{G}$	The strength of the fluctuating force
$\mathbf{G}_{rot}$	The strength of the fluctuating torque
$\alpha_T$	Thermal diffusion factor
$\mathbf{F}_T$	Thermophoretic force
$v_T$	Thermophoretic drift velocity
$\Lambda_T$	Thermodiffusion tensor
$D_s$	Translational self diffusion coefficient

$\gamma, \gamma_t$	Translational friction coefficient
$\alpha_T$	Thermal diffusion factor
$\chi_T$	Thermophoretic anisotropic factor
$\chi_H$	Thermophoretic heterogeneity
$\Psi_T$	Thermophoretic torque
$\tau$	Tangential unit
$\eta$	Viscosity
$v, \mathbf{v}$	Velocity



*To my family...*



# Chapter 1

## Background: asymmetry, soft matter and thermophoresis

### 1.1 Asymmetry and soft matter

The subject of this thesis is what we may simply call "*Asymmetric thermophoresis/thermoosmosis*". Before embarking on the analysis of this topic, it is instructive to recap briefly of asymmetry, soft matter and related thermally induced mass transport effects.

In the first place, the human mind is always fascinated by symmetry over asymmetry. Most of us prefer patterns or objects that are in some way symmetrical. For instance, both adults and infants like faces with higher symmetry [2, 3]. More interestingly, the appreciation of symmetry have evolved in different species [4].

#### 1.1.1 Symmetry in nature

Nature reveals various symmetrical objects around us. Sphere, the most symmetrical shape, has different counterparts in the universe such as water droplets, fruits and stars etc.. Antimatter, chiral molecular structures, all manifest symmetry in nature. Figuratively, multitudinous examples of symmetry can be found in nature. From galaxy systems to human body (Fig. 1.1), even downsize to atoms [5]. Deeping down into physical laws, they translate through space and time symmetrically and have no preferred directions. In this sense, symmetry means uniformity or invariance [6].



**Figure 1.1:** Nature exhibits the beauty of symmetry everywhere. (a) Spherical shape of earth, (b) snow crystals with complex symmetries, (c) a “Fibonacci spiral” is formed in the shell of a nautilus, (d) a human’s face demonstrates mirror symmetry. (e) Dazzling symmetry of the Nasir-Al-Mulk Mosque in Shiraz, Iran. Figure credits give to GOOGLE [7] and Mohammad Reza Domiri Ganji [8].

### 1.1.2 Asymmetry in soft matter

However, we shall notice that in soft matter — a research area that encompasses colloidal suspensions, (bio) polymer solutions, liquid crystals and amphiphilic mixtures, as well as self-propelled objects etc.— broken symmetries are ubiquitous. For instance, in a liquid crystal solution, the fact that the building blocks are elongated (or disk-like) largely enriches the phase behaviors with respect to the systems made by spherical particles, as drawn in Fig. 1.2.

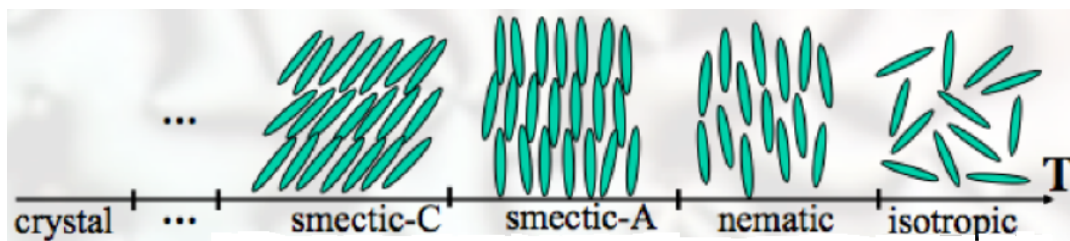


**Figure 1.2:** Phase transitions in liquid crystals. From left to right with increasing of temperature: Ordinary crystals. Smectic liquid crystals with layered translational order; smectic-C phase with tilted arrangement to the normal  $z$  of the layers, while the directions  $z$  and  $-z$  are equivalent in smectic-A phase. Nematic liquid crystals with a rotational order. Both continuous translational and rotational symmetry are stored in isotropic liquids. (Adapted from Ref. [9])

In the soft matter field, "biological systems present additional challenges because they are often far from equilibrium and are driven by strong spatially and temporally varying forces [10]". Lipids, proteins, self-organized superstructures, and tissues are highly asymmetric in shapes and chemistry (compositions) under complex biological processes [11]. Cells for example, are driven out of equilibrium due to the energy fed by the chemical reactions inside the cell. Additionally, external signals such as asymmetric chemical concentration (*Chemotaxis*), or even internal asymmetric myosin motors induced cortex relaxation can lead to cell polarization and directional protrusive motions of cells [12].

In a nutshell, soft matter systems accompanied with asymmetry take many forms to be far from equilibrium, this thesis focuses on one particular form: *thermophoresis*, in which temperature gradient triggers *directional* transport phenomena.

## 1.2 Thermophoresis: beating Brownian dance by temperature gradient

Thermal gradient is of vital relevance to a lot of interesting phenomena in soft matter. The first example would be “the Origin of Life” scenario [13, 14]. Recent studies have shown that temperature gradient on the earth might provide a favorable environment for molecular accumulation with high enough concentration, to form the nucleotide and RNA at the origin of life stage. Another example is the existence of temperature gradient in living cells, which is intrinsically related to fundamental cellular processes, such as the cell cycle and the stimulation of the mitochondria [15]. In colloidal suspensions, the existence of temperature gradient leads to colloidal migration and accumulation, as well as the slip flow in the ambient fluid, this is the so-called thermophoresis.

### 1.2.1 Brownian motion

When a colloidal particle immersed in a fluidlike environment, it suffers chaotic collisions from the solvent particles. Below the certain timescale, say, inertial timescale  $\tau_{\gamma,trans} = M/\gamma_t$  (here  $\gamma_t$  is the translational friction coefficient and  $M$  the colloid mass), a colloid suffers unbalanced collisional forces from the solvent, and is accelerated moving forward due to inertia effect; on the other hand, it is subject to the friction from the surrounding fluid. Beyond such time scale, the inertial force is counterbalanced (damped) by the solvent friction.

Theoretical interpretation of this phenomenon is reported by Paul Langevin in 1908 [16], this random, rapid “kicks” by solvent particles induce so-called thermal fluctuating forces drive colloid forward. The energy scale of these fluctuations is on the order of  $k_B T$ , and transfers this energy to the colloid which is dissipated by the fluid friction. Collisions of the fluid molecules relax much faster than the colloid moves (the typical relaxation time for fluids are of the order  $10^{-14}s$ , while the Brownian particles are  $10^{-9}s$  [17]). This large separation in time scales is sufficient to provide a description in terms of effective random forces  $\mathbf{f}(t)$  as follows [17],

$$\langle \mathbf{f}(t) \rangle = \mathbf{0}, \quad (1.1)$$

and

$$\langle \mathbf{f}(t)\mathbf{f}(t') \rangle = \mathbf{G}\delta(t - t'), \quad (1.2)$$

where  $\delta$  is the delta distribution and  $\mathbf{G}$  measures the strength of these fluctuating force  $\mathbf{f}(t)$  which is a  $3 \times 3$  matrix. During this stochastic process, the fluctuation of forces is regarded as Gaussian white noise. Considering all the mechanisms aforementioned, the time evolution of the linear momentum  $\mathbf{p}$  of translational motion is described by the Langevin equation [16],

$$d\mathbf{p}/dt = -\gamma\mathbf{p}/M + \mathbf{f}(t). \quad (1.3)$$

Likewise, the rotational Brownian motion can be expounded as Newton's equation of motion, supplemented with fluctuating torques resulting from collisions of solvent molecules with the colloids. The mathematical form is written as,

$$d\mathbf{J}/dt = -\gamma_r\Omega + \mathbf{T}(t), \quad (1.4)$$

where  $\mathbf{J}$  is the angular momentum and  $\gamma_r$  the rotational friction coefficient.  $\mathbf{T}(t)$  is termed as fluctuating torque, which obeys,

$$\langle \mathbf{T}(t) \rangle = \mathbf{0}, \quad (1.5)$$

and,

$$\langle \mathbf{T}(t)\mathbf{T}(t') \rangle = \mathbf{G}_{rot}\delta(t - t'), \quad (1.6)$$

where  $\mathbf{G}_{rot}$  is the strength of the fluctuation torque.

A typical value of the relaxation time of the translational and rotational motion of a colloid is both of the order of a *nanosecond*. In the following, we specialize to the time scales which beyond those relaxation time  $\tau_{trans}$  and  $\tau_{\gamma,rot} = \mathbf{I}/\gamma_r$  (where  $\mathbf{I}$  is the moment of inertia), at which the inertial forces and torques on the colloid can be neglected. Here we dubbed a time scale as *Brownian or diffusive time scale*  $\tau_D$  which is larger than  $\tau_{trans}$  (or  $\tau_{rot}$ ) but small enough to resolve position and orientation in sufficient detail.

### Short time Brownian motion

Conventionally, the thermal fluctuating force is assumed to be random and characterized by a Gaussian white noise spectrum. From Einstein's assumption, the kinetic energy of the colloid is damped into fluid by solvent friction with a constant friction coefficient. However, the fact is the ambient fluid is rearranged when the colloid collides with the ambient fluid particles. The momentum transferred from colloid to fluid particles, acts back on the colloid beyond the commonly named hydrodynamic timescale  $\tau_h = R^2\rho_0/\eta$ , such that the long range correlation has built [18, 19]. This phenomena is also termed as hydrodynamic memory effect [17], as the this stochastic process stores the "memory" of the movement of the colloid. Experimentally, Franosch [20] teases out the colored noise of solvent by trapping colloid with a harmonic potential. These studies confirm that the memory effect of solvent and the friction coefficient is dependent on the moving velocity of the colloid.

### 1.2.2 Transport effects induced by temperature gradient

Brownian motion is chaotic and therefore increases entropy to reach thermodynamic equilibrium. However, once a colloidal system driven out of equilibrium by a *temperature gradient*, the entropy decreases as the colloids undergo directional motion. Temperature gradient, is understood as a general thermodynamic force which beats chaotic Brownian dances. Since Ludwig found thermal diffusion in molecular mixture in 1856, all present researches about mass transport in temperature gradient somewhat share some common features but discrepant subtly. Therefore it is important to take a glance at thermal gradient induced mass transport effects.

#### Thermal diffusion in liquid mixtures

As stated above, thermal gradient plays a significant role in soft matter. In the framework of molecular mixtures, this transport effect is termed as *thermal diffusion*, or *Ludwig–Soret effect* [21, 22]. It describes that the component of the mixture and molecular counterpart travel in different directions along temperature gradient. It has been largely used to separate mixtures or for solute accumulation. In a binary mixture, two opposite mass fluxes counteracting each other in non-equilibrium steady states. The total mass flux  $J_m$

of component 1 vanishes at the stationary state, which is expressed as the following phenomenological equation,

$$J_m = 0 = -\rho D \nabla c - \rho c(1-c) D_T \nabla T. \quad (1.7)$$

$D$  is the Fickian diffusion coefficient,  $c$  the concentration of component 1 in weight fractions,  $\rho$  the mass density and  $D_T$  is the so-called *thermal diffusion coefficient*. Eq. (1.7) provides the definition of the well-known Soret coefficient  $S_T$

$$S_T \equiv -\frac{1}{c(1-c)} \frac{\nabla c}{\nabla T}. \quad (1.8)$$

Here  $S_T > 0$  means component 1 prefers cold area, while  $S_T < 0$  is in the opposite and this is the standard sign convention. Thermal diffusion in liquid mixtures has been a hot topic for several decades and arises many fundamental questions. For instance, the sign of  $S_T$  is determined by many parameters such as *mass, moment of inertia, size, molecular interaction*, although the relation between them is not always clear [21].

### Thermally driven motion in gases

Thermally directed motion of solid in gas phase has been studied over one century. Due to historic reason, it is also termed as “*thermophoresis*”, as the mechanism is similar but much simpler than what in the liquid phases. Aerosol colloids, or dust particles suspended in gases, was first observed by Tyndall in 1870 that promote to the cold side; Crookes found similar effect in radiometer.

The mechanism of thermophoresis in gases is relatively trivial, but subtly related to thermophoresis in liquids. Particularly, in the gas kinetic theory the thermophoretic force is calculated by solving the Boltzmann equation with the *specular* or *diffusive reflection* rule for the gas-colloid coupling. The gas kinetic theory usually considers a moderate or large *Knudsen* number  $Kn = \lambda/R$ , this is the ratio between the mean free path of gas molecular  $\lambda$  and aerosol particle radius, as illustrated in Fig. 1.3. In the case of low density gases  $Kn \gg 1$ , the direction of motion can be predicted intuitively. The momentum transferred by collision at the hot side of dust particle is significantly larger than that at the cold side, such that the dust particle maneuvers to the cold area. In the opposite limit, when  $Kn \ll 1$  and gas at moderate

pressure, sometimes is termed as “quasi-hydrodynamic regime”. This problem is actually fundamentally resolved by Maxwell [23]. With the presence of temperature gradient, and a solid boundary (aerosol particle) surface  $S$  submersed in rarefied gases, molecules suffer no molecular collision before hitting the wall within a length of  $\lambda$ . Taking the equilibrium distribution  $f_0(v)$  of the molecular speed, the total momentum exchange can be estimated with the first order of Boltzmann equation [24],

$$f(v) = \left[ 1 + Cv_z \left( 5/2 - \frac{mv^2}{2k_B T} \right) \right] f_0(v), \quad (1.9)$$

here  $m$  is the molecular mass,  $C$  is a normalized constant, and the thermal gradient is taken along  $z$ . Eq. (1.9) indicates that even in this *quasi-hydrodynamic* regime ( $Kn \ll 1$ ), the momentum transfer turns out to be larger for those molecules coming from the hot side. Shortly after Maxwell’s result, Epstein [25] derived the thermal drift velocity  $v_T$  as a function of gas viscosity  $\eta$ , number density  $\rho$ , and solid, gas thermal conductivity  $\kappa_p$  and  $\kappa_g$  respectively [24, 25]:

$$v_T = \frac{3\eta}{2\rho T} \left( \frac{\kappa_g}{2\kappa_g + \kappa_p} \right) \nabla T_\infty, \quad (1.10)$$

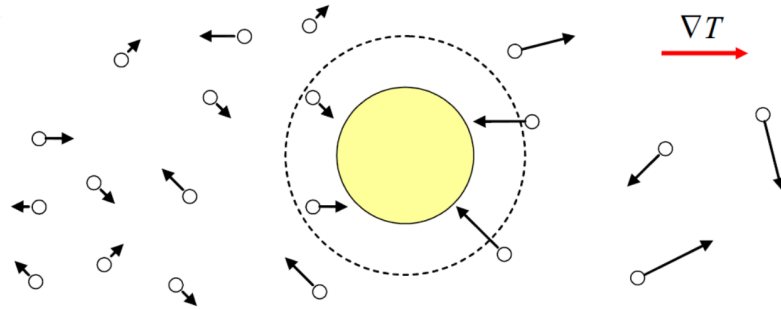


**Figure 1.3:** Particle suspended in a gas under a temperature gradient  $\nabla T$ . The dashed circle indicates the distance corresponding to the molecular mean free path  $\lambda$ . A thermal creep flow (not shown) in side this layer is formed and slides to higher temperature; accordingly the suspended particle moves to the lower  $T$ . (Adapted from Ref. [26])

We would like to underline that (i) within a thickness of the order of mean free path the  $\lambda$ , pressure tensor becomes anisotropic around the suspended particle; (ii) dust particle effectively drifts towards the cold side; (iii) bulk gas properties enter the problem only through the thermal conductivity  $\kappa_p$  of the

particle couples with  $\kappa_g$ , also influence the local temperature field around the particle via heat equation [27].

Gas thermophoresis can be understood by means of kinetic theory, the tendency of movement of the particle is always to the cold side. Nevertheless, the study of areal colloids in gases plays an vital role in aerosol industry [28, 29], and has been largely explored also for the dust particles of within different shapes. As we expect, the anisotropic effects of thermophoresis in gases is intuitive and easily exploited in the framework of kinetic theory and low Reynolds number hydrodynamics [30].

### Colloidal thermophoresis

As we discussed before, the large separation of time scales in colloidal thermophoresis enables us to coarsening the non-equilibrium thermodynamic equations. Furthermore, it has been discovered that the timescale for thermal diffusivity is much shorter than that for Brownian motion. In this sense the temperature profile can be understood to equilibrate *instantaneously*, in the time scale where the colloid moves. A simple linear dependence  $T(z) = T_0 + z\nabla T$  of temperature various is employed here. In dilute suspensions, the modified Smoluchowski equation describes the probability distribution function  $P$  under external field [17],

$$\frac{\partial P}{\partial t} = \nabla \cdot \left[ -\frac{P}{\gamma_t} \mathbf{F}_T + D_t \nabla P \right], \quad (1.11)$$

where  $\mathbf{F}_T$  is referred to as thermophoretic force,  $\gamma_t$  the translational friction coefficient and  $D_t = k_B T / \gamma_t$  the translational diffusion coefficient. This is a naive interpretation of thermophoresis which equalizes  $\mathbf{F}_T$  as an external global body force, just like system suffers gravitational field, electric field and magnetic field. If the solution contains a low density suspension of  $N$  Brownian particles of mass  $M$ , then linear superposition applies.  $c\mathbf{F}_T = k_B T$ , and  $c(\mathbf{r}) = NMP$ . Recalling the definition of *Soret* coefficient,

$$\frac{dc}{dz} = -cS_T \frac{dT}{dz}. \quad (1.12)$$

Substitution of Eq. (1.12) and the expressions above into Eq. (1.11), one obtained [31],

$$S_T \nabla T = -\frac{1}{k_B T_0} \mathbf{F}_T. \quad (1.13)$$

Using thermal diffusion factor  $\alpha_T = S_T T_0$ , which is a dimensionless number characterized the thermophoretic force. Then Eq. (1.13) is rewritten as,

$$\mathbf{F}_T = -\alpha_T k_B \nabla T. \quad (1.14)$$

Albeit the later discussions in Chapter 3 will reveal that  $\mathbf{F}_T$  is quite different from body force (e.g. Stokes drag), and stress that thermophoresis is the consequence of surface forces rather than a body force. Specifically, Eq. (1.14) denotes the relation between macroscopic thermophoretic force and external temperature gradient.  $\alpha_T$  also plays an important role in asymmetric colloidal systems. This theoretical derivation here is sufficient for us to understand linearized thermophoretic behaviors, which covers the major part of colloidal thermophoresis.

As a step further, Piazza [24] discussed thermophoresis with linear response theory. The temperature fields  $T(\mathbf{r})$ , auxiliary field  $\mathbf{w}(\mathbf{r})$  and external potential  $V(\mathbf{r})$  are assumed vary slowly in space and basically constant on the correlation length scale of the fluid. Thus, the local equilibrium can be defined and the distribution function is perturbed in the linear order. This based on the assumptions that the equilibrium free energy and chemical potential are still valid outside equilibrium but with local temperature. Due to large viscous dissipation, local equilibrium picture holds as long as mechanical equilibrium is satisfied [24]. In stationary states this leads to the linearized hydrodynamic equations: the continuity equation, the Navier-Stokes (NS) equation and the heat transport equation. Both local equilibrium and hydrodynamic approaches are delicately applied on thermophoresis [27, 32, 33]. Interestingly, a unified description which combines those two approaches has been reported in Burelbach et.al [34].

However, as also described by Piazza, the microscopic interpretation is not clear for thermophoretic phenomena. Despite this, his linear response description shows that colloidal thermophoresis, both in gases and in liquids, can be interpreted in the framework of continuum hydrodynamics.

### 1.2.3 Low Reynolds number hydrodynamics

As outlined above, thermophoresis is also understood in the framework of continuum low Reynolds number hydrodynamics. Before we derive the solution of thermophoresis which is the *slip velocity* via continuum approach

explicitly in Chapter 3, the basic concept of low Reynolds number hydrodynamics are presented below.

The Navier-Stokes equations provide a continuum description of the flow of a Newtonian, incompressible fluid [35]

$$\rho \left[ \frac{\partial \mathbf{v}}{\partial t} + (\mathbf{v} \cdot \nabla) \mathbf{v} \right] = -\nabla P + \eta \nabla^2 \mathbf{v} + \mathbf{f}, \quad \nabla \cdot \mathbf{v} = 0, \quad (1.15)$$

where  $\mathbf{v}(\mathbf{r}, t)$  is the fluid velocity at position  $\mathbf{r}$  and time  $t$  of a fluid of density  $\rho$  and dynamic viscosity  $\eta$  driven by a pressure gradient  $\nabla P$  and a body force (force per unit volume)  $\mathbf{f}$ . The terms on the left hand side of Eq. (1.15) are the inertial terms which describe the transport of momentum and  $\eta \nabla^2 \mathbf{v}$  describes the viscous dissipation that results from velocity gradients.

Dimensionless variables denoted by a tilde, can be defined by choosing a length scale  $L_0$  and a velocity scale  $V_0$

$$\tilde{v} = \frac{v}{V_0}, \quad \tilde{x} = \frac{x}{L_0}, \quad \tilde{\nabla} = L_0 \nabla, \quad \tilde{t} = \frac{V_0}{L_0} t, \quad \frac{\partial}{\partial \tilde{t}} = \frac{L_0}{V_0} \frac{\partial}{\partial t}, \quad (1.16)$$

In terms of the dimensionless variables the Navier-Stokes equation becomes

$$\left[ \frac{\partial \tilde{\mathbf{v}}}{\partial \tilde{t}} + (\tilde{\mathbf{v}} \cdot \tilde{\nabla}) \tilde{\mathbf{v}} \right] = -\frac{L_0}{V_0^2 \rho} \nabla P + \frac{\eta}{L_0 V_0 \rho} \tilde{\nabla}^2 \tilde{\mathbf{v}} + \frac{L_0}{V_0^2 \rho} \mathbf{f}, \quad (1.17)$$

Eq. (1.17) shows that relative magnitude of the inertial and viscous terms in the Navier Stokes equation is characterized by a dimensionless number, the *Reynolds number*

$$Re = \frac{\text{inertial response}}{\text{viscous response}} \sim \frac{\rho L_0 V_0}{\eta} \quad (1.18)$$

For water  $\rho/\eta \sim 10^6 \text{ s/m}^2$ , so colloids, polymers or microswimmers moving in microflows with length scales  $\sim 1 - 100 \mu\text{m}$  and velocity scales  $\sim 1 - 100 \mu\text{m s}^{-1}$  have Reynolds numbers  $Re \sim 10^{-6} - 10^{-2}$ . Thus the inertia terms can be neglected, and the Navier Stokes equations reduce to the Stokes equations

$$-\nabla P = \eta \nabla^2 \mathbf{v} + \mathbf{f}, \quad \nabla \cdot \mathbf{v} = 0, \quad (1.19)$$

The Stokes equations dominate the dynamics of the fluids in- and out-of-equilibrium, which plays a crucial role in a lot of soft matter systems.

## 1.3 Applications: separation, synthetic swimmers and microfluidics

Thermophoresis not only challenges the fundamental non-equilibrium statistical physics, also is of importance on several directions of application such as separation techniques, microfluidics, and synthetic microswimmers. As they are closely related, the applications of thermodiffusion in liquid mixture are also briefly reviewed.

### 1.3.1 Separation techniques

Even though the micromechanism of thermophoresis or thermodiffusion is still elusive, it has been utilized on separation science since early of last century [36]. In liquid mixtures, the components can be driven apart by the presence of temperature. As the result of drift motion induced by temperature gradient, different components react to the gradient disparately. Hence, thermodiffusion has been applied on isotope separation [37, 38]. Besides this, combining a capillary channel flow with orthogonally applied temperature gradient, the suspended particles (colloids, macromolecules and supramolecular assemblies) can be accumulated at the different positions at the channel walls along the channel. This is used in the well-known *thermal Field-flow Fractionation* (TFFF) [39, 40]. The separation mechanism is mainly that particles response differently to temperature gradient and shear rate. This technique has provided novel and efficient approach on fractionation.

### 1.3.2 Synthetic microswimmers

Thermophoresis has also been used as the basic principle to fabricate microswimmers, which is the synthetic analogy to natural swimmers such as paramecium, bacteria and sperm. By way of example, colloids with patchy metal coating of spherical particles under laser illumination, can create non-uniform temperature field and results in self-propulsion. These thermally active colloids exhibit exotic stochastic behaviors due to thermophobic and thermophilic properties [41, 42]. This strategy also can be applied in dimeric swimmers, as studied by Yang [43] and Wagner [44], dimeric swimmers with more degrees of tunability show different flow patterns from spherical Janus

swimmers, they also can form novel cluster structures due to lateral hydrodynamic attraction and size ratio.

### 1.3.3 Micromachines and micropumps

In the last years has been a large research activity in the development, optimization and miniaturization of thermophoretic microdevices, which aim to rectify recover unused heat into directed motions. By virtue of mesoscale hydrodynamics simulation, several pioneer works on fabrications of micromachines and micropumps have been reported by Ripoll's group. A microgear and microturbine are proposed in Ref. [45] and Ref. [46] respectively. The introduced microgear constructed by circular walls and circular ratchet with higher temperature in the center. Hence, different surface temperature gradients are formed along the asymmetric ratchet teeth. The gradient asymmetry results in unbalanced thermophoretic force and torque. Eventually the gear undergoes directional rotation at the steady state, perpendicular to the temperature gradient. Different from this, the microturbine, which takes the advantage of anisotropic thermophoresis and cross asymmetry of two blades, rotates parallel to the temperature gradient. Moreover, thermophoresis is rephrased as thermoosmosis in the sense of fluid manipulation. Ref. [47] suggests a series of micropumps which employ thermoosmosis and ratchet walls with five geometric descriptions. Consequently, the resulting diverse flow fields are reminiscent of shear flow, capillary flow, elongational flow, Rayleigh-Bénard convection flow and Couette flow.

## 1.4 The structure of this thesis

As reviewed above, thermophoretic mechanism offers a wide range of scientific insights in soft matter field. In this thesis, we aim to probe thermophoresis in the case of colloidal particles with geometric asymmetry (i.e. particles with asymmetrical shape and rugosity) and/or compositional asymmetries (i.e. particles are composed of different materials [11]), and their applications in microfluidics. In Chapter 2 we outline the basic simulation algorithm and how it models correct thermophoresis. Chapter 3 focuses thermophoresis in

spherical colloids, from both theory and simulation viewpoints. We especially elucidate how our simulation method properly captures the underlying physics of thermophoresis. In Chapter 4, we investigate thermophoresis beyond spherical shape, which is termed as anisotropic thermophoresis. Chapter 7 explores the thermophoretic orientation a heterodimer via both theory and simulations. Chapter 5 employs the basic mechanism of anisotropic thermophoresis for fluid pumping. In Chapter 6, inspired by the study of synthetic Janus particles, we propose and investigate the flow and flux of micropump fabricated by patchily coated pillars. Finally, in Chapter 8, we summarise our findings and discuss some avenues for future research in this area.

## Chapter 2

# Multi-Particle Collision Dynamics

### 2.1 Motivation

Complex fluids like colloidal suspensions, polymer solutions, as well as wide range of biological systems, contain billions of atoms with length scales range from nanometer to micrometer. Most related systems are out-of-equilibrium and elusive to theoretical and experimental studies. Computer simulations allow us to explore numerous systems and geometries at relatively low cost and at various levels of detail. Thus, computational physics is widely seen as a third approach to scientific discovery, complementing traditional experimental and theoretical techniques.

In thermophoresis, random, diffusive motion, hydrodynamics and solid-liquid interactions and often together with complex geometries must be all accounted for. Therefore, simulation study on thermophoresis is computationally accessible and feasible but with delicate considerations of coarse graining. On one hand, ordinary full atomic approach such as molecular dynamics (MD) is still computationally expensive; and continuum mechanics model such as finite element method (FEM) lacks the simplicity to describe thermal fluctuations and complex geometries. On the other hand, not all the molecular details of the colloid and the liquid are significant to influence the understanding of phoretic phenomena. In this Chapter, we sketch out one very efficient particle based algorithm known as multi-particle collision dynamics (MPC) and how it is coupled into complex colloidal systems.

## 2.2 Multi-particle collision dynamics and its coupling

### 2.2.1 Algorithm

It has been a fast and important development of several mesoscale hydrodynamic simulation techniques and their applications on soft matter systems since the past decades. They all aim to a coarse-grain description of the fluid, while maintaining the essential physics on the length and/or time scales of interest. In parallel with Lattice Boltzmann method (LB), Dissipative Particle Dynamics (DPD), MPC method with its efficient routine for implementation draws numerous attention since it was developed.

The MPC fluid is described by  $N$  point particles where two essential steps involved [10, 48, 49]. One is streaming step, at which all particles move ballistically, this is,

$$\mathbf{r}_i(t+h) = \mathbf{r}_i(t) + \mathbf{v}_i(t)h, \quad (2.1)$$

here  $\mathbf{r}_i(t)$  and  $\mathbf{v}_i(t)$  indicate the position and velocity of  $i$  th particle at time  $t$ , respectively;  $h$  is the collision time which indicates time interval between two consecutive collisions. In the language of kinetic theory, it is termed as mean free time. The other step is collision step, particles are grouped into cubic collision cells with size of  $a$ , and each particle interacts with other members in the same cell by performing stochastic collision, i.e. redirecting the relative velocity of particle by a certain angle  $\alpha$  with respect to the center of mass velocity in that certain cell. In three dimensions, this procedure can be explicitly expressed as,

$$\begin{aligned} \mathbf{v}_i(t+h) = & \mathbf{v}_{cm}(t) + \tilde{\mathbf{v}}_{i,\perp}(t) \cos(\alpha) + \\ & (\tilde{\mathbf{v}}_{i,\perp}(t) \times \mathfrak{R}) \sin(\alpha) + \tilde{\mathbf{v}}_{i,\parallel}(t), \end{aligned} \quad (2.2)$$

where  $\alpha$  is the fixed rotational angle,  $\mathbf{v}_{cm}$  the center-of-mass velocity of a certain collision cell,  $\tilde{\mathbf{v}}$  the particle's relative velocity with respect to the center-of-mass of a certain cell, its parallel and perpendicular components along the randomly picked rotation axis  $\mathfrak{R}$  (a unit vector) are distinguished by  $\parallel$  and  $\perp$  symbols. Moreover, to guarantee the Galilean invariance, all particles are shifted by the same random vector with components uniformly distributed in the interval  $[-a/2, a/2]$  before the collision step [50]. As we show here, MPC method intrinsically contains thermal fluctuations, and conserves

energy and linear momentum both globally and at the collision box level. The angular momentum conservation for MPC in this work has not been comprised, since recent work provided the evidence that angular momentum conservation in MPC fluid does not influence the hydrodynamics of phoretic behavior [51]. Moreover, the simple scheme of the MPC algorithm allows us to calculate various analytical expressions of transport coefficients of MPC fluid with high numerical stability and accuracy [10]. In contrast, other mesoscale particle-based algorithms such as DPD, provide 50% deviation of the computing of the fluid viscosity.

### 2.2.2 Temperature gradient

To study thermophoresis, proper heat transport behavior of the fluid should be accounted for in the simulated algorithm. The heat transport properties in MPC solvent have been systematically studied by simulations as well as analytical calculations [52–57]. The fluid environment rendered by MPC solvent can transfer heat with well-defined thermal conductivity. Temperature gradient in MPC fluid can be established via imposing thermostats or energy flux like a Maxwell demon at boundaries [57–60]. Here we settle the non-isothermal environment for colloidal particles by rescaling the temperature at two boundaries with layers of thickness  $a$  close to the walls by  $T_c = \bar{T} - \delta T$  and  $T_h = \bar{T} + \delta T$  after every collision step. To mimic no-slip boundary conditions, bounce back rule (the velocity of a particle is reversed from  $\mathbf{v}$  to  $-\mathbf{v}$  if it intersects a wall) is performed. After some relaxation time, the constant temperature gradient  $\nabla T$  is constructed. Afterwards, we repeat the same routine to maintain a stationary temperature profile.

The boundary conditions mostly used in the following chapters (i.e. from Chapter 3 to 7) are thermostats at the walls with no-slip boundary conditions. Alternatively, periodic boundary condition along temperature gradient direction is also employed to study thermoosmotic flow, pressure along walls or finite size study of thermal diffusion factor (Chapter 3).

### 2.2.3 Hybrid coarse grained methods

Colloids interact with MPC solvent via molecular dynamics scheme. The colloid solvent interaction is then accounted for as Lenard-Jones type potentials. Other coupling protocols are also possible to mimic the physics of

phoretic behaviors, such as MPC coupling, in which colloid is considered as heavier point particles and interplay with fluid particle via SRD [61]; or coupling with hard sphere with no-slip boundary conditions on the colloid surface [62–65] with proper thickness of boundary layer. In this thesis, the reason we consider Lenard-Jones type potentials for solid-liquid potential is twofold. One is that the soft potential can create the boundary layer nearby the colloid outer surface. Thus, a pressure gradient is formed inside the boundary layer in the occurrence of the local temperature gradient or concentration gradient, which captures the physics of phoretic phenomena. The other reason is it computationally straightforward, compared with those consider no-slip boundary conditions plus boundary layer or soft potentials.

### Molecular dynamics

In molecular dynamics simulations, the dynamics of the system are explicitly taken into account, and the particles move according to Newton's Law which defines the equations of motion of the particles in the system. In conventional MD, where the potential continuously changes as a function of the distance between particles, the equations of motion of the particles can be integrated with fixed time steps. The evolution of the system is then driven by time steps. The velocity-Verlet integration algorithm, has been used to update the equation of motion of particles since it provides a simple and accurate integration of the equations. Applying velocity-Verlet algorithm on a particulate system contains  $N$  particles with mass  $m_i$ , the update of particle position  $\mathbf{r}_i(t)$  and velocity  $\mathbf{v}_i(t)$  takes the form [66]

$$\mathbf{r}_i(t + dt) = \mathbf{r}_i(t) + \mathbf{v}_i(t)dt + \frac{1}{2m_i}\mathbf{f}_i(t)dt^2 \quad (2.3)$$

$$\mathbf{v}_i(t + dt) = \mathbf{v}_i(t) + \frac{1}{2m_i}[\mathbf{f}_i(t) + \mathbf{f}_i(t + dt)]dt. \quad (2.4)$$

Here the instantaneous net force on particle  $i$  exerted by other surrounding particles are obtained from  $\mathbf{f}_i(t) = -\nabla_{\mathbf{r}_i} \sum_{i=1, i \neq j}^N U(\mathbf{r}_{ij})$ , when a pair-wised potential  $U(\mathbf{r}_{ij})$  is applied. A complete update of particle position and velocity, the force  $\mathbf{f}_i$  should be renewed twice before and after employing Eq. (2.3).

In this thesis, the colloid (or solid obstacle) is modeled as one or multiple spherical beads. The excluded volume interactions between beads and the ambient solvent are performed via generalized Mie-Kihara type potentials [58,

67–69]

$$U_{cs}(r) = \begin{cases} \infty; r \leq \Delta \\ 4\varepsilon \left[ \left( \frac{d}{2(r-\Delta)} \right)^{2n} - \left( \frac{d}{2(r-\Delta)} \right)^n \right] + C; \Delta < r < r_c \\ 0; r_c \leq r \end{cases} \quad (2.5)$$

Here  $r = |\mathbf{r}_{cs}|$  is the distance between the bead center and the fluid particle,  $\varepsilon$  refers to the potential intensity, is taken as  $\varepsilon = k_B \bar{T}$ . The bead diameter is  $d = 2R$  ( $R$  the bead radius), and  $n$  is a positive integer describing the potential stiffness. Eq. (2.5) gives the well-known Lennard-Jones potential when  $n = 6$  and  $C = 0$  [70]; and renders the *Weeks-Chandler-Andersen* potential if  $n = 6$  and  $C = \varepsilon$  [71]. The parameter  $\Delta$  refers to a potential displacement [72, 73], which we fixed as  $\Delta = 0$  unless specified. The repulsive or attractive LJ potentials are obtained by simply considering  $C = \varepsilon$  or  $C = 0$  respectively, together with the adequate cutoff distance  $r_c$ . For the repulsive potential in Eq. (2.5),  $r_c = 2^{1/n}R$ . For attractive potential,  $r_c = 2.5R$  if  $n = 6$ ; in this case  $U_{cs,n=6}(r_c) \rightarrow 0$ . For  $n$  with other integers, the potential is truncated at the position where the  $U_{cs}(r_c) = U_{cs,n=6}(2.5R)$  [58].

The repulsive and attractive potentials with stiffness  $n = 6$  and  $\Delta = 0$  will be denoted as  $r6$  and  $a6$  respectively, and similar for other  $n$  values. If the potential is displaced by a distance  $2$ , i.e.  $\Delta = 2$  for instance, these will be  $(\Delta 2, r6)$  and  $(\Delta 2, a6)$  instead. The mass of colloid is chosen such that the it is neutrally buoyant, although our results are not really depending on this value at the over damped limit. Moreover, a cell-Verlet list is combined into MD integration to speed up the MD simulations.

### MPC-MD coupling

To couple the dynamics of colloids with MPC fluid, the outline of the MPC-MD simulation for colloidal system is described below:

1. Initialize the velocities and positions of the particles in the system. Make sure the MPC point particles at the outside of the colloid-solvent interaction range.
2. Initialize the cell-Verlet list for the system
3. Perform the molecular dynamics part.

4. After every  $N_{MD}$  MD time steps, say,  $N_{MD}dt = h$ , perform MPC streaming step for particles outside of the cell-Verlet list. Update the cell-Verlet list.
5. Perform the collision step for all of the MPC particles.
6. If necessary, employ isothermo- or nonisothermostats.
7. Repeat steps 3 6.

Given that the computation of the MD part is still time consuming and the system size has to be big enough to decrease influence of finite size effects, a parallelized code can largely accelerate the speed of simulations. Here we implemented the OpenMP computing for this hybrid code. This parallelized technique enables multiple threads in a computer to perform computations simultaneously for one simulation job, and the speed of computation can be accelerated to over fivefold.

#### 2.2.4 Simulation parameters in this thesis

We choose  $m = k_B T = a = 1$  in all the simulation implementations. Such that the length is measured in cell length unit  $a$  (or more practically the bead diameter  $d = 2.5a$ ). Time is quantified in unit of  $\sqrt{ma^2/(k_B T)}$ . The other physical parameters can be represented by *length*, *mass*, *time*. Although several parameters are different for specific setups, the most frequently used ones are following described:  $h = 0.1\sqrt{ma^2/(k_B T)}$ ,  $\Delta t = 0.002\sqrt{ma^2/(k_B T)}$ ,  $\epsilon = 1.0k_B T$ . These are the standard parameters which are employed in this thesis, unless otherwise stated. With this simplification, we can directly omit the MPC units. Table 2.1 summarizes the basic units in MPC algorithm and their meanings, also shows how to arrive other units. For convenience, we call this procedure as “MPC units convention”.

Basic Units			
Scale	Natural Unit	comment	value
Length	$a$	Cell size	1
Mass	$m$	Solvent particle mass	1
Energy	$k_B T$	Thermal energy	1
Rotation angle	$\alpha$	Rotation angle in SRD	$130^\circ$
Collision time	$h$	Mean free time	0.1
Derived Units			
Scale	Derived Unit	comment	value
Density	$\rho = \langle N_c \rangle / a^3$	Solvent particle density	10
Time	$\sqrt{ma^2 / (k_B T)}$	Alternatively $h = 0.1$	none
MD time	$dt$	MD time interval	0.002
Diffusivity & Viscosity	$\sqrt{a^2 k_B T / m}$	none	none

**Table 2.1:** MPC units convention: Units associated with MPC algorithm. After Ripoll and Shendruk [18, 74].

## 2.3 Transport properties of MPC fluid

The previous section outlines the simulation scheme of MPC. Compared with explicit expressions and detailed simulation procedures, we hereby quantify important physical quantities such as *self-diffusion coefficient*  $D_s$ , *shear viscosity*  $\eta$  at different values of the mean free time  $h$ .

### 2.3.1 Self diffusivity

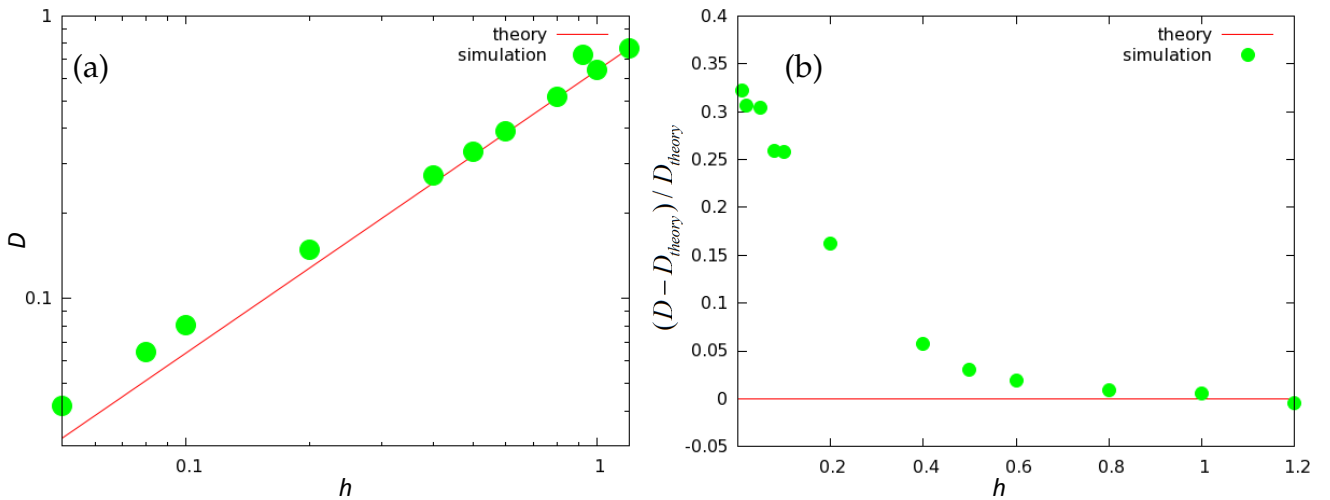


**Figure 2.1:** Self-diffusion coefficient  $D$  of a simple solvent simulated with MPC as a function of the collision time  $h$ . Adapted from Ripoll [18].

Self-diffusion describes the displacement of a single particle affected by the thermal interactions. In the MPC solvent, self-diffusion coefficient  $D$  can be derived analytically by *kinetic theory*. We calculate  $D$  by measuring mean square displacement (MSD) numerically. The agreement between analytical prediction and simulation is depicted in 2.1, where it is shown that when collision time  $h$  is larger than 0.1, the theoretical predictions describe numerical results nicely. However, deviation occurs when  $h$  is smaller than 0.1. This can be explained because small collision time results in the breakdown of molecular chaos assumption in the theory [10].

### 2.3.2 From Poiseuille flow to shear viscosity

*Poiseuille flow* [35], refers to the flow of a fluid along a channel with width of  $H$ , driven by a pressure gradient  $\partial P/\partial x$  between two parallel no-slip walls. Given that we are in the low Reynolds number regime, the flow velocity satisfies the Stokes equation

$$\eta \frac{\partial^2 v_x(z)}{\partial z^2} = \frac{\partial P}{\partial x}, \quad (2.6)$$

with boundary conditions  $v_x(0) = v_x(H) = 0$ . Solving this equation we obtain,

$$v_x(z) = \frac{(H-z)z}{2\eta} \frac{\partial P}{\partial x}, \quad (2.7)$$

which results in a maximum of  $v_x(z)$  at the channel center,

$$v_{x,max}(z) = \frac{H^2}{8\eta} \frac{\partial P}{\partial x}, \quad (2.8)$$

The applied pressure (stress) gradient, can be expressed as the average force  $f_x$  per unit volume of fluid element. Therefore, the averaged force per particle is  $g = f_x/\rho$ . According to Eq. (2.8), we can compute the shear viscosity of the solvent.

Shear viscosity  $\eta$  can be expressed as the sum of the *kinetic* and the *collisional* contributions. Here we measure the *kinematic viscosity*  $\nu = \nu_{kin} + \nu_{coll} = \eta/\rho$ . *Kinetic viscosity*,  $\nu_{kin}$ , is related to the transverse momentum transport of the flow of particles. Whilst, *collisional viscosity*  $\nu_{coll}$  comes from the momentum transport of particles within collision cells [10].

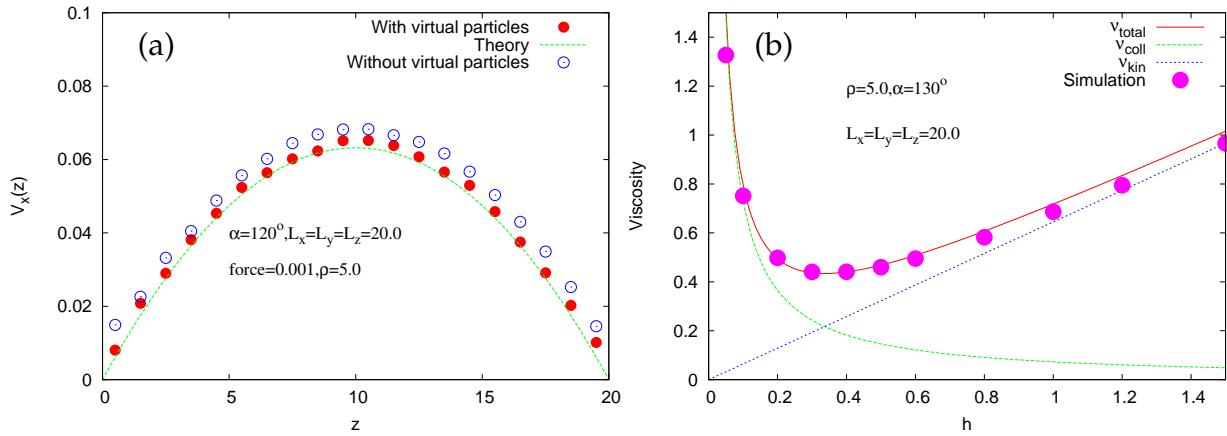


**Figure 2.2:** (a) Parabolic velocity profile of Poiseuille flow Simulation data with and without virtual particles, and analytical prediction are shown for comparison. (b) Shear viscosity as a function of  $h$ . Solid lines correspond to the kinetic theory, while symbols represent simulation results. Adapted from Ripoll [19].

Poiseuille flow in MPC simulation can be realized by implementing no-slip walls along  $x$  direction, and updating velocity with an acceleration  $g/m$  along the walls before streaming step. To enforce strict no-slip boundary conditions, virtual particle procedure has to be considered (for details, go to Ref. [75]). As shown in Fig.2.2(a), the simulation of velocity profile (symbols) along  $z$  direction nicely agree with the analytical calculation. Similarly, nice agreement between analytical and numerical results of viscosity is depicted in Fig.2.2(b). At  $h \gg 1$  region,  $\nu_{kin}$  dominates shear viscosity, while collisional contribution dominates  $h \ll 1$  area (solid green lines in (b)).

Moreover, Poiseuille flow is a typical paradigm of channel flow, such as in macroscale like water flow in a pipe at laminar regime, and blood flows in vessels at microscale.

### 2.3.3 Study on Brownian motion at short time scales

As briefly reviewed in Chapter 1, at short time scales, colloid receives momentum from the fluctuating fluid molecules, it also displaces the fluid in its immediate vicinity. The entrained fluid acts back on the particle and gives rise to long range correlations. This hydrodynamic ‘memory’ translates to thermal fluctuating forces, which have a colored noise spectrum [20].

MPC intrinsically incorporates thermal fluctuations, which can be used to study Brownian motion at short time scales. This can be elucidated by modeling a colloid trapped by a harmonic potential. We measure the position ( $x, y, z$  coordinates) time series and perform Discrete Fourier Transformation (DFT), then the power spectrum density can be computed. Here is an example that the hydrodynamic memory resonance peak has been found by MPC-MD coupling simulation, as shown in Fig.2.3. This result is consistent with a theory includes hydrodynamic vortex effect and differentiate from Lorentzian theory [76]. Compared with other mesoscale algorithms such as Langevin Dynamics, DPD, in which the noise is *usually* implemented by introducing a delta-correlated stationary Gaussian process with zero-mean and therefore is white, MPC doesn't need extra consideration of thermal fluctuation for the investigation of short time scale Brownian motion.

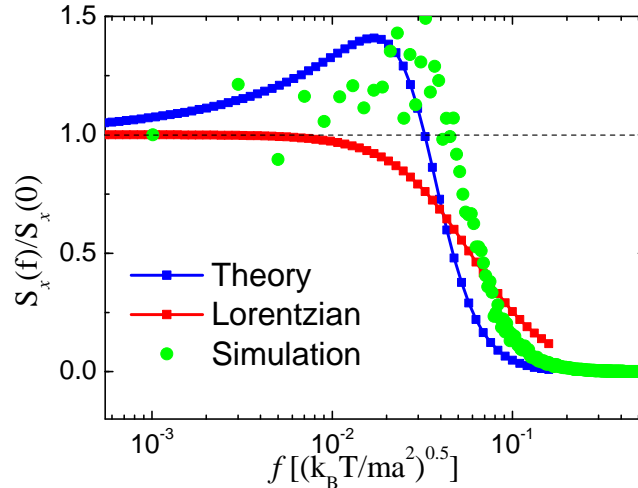


**Figure 2.3:** The displacement power spectrum density ( $S(x)$ ) in a MPC-MD simulation of particle suspended in solvent with a harmonic spring connected. Green symbols refer to simulation result, the blue line is the calculation with the hydrodynamic theory; the red line indicates harmonic oscillator solution, which is a standard Lorentzian curve. Here we set the spherical colloid with radius  $R = 2a$ , and the trapping stiffness (spring constant) to  $60k_B T/a^2$  in a  $(L_x, L_y, L_z) = (30a, 30a, 30a)$  box with periodic boundary conditions. Adapted from Ref. [20].

### 2.3.4 Hydrodynamical dimensionless numbers

Hydrodynamics are essential for the study of thermophoresis. MPC, as one of the most representative mesoscale hydrodynamics can capture hydrodynamics. Hereby, we show the most frequently used dimensionless numbers

in our simulations.

**Schmit number**  $Sc$  is the ratio between viscous damping and mass diffusing.

**Reynolds number**  $Re$  describes the competition between particle moving a certain length scale driven by inertia forces, and the viscous forces in fluids.

**Mach number**  $Ma$  is the ratio of the flow velocity to the speed of sound ( $u_c \sim \sqrt{k_B T/m}$  [77]) in the fluid medium. When the Mach number is small, the compressibility will not be an issue, except for fluids inside the boundary layers.

**Péclet number**  $Pe$ , which describes the competition between the transport capability driven by convection flow and by an appropriate gradient. In the context of mass transfer, for instance in this thesis, is the ratio of flow over a length scale to the self diffusion.

**Prandtl number**  $Pr$  is defined as the ratio of momentum diffusivity to thermal diffusivity. For example in thermophoresis in our simulations, the  $Pr = 5.6$  is comparable with water ( $\approx 7$ ).

Table 2.2 presents the values of those aforementioned dimensionless numbers calculated by using the frequently used simulation parameters (shown in Table 2.1). These calculations show that the simulations in this thesis are properly performed in liquid regime, with low  $Re$ ,  $Ma$ ; combined with adequate values of  $Pe$  and  $Pr$ . Thus, it ensures that all the simulation set ups are favorable for the study of phoretic behaviors.

$Sc$	$Re$	$Ma$	$Pe$	$Pr$
17	$\sim 10^{-2}$	$\sim 10^{-3}$	$\sim 1$	5.6
$\nu/D_s$	$u_f R/\nu$	$u_f/u_c$	$uR/D_c$	$\nu/\kappa_T$

**Table 2.2:** Typical values (or order of magnitudes) of dimensionless numbers in this thesis.  $\nu = 0.87$  is the kinematic viscosity;  $D_s = 0.05$  the self-diffusion coefficient of MPC solvent;  $u_f \sim 10^{-3}$  the flow velocity;  $u_c = 1$  the speed of sound;  $u \sim 10^{-3}$  colloid velocity;  $R \sim 3$  the typical size of a colloid;  $D_c \sim 10^{-3}$  the self-diffusion coefficient of colloid;  $\kappa_T = 0.15$ . All calculations are reduced to MPC units (Table 2.1), related analytical expressions can be found [10, 56, 57].

## 2.4 MPC simulation of thermophoresis

Combining colloid temperature gradient and colloid-MPC fluid coupling, we can probe thermophoresis of colloids in our system. Even if the mechanism of thermophoresis in liquids is intricate, the relationship between driving force and external temperature gradient in colloidal thermophoresis can always be simplified. *Firstly*, the heat transfer of solvent is much faster than the motion of the colloid. To reveal this in simulations, we estimate their diffusive times by kinetic theory. By way of example, for a simple MPC fluid with  $h = 0.1$ ,  $a = 1 = m = k_B T$  and  $\alpha_T = 130^\circ$ , the thermal diffusivity can be calculated as  $\kappa_T \approx 0.15a\sqrt{k_B T/m}$ . For *heat transport time*,  $t_{\kappa T}$ , over a length comparable with radius  $R = 3a$  of colloids is  $t_{\kappa T} \sim 10^1 \sqrt{ma^2/(k_B T)}$ . Similarly, the self-diffusion coefficient  $D_s$  of a spherical colloid can be obtained by the Stokes law, since the viscosity  $\eta$  of fluid media can be calculated by kinetic theory as well, which is  $\eta \approx 8.7\sqrt{mk_B T}/a^2$ . The *diffusion time*  $t_{diff}$  of a colloid with the same radius due to Brownian motion is around  $10^3 \sqrt{ma^2/(k_B T)}$ . This comparison can clarify that the solvent via heat transport relaxes much faster than colloids move due to Brownian motion, and maintain a stationary linear temperature gradient. *Secondly*, the temperature difference between two walls is always considered small such that the temperature in our simulation is treated as a constant but the temperature gradient effect remains. (For larger temperature differences, the spatial dependent temperature is considered.) *Furthermore*, the size of colloid is much heavier than single solvent particle, the driving force term from solvent particle is negligible [31]. *Additionally*, here we consider the infinite dilute colloidal system, such that the interactions between colloids are negligible. In the case that the excluded volume interaction between colloids plays a significant role, larger excluded volume should be taken into account to avoid algorithm-based depletion interaction [78].

### 2.4.1 Thermophoretic force measurement

The discussion above shows that in our simulations, we can readily employ linear response between the  $\nabla T$  and the thermophoretic drift force on the colloids (Eq. (1.14)). The positions of the colloids (composed of spherical beads) are fixed such that the thermophoretic force  $\mathbf{F}_T$  can be obtained by

directly summing the net temporal averaged force of all beads [58, 60],

$$\mathbf{F}_T = \sum_{i=1}^N \sum_{j=1}^{Nb} \mathbf{f}_{bs}, \quad (2.9)$$

where  $\mathbf{f}_{bs}$  indicates pairwise forces due to beads-solvent potential in Eq. (2.5),  $Nb$  the number of solvent particles around the  $i$  th beads,  $N$  is the number of beads in the constructed colloid or polymer we studied.

An equivalent way is trapping the position of colloids by harmonic springs, where  $F_T$  is counterbalanced by harmonic force, and the friction will be averaged out as well as the thermal fluctuations. Experimentally, colloids can be confined by external force (like laser tweezers) [79, 80].

## 2.5 Color coding in flow stream line patterns

To show the flow intensity, the background is color coded in the stream lines plots in this thesis (in Chapter 3, 7, 5 and 6). Hence, here and in what follows, the background color is prescribed via rescaling the magnitudes of local velocities  $|\mathbf{v}(x, z)|$  with a factor  $\Theta$ ,

$$\Theta = \frac{\log(|\mathbf{v}|/|\mathbf{v}|_{min})}{\log(|\mathbf{v}|_{max}/|\mathbf{v}|_{min})}, \quad (2.10)$$

here  $|\mathbf{v}|_{max}$  and  $|\mathbf{v}|_{min}$  denote the maximum and minimum of the magnitudes of velocities in the certain flow field. For example in Chapter 5 Fig 5.2(a), the legend tick labels indicate the rescaled component of  $|\mathbf{v}(x, z)|$  with respect to the maximum of  $|\mathbf{v}|_{max}$  in logarithmic scale. In this simulation,  $|\mathbf{v}(x, z)|$  spans two orders of magnitude. The flow close to obstacles, of course, has higher intensity; decays to almost zero when it is far away from obstacles or close to boundary walls. This rule of color coding will also be used in Chapter 3, 7, 5 and 6, but with different color schemes.

The color-coded background for other figures is simply linear.



## Chapter 3

# Thermophoresis of spherical colloids

### Synopsis

*Phoretic drift as well as associated osmotic flow, can be understood as being originated from an inhomogeneous pressure induced by local gradient at the solid-liquid interface. This chapter revisits the macroscopic theoretical description on phoresis based on the model of spherical colloid. The general solution of slip velocity on thermophoresis and diffusiophoresis is microscopically derived. To illustrate the general laws between different phoretic mechanisms, a precise comparison has been made between thermophoretic and diffusiophoretic behaviors simulated by MPC-MD model. Moreover, a simplified model is introduced which explicitly explains the microscopic mechanisms of thermophoretic simulations. We further show how physical quantities such as flow velocity, local pressure inside solid-liquid boundary layers can be calculated from both simulation and analytical theory viewpoints. Combined hydrodynamic simulation with analytical theory, the finite size effects on thermophoretic forces are unearthed.*

### 3.1 Introduction

Different phoretic behaviors share macroscopic features [81]. Before investigating colloids with asymmetries, we shall firstly review and investigate the dynamics in thermophoresis of spherical colloids. Regarding meso-scale simulations, numerous studies with various methods on different phoretic phenomena have been so far reported [58, 60, 82–85]. Multi-Particle collision dynamics, has been employed to study diffusiophoresis and thermophoresis from both fundamental and practical viewpoints [43, 46, 47, 58, 60, 86–

89]. However, albeit it is macroscopically intuitive to accept that simulation approach must reveal the same physical mechanisms of phoresis, the quantitative comparison between diffusiophoresis and thermophoresis based on MPC algorithm has not been explicitly made so far. Moreover, given that different microfluidic devices based on both phoretic principles indeed give similar behaviors, the generalized illustration of thermophoresis and diffusionphoresis emphasized from simulation viewpoint is timely.

In this Chapter, we mainly how MPC-MD model reveal correct thermophoretic behaviors, yet the microscopic structure of liquid has been coarse grained. Starting from a theoretical description, we derive the generalized slip velocity expression of the simulation mode. As the essence of thermophoresis is the local pressure gradient generated by temperature gradient at solid liquid interface, we show this pressure in simulation in both simplified model and spherical colloid model. Moreover, the finite size effects from different boundary conditions are precisely quantified.

## 3.2 Phoretic mechanisms: theory

It is generally accepted that colloidal thermophoresis can be understood in the framework of continuum hydrodynamics [27, 80, 90]. Instead of local equilibrium approach, the mechanical equilibrium of hydrodynamic stress and surface forces is applied [27, 81]. Usually there are two types of limit discussed:

1) One is the so-called *Huückel*" limit at which the particle radius  $R \ll \delta$ , where  $\delta$  is the thickness of the transition (boundary) layer where the colloid-solvent interactions are significant. In this case, such interactions are long ranged, and therefore the pressure gradient in Stokes' equation is negligible. In this case, we obtain that the drift velocity is essentially a Stokes drag, and therefore reads,

$$\mathbf{v}_T = \frac{\mathbf{F}_T}{\Gamma\pi\eta R}, \quad (3.1)$$

where  $\Gamma = 4$  for slip boundary conditions and  $\Gamma = 6$  for no-slip boundary conditions.

2) The other limit is *boundary layer limit* which is the opposite case of thin boundary layer and/or large particle size that  $R/\delta \gg 1$ . *In this thesis, we mainly focus on boundary layer limit. The dynamical processes within this thin*

boundary layer always determine the fluid dynamics outside. Specifically, the solid-fluid interactions in our simulations are mainly Weeks-Chandler-Anderson like repulsive potential, or short-ranged Lennard-Jones-like potential (Eq. (2.5)). This is more important for the case that the double layer is thin and electrostatic interactions are screened out.

### 3.2.1 Macroscopic linear transport

Anderson [81] detailedly reviewed phoretic processes based on boundary layer assumption within the framework of continuum theory. One parameter, the interfacial tension  $\gamma_\tau$ , accounts for all of phoretic phenomena. The main idea is that applying electrical field, temperature gradient or solution concentration difference, the interfacial tension inside this transition (boundary) layer becomes inhomogeneous along the interface. The gradient of interfacial tension  $\nabla\gamma_\tau$  drags the fluid and pushes the colloid towards the area where its interfacial tension could be reduced.

Phoretic movements of a particle are induced by the gradient of an external field  $Y_\infty$ , which are described by

$$\mathbf{v}_Y = b\nabla Y_\infty, \quad (3.2)$$

where  $\mathbf{v}_Y$  is the drift velocity, and  $b$  is the material parameter, determined by the interplay between colloid and solvent the type of gradient, and other local thermodynamic conditions.

Usually the slip boundary conditions are formed at the outer edge of the boundary layer where colloid-fluid interaction vanishes. On the other hand, the flow along the surface at the upper bound of the boundary layer is termed as *slip velocity*, denoted here as  $v_s(\tau)$  ( $\tau$  denotes the tangential direction). Locally, this parameter  $b$  also relates  $v_s(\tau)$  and the gradient decomposed along the (outer edge) surface  $\nabla Y^s$ , namely

$$\mathbf{v}_s(\tau) = -b\nabla Y^s. \quad (3.3)$$

Note that only *linear* transport phenomena are discussed here. The slip flow  $v_s(\tau)$  is characterized in the reference frame which is opposite to the direction of  $\mathbf{v}_Y$ . Thus leads to a minus sign in Eq. (3.3). It is usually considered that  $b$  is a constant. However, the description of flow inside the transition area is intractable, although models for no-slip and slip boundary conditions

of colloidal particle have been discussed [26, 27]. These linear relations are valid for phoresis in general, however, modification needed to account for *polarization* effect (the interfacial layer has a finite capacity to transport solute molecules) [81].

In our simulation model,  $b$  relies on the applied potential. For a spherical colloid interacting with fluid via LJ potential,  $b$  is a constant at the surface. Hence, it is instructive to observe the microscopic relation between microscopically the applied potential, local (pressure, density) gradient and the macroscopically resulting phoretic force, the associated slip flow, and the flow field in the surrounding viscous fluid.

### 3.2.2 General solutions of slip velocities for phoresis

Former discussion on phoresis encourages us to find general solutions for our MPC-MD coupling model. Based on fluid dynamics, we derive the solution of  $v_s(\tau)$  for thermophoresis and diffusiophoresis, which have been already studied via MPC method [43, 46, 47, 58, 60, 86–89].

Motion in a viscous continuum is governed by low-Reynolds number hydrodynamics [26]. The flow field  $v$  of the fluid (which is normally considered incompressible  $\nabla \cdot v = 0$ ) and is described by Stokes' equation (Eq. (1.19)).

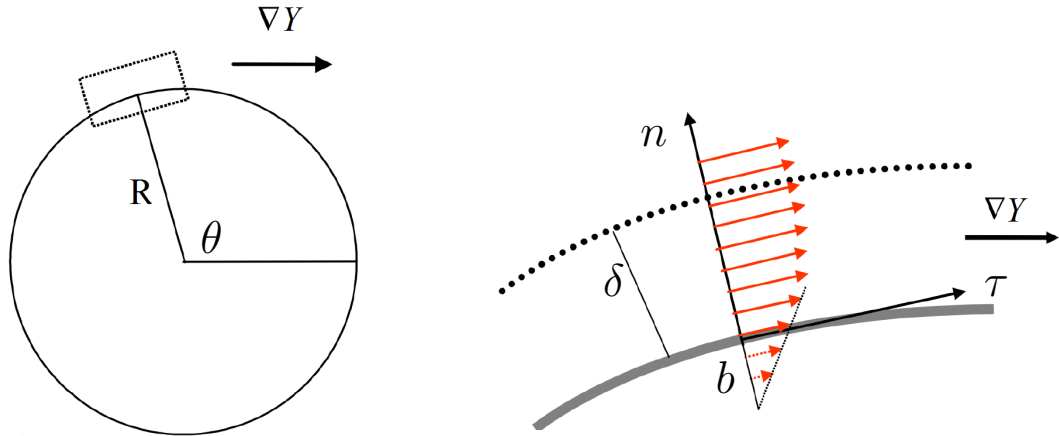


**Figure 3.1:** Schematic representation of spherical particle in an applied gradient  $\nabla Y_\infty$  (left). When  $\delta/R \ll 1$ , the boundary layer is planar like (right). The figure is adapted from Wüger [26].

In the case of  $\delta/R \ll 1$ , the boundary layer is treated as a plane and the local coordinate  $(\tau, n)$  is applied. As indicated in Fig. 3.1,  $n$  and  $\tau$  are the unit of the normal and tangential. Accordingly,  $n$  and  $\tau$  are the lengths described along normal and tangential. Close to the interface, the normal component

of velocity vanishes, i.e.  $v_n = 0$ . Thus, the normal component of Stokes' equation is written as

$$0 = \frac{\partial P}{\partial n} - f_n, \quad (3.4)$$

The integral of Eq. (3.4) gives the pressure

$$P(n) = P_\infty + \int_0^{R+\delta} f_n dn, \quad (3.5)$$

here  $P_\infty$  is the pressure out of the boundary layer (which satisfies the equation of the state of ideal gas in MPC fluid). Moreover, one should notice that  $f_n = 0$  when  $n > \delta$ . Since the boundary layer is treated planar like, the dependence on the normal direction of  $v_\tau$  is much larger than that on tangential direction. Here we consider  $v_\tau = v_\tau(n)$ . Consequently, the tangential component is written as

$$\eta \frac{d^2 v_\tau}{dn^2} = \frac{\partial P}{\partial \tau} - f_\tau. \quad (3.6)$$

Inserting boundary conditions (i)  $v_\tau|_{n=0} = 0$  and (ii)  $dv_\tau/d\tau|_{\tau=\delta} = 0$ , we obtain the apparent slip velocity

$$v_s(\tau) = \frac{1}{\eta} \int_0^{R+\delta} dn n \left( f_\tau - \frac{\partial P}{\partial \tau} \right). \quad (3.7)$$

Most of our studies use central potentials, such that no lateral component for body force density exists, namely  $f_\tau = 0$ . The integral of Eq. (3.7) is then determined by pressure gradient.

Following Eq. (3.4), the central potential inside the boundary layer is encoded as  $U(n)$ . The potential gives rise to the local force acting on the fluid, read as

$$f_n = -\rho(\tau, n) \frac{dU(n)}{dn}, \quad (3.8)$$

here  $\rho(\tau, n)$  the local density inside the boundary layer. We calculate the  $\rho(\tau, n)$  by the product of *outer edge density*  $\rho(s) = \rho_\infty$  which is the bulk density and a Boltzmann weight:

$$\rho(\tau, n) = \rho(s) \cdot \exp\left(-\frac{U(n)}{k_B T(\tau, n)}\right), \quad (3.9)$$

here local thermodynamic equilibrium is considered to cover the position dependence of temperature. Substituting Eq. (3.8) and Eq. (3.9) into Eq. (3.5),

the excess pressure reads,

$$P^* = P(\tau, n) - P_\infty = \rho(s)k_B T(s) \cdot \left[ \exp\left(-\frac{U(n)}{k_B T(\tau, n)}\right) - 1 \right]. \quad (3.10)$$

To obtain Eq. (3.10), the approximation that temperature inside the boundary layer hardly changes along normal direction is adopted. Hence, Eq. (3.7) can be rewritten as

$$v_s(\tau) = -\frac{1}{\eta} \frac{d}{d\tau} \left\{ \rho(\tau)k_B T(\tau) \int_0^{R+\delta} \left[ \exp\left(-\frac{U(n)}{k_B T(\tau, n)}\right) - 1 \right] n dn \right\}. \quad (3.11)$$

Eq. (3.11) agrees with the expression used on the study of thermophoresis in colloid-polymer mixtures [26]. Moreover, using the solution of slip velocity, we can also obtain the thermal diffusion factor  $\alpha_T$  (see Appendix A).

Here we derived the generalized expression of slip velocity which is valid not only for *thermophoresis* but also for *diffusiophoresis*. The only difference is that the temperature (concentration) is position dependent along the surface in thermophoresis (diffusiophoresis). Hence, different micro-mechanisms result in the similar (macroscopic) slip velocities. Moreover, it is logical to think that this feature also holds for simulation models of thermophoresis and diffusiophoresis. In the following, I further show that thermophoresis is akin to diffusiophoresis at macroscopic level.

### 3.3 Simulation studies on macroscopic phoresis

By virtue of mesoscale hydrodynamic simulations, we show that different microscopic phoretic origins can eventually lead to same features microscopically. The comparison is made between *thermophoresis* and *diffusiophoresis*.

- **Diffusiophoresis [89]:**

$$\mathbf{F}_D = \alpha_D \nabla c = \frac{\gamma D_{DP}}{c} \nabla c. \quad (3.12)$$

Here  $\mathbf{F}_T$  (or  $\mathbf{F}_D$ ) is named thermophoretic (diffusiophoretic) force,  $\alpha_T$  (or  $\alpha_D$ ) is a dimensionless factor characterizes the force. Due to historical reasons,  $\alpha_T$  is also often expressed as the product of the Soret coefficient  $S_T$  and corresponding average temperature  $\bar{T}$ . Likewise,  $\gamma$  and  $D_{DP}$  refer to the friction

coefficient and diffusiophoretic mobility [91]. Basically, Eq. (1.14) and (3.12) are just different expressions of Eq. (3.2), in terms of phoretic forces.

In the following, we show simulation results of linear transport properties driven by both phoretic mechanisms.

### 3.3.1 Simulation implementation

For thermophoresis, the realization of temperature gradient is meticulously discussed in Chapter 2, and also in various references [57, 60].

To implement the system for the study of diffusiophoresis, we consider two types of solvent particles  $A$  and  $B$  with equi-molar fractions in a cuboid simulation box interact with colloids. Within the employed coarse grained scheme, different species are distinguished only when interacting with the colloid. From now on, we mostly apply  $r3$  potential between colloid and particle  $A$ , and  $r24$  potential for particle  $B$ , respectively. The interaction between the same and different solvent species are included in the collision step of MPC. Similar with the boundary conditions applied in Ref. [89], two walls with no-slip boundary conditions are realized by bounce back rules. Additionally, the wall at  $z = 0$  acts as a chemical reservoir and enable chemical reaction  $B + W1 \rightarrow A + W1$ . Likewise, reaction  $A + W2 \rightarrow B + W2$  happens at  $z = L_z$ . The reaction rate  $0 < \zeta < 1$  for both chemical reactions are employed. At steady state, the linear concentration gradients of species  $A$  and  $B$  are established.

As shown in Fig. 3.2, the constant concentration gradient is established at the steady states and  $c_A + c_B = 1$ . With  $L_z = 30$ , we obtained  $\nabla c_A = \nabla c_B = 0.0133$  for  $\zeta = 0.7$  and  $0.0345$  for  $\zeta = 1.0$ .

The phoretic forces are obtained via temporal average of colloid-fluid interaction forces; correspondingly, the flow field is calculated by time-averaging particle velocity inside every binned cell.

### 3.3.2 Results

Simulations of a colloid in both a temperature gradient and a concentration gradient are performed to evaluate the phoretic force with various values of the gradients. Results for a colloid of  $R = 3$  in a cubic box with size of  $(L_x, L_y, L_z) = (30a, 30a, 30a)$  are shown in Fig. 3.3. For thermophoresis,  $r3$

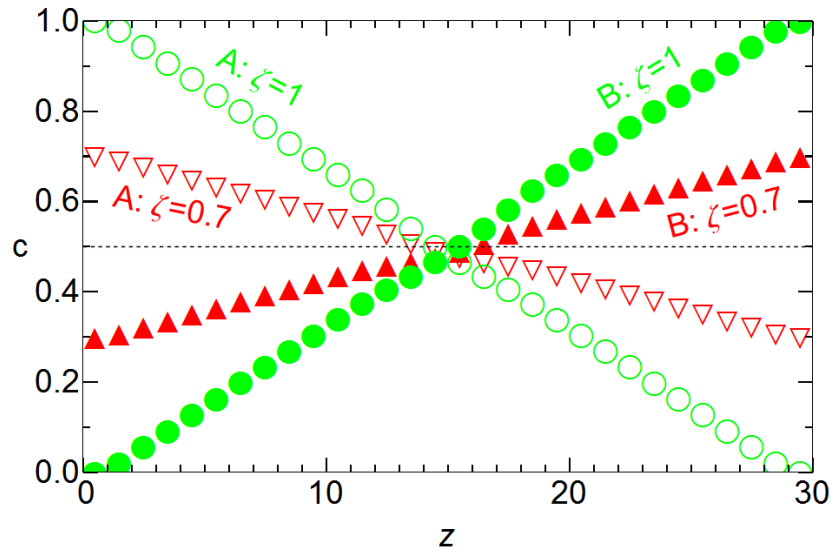


**Figure 3.2:** Linear concentration profiles of different particle species along  $z$  direction. Green circles refer  $\zeta = 1.0$ , and red triangles to  $\zeta = 0.7$ . Open symbols refer to concentration of  $B$  and close symbols to species  $A$ . Simulations are performed in cubic box with size of  $(L_x, L_y, L_z) = (30, 30, 30)$  (a spherical colloid with radius  $R = 3$  is placed in the center of the box).

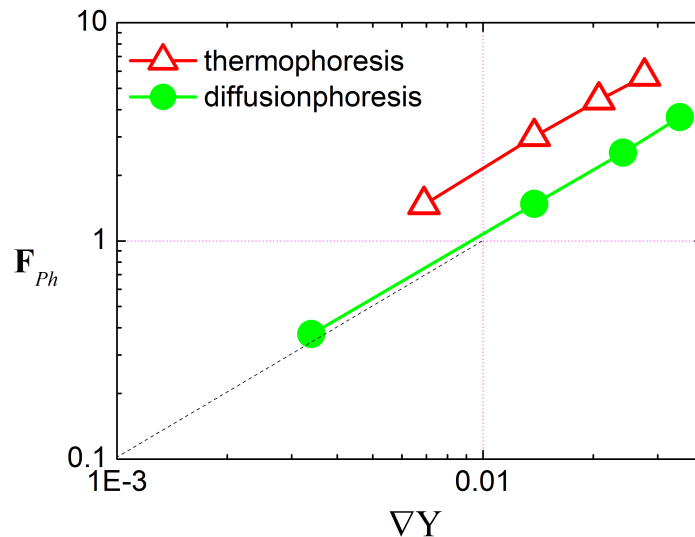


**Figure 3.3:** Simulation results of phoretic forces  $F_{ph}$  as a function of external gradient  $\nabla Y$ . Here  $\nabla Y$  represents  $\nabla T$  and  $\nabla c$ . In all simulations, the system size is  $(L_x, L_y, L_z) = (30, 30, 30)$ . The logarithmic coordinate is used to emphasize the strict linear behavior (the slope of both lines is 1) of phoresis.

potential is employed; whilst  $r_{33}$  and  $r_{12}$  potentials for diffusiophoresis. The phoretic forces  $\mathbf{F}_{ph}$  are measured in different external gradients. Although the  $\nabla Y$  varies over one decade,  $\mathbf{F}_{ph}$  obeys linear relation with  $\nabla Y$ . Therefore, in MPC simulations, thermophoresis and diffusiophoresis macroscopically indeed obey linear transport laws. Moreover, using thermal diffusion factor  $\alpha_T$  as a role model, it is reasonable to introduce diffusion phoretic factor  $\alpha_D$ .

### 3.3.3 Far field flow around phoretic colloids

Turning now to the phoretic responses of the fluid. Selected from the simulation results from the previous subsection, the representative flow patterns of fixed colloids induced by thermophoresis and diffusiophoresis are illustrated in Fig. 3.4. For thermophoresis,  $T_c = 0.8$  and  $T_h = 1.2$  are applied. Hence we obtain thermophoretic force  $\mathbf{F}_T^{sim} \approx 3.0$  and  $\alpha_T^{sim} \approx -218$  without finite size effects correction, which will be comprehensively discussed in the next section. In contrast, with the same boundary conditions, the concentration gradients for particle species  $A$  and  $B$  are  $\nabla c_A = \nabla c_B = 0.03448$ , respectively. We measure the diffusion phoretic force  $\mathbf{F}_D^{sim} \approx 3.69$ , and diffusion phoretic factor  $\alpha_D^{sim} = -217.5$  to the side has higher concentration of species  $B$ .

The flow maps induced by thermophoretic and diffusiophoretic mechanisms at far field are almost identical. We can compute the comparable drift velocity of freely moving colloids:  $v_T = 0.0091$  and  $v_C = 0.0113$ .

Following the work by Braun [90], Würger [27] and Leonardo [80], the flow field of spherical colloid in  $\nabla T$  can be analytically resolved [26, 35]. To keep such a particle stationary in the temperature gradient, an external body force applied on the colloid to counter balance the thermophoretic force  $\mathbf{F}_T$ . Solving the Stokes equation with (i) vanishing flow at infinity, (ii) the application of a net force  $\mathbf{F}_T$ , and (iii) the normal component of fluid flow at the particle surface vanishing in the laboratory frame, such that the flow field is given by [51, 60, 80],

$$\mathbf{v}(\mathbf{r}) = -\frac{1}{8\pi\eta r}(\hat{\mathbf{r}}\hat{\mathbf{r}} + \mathbf{I}) \cdot \mathbf{F}_T + \frac{R^2}{8\pi\eta r^3}(3\hat{\mathbf{r}}\hat{\mathbf{r}} - \mathbf{I}) \cdot \mathbf{F}_T, \quad (3.13)$$

where  $\mathbf{r}$  is the distance between fluid particle and the colloid center,  $\hat{\mathbf{r}}$  the unit vector of  $\mathbf{r}$ ,  $\mathbf{I}$  the unit tensor. The first term at the right side of Eq. (3.13)

is a Stokeslet, which describes the Stokes drag nature of thermoosmotic flow at far field, and decays as  $1/r$  being long range. The second term is so called source dipole, contributes the surface flow which decays as  $1/r^3$  being short range. In particular, Ref. [60] shows that the analytical calculation of thermophoretic flow field for a moving colloid quantitatively agrees with simulation results, even though without PBCs corrections.

The quantitative comparison of both phoretic mechanisms is made in Fig. 3.4, where it can be seen that the shape of the stream lines is identical in both cases. The quantitative comparison of the velocity field is shown in Fig. 3.5. The far field flow determined by different phoretic mechanisms is made in Fig. 3.5. Fig. 3.5(a) indicates the  $z$  (gradient direction) component of flow velocity profiles in the cross sections  $a$  (distinguished by  $a_c - a_h$  in Fig. 3.4(a), the subscripts "c" and "h" denote the "cold" and "hot" sides) and  $a_l - a_h$  in Fig. 3.4(b) (the subscripts "l" and "h" denote the "low" and "high" concentration sides of particle species  $B$ , see in Fig. 3.2), respectively. Like wise, Fig. 3.5(b) refers to  $v_z$  profile in the cross sections  $b$  (namely  $b_d - b_u$ ), subscripts "d" and "u" denote the "down" and "up" sides. The results in Fig. 3.5 show that the data of simulations for thermophoresis diffusiophoresis and theoretical calculation collapse when the velocity is rescaled by the associated phoretic force  $\mathbf{F}_P$ , despite the theoretical calculation is obtained from thermophoresis. This is because that the slip boundary conditions at the upper edge of the boundary layer for different phoretic phenomena are akin to each other [81], thus their resultant flows are very similar as well.

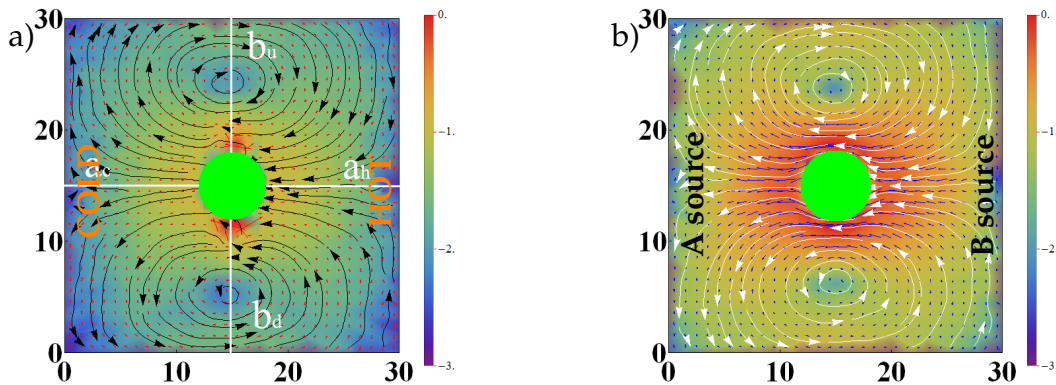


**Figure 3.4:** Flow field and stream lines representations of phoretic colloids in simulations with PBCs. Background color coding (flow intensity) is prescribed in Chapter 2 Sec. 2.5. (a) *Thermophoresis*. (b) *Diffusiophoresis*.

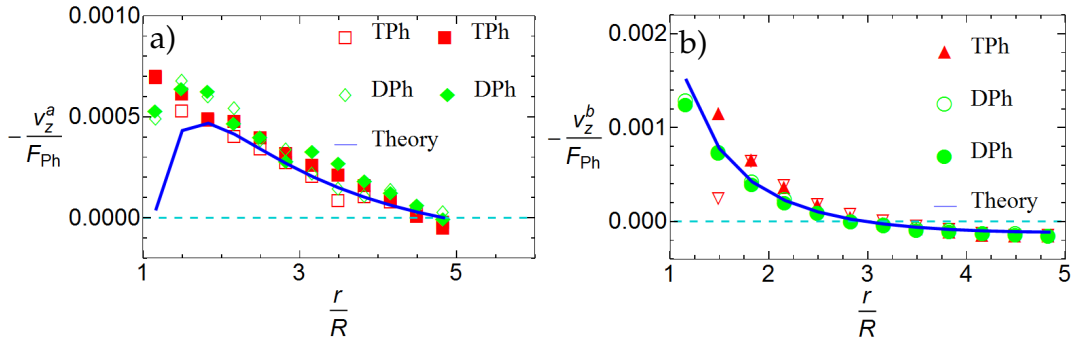


**Figure 3.5:** Flow velocities component  $v_z$  as a function of relative distance to colloid center. Values are normalized by phoretic force  $F_P$  at (a) cross section  $a$  and (b) cross section  $b$  (indicated in Fig. 3.4). Open and solid symbols represent  $v_z$  at different sides (left or right, up or down) of colloids.

## 3.4 Microscopic mechanism of thermophoretic simulation

To reveal the microscopic mechanism, and compare with theory, we measure the local pressure, as well as the slip velocity at the boundary layer. It is an essential step for particle based simulation, as all the theories assume that macroscopic thermodynamics or hydrodynamics only hold close to the interface. This would not be a reasonable postulation, if for example, the viscosity inside the boundary layer in Eq. (3.11) is not constant [92]. Therefore, it is of great importance to compute the local pressure in simulation. Instead of dealing with the redundant mathematical integration of a spherical colloid, we firstly introduce a simplified model composed by two planar solid walls filled with liquid in between, to illustrate thermophoretic mechanism in MPC-MD approach. In the limit of  $\delta \ll R$ , this of course will be a good simplification (Fig. 3.1).

### 3.4.1 Inhomogeneous pressure

In MPC-MD coupling model, the interaction between colloid with radius  $R$  and solvent forms the boundary layer (Fig. 3.6(a)). The local variables (pressure or flow) are measured inside of each bin by temporal average. In order to increase resolution, we choose a bin size 5 times smaller than MPC collision cell size  $a$ . Before studying the spherical model (Fig. 3.6(a)), a similar but simplified system is proposed here to elucidate phoretic mechanism. As

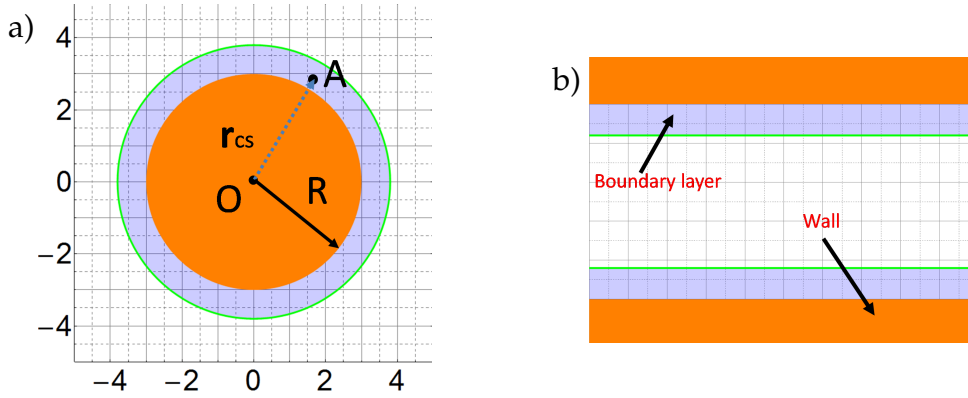


**Figure 3.6:** Sketches of the MPC-MD coupling model for a (a) spherical geometry, and (b) the wall geometry. Solid orange denotes excluded volume area, light blue shaded area is the boundary layer. Solid lines indicate the MPC collision boxes and dashed lines the refined binning grids.

sketched in Fig. 3.6(b), the MPC fluid is constrained between two solid planar walls interact with walls via aforementioned Lennard-Jones potential. The periodic temperature gradient along the walls ( $z$  axis direction) is imposed such that the thermophoretic flows are obtained [58, 60].

The local scalar pressure inside a certain local bin is given by the equation of state of MPC fluid,

$$P(\vec{r}) = \left\langle \frac{N(\vec{r})k_B T(\vec{r})}{V} \right\rangle. \quad (3.14)$$

The virial contribution to the fluid pressure vanishes since there are no potential interactions between fluid particles. The density and temperature are position dependent, which is a consequence of both the potential and the temperature gradient. In Fig. 3.7 (a) we show the simulation of thermophobic

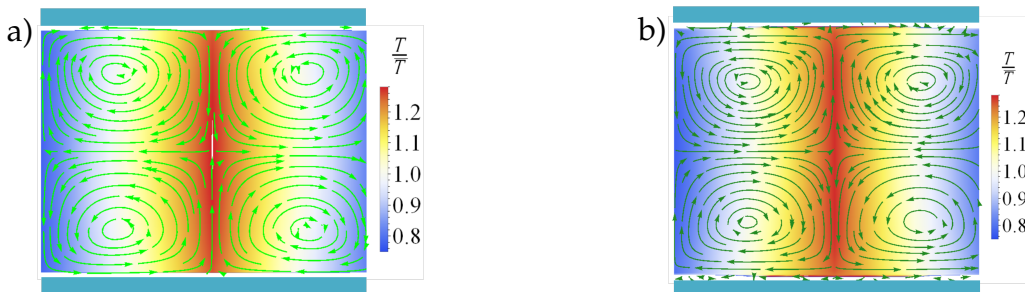


**Figure 3.7:** The flow fields of the simplified model for thermophoresis. With other standard simulation parameters,  $(L_x, L_y, L_z) = (20, 20, 20)$  and  $\nabla T \approx 0.0502$  applied along the walls is periodic [58]. (a) Left, thermophobic walls with  $a48$  potential with  $\sigma = 3$ ; (b) right, thermophilic walls with  $r3$  potential with  $\sigma = 3$ . The background color codes the local temperature.

osmotic flow along the solid walls combined with periodic boundary conditions form the symmetric flow stream lines pattern. The warmest position is the middle position of the system along  $z$  axis. With thermophobic property of solid walls, the flow close to the walls tends to warm side; in contrast, thermophilic walls enable flow go to cold area (Fig 3.7(b)).

In order to clearly understand the underlying physics in this simplified model, here we calculate the pressure gradient along the walls. In the bulk the pressure is constant, and the bulk solvent density obeys the equation of the state of MPC fluid,  $\rho_\infty(z) = P_\infty/k_B T(z)$ . On the base of the local thermodynamic equilibrium (LTE), inside the boundary layer near the wall, Eq. (3.9) is satisfied, rewritten as,

$$\rho(x, z) = \rho_\infty(z) \exp(-U(x)/k_B T(z)). \quad (3.15)$$

Using Eq. (3.15) and the ideal gas equation of state, we have the pressure tensor in  $z$  direction,

$$P_{zz}(x, z) = \rho(x, z)k_B T(z) = P_\infty \exp(-U(x)/k_B T(z)). \quad (3.16)$$

Hence, the pressure gradient is,

$$\frac{\partial P_{zz}(x, z)}{\partial z} = P_\infty \exp(-U(x)/k_B T(z)) \frac{U(x)}{k_B T^2(z)} \frac{\partial T}{\partial z} = P_{zz}(x, z) \frac{U(x)}{k_B T^2(z)} \frac{\partial T}{\partial z} \sim \mathbf{f}_T. \quad (3.17)$$

where  $\mathbf{f}_T$  is the force density of the fluid. Clearly, for a general  $U(x)$  the pressure gradient is nonvanishing within the boundary layer (vanishing when  $U(x) = 0$  in the bulk and  $U(x) = \infty$  inside the wall). The nonzero pressure gradient drives the fluid flow, and constitutes the thermodynamic contribution of the thermophoresis. The slip velocity can also be calculated by substituting Eq. (3.17) into Eq. (3.7). In addition, the thermophoretic force  $\mathbf{F}_T$  can be calculated via local pressure gradient. (*Different solutions for  $\mathbf{F}_T$  and  $\alpha_T$  are presented in Appendix A.*)

To avoid poor statistics of exact local pressure in simulation, we calculate the local pressure inside boundary layers average perpendicular to  $\nabla T$ , both numerically and analytically (based on Eq. (3.16)). Hence, the average local pressure  $\hat{P}_{zz}$  is written as,

$$\hat{P}_{zz}(z) = P_\infty \left( \frac{1}{\delta} \int_R^{R+\delta} \exp(-U(x)/k_B T(z)) dx \right). \quad (3.18)$$

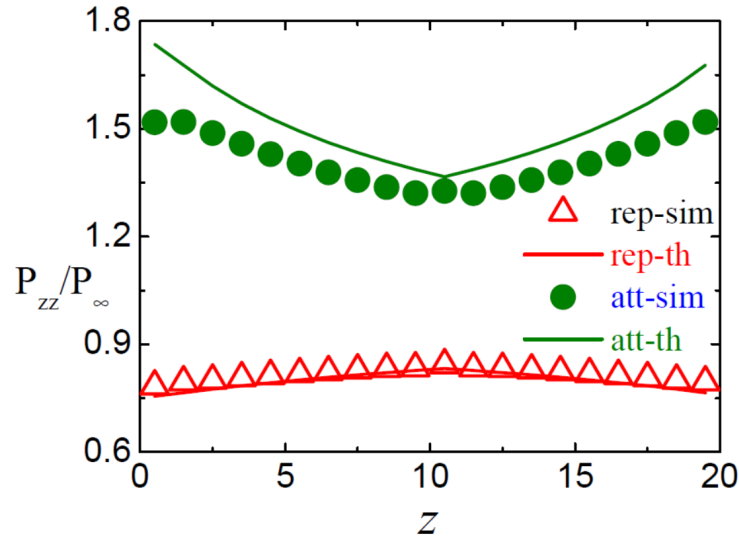


**Figure 3.8:** Local pressure profile calculated from simulation and analytical theory in thermophobic and thermophilic cases.

Fig. 3.8 shows the local average pressure as a function of position.  $\partial P_{zz}/\partial z$ , which is opposite from the osmotic flow direction (Fig. 3.7). Specifically, the analytical theory curves based on Eq. (3.18) for both thermophobic ( $a48$  potential) and thermophilic ( $r3$  potential) behaviors agree with simulation results (Temperature can be analytically calculated by solving Laplace equations, as will be done in Chapter 6 section 2. But we can also directly use  $T(z)$  from simulation results). Some deviations are still observed, this might be due to the employed large temperature gradient which breaks down the local equilibrium assumption, also the impact from finite system size effects.

The above theoretical rendition is based on the LTE, similar to the studies by Derjaguin and by Frenkel and their collaborators [92]. Therefore, the physical mechanism underlying thermophoresis is correctly captured by MPC-MD coupling simulation method. Besides this thermodynamic contribution, our results also naturally include the kinetic contribution of the thermophoresis which is ignored in the LTE-type calculations (might also explains the deviation in Fig. 3.8).

- *Thermophilic or thermophobic?* As we discussed above, the local pressure gradient  $\partial P_{zz}/\partial z$  is the thermophoretic response from the fluid in Eq. (3.17). It indicates how much thermophoretic (or thermoosmotic) force per volume of fluid is suffered ( $\mathbf{f}_T$ ). The direction of total thermophoretic force  $\mathbf{F}_T$  is the same as  $\partial P_{zz}/\partial z$  close to the interfacial layer.

The sign of  $\mathbf{F}_T$  is therefore determined by the sign of the potential inside the boundary walls. With the common used Lennard-Jones potentials we applied, repulsive one gives positive sign is the same as  $\partial P_{zz}/\partial z$ , such that the same as  $\partial T/\partial z$ ; while, attractive L-J potential inside boundary layer is negative sign (note that in most of cases, the contribution of short ranged repulsion to  $\mathbf{F}_T$  is negligible), thus  $\partial P_{zz}/\partial z$  is opposite from  $\partial T/\partial z$ . In nutshell, Eq. (3.17) numerically explains the reason of thermophilic and thermophobic behaviors due to different potentials.

### Local pressure computation around spherical colloid

Despite that the physical mechanism can be revealed from the aforementioned simplified model, the pressure gradient effect is of interest for the understanding of the simulation study on thermophoresis of spherical colloids. Simulations are performed in a  $(L_x, L_y, L_z) = (30, 30, 30)$  box, with  $r3$  and  $a24$  potentials and  $\nabla T = 0.0216$  along  $z$  axis applied. The temporal assemble average is refined into cubic bins with size of 0.2, collected with an cylindrical average. Therefore extensive statistics are required. Likewise, the flow field inside the boundary layer is also measured in this way which is shown below.

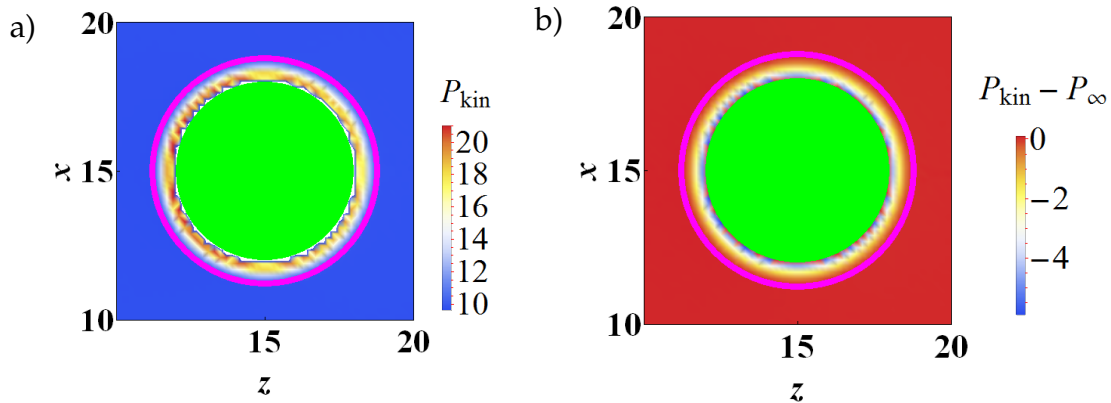


**Figure 3.9:** Pressure field: (a) and (b) are thermophobic and thermophilic cases, respectively. The pink solid line distinguishes the outer edge of the boundary layer. For better visualization, in (b) the pressure at the bulk  $P_{\infty}$  is subtracted, the excess pressure is shown here.

Apparently, the pressure field in Fig. 3.9 show that out of boundary (interaction) layer (the pink solid line), the pressure is homogeneous everywhere. The radial gradient of the pressure from the colloid surface until the edge of the boundary layer is easy to identify, but not so much the gradient along the tangential direction, although a slight effect has been seen when looking carefully at the thermophobic case. However, we realize that the thermophobic case is hardly to distinguish the tangential gradient effect, even though the bulk pressure  $P_\infty$  is subtracted.

To quantify the pressure gradient effect, we calculate the average local pressure inside boundary layer using the same protocol as in planar walls model and Eq. (3.18). The local pressure (to obtain the less noisy value, block average is applied) as a function of polar angle for thermophobic and thermophilic colloids are shown in Fig. 3.10. The green dashed lines correspond to theoretical prediction by Eq. (3.18), the only modification is that the temperature term is polar angle dependent. The pressure gradient directions are consistent with (opposite from) the thermophoretic flow directions. This measurement accompanied with thermoosmotic flow, reveal how our model is able to capture the physical mechanism of thermophoresis. In MPC-MD simulations, the thermophoretic force, is dominated by the tangential pressure gradient, rather than by the asymmetric density distribution (due to temperature gradient) resulted net central forces.

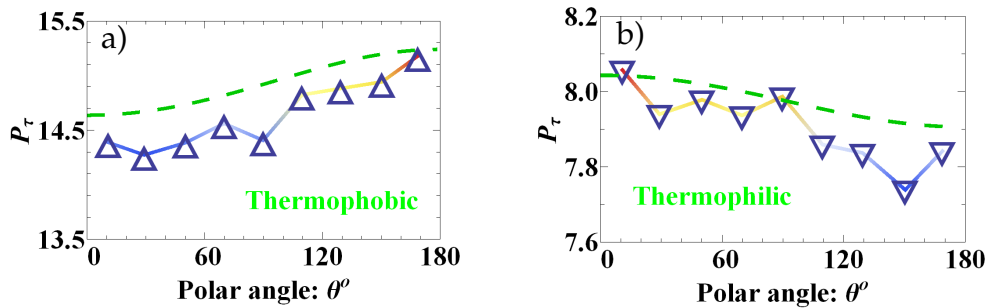


**Figure 3.10:** Pressure averaged at the colloid surface as a function of polar angle  $\theta$  in (a) *thermophobic* and (b) *thermophilic* colloids. The green dashed lines refer to analytical prediction in Eq. (3.18) for spherical colloid case. Note that  $\theta = 0^\circ$  corresponds to at the warm side of colloid, and  $\theta = 180^\circ$  to the cold side.

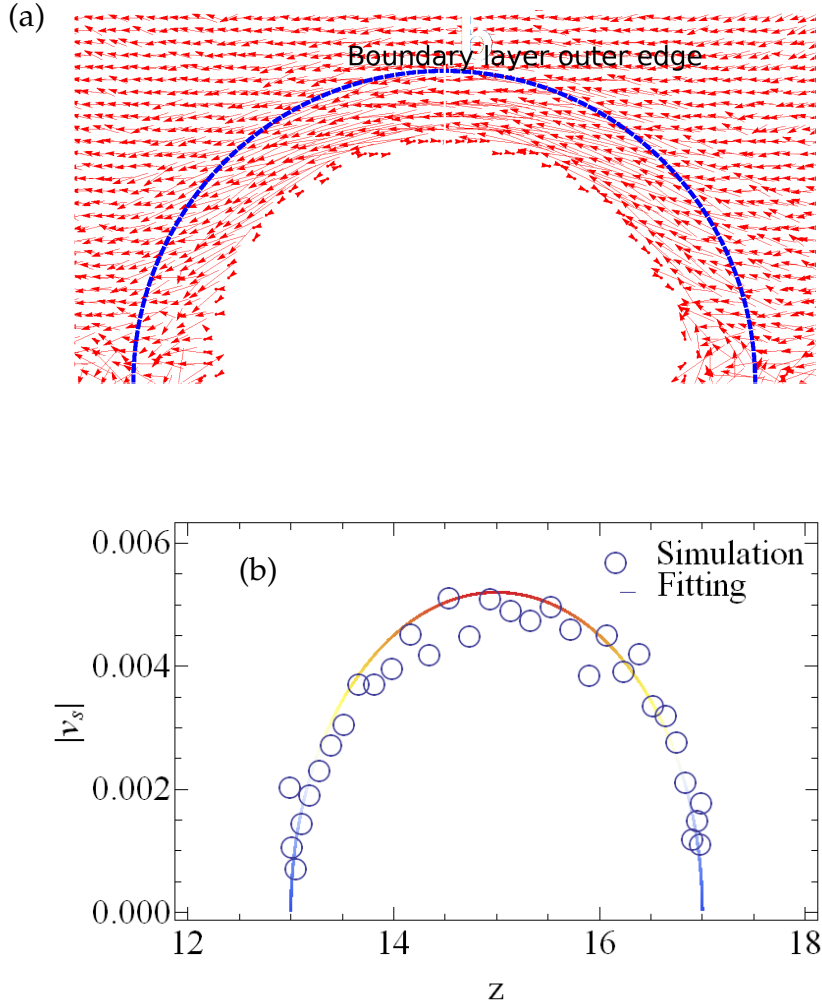


**Figure 3.11:** Flow inside boundary layer. (a) Time averaged vector field of flow velocities around boundary layer. The blue line indicates the outer edge of interaction range or interfacial layer. (b) Magnitude of the averaged slip velocity at the interfacial area.

### 3.4.2 Near field flow maps induced by phoretic forces

At steady state, the *slip velocity* varies with the sine of the polar angle [26],

$$v_s = v_B \sin \theta, \quad (3.19)$$

with the maximum of  $v_B$  at the polar angle  $\theta = \pi/2$ . The thermophoretic force  $F_T$  can be obtained from thermophoretic drift velocity  $v_T$  since this is the velocity that the colloid will reach when the hydrodynamic friction force  $F_\gamma$  counterbalances  $F_T$ . Namely rewriting Eq. (3.1),

$$\mathbf{F}_T = \mathbf{F}_\gamma = \Gamma \pi \eta R v_T. \quad (3.20)$$

We now measure the flow field near by the colloid boundary layer with bin size 10 times smaller of the collision cell size. Fig. 3.11(a) illustrates the flow vector field around a fixed colloid in temperature gradient. Concerning flow close to the boundary layer, the normal components are negligible while the tangential components varies along the spherical surface. We show that the magnitude of  $v_s$  changes with polar angle  $\theta$ , which is consistent with Eq.(3.19).

The simulation have been performed also serves us to check the validity of the first equality in Eq (3.20). Here we obtain the maximum of slip velocity of fixed colloid  $v_B \approx -0.0052$ . This value together with  $\Gamma = 4$ ,  $\eta = 8.7$  known from our simulation parameters, and taking that  $v_B \approx v_T$  (colloid with slip boundary conditions in Eq. (3.13)), allow us to calculate  $\mathbf{F}_T = -4\pi\eta Rv_B \approx 1.14$ , which reasonably compares with the value  $\mathbf{F}_T = 1.3$  calculated directly in the simulations. This larger value obtained in simulation is due to the effet of the back flow induced by the PBCs or walls. This effects will be studied in detail in the next section.

### 3.5 Hydrodynamic origin of finite size effects

Numerical simulations of particulate systems are unavoidably limited to a finite system sizes. Different boundary conditions of a system with finite size seem play significant role on the measurement of thermophoretic force [58, 60]. However, the origin is still elusive. By fixing a colloid in temperature gradient, its thermophoretic force can be attained in simulations via summing all of colloid-solvent individual forces (Chapter 2) [60]. Physically, the temperature gradient brings in the inhomogeneity of solvent at the colloid-solvent interface, what results in a directed force (*thermophoretic force*). In the case of colloids with boundary conditions such as being *confined between walls* [60] or in *open periodic systems* [58, 60], the presence of a back flow originated at the walls or at the periodic images, influence the measurement of thermophoretic force. According to a previous simulation study [58] which combines empirical fitting, with the measured thermophoretic forces,  $\mathbf{F}_T^{sim}$  are always larger than its value extrapolated to an unconfined system  $F_T^\infty$  due to finite system size. Hence, it is also termed as finite size effects (FSEs).

- **The origin and calculation of effective friction:** In the framework of hydrodynamics, we ascribe the enhancement in measured  $F_T$  (or its corresponding *thermal diffusion factor*  $\alpha_T$ ) to an effective additional friction  $F_T^\gamma$ . This  $F_T^\gamma$  is essentially exerted by a net hydrodynamic flow  $\mathbf{v}_T^\gamma$  induced by all the periodic images and confinements. We adopt an analytical calculation approach to quantify  $F_T^\gamma$ . Here  $\mathbf{v}_T^\gamma$  can be calculated analytically considering influence from the periodic images and the boundary walls. By *Stokes' law*  $F_T^\gamma = 4\pi\eta \cdot R \cdot \mathbf{v}_T^\gamma$  (slip boundary condition),  $F_T^\gamma$  is obtained.
- **FSEs correction via analytical calculation:** The system size dependence of thermal diffusion factor  $\alpha_T^{sim}$  can be readily measured via simulation [58]. With the aforementioned protocol, we achieve this by analytical calculation as well. To confirm the correctness of calculation, an essential step is to construct the thermophoretically induced flow fields (which have been studied in simulations [60]) of colloids via analytical calculation. Moreover, we investigate the system size dependence of  $F_T^\gamma$ .

### 3.5.1 Analytical evaluation of FSEs factor

The thermodiffusion factor  $\alpha_T$  is measured in the simulations,  $\alpha_T^{sim}$  is known to depend on the system size what can be characterized by measurements at various system sizes from which an extrapolation of the factor for a system of infinite size  $\alpha_T^\infty$  [58] can be obtained,

$$\alpha_T^{sim} = \alpha_T^\infty \left(1 + \lambda \frac{d}{L_z}\right), \quad (3.21)$$

where  $\lambda$  is termed as FSEs factor which quantifies the significance of FSEs. When the colloid is confined at the middle of two parallel walls and temperature gradient  $\nabla T$  is employed perpendicular to wall-planes, thermophoretic flow velocity at the boundaries vanishes due to stick boundary conditions (with slip boundary conditions at walls, the component along  $\nabla T$  of velocity vanishes). As mentioned previously, due to the finite system sizes, measured thermophoretic force  $\mathbf{F}_T^{sim}$  is represented by,

$$\mathbf{F}_T^{sim} = F_T + F_T^\gamma. \quad (3.22)$$

Assuming that a constant back flow  $\mathbf{v}(L_z/2)$  along  $\nabla T$  direction (calculated from Eq. (3.13)) bounces back at the walls has proven to be a very reasonable

approach [60]. Such back flow exerts an additional friction on the colloid,

$$\mathbf{v}_T^\gamma = \mathbf{v} \left( \frac{L_z}{2} \right) = \frac{1}{8\pi\eta\frac{L_z}{2}} \cdot 2 \cdot \mathbf{F}_T = \frac{-\alpha_T^\infty k_B \nabla T}{2\pi\eta L_z}. \quad (3.23)$$

Substituting the *Stokes* friction coefficient  $\gamma = 4\pi\eta R$  into Eq. (3.22), and comparing with Eq. (1.14) and Eq. (3.21), allows us to obtain  $\lambda = 1.0$ .

### 3.5.2 Flow field: simulation vs. analytical theory

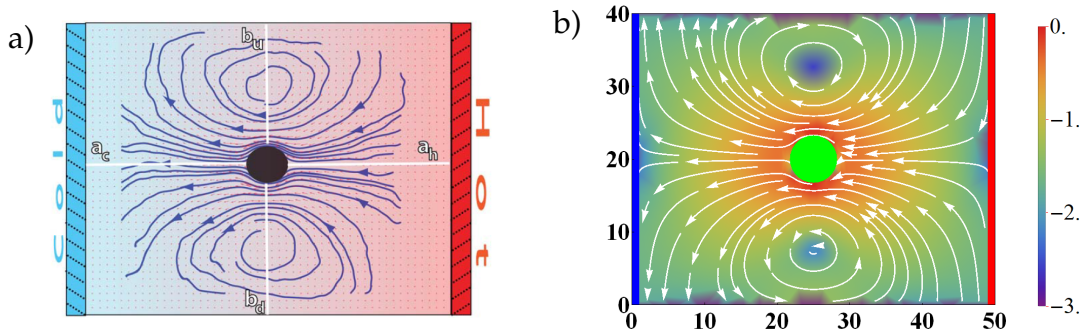


**Figure 3.12:** Cross-section of the thermophoretic flow field of a colloid confined between walls. Parameters and setups: cuboid box with  $L_x = L_y = 40$ ,  $L_z = 50$ , thermophoretic force applied in Eq. (3.23) is the same as in Ref. [60], i.e.  $F_T = 2.5$ . (a) Flow field measured via simulation, taken from Ref. [60]. (b) Analytical calculation of flow field with slip wall boundary conditions. Background color coding (flow intensity) is prescribed in Chapter 2 Sec. 2.5.

We analytically calculate the flow velocity induced by a thermal gradient applied on a confined colloid, by considering the solution of the Stokes equation in Eq. (3.13) and superposing with constant back flow (along gradient direction), and numbers of images along two directions perpendicular to  $\nabla T$ . Note that the simulations in Ref. [60], bounce back rule is applied at the walls which satisfies no-slip boundary conditions. However, the measurement of thermophoretic force  $F_T$  is only influenced by the  $z$ -component of the flow velocity, and independent the wall is slip or no-slip. Therefore, the above treatment of flow field is still sufficient for the evaluation of the effective friction  $F_T$ . (Detailed calculations for two types of boundary conditions are presented in Appendix B.)

For boundary conditions where the colloid is confined between walls, central image we found that the analytical calculation of thermophoretic flow fields resemble very nicely the simulation results in reference [60] (Fig. 3.12

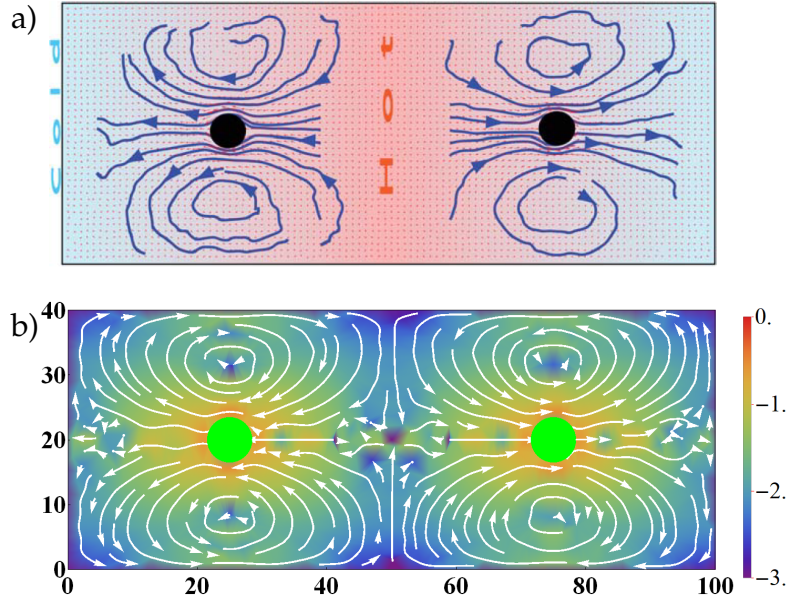


**Figure 3.13:** Cross-section of the thermophoretic flow field induced by twin colloids in periodic temperature gradient [60]. (a) Flow field visualized from simulation, taken from Ref. [60]. (b) Analytical calculation of flow field, parameters: cuboid box with  $L_x = L_y = 40$ ,  $2L_z = 50$ ,  $F_T = 2.5$  is applied in Eq.( 3.23). Background color coding (flow intensity) is prescribed in Chapter 2 Sec. 2.5.

(a). This further confirms the validation of back flow assumption in Ref. [60]. With full PBCs, the twin colloids are placed in a periodic temperature gradient [58, 60], a discrete Fourier transformation (DFT) is applied to obtain the flow field analytically. Importantly, we notice that the source dipole term in Eq. (3.13) decays much faster (with  $r^{-3}$ ) than the Stokeslet term (with  $r^{-1}$ ), such that the DFT is only applied on the Stokeslet term (Appendix B). The thermophoretic flow stream lines and analytical calculation show to be qualitatively the same. Interestingly, the flow pattern with symmetrically placed colloids in periodic temperature gradient resembles the flow induced by force dipole, which is a standard flow field model for microswimmers [93].

### 3.5.3 Finite system size scaling

Applying the aforementioned protocol, we analytically quantify the enhanced contribution in  $F_T$  measurement by calculating  $\mathbf{v}_T^\gamma$  (Eq. (3.23)). In this way,  $\alpha_T^{sim}$  (analytically) in Eq (3.21) can compare with simulation results.

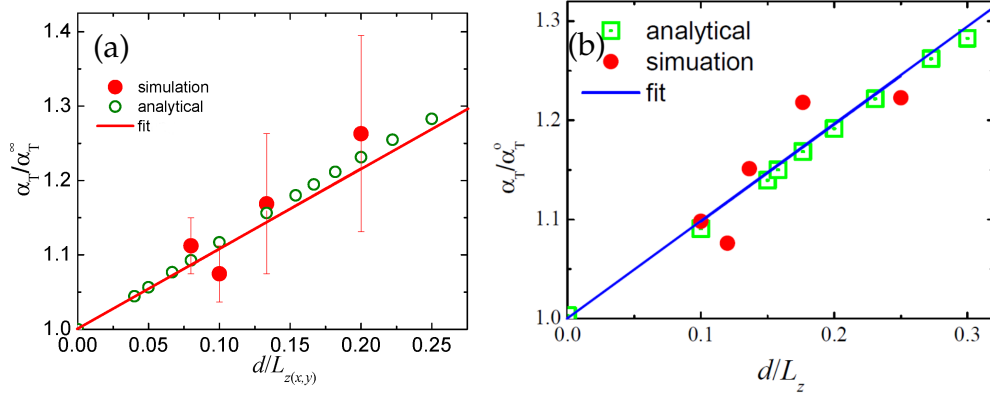


**Figure 3.14:** Thermal diffusion factor as a function of system size with different boundary conditions. (a) Colloids confined between walls (Fig. 3.12). Open circles are the analytical calculation, red symbols and red line correspond to simulations and a linear fit with  $\lambda = 1.1$ . Here  $r_3$  potential is applied, and  $\alpha_T^\infty = -53$  (b) Colloids with  $r_6$  potential symmetrically placed in periodic  $\nabla T$ , open squares refer to analytical calculation, red solid symbols are simulation results with linear fit indicated by solid blue line, with  $\lambda = 0.98$  and  $\alpha_T^\infty = -89$ .

For colloids confined between two boundary walls (see in Fig. 3.12),  $\lambda = 1.1$ . The nice agreement of FSEs study in Fig. 3.14(a) indicates that our quantitative approach is robust.

For open periodic boundary conditions, we gain  $\lambda \approx 1.0$  via both analytical calculation and simulation results (see in Fig. 3.14(b)). According to the author's experience, the approach to calculate the error bar by measuring the force component perpendicular to the gradient might not be very accurate. Therefore, our linear fitting also fluctuates significantly. We speculate that this might be the reason that the previous simulation [58] study provides  $\lambda_{sim} \approx 2.2$ . Nevertheless, in the framework of hydrodynamics, we validate analytically and theoretically that  $\lambda = 1.0$  would be a favorable estimation of finite size effect on simulation study of phoresis. It is also interesting to note that these finite size effects are not dependent on the algorithm we use, but on the confinement or the boundary conditions.

### 3.6 Conclusions

In this Chapter, we have derived the expression of the fluid slip velocity around a colloid immersed in a fluid with a temperature (concentration) gradient which reveals the mechanism of phoretic behaviors. By means of

MPC-MD simulations, we have shown that thermophoresis is akin to diffusiophoresis at macroscopic level. Their transport forces, together with associated flow velocity, obey the same linear relations.

A simplified model, which consists of two solid planar walls and filled with viscous fluid in between in the presence of temperature gradient, has been introduced to illustrate the microscopic mechanism of thermophoresis simulation. It is theoretically and numerically shown that repulsive or attractive LJ potential leads to different direction of pressure gradient, yet the temperature gradient is the same. This is because the sign of the repulsive or attractive potential is opposite inside the boundary layer. Therefore, macroscopically repulsive potential results in thermophilic behavior, while attractive one causes thermophobic behavior. We have further shown that the measurement of the local pressure around spherical colloids as well as the directions of the resultant pressure gradients are also consistent with the results of the simplified model. Therefore, we have explicitly shown that the MPC-MD model nicely captures the physics of thermophoresis in liquids. The local pressure gradient expression can be used to evaluate the local slip velocity and the total thermophoretic force for spherical colloids (Appendix A). Finally, we point out that our present model does not consider the effect of solvent-solvent potential interactions (such the solvent microscopic details as polarization effect can not be accounted for) on the thermophoresis.

Finally, we analytically obtained the flow fields considering the boundary conditions such as solid walls and PBC images, which agree well with previous simulation results. More importantly, calculating the flow field and the resulting effective friction, we have found that the finite size enhancement factor  $\lambda \approx 1.0$  can be directly calculated from flow field and effective friction due to two different boundary conditions, which means that the phoretic finite size effects don't depend on specific potentials or any other algorithm detail.



## Chapter 4

# Anisotropic thermophoresis <sup>1</sup>

### Synopsis

*In contrast to particles with spherical shape, we show that elongated colloids may have a thermophoretic response that varies with the colloid orientation. Remarkably, this can translate into a non-vanishing thermophoretic force in the direction perpendicular to the temperature gradient. Oppositely to the friction force, the thermophoretic force of a rod oriented with the temperature gradient can be larger or smaller than when oriented perpendicular to it. The precise anisotropic thermophoretic behavior clearly depends on the colloidal rod aspect ratio, and also on its surface details, which provides an interesting tunability to the devices constructed based on this principle. By means of mesoscale hydrodynamic simulations, we characterize this effect for different types of rod-like colloids.*

### 4.1 Introduction

As we know, the study of mass transport phenomena in temperature gradient ranges from liquid mixtures to colloid suspensions. Questions about the influences of moment of inertia and shape have been accessed via simulation or experimental techniques. In fluid mixtures the effect of the particle moment of inertia has been extensively studied [94–96], concluding that increased moment of inertia facilitates migration. Rodlike colloids have been experimentally investigated [97, 98] and characterized as a function of their electrostatic interactions. Nevertheless, no systematic study has been yet

---

<sup>1</sup> A paper based on some of the work described in this chapter has been published by *Soft Matter*. (ZT, M. Yang and M. Ripoll, 2017)

done to investigate the thermophoretic properties of colloids as a function of their shape.

The major question we want to address is how is the thermophoretic behavior of colloids affected when their shape is not spherical but elongated. A valuable and interesting parallelism can be made here between thermophoretic and friction forces. An elongated object moving with constant velocity in a fluid in a fluid along its axis is known to experience frictional force proportional to  $\gamma_{\parallel}$ , which is typically much smaller than the friction experienced by the same rod moving perpendicular to its axis proportional to  $\gamma_{\perp}$ . This is a well-know fact, which in the case of a shish-kebab model of adjacent beads has been calculated to be  $\gamma_{\perp} = 2\gamma_{\parallel}$  for aspect ratios larger than 20 [99].

It is therefore intuitive, that an elongated object with its axis aligned with a temperature gradient, will not have the same thermophoretic response as when the axis is perpendicular to the gradient. Hence and in contrast to colloids with spherical symmetry, colloids with an anisotropic shape should be characterized by two or more thermal diffusion factors, which is the main concept of the *anisotropic thermophoresis* [46]. The corresponding effect was already predicted for elongated particles in gases, where the propulsion of particles aligned with the gradient was expected to be larger than that of particles perpendicular to the temperature gradient [29, 100]. Therefore, the effect for elongated colloids in liquid solutions still remains to be explored.

Practical applications of thermophoresis have developed over several decades and are currently in a significant expansion stage. Some relevant examples are crude oil characterization [101], separation techniques [39], strong components accumulation in prebiotic conditions [13, 102], the precise characterization of proteins, for which thermophoresis can even distinguish between different binding states [103]; also various application in microfluidics [47, 104], or the fabrication of synthetic microswimmers [41, 43, 62]. The traditional versatility of thermophoresis is therefore importantly increased by considering different shaped objects.

In this work we investigate the anisotropic thermophoretic properties of colloidal rods by means of hydrodynamic computer simulations. We study the dependence of the thermophoretic forces for moving rods and for fixed rods at different orientations, with various aspect ratios and surface properties. The anisotropic effect can for example be reversed by changing the surface rugosity, which can be understood in terms of the associated temperature properties of the fluid in the vicinity of the colloid. Interestingly,

this anisotropy can induce a thermophoretic effect non-aligned with the temperature gradient. This thermophoretic force perpendicular to the temperature gradient has already shown to be the basic mechanism that allows the construction of thermophoretic turbines, which rotate in the presence of an external temperature gradient [46]. The anisotropic thermophoretic effect is also especially promising for microfluidic applications where significantly large and well-localized temperature gradients can be generated and precisely controlled in time and space. Applications of anisotropic thermophoresis in the presence of external temperature gradients offer then the possibility of engineering devices able to harvest waste heat energy.

## 4.2 Model of rods

The rod is constructed with the “shish-kebab” model built by  $N$  connected beads in a linear disposition as shown in Fig. 4.1. The excluded volume interactions between colloid and solvent are performed via MD with Lennard-Jones (LJ) type potentials (Eq.(2.5)). The bead diameter is taken as  $d = 4a$ . The mass of each bead is chosen such that the rod is neutrally buoyant, although results are not really depending on this value. The equations of motion of the beads and interacting fluid are integrated with a velocity-Verlet MD algorithm. The rod length  $L$  is given by  $L = d + (N - 1)l$ , such that the aspect

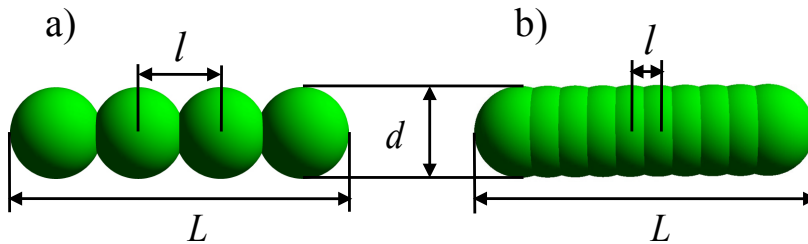


**Figure 4.1:** Sketch of the “shish-kebab” model of a colloidal rod of aspect ratio  $L/d = 3.7$  with variable number of beads  $N$ , and variable inter-bead separation  $l$ . (a) “Rough” rod with  $N = 4$  beads and  $l = 0.9d$ . (b) “Smooth” rod with  $N = 10$  beads and  $l = 0.3d$ .

ratio  $L/d$  can be fixed for more than one combination of  $N$  and  $l$ . Besides the particular solvent-bead potential, the rod surface properties are going to be determined by the interbead separation, which we characterize with  $l/d$ , the rugosity parameter. As can be seen in Fig. 4.1, a rough rod is obtained when  $l \simeq d$ , while a smooth rod is obtained when  $l \ll d$ . In order to prevent

the penetration of the fluid inside the rod, the maximum value of the rugosity parameter we employ is  $l/d = 0.9$ . We consider a three-dimensional box with periodic boundary conditions changing from 3 to 4 times the rod length  $L$ . Two types of simulations are performed. Simulations with fixed rods only need the colloid solvent interactions to be specified. Simulation with freely rotating rods and fixed central of mass, in which the rod motion is additionally accounted with rigid body dynamics [66].

### 4.3 Results

The migration of a particle in a temperature gradient is driven by the thermophoretic force  $\mathbf{F}_T$  [31, 105, 106].

A straightforward generalization of  $\mathbf{F}_T$  in Eq.(1.14) for a rodlike colloid can be written in terms of the *thermodiffusion tensor*  $\Lambda_T$ , reads,

$$\mathbf{F}_T = -\Lambda_T \cdot \nabla T. \quad (4.1)$$

In a very general case, colloids with arbitrary shape and arbitrary surface properties can be defined by a symmetric tensor with independent coefficients. Of particular interest is the case of an homogeneous colloidal rod with cylindrical symmetry. In this case, two independent coefficients are expected to be enough to determine the thermodiffusion tensor as

$$\Lambda_T = \alpha_{T,\parallel} \hat{\mathbf{u}}\hat{\mathbf{u}} + \alpha_{T,\perp} (\hat{\mathbf{I}} - \hat{\mathbf{u}}\hat{\mathbf{u}}), \quad (4.2)$$

with  $\hat{\mathbf{u}}$  the unit vector of long axis of rod. Here  $\alpha_{T,\parallel}$  is the thermodiffusion factor of the long rod axis, or equivalently the thermophoretic factor that characterizes a rod with the long axis aligned with the temperature gradient, as displayed in Fig. 4.2a. Reciprocally,  $\alpha_{T,\perp}$  is the thermodiffusion factor of the short rod axis, or of a rod with the long axis oriented perpendicular to the temperature gradient (see Fig. 4.2b).

#### 4.3.1 Linear decomposition of the thermophoretic force

The thermophoretic force acting on a rod with arbitrary orientation can be determined by the linear superposition of the two components with orthogonal thermodiffusion factors  $\mathbf{F}_T = \mathbf{F}_{\parallel} + \mathbf{F}_{\perp}$ . The temperature gradients along

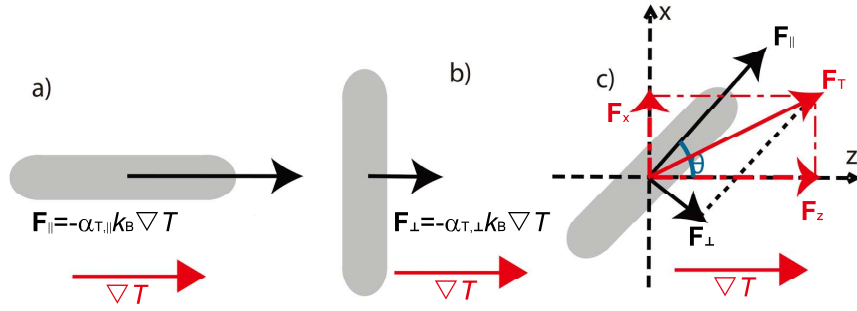


**Figure 4.2:** Sketch of the thermophoretic force of a colloidal rod fixed with different orientations with respect to the temperature gradient: a) parallel, b) perpendicular, c) with an arbitrary  $\theta$  angle.

the long and short axis are respectively  $\nabla T_l = \cos\theta\nabla T$  and  $\nabla T_s = \sin\theta\nabla T$ , with  $\theta$  the angle between the particle long axis and the temperature gradient, as displayed in Fig. 4.2c. The total force can then be expressed in terms of its components, parallel and perpendicular to the temperature gradient  $\mathbf{F}_T = \mathbf{F}_z + \mathbf{F}_x$  as,

$$\mathbf{F}_z = -(\alpha_{T,\perp} \sin^2\theta + \alpha_{T,\parallel} \cos^2\theta) k_B \nabla T, \quad (4.3)$$

$$\mathbf{F}_x = (\alpha_{T,\perp} - \alpha_{T,\parallel}) \sin\theta \cos\theta k_B |\nabla T| \mathbf{n}_x \quad (4.4)$$

where  $\mathbf{n}_x$  is the unit vector perpendicular to  $\nabla T$ . Equation (4.4) comes as a straightforward result of the tensorial character of the thermodiffusion tensor in Eq. (4.1), and strikingly implies that a non-vanishing thermophoretic force exists in the direction perpendicular to the temperature gradient. This force can in fact be easily measured in our simulations as shown in Fig. 4.3, such that it could also be measured experimentally [79, 107]. The measured force perpendicular to the temperature gradient is clearly non-vanishing, and it increases linearly with the applied temperature gradient, as expected from Eq. (4.4). This nicely confirms the tensorial character of the thermophoretic effect for objects without spherical symmetry.

Simulations with single rods fixed by an angle  $\theta$  with respect to the temperature gradient are performed for different orientations, as shown in Fig. 4.4. The values of  $\alpha_{T,\parallel}$  and  $\alpha_{T,\perp}$  can be obtained by fitting the expressions Eqs. (4.3) and (4.4) to the simulation results, or more efficiently, just by fixing the rod parallel ( $\theta = 0$ ) or perpendicular ( $\theta = \pi/2$ ) to the temperature gradient. The linear decomposition of the thermophoretic force in Eqs. (4.3) and (4.4) is clearly verified by these simulation results.

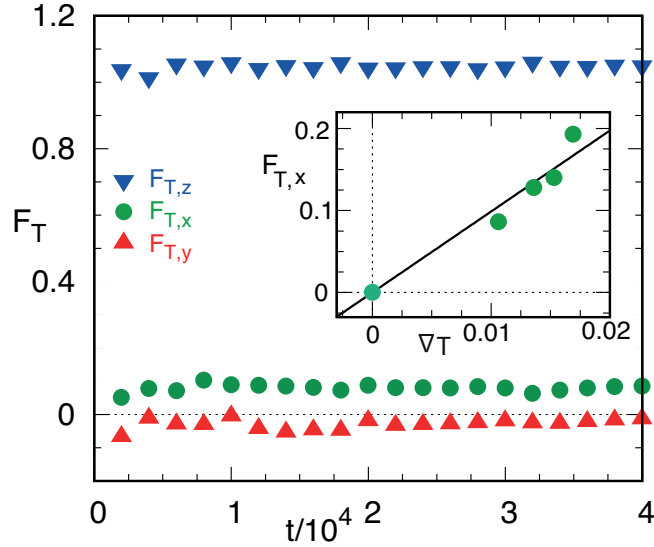


**Figure 4.3:** Thermophoretic force obtained from simulations as a time average for a fixed smooth rod ( $l/d = 0.3$ ), of aspect ratio  $L/d = 3.7$ , and interaction potential  $r6$ . The rod is fixed with an angle  $\theta = 45^\circ$  with respect to  $\nabla T$ . The force perpendicular to  $\nabla T$ ,  $F_{T,x}$ , is non-vanishing as predicted by Eq. (4.4). The inset shows the value of  $F_{T,x}$  for various values of  $\nabla T$ .

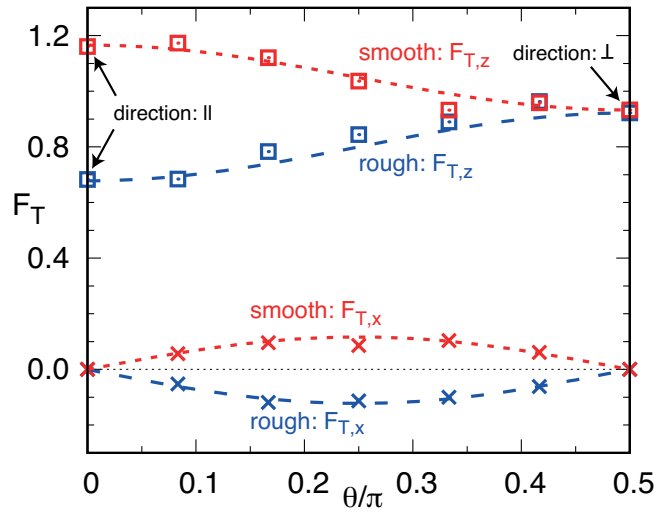


**Figure 4.4:** Thermophoretic force for fixed smooth ( $l/d = 0.3$ ) and rough ( $l/d = 0.9$ ) rods with  $L/d = 3.7$  and  $r6$ . The angle  $\theta$  denotes the rod orientation with respect to  $\nabla T$ , as sketched in Fig. 4.2c. The force  $F_{T,z}$  is measured in the direction parallel to  $\nabla T$  and  $F_{T,x}$  perpendicular to it. Symbols correspond to simulation results and lines to the expressions in Eq. (4.3) and (4.4).

Results in Fig. 4.4 also show that, depending on the simulated rods,  $F_{T,\parallel}$  can be larger or smaller than  $F_{T,\perp}$ , such that the force perpendicular to the gradient,  $F_{T,x}$ , can appear in both directions. This is in strong contrast to the friction force, which is always larger for rods oriented perpendicular to the

flow than for those parallel to it. Hence, the anisotropic thermophoretic effect is fundamentally different from the anisotropy of the translational friction.

### 4.3.2 Does thermophoretic anisotropy induce orientation?

As just discussed, elongated particles fixed aligned with the temperature gradient or perpendicular to it, can experience well-differentiated thermophoretic forces. Nevertheless, a freely moving rod in a temperature gradient, suffers a force exerted on one half of the rod which is exactly the same as in the other half, such that there is no net torque on the particle. For the same reason, friction forces are also known not to induce any orientation effects on elongated particles, in spite of their anisotropy. Orientation is induced only in the case that the flow field is in itself not homogeneous, as it is the case of a shear flow. The thermophoretic anisotropy does therefore induce no particle alignment. A freely rotating rod in a temperature gradient, will then change its orientation only due to stochastic interactions, being then characterized by a unique thermodiffusion factor,  $\alpha_{T,iso}$ , which would be determined by the average over all possible rod orientations. Simulations allowing particle rotation limited to two dimensions confirm this statement for the two parameter sets in Fig. 4.4, and the measured thermodiffusion factors verify that

$$\alpha_{T,iso} = \frac{1}{2} (\alpha_{T,\perp} + \alpha_{T,\parallel}) = \alpha_{T,\parallel}|_{\theta=45}. \quad (4.5)$$

This can be generalized to rods freely moving in three dimensions as

$$\alpha_{T,iso} = \frac{1}{3} (2\alpha_{T,\perp} + \alpha_{T,\parallel}). \quad (4.6)$$

While alignment refers to the first moment of the induced orientation, we could wonder if the effect exist in higher moment orders. It is therefore interesting to investigate if the presence of an external temperature gradient could modify the particle rotational diffusion. We measure the rotational diffusion coefficient by characterizing the long time behaviour of the mean squared orientation displacement. For computational efficiency, these simulations consider rods composed of smaller beads,  $d = 2a$ . The normalizing factor  $D_r^0 \simeq 8 \times 10^{-4}$  is obtained for the rough rods in the absence of temperature gradient. In the presence of non-vanishing temperature gradients, simulations are performed by keeping the rod center of mass fixed in the middle of the simulation box where the solvent average temperature is  $k_B \bar{T} = 1$ . The

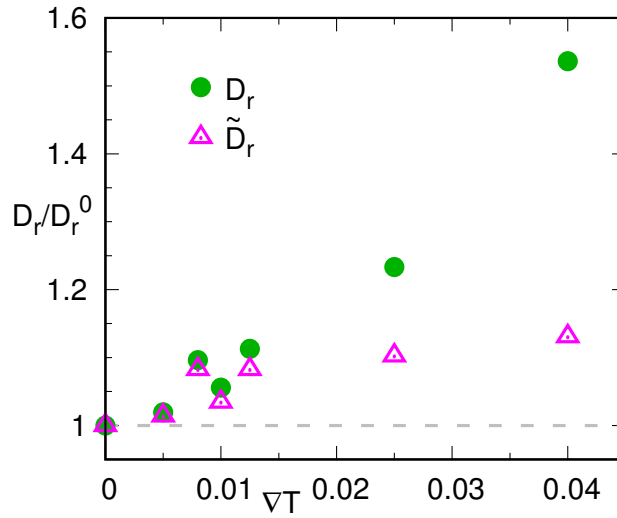


**Figure 4.5:** Normalized diffusion coefficient for a freely rotating rod (with  $l/d = 0.3$ ,  $L/d = 3.7$ , and  $r/6$ ) at various temperature gradients. Bullets correspond to the direct simulation measurements  $D_r$ , and triangles to the coefficient rescaled with the density correction  $\tilde{D}_r$ .

simulation data in Fig. 4.5 show to increase with the applied temperature, but this is mainly due to the particular equation of state of the employed MPC fluid, which is that of an ideal gas. Given a spatial linear increase of the temperature, the related position dependent density will be only approximately linear [57]. The density in the middle of the simulation box will then differ from the average one, which will affect the rotational diffusion coefficient. If we consider that  $D_r \propto 1/\eta$ , and that  $\eta \propto (\rho - 1)$  [108] we can explain the major  $D_r$  by considering the rescaled coefficient  $\tilde{D}_r = D_r(\rho|_{L_z/2} - 1)/(\rho - 1)$ . The factor  $\rho|_{L_z/2}$  can be measured in the simulations, or calculated from the ideal gas equation of state as  $\rho/\rho|_{L_z/2} = \bar{T} \ln(T_h/T_c)/(T_h - T_c)$  [57]. The rescaled coefficient  $\tilde{D}_r$  in Fig. 4.5 shows to be mostly independent of the applied temperature gradient within the precision of the data, which demonstrates that the temperature gradient has no effect in the particle orientation.

It is interesting to mention that *thermomolecular orientation* has been previously reported in diatomic fluids [109–111]. In these cases, elongated molecules made of two atoms with unequal sizes show to display certain average orientation towards the direction of the temperature gradient. This does not contradict the discussed lack of orientation induced by anisotropic thermophoresis, since the particles we discuss are elongated but intrinsically symmetric, namely composed of indistinguishable building blocks.

### 4.3.3 Aspect ratio effect

For spherical colloids, the size is well-known to influence  $\alpha_T$ , the particle thermodiffusion factor [58, 112, 113]. The overall increase of size of the rod will therefore also translate into an increase of  $\alpha_T$ , but how does the rod aspect ratio influence the anisotropic effect, still needs to be clarified.

Simulations of rods with orientations parallel and perpendicular to the temperature gradient are performed for different aspect ratios and for two rugosities as shown in Fig. 4.6 and Fig. 4.7. In order to compare with two different experimental approaches, we change the rod aspect ratio following two different strategies. The first strategy consists in fixing the particle diameter and changing its length. This is the case of polymeric rods made out of different number of monomers. We simply simulate rods with various numbers of adjacent beads, results are shown in Fig. 4.6. Obtained measure-

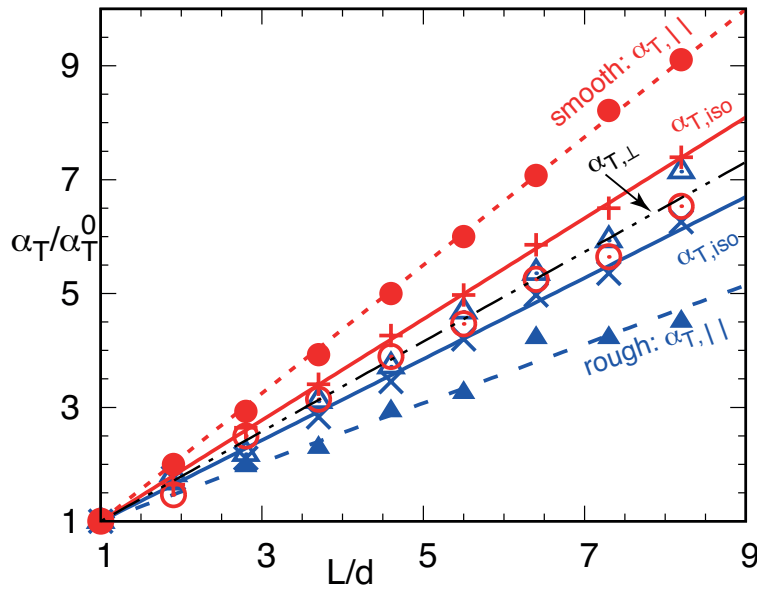


**Figure 4.6:** Normalized thermodiffusion factors for rods of fixed diameter  $d$  and varying length  $L$ . Parallel (open symbols), perpendicular (filled symbols), and freely rotating (crosses, calculated from Eq. (4.6)) thermodiffusion factors are presented together with linear fits. Results are presented for both smooth and rough rods (rugosity parameters  $l/d = 0.3$  and  $0.9$ ) with  $r6$  interaction potential.

ments are normalized with  $\alpha_T^0$ , the thermal diffusion factor of a single bead of the same characteristics as the ones employed to build the rod, such that for  $L = d$ ,  $\alpha_{T,\perp} = \alpha_{T,\parallel} = \alpha_T^0$  by definition. The four analyzed cases in Fig. 4.6 show a very clear linear increase of  $\alpha_T$  with the aspect ratio  $L/d$ , although with different slopes. This linear increase means that by characterizing the

values of  $\alpha_T$  at two different aspect ratios with enough precision, would allow us to easily extrapolate to other aspect ratios; also in the case that one of those values is the limiting spherical case  $\alpha_T^0$ .

Interestingly, in the case of a freely rotating colloidal rod, the overall thermodiffusion factor also increases linearly with the aspect ratio of the colloidal rod, given the verified expression in Eq. (4.5) and Eq. (4.6). This is very interesting by itself, and reminiscent of the well-known effect of the particle moment of inertia on the thermal diffusion in molecular mixtures [94–96]. The linear increase agrees with the theoretical expression in Ref. [98] in the case of very thin double layer. The increase is also consistent with the experimental results in Ref. [114] for double and single stranded DNA with two different number of monomers.

The second strategy to investigate the effect of the aspect ratio consists in keeping the colloid surface area constant, such that the increasing the length is accompanied by a decrease of the particle diameter. This can correspond to deformable structures such as vesicles, droplets, or polymeric globules [114]. In order to keep similar thermophoretic effect per unit area [58, 59], we maintain the interaction range constant for increasing bead size by making use of the displaced potential in Eq. (2.5). We fixed  $d = 4$  and increase  $\Delta$  such that the effective bead diameter is  $d_{ef} = d + 2\Delta$ . We approximate the surface of simulated shish-kebab rod in Fig. 4.1, by that of a spherocylinder such that  $S = \pi d_{ef} L$ , quantity that we keep then constant together with the rod rugosity. We take as reference the rod simulated in Fig. 4.6 with  $L/d = 6.4$ , then we decrease the number of beads by increasing the rod thickness by increasing  $\Delta$ . Figure 4.7 shows that in this case all thermophoretic factors decrease in magnitude with aspect ratio  $L/d_{ef}$  which agrees with the theoretical expression in Ref. [114].

To understand the linear increase of  $\alpha_{T,\perp}$  and  $\alpha_{T,\parallel}$  with  $L$  for fixed  $d$ , we can employ a geometrical argument by approximating the rod to an elongated parallelepiped of dimensions  $d \times d \times L$ . The surface aligned with the temperature gradient for a rod aligned with the gradient is  $4dL$ , while for a rod perpendicular to the gradient this surface is  $2dL + 2d^2$ , both increasing with  $L$ . Then, if we assume that each  $\alpha_T$  is directly proportional to the surface aligned with the temperature gradient, the effect would be explained. Similar reasoning for the case of fixed  $S$  would predict an increasing  $\alpha_{T,\parallel}$ , and decreasing both  $\alpha_{T,\perp}$ , and  $\alpha_{T,iso}$ . This is still very reasonable, since the assumed direct proportionality of the surface and the thermophoretic force is

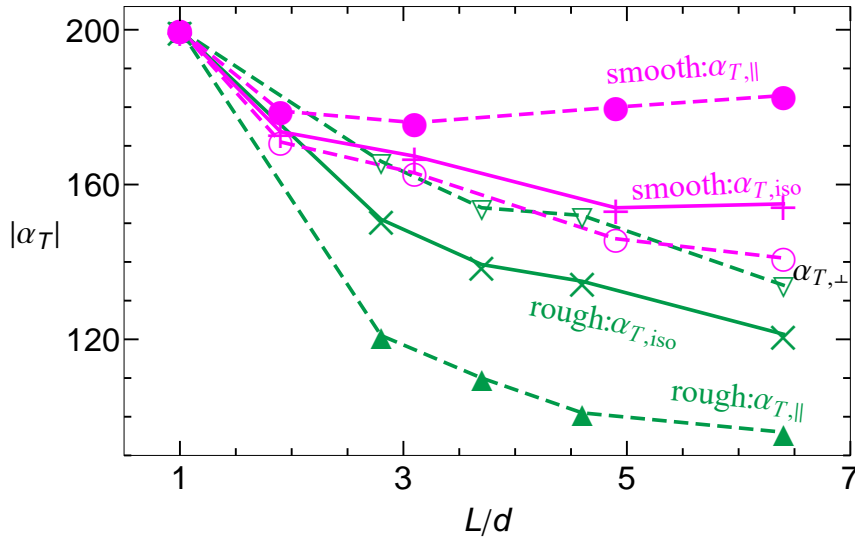


**Figure 4.7:** Thermodiffusion factors for rods of fixed surface area  $S$ . Symbols, potential, and rugosity parameters are similar to Fig. 4.6. Lines connect symbols as guide to the eye.

not necessarily precise; as well as the contribution of the balance of the two surfaces at constant temperature might not be negligible.

#### 4.3.4 Surface effects

The rod surface is modified in our model in two different manners. On the one hand, the surface shape as described in Fig. 4.1 modifies its rugosity with the parameter  $l/d$ . On the other hand, the choice of the employed potential, attractive-repulsive, soft-steep will also modify the thermophoretic properties of the rod. To analyze more in detail these effects, further simulations calculate  $\alpha_{T,||}$  and  $\alpha_{T,\perp}$  as a function of the different potential interactions and the rugosity parameter  $l/d$ , as shown in Fig. 4.8 and Fig. 4.9. In the case of spherical colloids, the thermodiffusion factor  $\alpha_T^0$  is known to depend on the colloid-surface interactions, and on the colloid size [24, 58]. With rods of fixed aspect ratio, we perform simulations with repulsive and attractive potentials, and with different  $n$  values in Eq. (2.5), for which  $\alpha_T^0$  is also evaluated. The parallel  $\alpha_{T,||}$ , and perpendicular  $\alpha_{T,\perp}$ , thermodiffusion factors are compared with  $\alpha_T^0$ , as displayed in Fig. 4.8. Values larger than the reference linear increase in Fig. 4.8, in absolute numbers, indicate the enhancement of the thermal diffusion factors due to the increase elongation of the rod. This

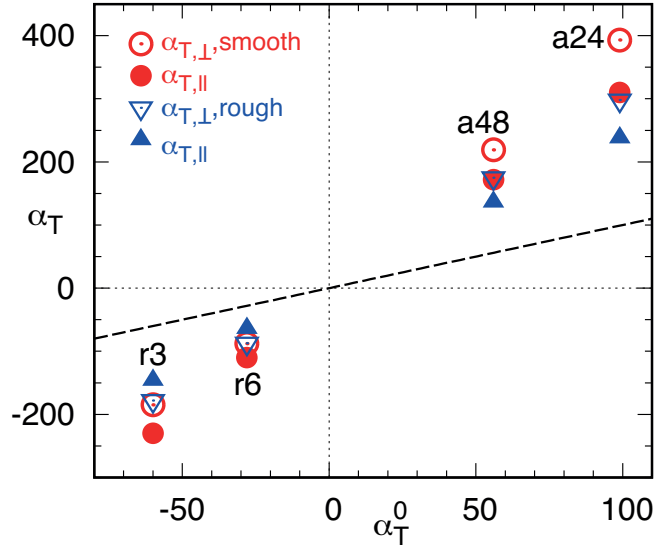


**Figure 4.8:** Parallel and perpendicular thermodiffusion factors for rods with  $L/d = 3.7$  with various interaction potentials (indicated in the labels) as a function of  $\alpha_T^0$ , the thermodiffusion factor of a single bead. Results are provided for the same two rugosity parameters as in Fig. 4.6. The dashed line has slope one and is a guide to the eye.

enhancement is clear in all investigated cases, although its magnitude differs for the different potentials, rugosities, and orientations. In general, the increase of  $\alpha_{T,\parallel}$  and  $\alpha_{T,\perp}$  shows to be larger, the larger the  $\alpha_T^0$ .

The effect of the surface rugosity can already be observed in Fig. 4.4 and Fig. 4.6 where simulation results of two well-differentiated rod rugosities are presented. For the repulsive potential and aspect ratio here employed, the rough rod shows  $|\alpha_{T,\parallel}| < |\alpha_{T,\perp}|$ ; *i. e.* the thermophoretic force for the rod aligned with the temperature gradient is smaller than for the perpendicular one. Meanwhile the smooth rod with the same potential shows the opposite behavior,  $|\alpha_{T,\parallel}| > |\alpha_{T,\perp}|$ . This means that by changing the rugosity of the rod, the forces perpendicular to the temperature gradient can invert their direction, as shown in Fig. 4.4. This is though not the case for the rods simulated with attractive interactions where  $\alpha_{T,\parallel} < \alpha_{T,\perp}$  for both the smooth and the rough surfaces. Note that the sign of the thermodiffusive factors is never modified, such that the thermophilic/thermophobic character of the colloids does not change with its shape change from spherical into elongated, and it will be therefore the same for both components  $\alpha_{T,\parallel}$  and  $\alpha_{T,\perp}$ .

The dependence of the thermal diffusion factors with the rugosity parameter  $l/d$ , is shown in Fig. 4.9. With increasing rugosity of the rod surface, the thermal diffusion factor shows to decrease, or to remain unchanged. In

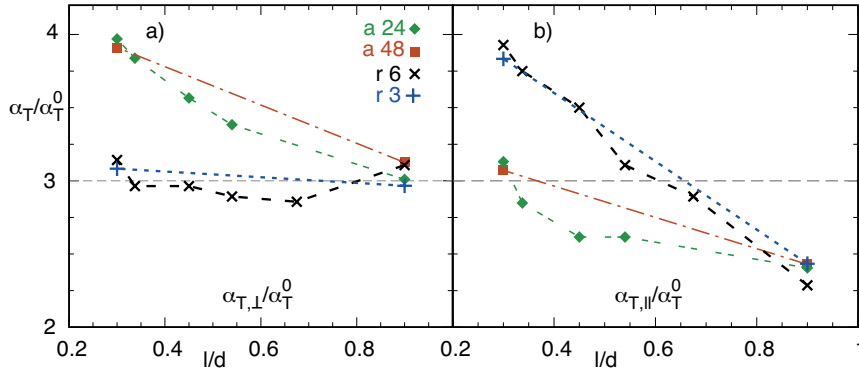


**Figure 4.9:** Normalized parallel and perpendicular thermodiffusion factors for rods with  $L/d = 3.7$  as a function of the rugosity parameter  $l/d$ . Simulations with various interaction potentials are reported and indicated in the corresponding labels. The horizontal line is a guide to the eye.

other words, smoother surfaces produce larger thermophoretic responses or eventually similar than their rough counterparts. The clear decrease of  $\alpha_{T,\parallel}$  with increasing rugosity is what eventually changes the relative importance of both factors and the direction of the force perpendicular to the temperature gradient.

To explain these dependencies, we should discuss two types of contributions, which are again related to the rod-solvent interaction potentials and the surface shape. The finite range of the solvent-bead interactions results in overlapping regions, in which solvent particles can simultaneously interact with more than one neighboring bead. The size of these overlapping areas decreases with increasing roughness, or potential steepness, modifying the effective rod-solvent potential. This effect is smaller for rough rods, for which the thermodiffusion factors in Fig. 4.9 have little dependence of the type of potential. Smooth rods interestingly show a difference between attractive (thermophobic) potentials, and repulsive (thermophilic) ones, but not between those with different steepness. The second type of contribution is in this case dominant, and related to the surface shape, and in particular with the presence of surface indentations which can explain the decrease of  $\alpha_{T,\parallel}$  with increasing roughness. To estimate the contribution to thermophoretic force between two arbitrary points at the rod surface, we consider first that the thermophoretic factor along a wall, can be assumed to be directly proportional to the wall length, which has been shown in Fig. 4.6. By considering Eq. (1.14), and that the gradient depends on the inverse of the distance, the contribution to thermophoretic force can then be determined by the difference of temperatures between these two points  $T_c$  and  $T_h$ . Fig 4.10 illustrates

the thermophoretic forces along a wall with an indentation,  $F_A$ , and a flat wall  $F_B$ , which are both considered to be the sum of two contributions by considering the temperature at the middle of the wall  $T_m$ . Indented and flat walls have different lengths, but the temperatures at their ends are the same. The wall length increase exactly cancels with the decrease of the temperature gradient, such that the wall thermophoretic forces are precisely the same, this is  $F_{A1} = F_{B1}$  and  $F_{A2} = F_{B2}$ . The total force in both cases is though not the same due to the angle  $\theta$  that determines the indentation, as sketched in Fig. 4.10, such that the force in the indented surface  $F_A$  is a factor  $\cos\theta$  smaller than the force in the perfectly smooth surface  $F_B = F_A/\cos\theta$ . This effect is

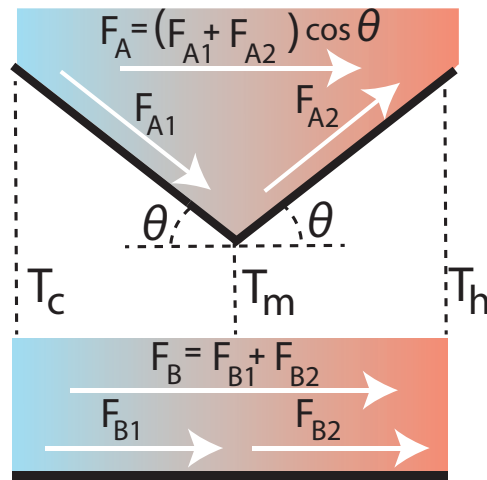


**Figure 4.10:** Sketch illustrating the decrease of the thermophoretic force along an indented surface.

very clear when the rod is aligned with the temperature gradient, and explains the clear decrease of  $\alpha_{T,\parallel}$  with  $l/d$  for all potentials in Fig. 4.9b). When the rod is perpendicular to the gradient, the effect of the indentation is subtly different but still present due to employed three-dimensional structure. However, the overall contribution is smaller which explains the unchanged or decreasing dependence of  $\alpha_{T,\perp}$  with  $l/d$  in Fig. 4.9a). In AppendixB, an detailed explanation has been provided.

### 4.3.5 Thermophoretic anisotropy factor

The importance of the anisotropic effect is determined by how different are the thermophoretic forces of the rods aligned and perpendicular to the temperature gradient. We therefore define the dimensionless *thermophoretic anisotropy*

factor as

$$\chi_T = \alpha_{T,\perp} - \alpha_{T,\parallel}. \quad (4.7)$$

The intensity and the sign of the force perpendicular to the temperature gradient is simply determined by  $\chi_T$ , as already shown in Eq. (4.4). The direction of the perpendicular force will have crucial importance in applications of the effect, determining for example the rotation direction of the thermophoretic turbines [46]. This means that the sign of  $\alpha_T^0$  will not be enough to know the direction of the perpendicular force; or, in other words, the thermophilic or thermophobic character of the surface does not determine the direction of the transverse phoretic effect.

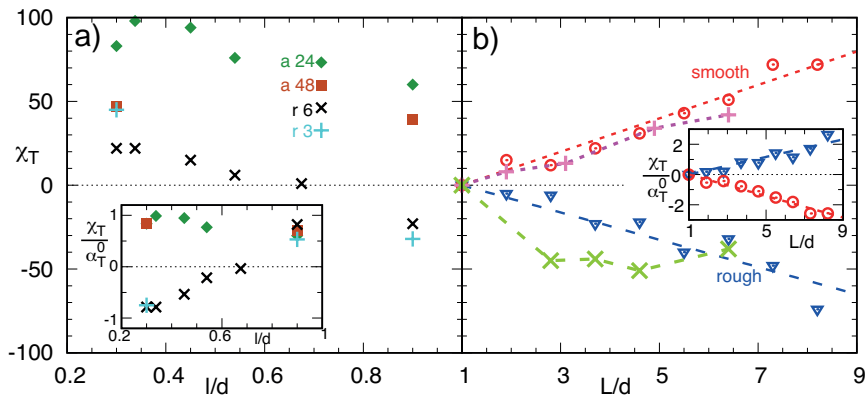


**Figure 4.11:** a) Asymmetric thermophoretic factor  $\chi_T$  as function of the rod rugosity parameter, for various interaction potentials, with  $L/d = 3.7$  from the data in Fig. 4.9. b)  $\chi_T$  as a function of the aspect ratio for  $r6$  interaction potential and rugosities  $L/d = 0.3$  and  $0.9$ . Circles and triangles correspond to the data in Fig. 4.6 for rods of fix diameter. The insets correspond to the ratio  $\chi_T/\alpha_T^0$  for the same data. Pluses and crosses correspond to the data in Fig. 4.7 for rods of fixed surface area.

The value of  $\chi_T$  is displayed for various potentials and rugosities in Fig. 4.11, where it can be observed that  $\chi_T > 0$  in the majority of the cases. This means that the perpendicular force happens most of the time in the same direction, which is positive with the convection in Fig. 4.2. In the thermophobic case, where the thermodiffusion factor is positive,  $\chi_T > 0$  corresponds to  $|\alpha_{T,\perp}| > |\alpha_{T,\parallel}|$ . This resembles the well-know translational friction case and provides the opposite trend as the predictions for aerosols [29, 100], showing to be an effect specific of colloids in solution. On the other hand, in the thermophilic case, where the thermodiffusion factors are negative,  $\chi_T > 0$  corresponds to  $|\alpha_{T,\perp}| < |\alpha_{T,\parallel}|$ . For comparison, the insets in Fig. 4.11 show the ratio  $\chi_T/\alpha_T^0$ , which will be positive in the friction-like cases, and negative

otherwise. This normalization also provides a rapid estimation of the magnitude of the effect which can be as expected to be as large as the phoretic effect itself, even for the small aspect ratios here considered. Note though that these are the results obtained by means of computer simulation and that in practical experiments, the results can show a much richer behavior. With our simulation results, we observe that by changing the surface rugosity, the anisotropic effect can reverse its direction in the case of thermophilic rods. We expect this behavior to be reproducible experimentally by changing the surface coating, electrostatic interactions, average temperature, or any of the factors that are known to affect the thermophoretic behavior.

## 4.4 Conclusions

Anisotropic thermophoresis refers to the different phoretic thrust that an elongated particle suffers when aligned with the temperature gradient and when perpendicular to it. This difference results in the thermophoretic force perpendicular to the temperature gradient when the rod is fixed oblique to the gradient. This anisotropy does not have any relevant effect on the particle orientation, nor on the rotational diffusion of the particle, given the considered symmetry of the colloidal rod. The existence of anisotropic thermophoresis is relatively intuitive, especially by comparing with the translational friction of a rod which is also noticeable different if aligned with the flow, or perpendicular to it. Here we analyze this effect in detail, showing that the intensity and the direction of the force is a function of the aspect ratio, the surface geometry, and the colloid-fluid interactions. Increasing aspect ratio by fixing the particle radius, increases the anisotropic phoretic effect in a straightforward manner. The rugosity of the colloidal surface is also relevant, being smooth surfaces the ones with larger anisotropic thermophoretic effect. In general, surfaces with larger phoretic effect also have larger anisotropic phoretic effect. Interestingly, for the simulation potentials employed in this work, the direction of the phoretic force perpendicular to the gradient is the same for both thermophobic and thermophilic colloids. Only rods with thermophilic and rough surface have shown in our simulations to display the perpendicular forces with opposite direction. We expect that experimental results will show an even richer behavior, in which the intensity and the direction of the effect could depend on many factors such as intrinsic surface

properties, eventual coatings, average fluid temperature and density, presence of salt ions, and various other factors. Note that since our simulation model does not include any of these aspects, only qualitative trends can be predicted. For example, the model has already been able to explain the experimentally observed dependence of the isotropic thermophoretic factor with the rod aspect ratio, with two types of DNA [114]. Two first practical applications of anisotropic thermophoresis have already been proposed for the construction of phoretic microturbines and micropumps. In the presence of external temperature gradients, the blades of a microturbine will rotate when being anisotropic [46], and a microchannel will experience some spontaneous directed fluid motion when including elongated tilted obstacles [115].

Although the work presented here has been exclusively focused in the thermophoretic effect, very similar results are expected with other phoretic effect such as diffusiophoresis. A direct proof for this is the fact that a similar microturbine placed in an external concentration gradient has shown to display similar behavior due to the related anisotropic diffusiophoresis [89]. In summary, with this investigation, we provide a deep insight into the anisotropic thermophoresis of elongated micro-meter size objects; effect that we hope will be soon experimentally verified, and find applications in different fields like particle characterization, microfluidics, or biomedicine.



## Chapter 5

# Microfluidic pump driven by anisotropic thermophoresis <sup>1</sup>

### Synopsis

*We propose a microfluidic pump that converts external heat into directed fluid motion on the base of anisotropic thermophoresis. An external temperature gradient is applied perpendicularly to the microchannel replete with viscous fluid; equidistant-elongated obstacles are fixed tilted to the walls. The fluid is driven continuously along the channel due to the thermophoretic forces perpendicular to the gradient. We investigate the resulting flow via mesoscale hydrodynamic simulations. Besides channel geometrical effects such as the obstacle inter-separation and channel width, the magnitude, the flow path and the direction of the net flux are determined by the obstacle aspect ratio, the surface structure and the nature of the solvent-solute interactions. We additionally relate thermophoretic anisotropy factor to the flux density in a linear fashion. This relation also underpins the linear nature of anisotropic thermophoresis.*

### 5.1 Introduction

Manipulating a small amount of fluids at nano- and microscales has become one of the most challenging goals of physics and engineering [116, 117]. The most extended approach to generate fluid flow in a channel is global forcing, namely mechanically exerting external forces by a pressure difference between an inlet and an outlet flows [118–120]. In contrast, local forcing,

---

<sup>1</sup> A German patent application 102017003455.9 is pending for the work described in this chapter. (M. Ripoll, ZT and M. Yang, 2017)

such as those found in biological systems, provides higher efficiency on microfluid pumping [47]. Numerous microorganisms move elongated flexible ancillaries such as cilia or flagella at the boundaries in an organized fashion to generate localized stresses. For instance, the self-propulsion of *Paramecium* is strongly correlated to the directional flow induced by regulated waving of cilia tied up on the cell walls [121–123].

Recently, a plethora of *modern* micromachines driven by surface forcing have sprung out in both experimental and theoretical studies [47, 124, 125]. Their motions are triggered by either local fields or gradients. Thermophoresis, as one of the local driving mechanisms, has become a versatile means for maneuvering colloidal suspensions and fluid pumping [41, 47]. For instance, thermophoresis can be applied to pump fluids in a microchannel with proper solid-liquid boundaries or periodic temperature inhomogeneities [60, 126].

Besides accurate driven mechanism, some degrees of spatial symmetry breaking is another essential factor to harness flow. Typical broken spatial symmetries are chemical asymmetry [127], spontaneous symmetry breaking [128, 129] and geometric broken symmetry [47, 124, 130]. Geometric asymmetry such as a *ratchet interface*, has been broadly utilized on micromotors and micropumps. First example is the Bénard-Marangoni convection based fluidic [131], with temperature difference orthogonally crossing ratcheted solid-fluid and fluid-fluid interfaces, the thermally driven convection can be rectified to a net global flow. Another example is rarefied gas pump [132–134], whose net flow is produced by asymmetric temperature profile and thermal creep. Similar to gas pumping, ratchet effect has been transplanted into phoretic, osmotic and even bacteria thrust [135] microfluidics mediated by liquid. Yang et.al and other pioneers proposed a series of ratchet phoretic pumps or motors [45, 47, 124, 125, 136, 137]. These works share two commons: (i) They make use of precise and versatile phoretic mechanisms. (ii) Ratchet surface does the job of breaking the geometric symmetry.

Nonetheless, all these aforementioned phoretic fluidics either have difficulties on construction of intricate differentiated compositions [125, 126] or ratchet geometries of channel walls, or on applying complex gradients [60]. Several very recent observations on anisotropic phoresis [46, 89] highlight their application capability on microfluidics with simplicity and versatility. Instead of considering the complicity of the channel walls or external gradients, we present a micropump focuses on the tunable properties of immersed solid obstacles with thermophoretic anisotropy inside the channel. Specifically, with

the non-zero thermophoretic force components along the microchannel, a net flow propagates continuously through the channel under a lateral temperature gap across it. We structure the script as follows. Firstly we describe the construction and the simulation setups of this micropump. Then the resulting flow, flux and its mechanism of this machine are discussed quantitatively. We further explore the effects of the channel geometries along both longitudinal and transverse directions of the channel. Moreover, the role of interfacial properties such as aspect ratio, rugosity and colloid-solvent interactions on flows and pumping capability are extensively investigated. Finally, we show that different from ratchet pumps, the flux density of the present micropump is linearly related to the thermophoretic anisotropy factor.

## 5.2 Model and methods

### 5.2.1 Device setup

The thermophoretic micropump is sketched in Fig. 5.1(a) (3D) and Fig. 5.1(b) (2D  $x - z$  cross section). The device consists of a microchannel with width of  $H$  replete with fluid, with embedded solid elongated obstacles (pillars) tilted at an angle  $\theta = 45^\circ$  with respect to the walls which are placed with separation (or *inter-pillar separation*)  $D$  to each other. Opposite walls have fixed different temperatures, such that the obstacles feel temperature gradients along obstacle surface (Fig. 5.1(b)). The thermophoretic properties of the surface of the obstacles will induce a net flow along the microchannel, parallel to the walls.

### 5.2.2 Simulation setups and parameters

Most simulations are performed in a cuboid box  $(L_x, L_y, L_z) = (30, 20, 30)$  (note that  $L_z \equiv H$ ) unless specified to other values, and with PBCs applied along  $x$  and  $y$  directions. The temperature at the no-slip walls are  $T_h = 1.2$  and  $T_c = 0.8$  then  $\nabla T \approx 0.0138$  in MPC units (Chapter 2). Moreover, as indicated in Fig. 5.1(c), obstacles are modeled by spherical beads with diameter of  $d$  on triangular lattices. The bead-fluid interactions are simulated by Molecular Dynamics (MD) with Lennard-Jones (LJ) potentials as denoted in Eq. (2.5). The rugosity parameter, can be modified by adjusting the bond length (or lattice length)  $l$  and number of beads, is denoted as  $l/d$ , the same as

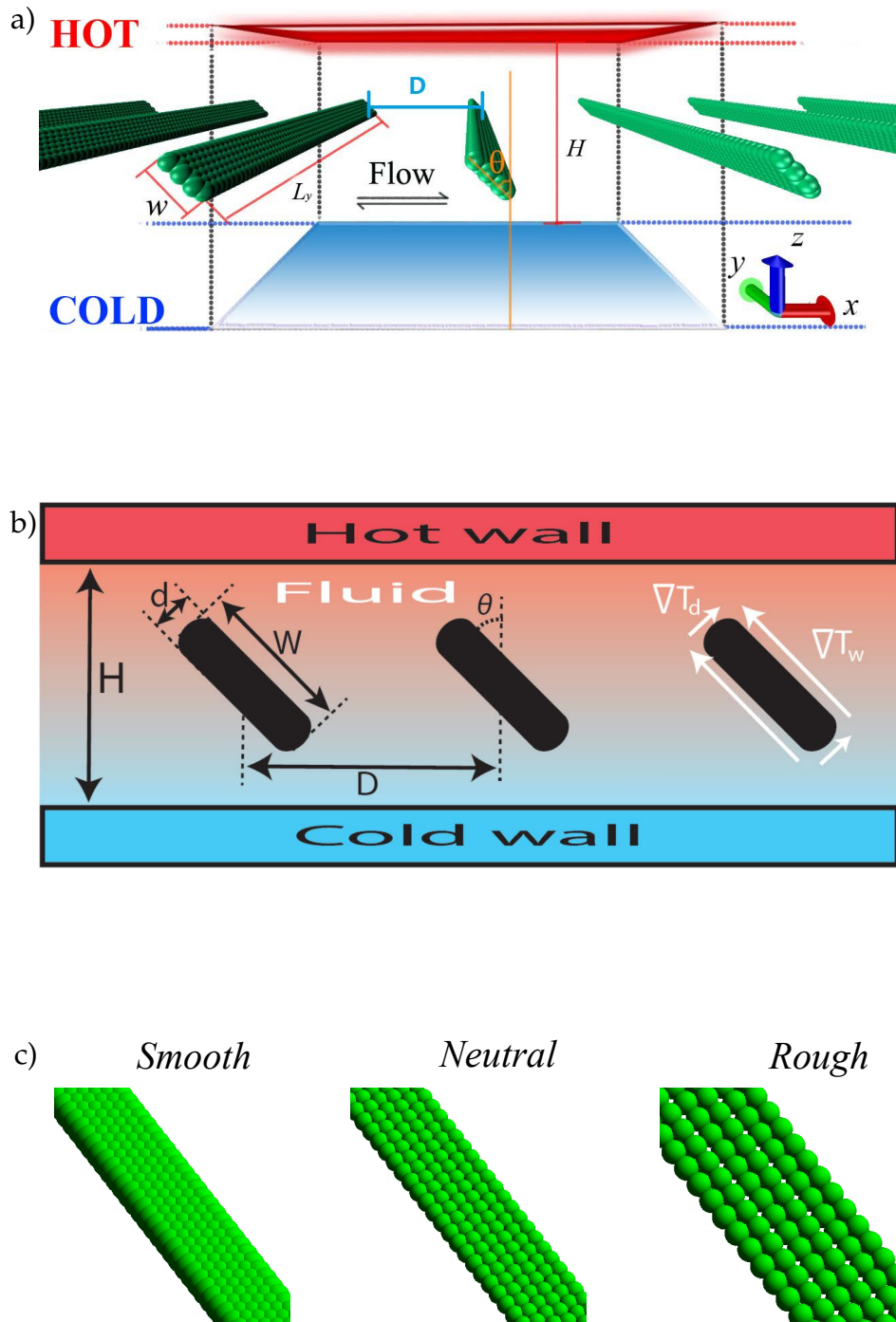


**Figure 5.1:** Schematic representations of the model of micropump and obstacles with various rugosities. (a) 3D scheme of anisotropic micropump. A microchannel modeled by two planar walls with different temperatures, replete viscous fluid (unshown) in between. Solid obstacles (obstacles) act as pump and inclined to the gradient with an angle  $\theta$ . (b) A sketch of the device at  $x - z$  cross section. The channel width is  $H$ . The obstacle with length of  $W$  and thickness of  $d$  are separated by a distance  $D$ . The obstacles suffer surface temperature gradients  $\nabla T_d$  and  $\nabla T_w$  along the long and short axes, respectively. (c) Schematic representations of obstacles with 3 different rugosities: "Smooth",  $l/d = 0.4$ ; "Neutral",  $l/d = 0.8$ ; "Rough",  $l/d = 1$ .

Chapter 4. The obstacle length is  $W$  (5.1(b)), the thickness (or the diameter of beads)  $d = 2.5$ . The obstacle extends over the whole box, which together with the effect of PBC models the effect of a very long pillar. Consequently, the detected flow at an arbitrary  $x - z$  section is identical, such that we average the flow field at each  $x - z$  section to enhance the statistics of measurement. The flow field at steady state are temporal average over  $5 \times 10^5 \sqrt{ma^2/(k_B T)}$  with at least 24 simulation measurements. Note that the temperature gradient perpendicular to the channel is not the same than along the obstacle walls, not along the long and short walls, which are  $\nabla T_W$  and  $\nabla T_d$  as indicated in Fig. 5.1(b).

## 5.3 Results

To elucidate the feasibility of the micropump, we show the flow pattern and its corresponding flow flux in a typical simulation. Later, the discussion of the influence from PBCs is provided.

### 5.3.1 Flow pattern and flow flux

A representative simulation output of the temporally averaged flow stream lines of a cross-section in  $x - z$  plane with  $(L_x, L_y, L_z) = (36d, 8d, 12d)$  is illustrated in Fig. 5.2(a). This flow pattern shows two differentiated types of regions, one is the “effective flow” region, distinguished by black stream lines, where fluid passes through the obstacles along the microchannel periodically sinusoidal-likely; the second type of region is the “vortex” region, labeled by green stream lines, where the flow rotates around an stagnation points with flow velocity zero. Fig 5.2(a) shows three obstacles in a primary simulation box with length of  $W = 2.73d$  which are equal-distantly placed with  $D = 12d$ . Hence, the flow pattern around each obstacle is identical.

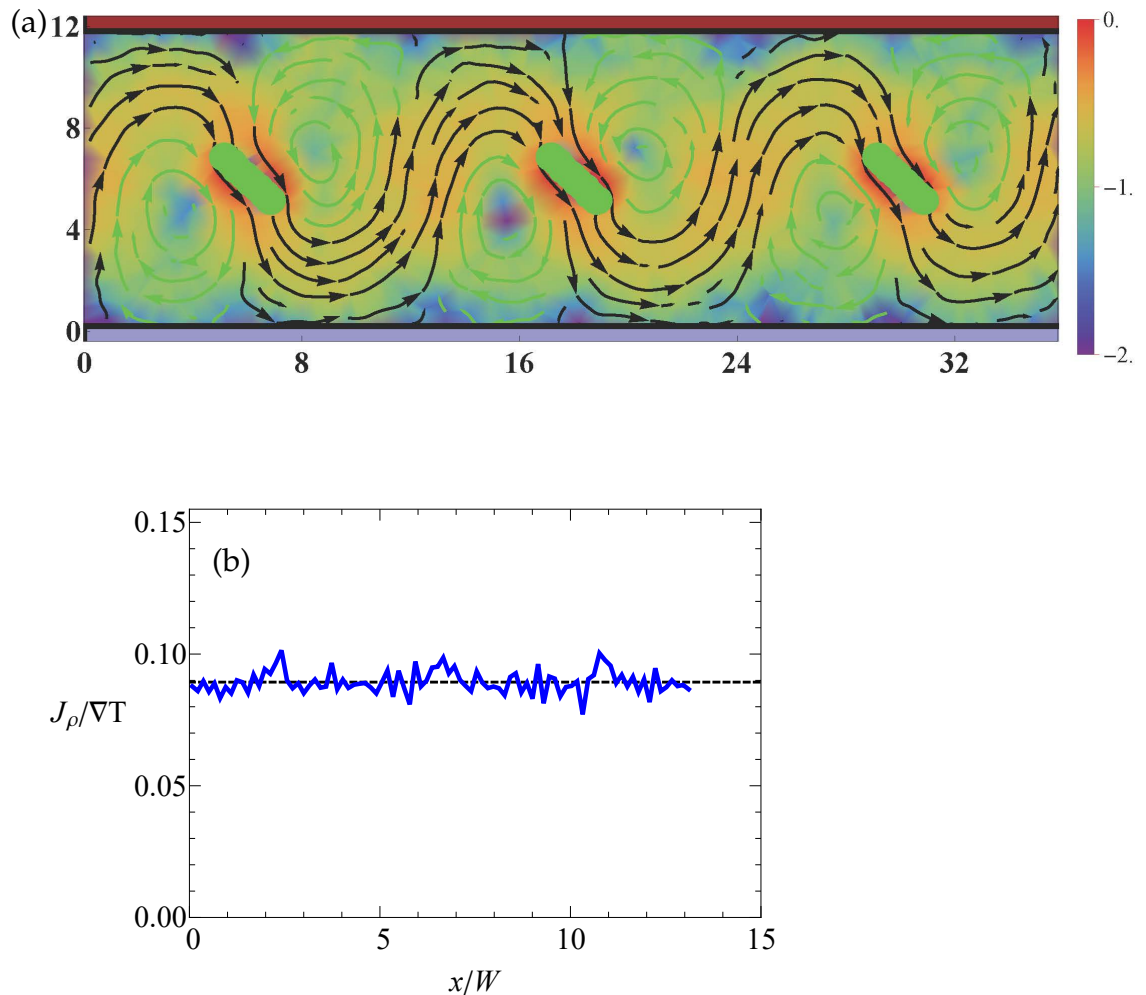
To characterize the pumping ability of the microdevice, we calculate the flux density  $J_\rho(x)$  defined as the particle flux per unit volume, that is,

$$J_\rho(x) = \frac{\int_0^H \rho(x, z) \cdot v_x(x, z) dz}{H}, \quad (5.1)$$

Eq. (5.1) can be discretized into the collision cell level, namely  $\delta = dx dy dz = a^3$  is the volume element for flux density calculation, and “ $(\cdot, \cdot)$ ” represents

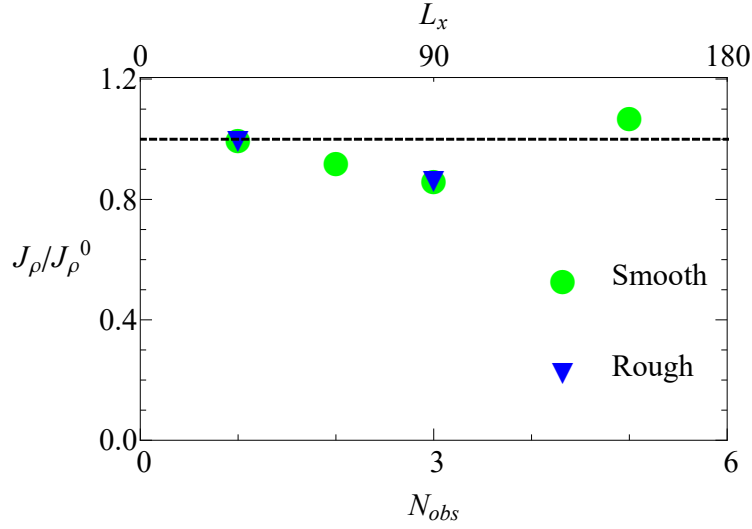
quantities in Cartesian coordinate at  $\cdot\text{-}\cdot$  (e.g.  $x\text{-}z$ ) cross section. The position is simplified due to the identity along  $y$  axis direction.  $\rho(x, z)$  and  $v_x(x, z)$  are the average density and velocity of the fluid in the position  $(x, z)$ . Given that the dimensions of the microchannel also influence the flux even with the same obstacle, here we choose the flux density rather than the flux as the measure of the capability of fluid pumping.

Fig. 5.2(b) indicates the  $J_\rho(x)$  along the channel at the steady state. Note that the data here is rescaled by  $\nabla T$ , since according to our previous study,  $\bar{J}_\rho$  linearly relies on  $\nabla T$ . Most important is that  $J_\rho(x)$  is a constant along the channel and its average  $\bar{J}_\rho = 0.001233$ . Hence, here and in what follows,  $J_\rho$  refers to the *average* flux density.



**Figure 5.2:** (a) The flow stream lines of this device. Background color coding relates to the fluid flow intensity as described in Chapter 2 Sec. 2.5. (b) The corresponding flux density (rescaled by  $\nabla T$ ) is constant along the channel. Simulations are performed with  $D = H = 12d$ ,  $W = 2.93d$ .

### 5.3.2 Influence of PBCs



**Figure 5.3:** Normalized flux density  $J_\rho/J_\rho^0$  calculated with different number of obstacles in the primary simulation box (called  $N_{obs}$ ).  $J_\rho^0$  is the flux density with one obstacle in the primary box. Other parameters similar as Fig. 5.2.

Due to the PBCs along the channel, different number of obstacles in the primary simulation box ( $N_{obs}$ ) should give almost the same simulation results when all the other parameters are kept constant. In particular, if the dimensions along the channel  $L_x$  results in a constant separation of the obstacles, it should be of irrelevance how many obstacles are simulated. However, PBCs also lead to fluid correlation and it is enhanced in smaller system sizes [138]. This intrinsic correlation may differ  $J_\rho$  and the flow field. With fixing other parameters, we measure  $J_\rho$  by placing different  $N_{obs}$  with  $D = 12d = 30$  with the same in the primary simulation box. According to Fig. 5.3,  $J_\rho$  has some fluctuations around a constant value. Besides their comparable flux density, flow patterns around each obstacle are identical for different  $N_{obs}$ , we thereby conclude that flux density and flow field are essentially independent on the fluid correlation or  $N_{obs}$  in a primary simulation box.

### 5.3.3 Mechanism: anisotropic thermophoresis

To understand the underlying mechanisms of this micropump, we recap the concept of anisotropic thermophoresis in Chapter 4. In the microchannel

configuration of Fig. 5.1(a), the ambient fluid of solid obstacles endures thermosmotic forces and flows around them. If obstacles are elongated structures (with  $(W \neq d)$  and  $0^\circ < \theta < 90^\circ$ , a net fluid flow will be generated parallel to the channel walls (Fig. 5.2(a)) due to the anisotropic effect. As illustrated in Fig. 5.1(b), this resulting flow is induced by the immersed solid-fluid interfaces under the environment with temperature gradients along the length axis (long axis) and short axis of obstacle  $\nabla T_W$  and  $\nabla T_d$ , respectively.

To estimate the flow flux density, we hereby relate the *thermophoretic anisotropy factor* which is a function of obstacle aspect ratio  $W/d$ , rugosity  $l/d$  and potential parameters ( $\epsilon$  and stiffness parameter  $n$  etc. in Eq. (2.5)), to  $J_\rho$ ,

$$J_\rho = \chi_T k_B |\nabla T| \sin \theta \cos \theta \frac{\rho}{A_0 \eta} \propto \mathbf{F}_{T,x}, \quad (5.2)$$

As shown in Eq. (5.2),  $\chi_T$  influences not only the magnitudes, also the direction of the flux. The prefactor  $A$  above is used to modify the effective friction at the obstacle-liquid interface. the expression above takes the aspect ratio effect into account, as well as the fluid viscosity. Moreover, to simplify the analysis of PBCs along  $y$  direction (the obstacles expand infinitely), both  $\alpha_{T,\perp}$  and  $\alpha_{T,\parallel}$  are redefined as thermal diffusion factors per length  $a$  along  $y$  axis.

The flow patterns are dependent on geometrical facts such as  $H$  and  $D$ . The flux density can be described as proportional to the perpendicular phoretic force in Eq. (4.4) and a geometrical function its associated parameters, based on the relation,

$$J_\rho = \chi_T k_B |\nabla T| \sin \theta \cos \theta \frac{\rho}{A_0 \eta} g_0(H/W, D/W), \quad (5.3)$$

where  $g_0(H/W, D/W)$  represents the effects of channel width and inter-separation distance. In the following chapter we observe the effects of channel width  $H$ , inter-pillar separation distance  $D$  and interfacial properties  $\chi_T$  on flow pattern and the net flux.

### 5.3.4 Channel geometrical properties

Based on previous discussions, the direction and intensity of the flow depend on quantities related to the geometrical description of the microchannel, they are  $D, H$ . Besides the optimal aligning angle  $\theta = 45^\circ$  is known (Eq. (5.2), Eq. (5.3) and Eq (4.4)), we discuss how  $J_\rho$  relies on these parameters.

## Transverse direction: effect of channel width

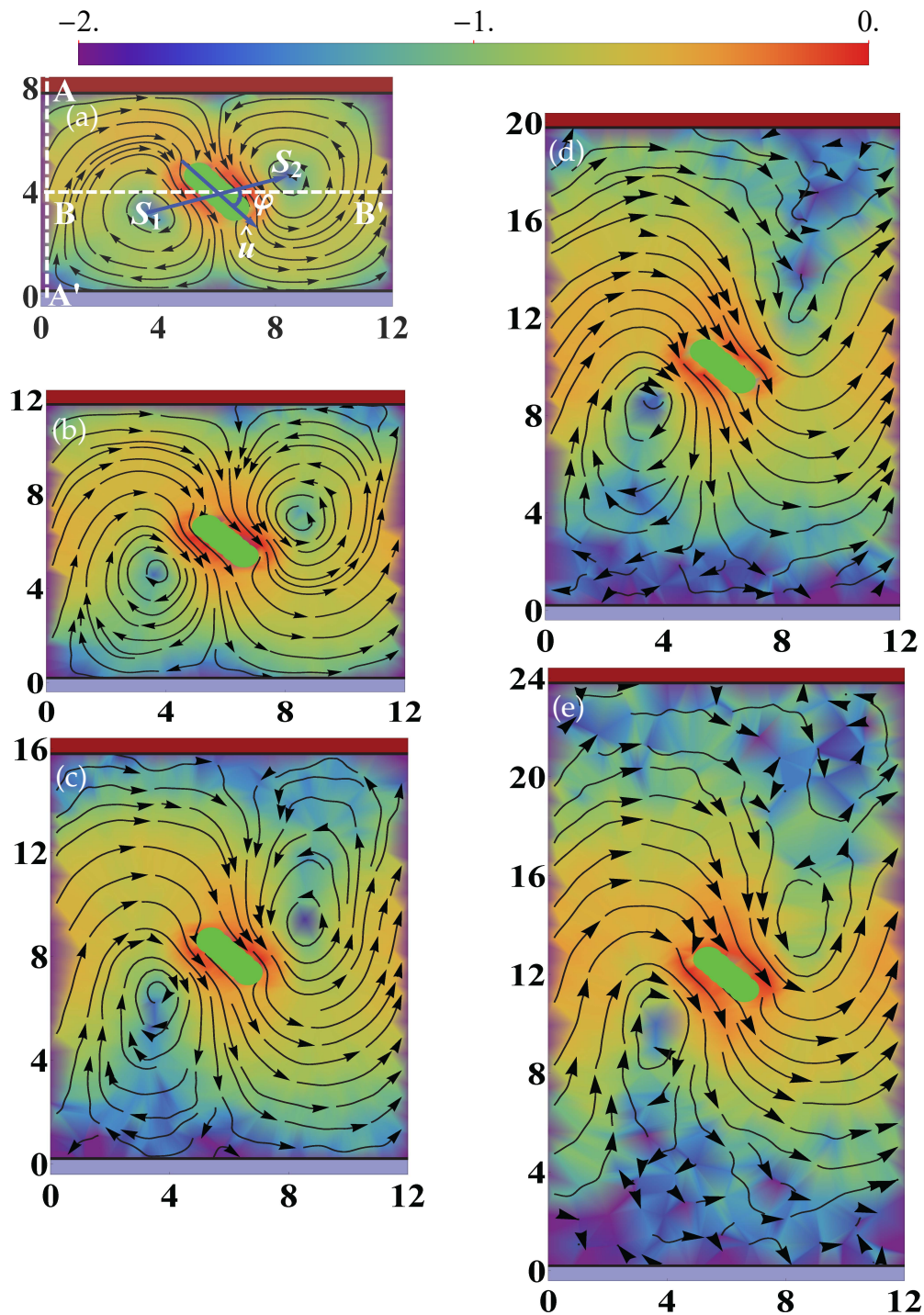


**Figure 5.4:** The flow field varies with channel width  $H$ . Background color coding is prescribed in Chapter 2 Sec. 2.5. (a)  $H = 2.93W$ . This figure shows the description of the stagnation points with the associated angle  $\varphi$  and the separation. (b)  $H = 4.39W$ . (c)  $H = 5.86W$ . (d)  $H = 7.32W$ . (e)  $H = 8.78W$ .

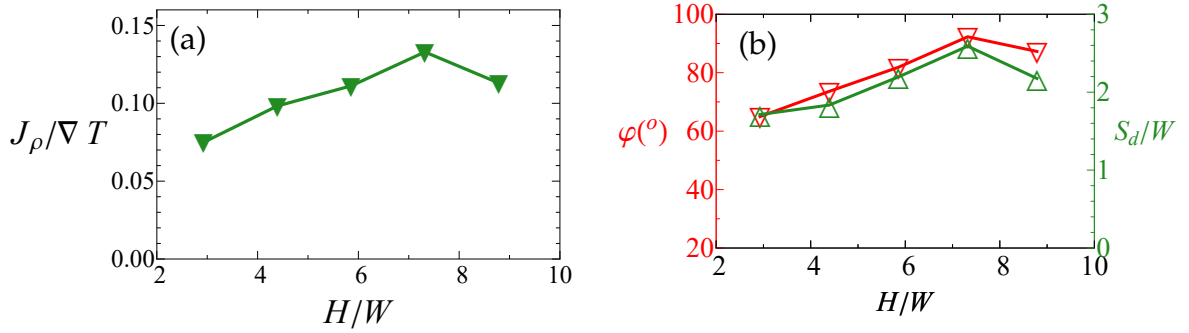


**Figure 5.5:** (a)  $J_\rho / \nabla T$  as a function of  $H$ . (b)  $\varphi$  as a function of  $H$ .

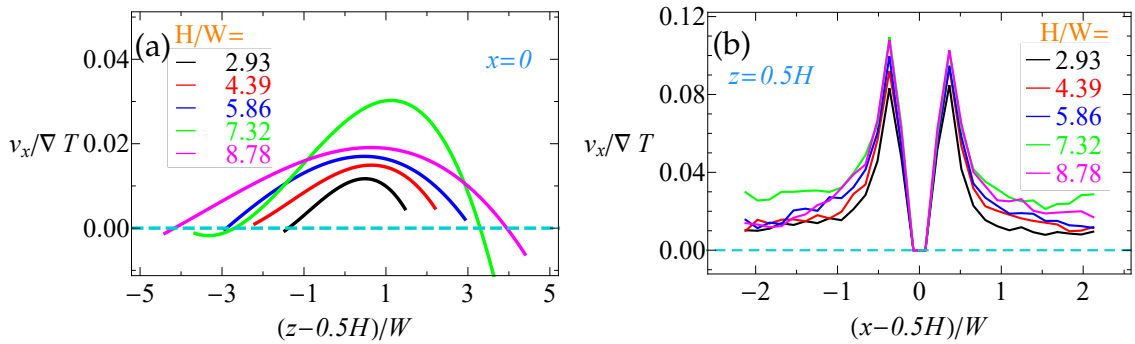


**Figure 5.6:** Velocity profiles  $v_x$  at different cross sections for various channel widths. (a)  $v_x$  profile at the cross section of  $x = 0$  (e.g.  $A - A'$  in Fig. 5.4(a)). To obtain a clear comparison, a polynomial fit is performed on the data. (b)  $v_x$  profile at the cross section  $z = 0.5H$  (e.g.  $B - B'$  in Fig. 5.4(a)).

To study the channel width effect, we keep the temperatures at walls  $T_h = 1.3125$  and  $T_c = 0.6875$ , but vary the channel width sequentially by keeping constant the obstacle aspect ratio and the inter-obstacle separation. The flow patterns with different  $H$  are illustrated in Fig. 5.4. Note that the channel width is varied from approximately 3 to 9 times the obstacle length. From Fig. 5.4(a) to (f), it is clearly distinguishable that the percentage of the effective flow region expands as  $H$  increases, albeit the velocity at the area far from the phoretic obstacle strongly decreases (Fig. 5.4(f)). At the same time the vortex region is also importantly affected, by changing its location and size with the channel width. Hence the increasing of  $J_\rho$  with increases  $H$  is expected as well. In order to study the flow patterns quantitatively, we characterize the stagnation points (points of zero flow velocity) by defining the stagnation angle  $\varphi$  and the normalized stagnation distance  $S_d/W$ . As indicated in Fig. 5.4 (a),  $S_d$  is the stagnation distance represented as the distance

between two stagnation points  $S_1$  and  $S_2$  around the same obstacle. Hence, enlarging of  $H$ , results in  $\varphi$  and the accompanied  $S_d$  tend bigger. Specifically, smaller  $\varphi$  and  $S_d$  are observed in Fig. 5.4(a) than what in Fig. 5.4(f).

Fig. 5.5(a) indicates that  $J_\rho/\nabla T$  grows gradually with channel width reaching an optimum at  $H/d \approx 20$  (or  $H/W \approx 7.32$ ), then decreases as the channel gets wider. According to the flow patterns in Fig. 5.4(a)-(e), the occurrence of this optimal channel width, say  $H_m$ , is explained as follows. The confinement provided by the no-slip channel walls influence the flow in two different ways. It restricts the expanding of the effective flow domain but also adjusts fluid flows horizontally rather than orthogonal to the channel direction. When  $H$  is as small as shown in Fig. 5.4(a), the "vortex" region takes up large part of the microchannel due to the significant confinement in the gradient direction, the distance between two associated stagnation points along  $\nabla T$  axis (i.e.  $\overrightarrow{S_1 S_2} \cdot \mathbf{e}_z$ ) is very close. In turn, as the channel gets wider, the enlarged distance along the diagonal where the long axis of obstacle located, enables the "effective flow" region to expand. Hence, the flux rises to a peak at  $H_m = 7.32W$  where  $\varphi$  is almost  $90^\circ$  (Fig. 5.5(b)). Further, the intensity of the flow, however, degenerates to  $10^{-2} |v|_{max}$ , at the areas far away from the obstacles and in the vicinity of the channel walls. This situation somewhat weakens the role of the confining walls and leads to a decrease of flux density (Fig. 5.4(d) and Fig. 5.4(e)). These two effects result in the  $H_m$ . Interestingly, the shapes of the curves, which represent the  $H$  dependence of both the stagnation angle  $\varphi$  and the stagnation distance  $S_d$  in Fig. 5.5(b), basically ensemble that of flux density in Fig. 5.5(a). This can be understood since increasing the channel width does not only favor the expanding of effective flow, but also creates more space for vortex regions to orient on the walls. Therefore, larger channel width is beneficial for fluid pumping, and also leads to larger values of  $\varphi$  and  $S_d$ .

To show the  $H$  dependence quantitatively, we analyze the velocities  $v_x(z)$  in the cross sections with different  $H$  at two cross sections along the channel. The first cross section is chosen at the midpoint between two neighboring obstacles (denoted as  $A - A'$  as the representative in Fig. 5.4(a)), where the flow is dominated by the effective flow. As shown in Fig. 5.6(a), the  $v_x(z)$  rescaled by  $\nabla T$  is clearly dependent on  $H$  and exhibits maximum at position close to  $0.5H$ . Therefore, we can conclude that each obstacle size has an optimal channel width; since the channel has to be wide enough to increase

the effective flow region and it should be narrow enough to confine the orthogonal flow along the channel. Thus,  $v_x(z)/\nabla T$  for  $H = 7.32W$  is relatively higher than the others. Since the average fluid density in the cross section of different  $H$  is the same, larger  $v_x(z)$  contributes to higher  $J_\rho$ . Similarly, Fig. 5.6(b) gives  $v_x(z)$  at the cross section crosses the middle of the channel at  $z = 0.5H$  (denoted as  $B - B'$  as the representative in Fig. 5.4(a)). The normalized velocity of  $H = 7.32W$  is also generally higher than the other velocities in concordance with previous quantities. Hence, the investigation of the velocity profile also confirms the occurrence of  $H_m$ .

This observation shows that an optimum of  $H$  for micropump which enhances the flux flow most. However, we speculate this value might not be an unique ratio  $H/W \approx 7$ , in the sense that interfacial properties and other confinement effects also vary the pumping capability.

### Longitudinal direction: the role of the separation between obstacles

It is intuitive to understand that the separation between obstacles has an important impact. Fig. 5.2(a) already shows that the effective flow region needs to occupy certain space in between obstacles. Therefore, in the limit of vanishing separation, no net flux will be generated. In the opposite limit, it is clear that one single obstacle will not be able to generate a considerable flux in an arbitrary long channel. In Figure 5.7, we show results for various simulations performed with three obstacles placed at various separations. The first observation that can be made is that the tortuosity of the stream lines decreases with increasing obstacle separation. This can be understood since the flow field in the most immediate proximity of the obstacle is mostly independent on the presence of neighbouring obstacles and has an intensity and direction determined by the surface rod properties. The flow further away from the rod just needs to adapt to the given boundary conditions.

The dependence of normalized flux,  $J/\nabla T$ , with increasing obstacle separation,  $D/W$ , is shown in Fig. 5.8(a). These results show that small but not vanishing separation of the obstacles the direction of the net flow can even be reverted. This can be also seen in the stream lines in Fig. 5.7 (a),(b) where the contribution provided by the vortex region shows to be larger than that of the effective flow region. Since the rotation in the vortexes occurs in opposite direction as the effective flow region the net flow results to have opposite direction. For larger separations (from  $D/W \approx 2.5$ ), the flux quickly increases

until a maximum value is obtained ( $D/W \approx 7$ , for the parameters here employed). For separations larger than this optimal value, the flux decays with increasing separation but interestingly, this decay occurs very slowly. In this way, for the case with largest separation where simulation have been here performed ( $D/W \approx 18$ ) the total flux is just 50% smaller than that with the optimal separation. This result can be practically advantageous, since devices with a smaller number of obstacles will be easier and cheaper to produce.

To understand in depth the shape of the flow, we also first quantify the position of the stagnation points via the stagnation angle  $\varphi$  and the stagnation distance  $S_d$  as can be seen in Fig. 5.8(b). These results show how the location of the vortexes center changes with increasing obstacle separation until they reach an stable location which is not anymore modified with increasing separation. With fixed channel width, the location of the vortex seems then to determine that separation with maximum flow flux.

The velocity profile at a cross section also reveals the overall flow flux for each separation distance. Fig. 5.9(a) shows the velocity profiles in the cross section in between the pillars. Although the trend is not straightforwardly monotonous, we can conclude that for moderate inter-pillar distances ( $D/W$  ranges from 2.93 to 10.98), the velocity is positive (towards right) and occupies almost the whole cross section with a maximum velocity occurs close to the middle. Their similar profiles suggest their comparable flow flux. However, larger  $D$  means weaker thermoosmotic force per unit length of fluid along the channel, therefore  $v_x(z)$  gets flattened with smaller flow velocities when  $D = 17.57W$ . On the other hand, when obstacles get closer such as  $D < 2W$ , the velocity towards left cancels the one to the right, and even flips the overall velocity direction at  $D = 1.46W$ . Also instructive is to analyze the flow parallel to the walls and in the middle of the channel ( $z = 0.5H$ ) as shown in Fig. 5.9(b). As we observed that the left half of the profile is akin to the right half, only the right half profile has been shown here. It can be seen that increasing of the separation distance elevates the velocity profile ( $D < 2.9W$ ) and then leads to the profile collapse ( $D > 2.9W$ ), until the profile starts to have a noticeable decrease at  $D = 17.57W$ .

Therefore, varying the separation distance can enhance or weaken flux as well as the flow velocity. In the case that inter obstacle distance is extremely close, the vortex flow domain seems to play a dominant role that suppresses or even reverses the flow flux. Interestingly, this observation also suggests the flux density reaches maximum at  $D/W \approx 7$ .

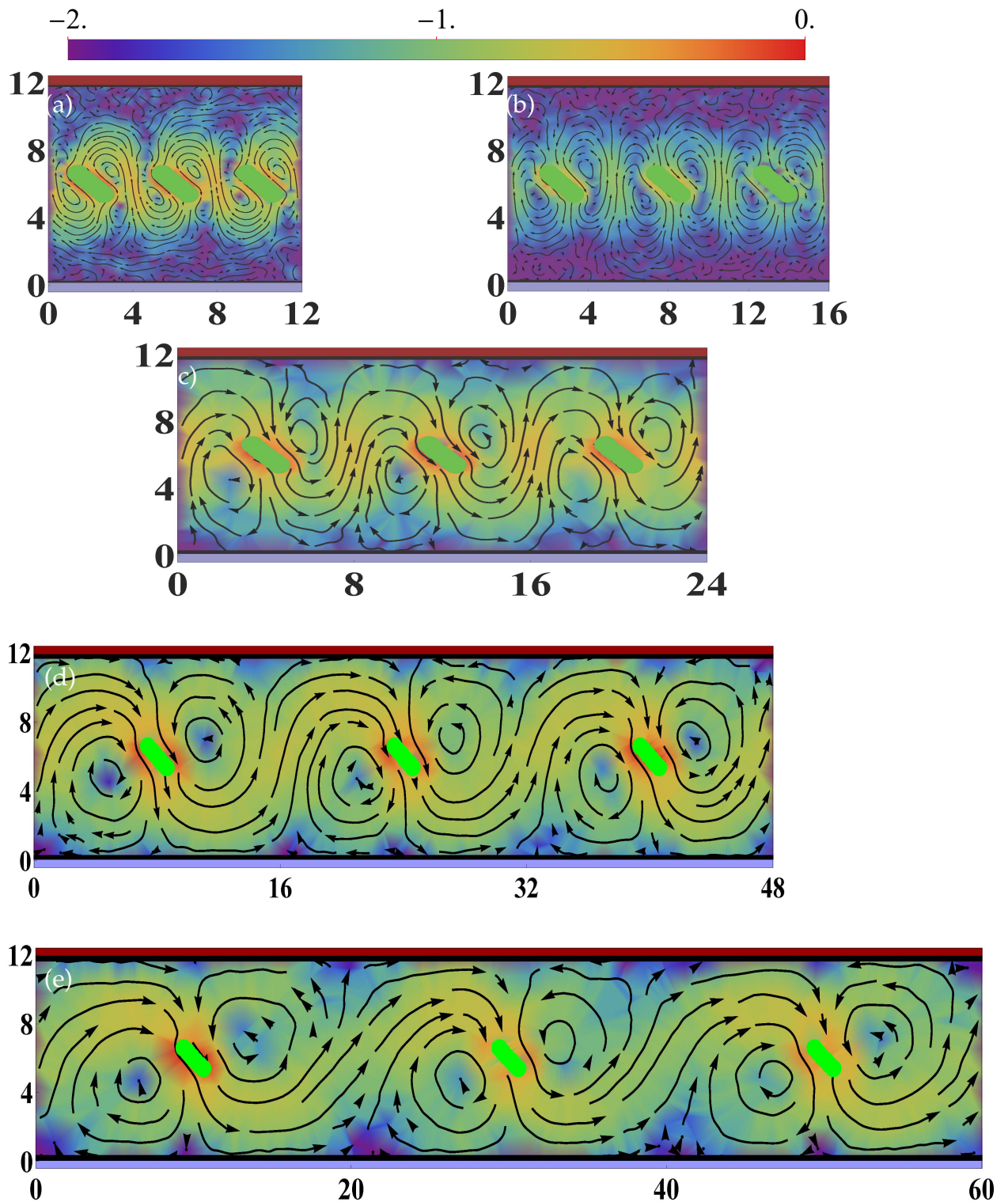


**Figure 5.7:** The flow patterns vary with changing of obstacle separation  $D$ . Background color coding is prescribed in Chapter 2 Sec. 2.5 (a)  $D = 1.46W$ , the flow is redirected when the stagnation points close to each other; (b)  $D = 1.95W$ , the flux is almost zero; (c)  $D = 2.93W$ ; (d)  $D = 5.86W$ ; (e)  $D = 7.32W$ .

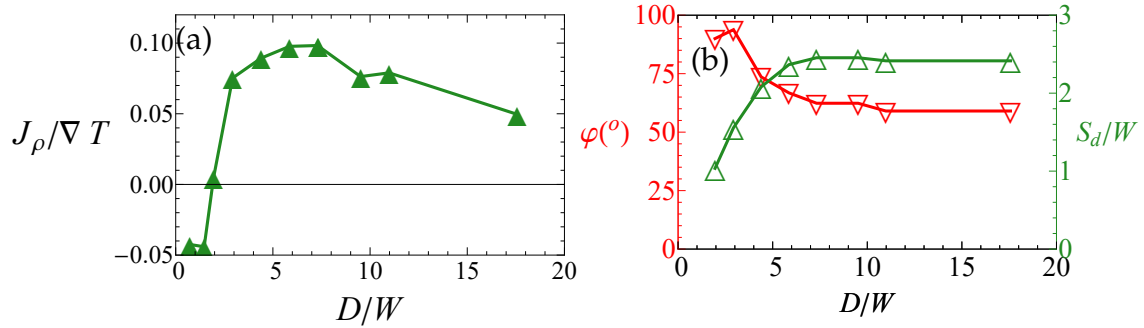


**Figure 5.8:** (a)  $J_\rho/\nabla T$  dependence with obstacle inter-separation distance  $D$ . (b) Corresponding  $\varphi$  and  $S_d$  as a function of the separation distance  $D$ .

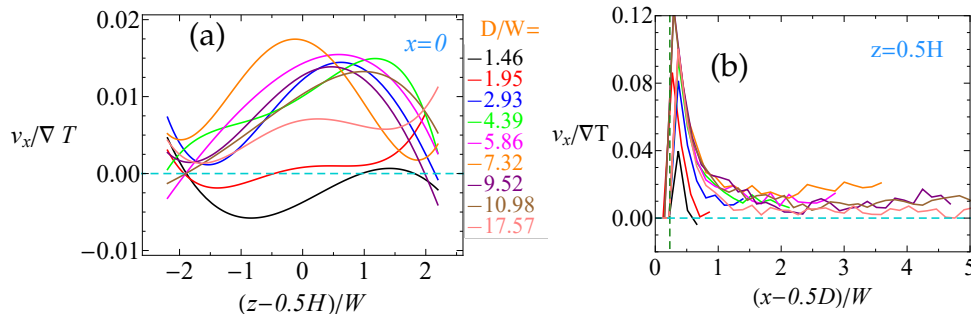


**Figure 5.9:** (a)  $v_x$  of the cross section at  $x = 0$  (just in between two pillars, similar to  $A - A'$  in Fig. 5.4(a)). To obtain a clear comparison, a polynomial fit is performed on the data. (b)  $v_x$  profile at the cross section  $z = 0.5H$  (similar to  $B - B'$  in Fig. 5.4(a)). Due to the periodicity of obstacles, the origin of the coordinate is shifted to a obstacle center, and only the data in the range of  $[0.0, 0.5D]$  are considered. The color legend is the same as Fig. 5.9(a)

### 5.3.5 Interfacial properties

#### Relating thermophoretic anisotropy factor to flux density

We analyze in depth the dependence of surface properties when the geometry of the micropump is fixed. The intensity and direction of the flow will then be strongly influenced by the length of the obstacle, the rugosity of obstacles and the solid-liquid interaction (e.g. thermophilic or thermophobic properties), which are all included in  $\chi_T$ . The thermophoretic anisotropy factor  $\chi_T$  defined in Eq. (4.7) characterizes the anisotropic thermophoretic effect, determinates the flow intensity. As discussed in Subsection 5.3.3, the inter-

	(rough, $r3$ )	(neutral, $r3$ )	(smooth, $r3$ )	(smooth, $a12$ )	(smooth, $a24$ )
$\chi_T$	-2.88	0.050	2.700	4.8	11.950
$J_\rho/\nabla T$	-0.086	0.011	0.104	0.103	0.249

**Table 5.1:**  $\chi_T$  and corresponding rescaled flow flux  $J_\rho/\nabla T$  of micropump with different rugosities and interaction properties. Interfacial properties of obstacle are represented by and rugosity ("rough", "neutral" and "smooth" are associated with  $l/d = 1, 0.8$  and  $0.4$  in Fig. 5.1(a)), and potential parameters (Chapter 2 Eq. (2.5)).

facial properties of obstacles is closely related to thermophoretic anisotropy factor  $\chi_T$  (Eq. (5.3)). With fixed the channel geometrical parameters ( $H = D = 30a$ ), the simulation results (see Table 5.1 and Fig. 5.10) reveal that the normalized flux density  $J_\rho/\nabla T$  exhibits linear scaling with  $\chi_T$ , which corresponds to various types of interfacial properties of obstacles.

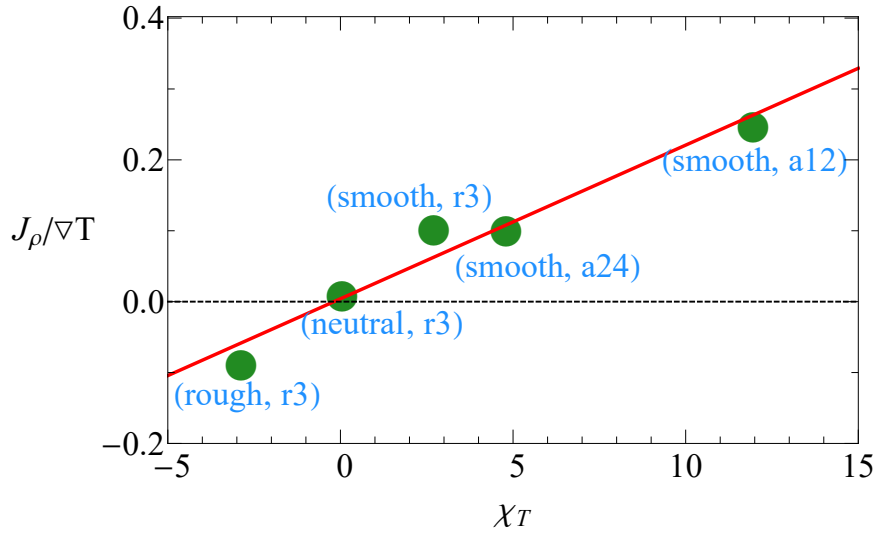


**Figure 5.10:**  $J_\rho/\nabla T$  calculated with different  $\chi_T$ . The blue colored labels denote the rugosity and interaction potential, namely (“rugosity”, “potential”). Other simulation parameters are fixed the same as the standard values. Note that the aspect ratio  $W/d$  smooth, neutral and rough obstacle are 2.73, 3.08 and 3.60, respectively.

### The role of the obstacle aspect ratio

In Chapter 4 we discussed how the thermophoretic force on a rod varied with its aspect ratio. Similar dependence is expected in the thermoosmotic effect close to the obstacle surface. Here we investigate how this affects the flow field in the microchannel.

To fairly compare the flow fields, considering our previous results, together with the length of the obstacle  $W$ , we vary the hot and cold temperatures of the channel walls, keeping  $\nabla T = 1.05 \times 10^{-2}$ , and we also change the channel width  $H$  and obstacle separation  $D$  such that  $H = D$  and  $D/W = 2.93$ . Interestingly, Fig. 5.11 shows that the flow stream lines with different  $W/d$  exhibit similar patterns. What verifies that the shape of the flow stream lines is determined by the ratio  $H/D$  and  $D/W$ . As shown in Fig. 5.12(a),  $J_\rho$  vs.  $W/d$  agrees with linear relation very well, as could be expected from Eq. (4.7) and the relation is  $\chi \propto W/d$ . Note that the red dash line (obtained from linear fitting) crosses  $J_\rho = 0$  where  $W/d = 1$ , this is consistent with zero density flux when the pillar with cylindrical shape. Moreover, this similarity can be inferred also from the constant stagnation angle  $\varphi$  as well as the rescaled stagnation distance  $S_d/W$  for different aspect ratios (Fig. 5.12(b)). This is because that thermoosmotic force on fluid increases linearly with  $W/d$ , and is

parallel

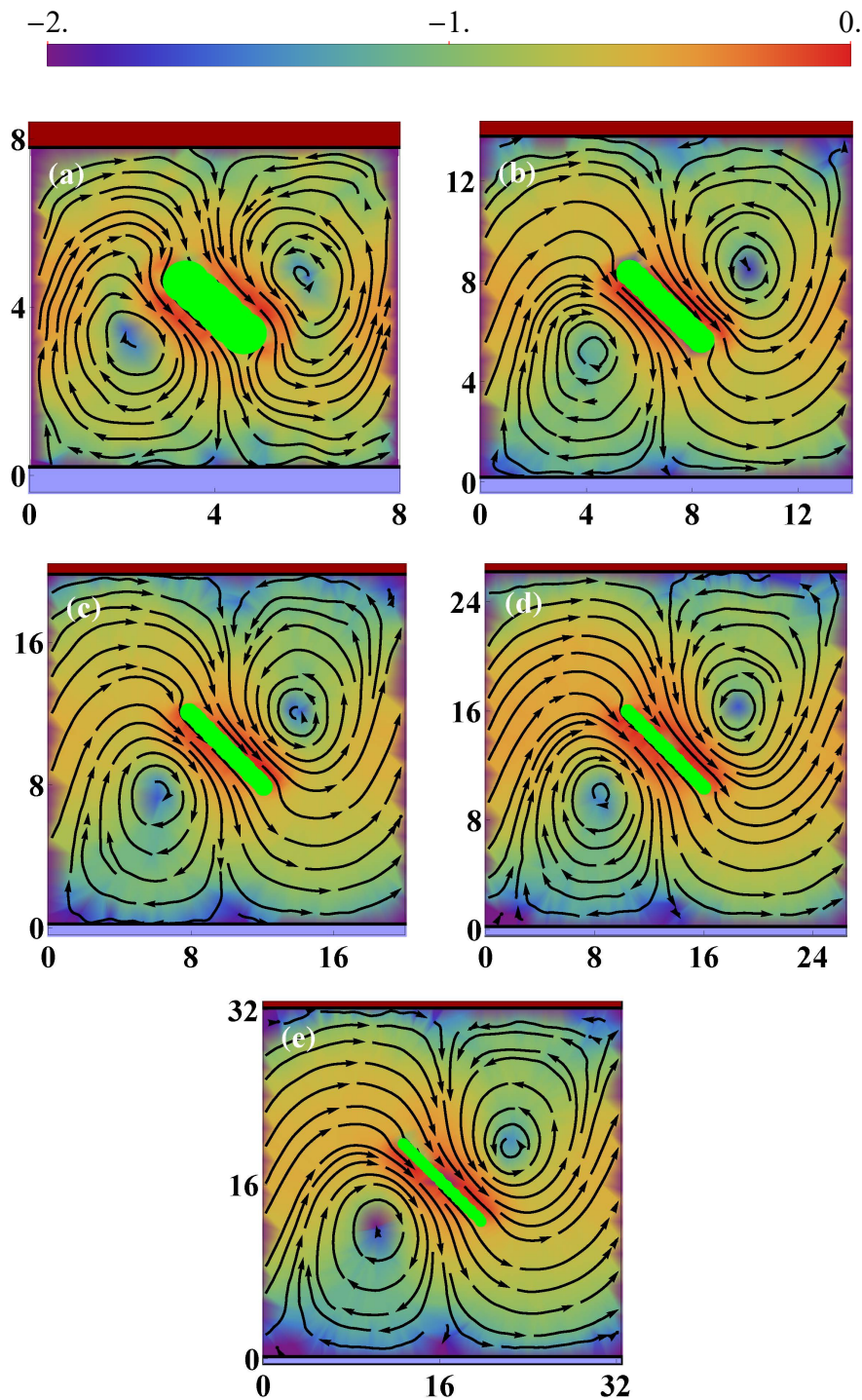


**Figure 5.11:** Flow stream lines in microchannels with obstacles of varying aspect ratio  $W/d$ . With fixed  $\nabla T = 1.05 \times 10^{-2}$  and  $D(=H)/w = 2.93$ , we sequentially vary  $W$  and the corresponding channel width  $H$  and  $D$  (to emphasize the similarity of their flow patterns, the actual figure sizes are rescaled by  $W$ ). (a)  $W/d = 2.73$ ; (b)  $W/d = 4.81$ ; (c)  $W/d = 6.89$ ; (d)  $W/d = 8.97$ ; (e)  $W/d = 11.05$ . Background color coding is prescribed in Chapter 2 Sec. 2.5

to  $x - z$  cross section in our simulation, which leads to the flow field various linearly both in  $x$  and  $z$  directions.

The flow velocity profile  $v_x(z)$  with polynomial fitting at the middle of two consecutive obstacles with different  $W/d$  are shown in Fig. 5.12(c). These curves display similar shape with different magnitude, reflecting the different obstacle dimensions and fluxes. Interestingly, as illustrated in Fig. 5.12(d), data collapse into one master curve when they are normalized by  $W/d$  with a small deviation for the smallest aspect ratio. This is due to the aforementioned statement that larger aspect ratio linearly strengthens the thermoosmotic flow velocity.

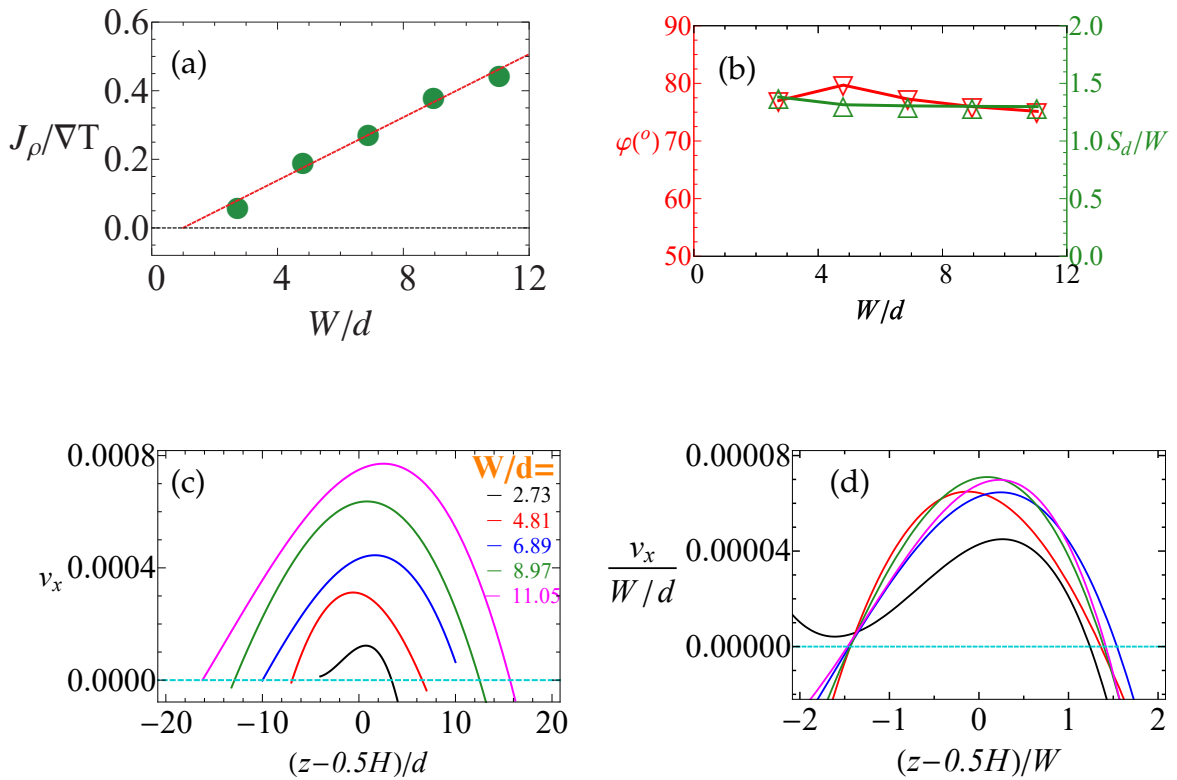


**Figure 5.12:** (a)  $J_\rho / \nabla T$  as a function of aspect ratio  $W/d$ . (b) Stagnation angle  $\varphi$  as a function of  $W/d$ . (c) Flow velocity profile  $v_x$  at the cross section of  $x = 0$  (similar to  $A - A'$  in Fig 5.4(a)). (d) The same data collapse into one master curve when both velocity and position are both normalized by  $W/d$ . To obtain a clear comparison, a polynomial fit is performed on the data in (c) and (d).

This linear behavior implies that even with small aspect ratio, we still obtain the same features of the study on the flow patterns and the  $J_\rho$ . The cases of larger  $W/d$  therefore can also be predicted by the study of smaller  $W/d$ . It is

important to emphasize that the linear relation between  $J_\rho$  and  $W/d$  relies on varying  $H$  concurrently with  $D$ .

### Rugosity dependence: flow direction variation

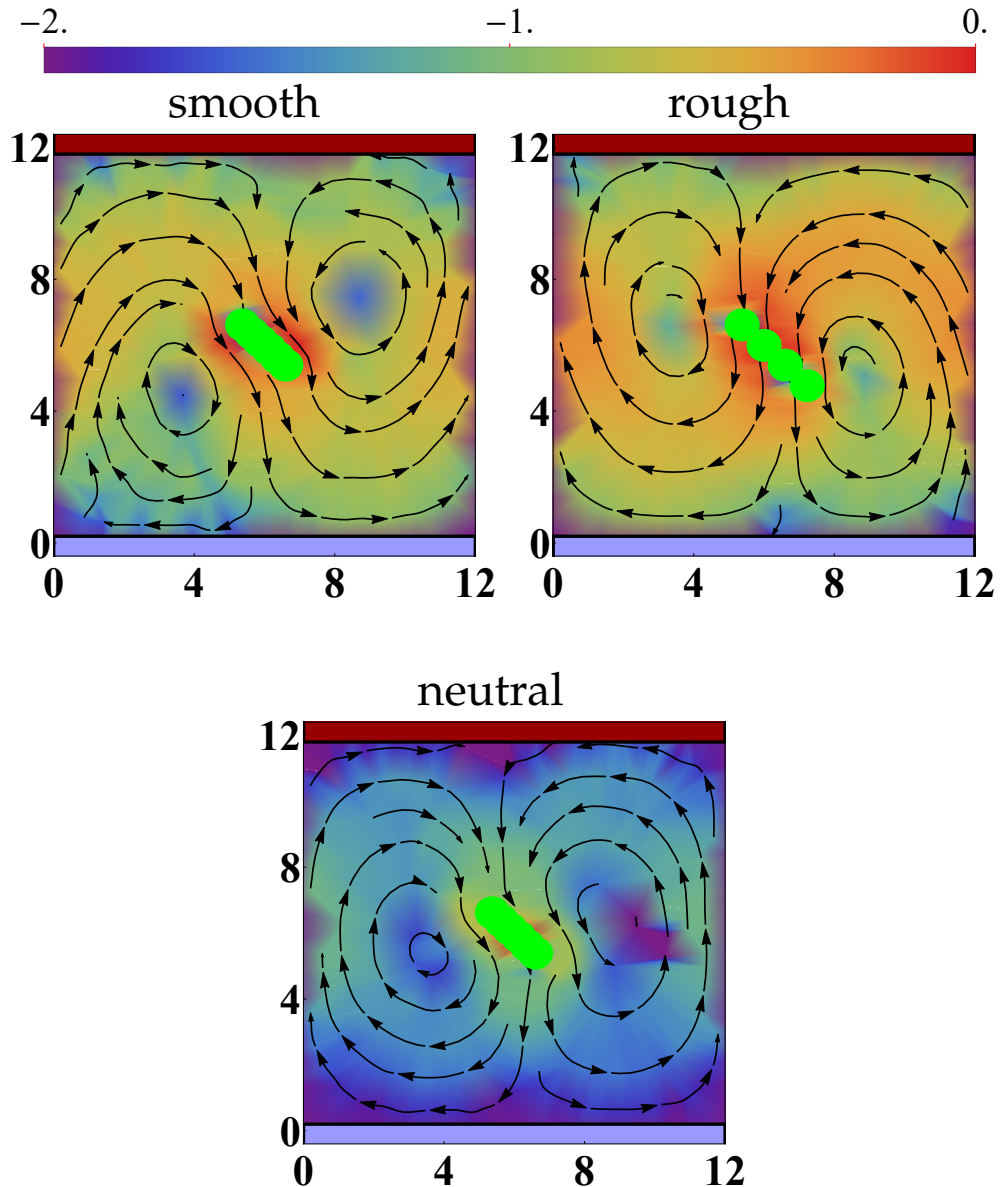


**Figure 5.13:** Flow field variation with changing of the obstacle rugosity (Fig. 5.1(c)). Background color coding is prescribed in Chapter 2 Sec. 2.5 (a) Obstacles with smooth (i.e  $l/d = 0.4$ ) surface and  $W = 2.93d$ .  $(L_x, L_y, L_z) = (30, 20, 30)$  and  $\nabla T = 0.0138$  is applied. (b) Obstacles with rough ( $l/d = 1.0$ ) surface, in this case the flow can penetrate the obstacles.  $(L_x, L_y, L_z) = (30, 25, 30)$  and  $\nabla T = 0.0207$ . (c) Obstacles with neutral ( $l/d = 0.8$ ) surface.  $(L_x, L_y, L_z) = (30, 20, 30)$  and  $\nabla T = 0.0138$ .

Besides changing the  $\chi_T$  and the flux density, varying rugosity also results in various flow patterns. Fig. 5.13 shows three examples of micropumps, all with the standard geometrical dimensions but obstacle with various rugosities. Given that the results in Chapter 4, where a change of the sign in  $\chi$  was described, with varying rugosity, we expect the flow field will also be qualitatively different. Here the pillar with thermophilic property ( $r3$ ), the flow stream lines display a clear  $l/d$  dependence. In the smooth obstacle case (with  $l/d = 0.4$  in Fig. 5.13(a)), the flow starts at the warm side then passes along the long side of the obstacle surface, towards the cold side but convected by the channel wall; quite the contrarily, rough-porous micropump (with  $l/d = 1.0$  Fig. 5.13(c) generates flow from the warm side, penetrates the loose obstacle, to the cold and left-hand side. Figuratively, the “hot-to-cold” protocol comes from the nature of thermophilic property; while the different directions of the “effective flow” reveals that rough obstacle has opposite sign of  $F_{T,x}$  from smooth one (Chapter 4). Concerning the “vortex” region, the locations of these two stagnation points are opposite. They cross the long axis of the obstacle orthogonally in the smooth pump, while align to it in the rough pump. More interestingly, when  $l/d = 0.8$ (Fig. 5.13(b)), the flow velocity is every small, and the flow field shows symmetric pattern and ensembles the one induced by isotropic colloid [60]. Since with  $l/d = 0.8$ , the anisotropic thermophoresis effect barely exists. Quantitatively, we obtain the consistent opposite signs of the  $J_\rho/\nabla T$  for smooth and rough types of pump in Fig. 5.10. Noticeably, for the neutral (i.e.  $l/d = 0.8$ , neither smooth nor rough) pump  $J_\rho/\nabla T$  is almost zero, since  $F_{T,x} \approx 0k_B T/a$  vanishes at  $l/d \approx 0.8$ (Chapter 4).

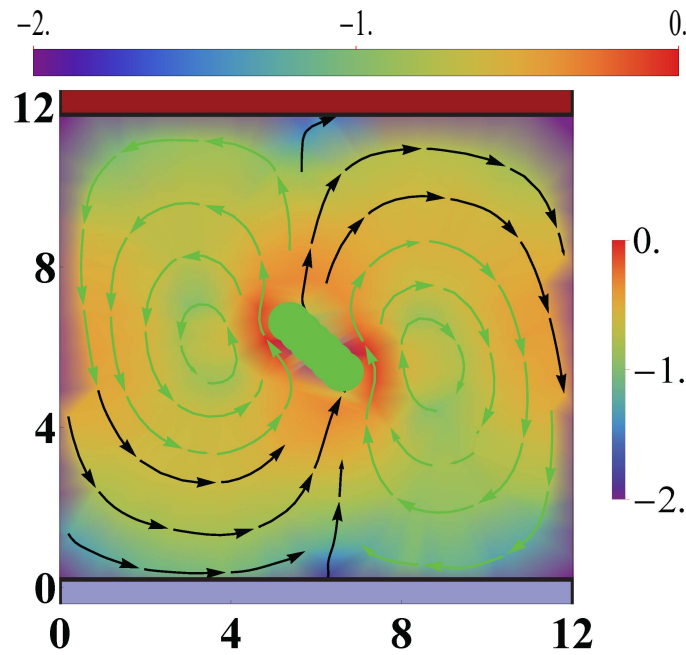


**Figure 5.14:** Flow pattern of obstacles composed with thermophobic property,  $n_{24}$  potential,  $l/d = 0.4$  and  $\nabla T = 0.0172$ . Background color coding is prescribed in Chapter 2 Sec. 2.5. To distinguish the flow pattern from thermophilic obstacles in Fig. 5.13(a), the vortex region is highlighted.

### Thermophilic or thermophobic: flow path alternation

Now we investigate how the micropump behaves under different solid-liquid interactions. Interestingly, the smooth ( $l/d = 0.4$ ) obstacles in Fig. 5.13(a) with thermophilic and Fig. 5.14 with thermophobic properties, the net flow directions are both right-hand sided due to the same sign of  $\chi_T$ , but the flow paths are different. Compared to the thermophilic pump, the "effective flow" path in the thermophobic pump is "left-right-down-up" like. The "left-right" feature is due to the emergence of thermophoretic force component  $F_{T,x}$  points to left handed side; while the "down-up" scenario is determined by its thermophobic nature. Therefore, the resulting  $J_\rho/\nabla T$  for both types of pumps are positive, as shown in Fig. 5.10. Their positive signs for thermophilic and thermophobic confirm the directions of the  $J_\rho$  are both right-hand sided.

## 5.4 Conclusions

In this work, we systematically investigate a novel micropump based on anisotropic thermophoresis [46, 139]. With the simplicity of construction, our device exhibits exotic traits on pumping capability and flow patterns, even though something very special of this micropump is that it does not require any movable part.

The previously proposed phoretic micropumps usually break the spacial symmetry at the channel walls (e.g. ratchet surface), which may have intractable difficulties on either intricate compositions/geometries or complex gradient realizations. In contrast, the present device requires solid obstacles fixed at the channel center. In this way, the geometrical asymmetry is induced by the obstacles tilting to the gradient. The separation between walls and obstacles enables flexible tunability of the flow by adjusting the obstacles in the microchannel. For example the flow direction, magnitude can be precisely controlled by regulating the tilting angle, separation distance or even replaced by other type of solid obstacles in the same channel. Furthermore, obstacles fully immersed inside the liquid, contributes more surface forces than the case of ratchet walls, in which the wall surface only partially contact with the fluid.

Anisotropic thermophoresis is viewed as the underlying mechanism to build the current phoretic pump. The resulting net flow flux along the channel originated by the superposition of surface thermoosmotic flow at the obstacle edges. This surface flow is induced by local temperature gradients at the solid-liquid interface along the obstacle edges. Geometric asymmetry together with phoresis result in non-zero thermophoretic force or thermoosmotic flow perpendicular to thermal gradient. Based on the study in Chapter 4, we found that the flux density is proportional to thermophoretic anisotropy factor and temperature gradient. Furthermore, it relies on the channel geometrical parameters: channel width and inter-pillar separation distance.

More specifically, the surface detail of the obstacle plays a vital role for fluid pumping. With fixed other parameters, the flux can be enhanced linearly with increasing of aspect ratio. The rugosity is related to a direction change of the flow. This is ascribed to the third dimension of the fixed obstacles can be fabricated with more complicated geometry. In this study we design the obstacles as smooth or rough loose structures. The rough pump allows the

surface flow to go through between beads, which results in the flow opposite to the one induced by smooth and impenetrable obstacles. Experimentally, intensity and direction of the flow can also be reversed or modified in several other ways as for instance changing the surface coating of the obstacle, and with it its composition or by adding an additional component to the fluid; or by tuning the rod orientation or modifying the average temperature [41, 137, 140].

The optimal set up of micromachine is dependent on the specific requirements and purposes. Note that the micromachine we reported here not only services for driving fluid but also renders environment for colloidal particle mixing [119, 141–143]. To obtain an optimum of pumping capability, our investigations suggest that obstacles which have stronger anisotropic effect, namely larger thermophilic or thermophobic properties, rugosity and larger aspect ratio, together with favorable channel width  $H$  and separation distance are important.

Furthermore, the current micropump needs only the presence of the walls and a simple fluid, but it will also be effective in the presence of a multi-component fluid in a single phase or in a multiphase situation, where the obstacles can interact with interfaces and their properties in the presence of the gradients. Additionally, thermal gradient driven motion has promising prospectives since it works equally well in charged and neutral solutions, and it is pollution-free due to the absence of surfactants or chemical fuels, which enables the way to bio-compatible applications. Thermal gradient-driven motion allows optical microscale operations with optical heating which is the basic principle of the emerging field of optofluidics [144]. Finally, our study focuses particularly on the case of thermophoresis. Given the shared features of phoretic phenomena, our results can therefore be generalized into the cases of diffusiophoresis and electrophoresis.

## Chapter 6

# Pumping fluid by partially heated pillars

### Synopsis

*An alternative micropump is driven by periodically aligned obstacles in a microchannel is suggested here. With laser illumination technique, a temperature gradient can be established due to the different heat conductivity of the metal and the non-metal compositions. Our simulation results show that temperature field is almost not deformed by changing the length of non-metal part in the obstacle. The corresponding far field flow resembles Poiseuille flow but with a more precise surface forcing control. By studying the flux density, we observed the pumping capability strongly depends on the length of the non-metal part and the inter-separation distance of the obstacles, but is not so strongly dependent on channel width. Compared with other thermophoretic pumps, our research suggests that partially heated micropump has higher pumping capability, but requires more delicate techniques on construction.*

### 6.1 Introduction

As discussed intensively in Chapter 5, phoretic local forcing approach has been recently promoted as basic mechanism to design novel microfluidics. The anisotropic thermophoretic micropump, with thermophoretic forces induced by immersed tilted pillars, can drive fluid moving along the microchannel. Instead of breaking symmetry geometrically as in Chapter 5, an alternative micropump based on compositional asymmetry debuts in this Chapter.

Specifically, this is inspired by recent researches on fabrication of Janus particles.

Janus particles (JPs), named after a roman god with two (or many) faces, bring asymmetry and can thus provide dramatically distinct chemical or physical properties within a single particle. Scientists have witnessed the rapid development of Janus particles on research areas ranging from single particle nanomotors [145] to collective self-assembly structures [11]. Due to symmetry breaking of individual particles, the motility and hydrodynamic interactions of these JPs enrich the phase behaviors of colloidal suspensions [146, 147].

Focusing at the single particle level, JPs have served as synthetic microswimmers, whose natural counterparts are micro-organisms such as parameciums, E.coli or sperm cells etc.. With advanced synthetic methods, different types of JPs can be manufactured, including simple spherical shape, cylinders, disks, dumbbell shapes, and even vesicles, or capsules (Fig. 6.1). As stated before, thermophoresis is non-toxic and environmental friendly, and therefore is an excellent resource for particle or fluids manipulation at nano- and micro-scales. The phoretic transport mechanism has shown that they can be used in designing self-propelled particles [41, 148]. A spherical phoretic JP swims in a viscous fluid, the ambient fluid forms a source dipole like velocity field, which also resembles the flow field of moving particle driven by phoresis [60, 62, 83]. Self-thermophoretic spherical JP has been fabricated via half-metal coating (made of silica and half-coated with gold in Ref. [41]). Under laser irradiation, the higher efficiency on heat adsorption at the metal-coated side of the particle creates local temperature gradient which induces thermophoretic force on the non-metal part of the particle. Collective behaviors such as polarization in an external gradient have been characterized in Ref. [149].

Most of the current research focuses on synthetic self-thermophoretic particles. Immobilized phoretic particles can also be employed for fluid pumping [150], especially due to the long range attenuation of the strength of the flow.

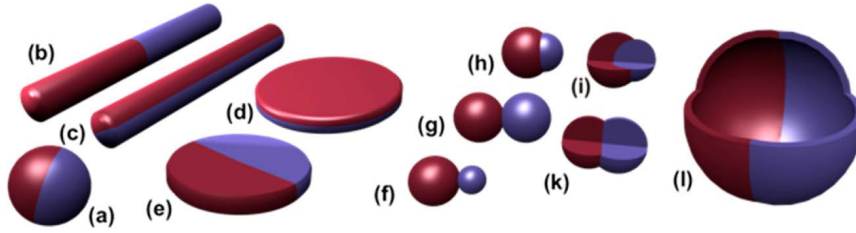


**Figure 6.1:** Different types of JPs can be fabricated with modern synthetic techniques. Spherical(a), two types of cylindrical (b,c), and disc-shaped (d-e) JPs. (f-k) Various kinds of dumbbell-shaped JPs with asymmetric or certain size ratio(f), symmetric appearance (g,k), attached nodes (h), and eccentric encapsulation(i). (l)Janus vesicles or capsules. Figures are taken from Ref. [11].

## 6.2 Model and method

### 6.2.1 Composition of the device

The device is composed with pillars immersed in fluid environment and confined in a long microchannel, as shown in Fig. 6.2(a). For briefness, we maintain the parameters' notation in Chapter 5. Compared with the anisotropically thermophoretic pump, the main difference of construction here is the heating protocol. Instead of walls with different fixed temperatures, the temperature inhomogeneity is brought to the microchannel by the difference of external-energy-to-heat transfer between coated and non-coated pieces when the channel is illuminated by lasers. Due to phoretic mechanism, those periodically distributed pillars induce thermoosmotic flow which propagates along the channel.

### 6.2.2 Simulation implementation

As illustrated in Fig. 6.2 (a), the pillars are constructed by fixing spherical beads on the nodes of triangular lattices with lattice size  $l$ . To realize higher temperature at the coated surfaces, we directly thermalize a thin layer of solvent particles with thickness of  $0.2a$  around the first column of beads along  $y$  axis direction [43]. The thermostat keeps the temperature of solvent around heated beads  $T_{hb} = 1.5k_B T$ . Similarly, for the cylindrical pillar case (modeled by , a single column), half of the pillar is heated (Fig. 6.1(c)). To avoid overheating of the system, we keep the temperatures lower at the channel walls,

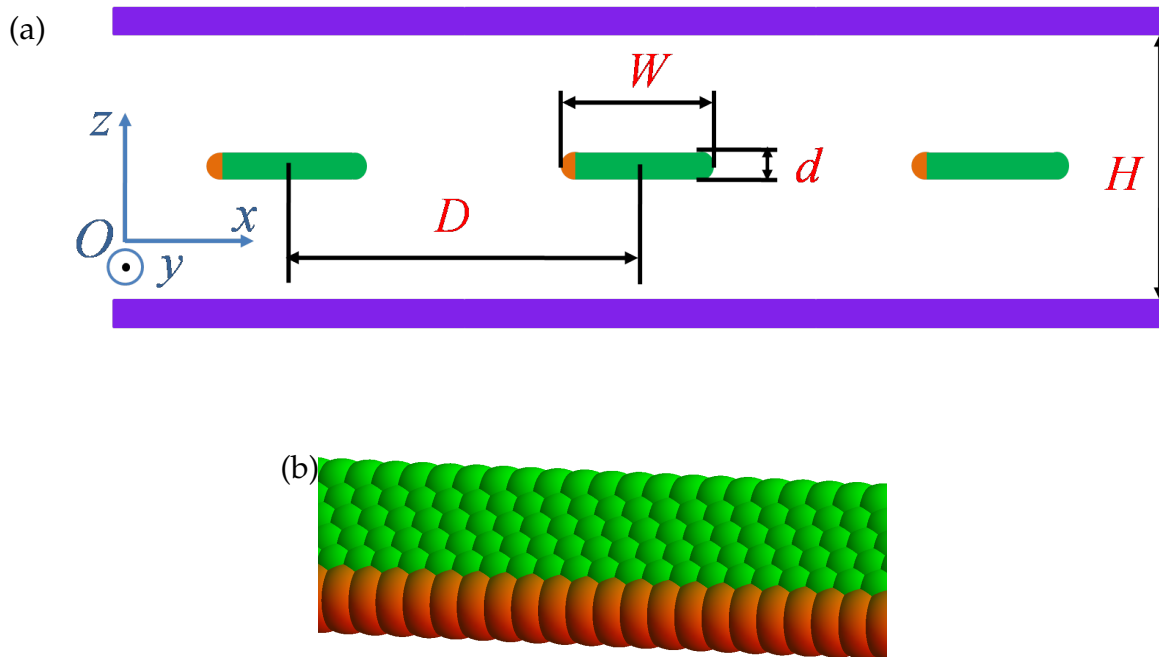


**Figure 6.2:** (a) Schematic representation of micropump realized by partially heating. Relevant sizes are specified, (with notation similar to Fig. 5.1) (b) Pillar sketch. The orange segment of the pillar is coated with gold, which can adsorb heat much faster than the green colored material (e.g. silica).

namely thermalizing  $T_w = 0.9$ . Such that  $\bar{T}$  of the system will be approximately  $1.0k_B T$ . This local heating protocol is applied at every MPC time step. Since heat conduction of the solvent is much faster than the mass diffusivity, after some relaxation time, a stable temperature gradient will be formed. With the same MPC-MD coupling routine as in Chapter 5, all the simulation results are obtained with the following parameters:  $d = 2.5a$ ,  $l = 1.0a$ ,  $L_x \times L_y \times L_z = 30 \times 20 \times 30a^3$  and  $r3$  type colloid-solvent potential.

## 6.3 Discussion

### 6.3.1 Influences of aspect ratio

#### Temperature field

As shown in Fig. 6.3, two examples of temperature field for pillars with different aspect ratio at  $x - z$  cross sections are well established at steady state, simulation data are computed by temporal averaging. The temperature gradients show to be radially distributed in the bulk solvent media. Given that

the PBCs are applied along the  $x$  and  $y$  axis directions, the temperature field will be the same for heating at different positions along the middle  $z$  axis of primary box, as long as  $D$  is fixed.

One related issue is how much do pillars with different  $W$  influence the temperature field? To elucidate this, hereby we plot temperature at  $x - z$  cross section along different axes. The axes are specified in Fig. 6.4(a). Three of them are placed parallel to the walls in three positions: close to the obstacle, close to the walls and between obstacle and wall; together with other two perpendicular to the channel: crosses heated part of pillar and cross middle point between two pillars respectively. Due to symmetry, the temperature along axis with prime notation ( $A'_1 - A'_2$ ) is the same as that along the one without it ( $A_1 - A_2$ ). We collect the data by taking the average of both axes, but only present them as " $A_1 - A_2$ " axis in the following text. To give a clearer comparison of the quantity, observation window (whose size is the same as that of the primary simulation box) is shifted along  $x$  axis to keep the heated point at the center. Analytically, the expected temperature field can be obtained by solving the Laplace equation with different *Dirichlet* boundary conditions, read as,

$$\begin{cases} \frac{\partial^2 T(x,z)}{\partial x^2} + \frac{\partial^2 T(x,z)}{\partial y^2} = 0; \text{ at the bulk} \\ T(x, 0) = T(x, H) = T_c; \\ T(x, y) = T_{hb}; (x, y) \in \varsigma\Gamma \end{cases} \quad (6.1)$$

where  $\Gamma$  is a circular boundary at the middle of modeled system represented by  $(x - 0.5L_x)^2 + (x - 0.5H)^2 = (R + 0.2a)^2$ . In our simulations one single column of metal beads are heated partially, then the prefactor  $0 \leq \varsigma \leq 1$  comes in. For example in the cylindrical pillar case  $\varsigma = 0.5$ , the other cases  $\varsigma \approx 0.7$ .

The temperature profile at  $a_1 - a_2$  axis as a function of distance to the heated center  $|\mathbf{r}_h|$  is shown in Fig. 6.4(b). The dashed black curve is theoretical calculation with full-circular heating (Fig. 6.3(c)), and magenta one with half-circular heating (Fig. 6.3(d)). The temperature shows to be independent on  $W$ ; the slight discrepancies in the cylindrical case ( $W/d = 1$ ) come from the difference of heating region. Besides small deviations, all the simulation results of different obstacle aspect ratio  $W/d$  agree with theoretical curves without considering embedded obstacles.

Similarly, the temperature along  $A_1 - A_2$  axis with different  $W/d$  is shown in

Fig. 6.4(c). They are also consistent with theoretical calculations. Note that the left sided temperature is marginally higher than the right one, because of the heat adsorption in both solvent and non-heated (coated) part of pillar on the right side. Fig. 6.4(d) shows the temperature variation close to the walls at axis  $C_1 - C_2$ . We observe the temperature variation here is around  $6 \times 10^{-3}$  and  $\nabla T_{wall} \approx 6 \times 10^{-4}$ . Since the temperature gradient at the walls is tiny, thermal creep effect [60] is negligible. In conclusion, the temperature field is correctly described by simulation and is determined by the presence of the heated elements, the deformation introduced by the pillars is negligible. This happens since the thermal conductivity of colloid or pillars is similar with that of the solvent.

### Flow fields and velocity quantification

Once the steady temperature gradient is established, a thermoosmotic flow is generated. The flow stream lines of micropumps with different  $W$  are presented in Fig. 6.5. As  $r^3$  potential is applied, the thermoosmotic flow is thermophilic thus propagates to the cold area.

The flow in the cylindrical pillar case in Fig. 6.5(a) is almost identical to the flow field around fixed spherical self-thermophoretic Janus particle [62, 83, 150], since they have the same composition structure in  $2D$ . The flow patterns far away from the pillars are independent on  $W$  which shows that the long range hydrodynamic interaction are not perturbed by the pillar shape. The background color in Fig. 6.5 indicates the magnitude of the flow velocity around cylindrical shaped pillar, and it shows the flow decays faster (with respect to the maximum velocity close to the heat source.) the more elongated is the pillar. decays slower than that of the elongated ones. These results with flow lines straightforward along the channel are the first proof that this device can serve as an efficient pump.

In Fig. 6.6 we further plot the flow velocity  $v_x(x, z)$  in the different cross sections. The flow profiles at  $a_1 - a_2$  and  $b_1 - b_2$  axes are displayed in Fig. 6.6(a) and Fig. 6.6(b). The data show that the overall flow velocity monotonously increases as increasing of  $W/d$  saturating at large values of  $W/d$ , except for  $W/d = 8.97$ . This tendency is due to the competition between the aspect ratio dependence of phoretic mechanism and friction. When  $W/d$  is large enough, the non-heated part of the pillar far away from the heat source feels negligible temperature gradient (the gradient decays as  $1/|\mathbf{r}_h|$ , with  $\mathbf{r}_h$  the distance to

the hot area). Thus the phoretic force of this area is insignificant. In contrast, the large  $W/d$  pillar undergoes larger overall friction. The inset of Fig. 6.6(a) shows the corresponding maximum flow velocity  $v_x^{max}$  as a function of  $W/d$ . This maximum velocity is directly related to the surface force and  $v_x^{max}$  is of relevance to surface force, reaches a plateau as increasing of aspect ratio. This is also a consequence that the previously explained phoresis-friction competition.

The flow far away from the solid pillar is parabolic-like for different  $W/d$  as shown in Fig. 6.6 (b) (due to friction and PBCs, the maximum of  $v_x$  is suppressed or flattened for  $W/d > 2.73$ ), similar observations can be found in Ref. [60] about periodic pumping by fixed spherical colloid. The solid lines refer to a parabolic fit (similar in the following cases along  $b_1 - b_2$  axis). It is a reminiscent of aforementioned *Poiseuille flow* in Chapter 2, which interprets the laminar flow driven by a constant pressure gradient. In the present microfluidic case, the fluid is pumped by *periodic* phoretic forces.

Along the flow direction in Fig. 6.6 (c),  $v_x$  of the cylindrical pillar at the back of heated area is almost the same as that at the front. In contrast, the flow velocities of elongated pillars, due to stronger thermophoretic forces at the non-heated part, are largely enhanced, as well as display a spatial decay. Moreover, the periodical distribution of those pillars along the channel also elevate the total flow. Similarly, the pillar with larger  $W$  endures larger friction and results in lower  $v_x$  where fluid is close to the axes  $A_1 - A_2$ . Interestingly, the heated part of solid pillar endures zero gradient and thus results in the (local) minimums of  $v_x$  at axes  $B_1 - B_2$  (Fig. 6.6(d)).

### Flux density

The pumping capability can be quantified by flux density  $J_\rho(x)$  as introduced in Eq. 5.1. As illustrated in Fig. 6.7 (a),  $J_\rho(x)$  is constant along the channel which is actually a consequence of the momentum conservation in the fluid. The average flux density  $\bar{J}_\rho$  (we omit the bar symbol in the following) as a function of  $W/d$  is illustrated in Fig. 6.7 (b). For small values of the obstacle aspect ratio,  $J_\rho$  increases with increasing  $W/d$ , until it seems to saturate for intermediate  $W/d$ . For large enough values of  $W/d$ ,  $J_\rho$  starts to decrease. As described before, the surfaces far away from heated part have a negligible contribution to the phoretic effect but additionally leads to larger friction.

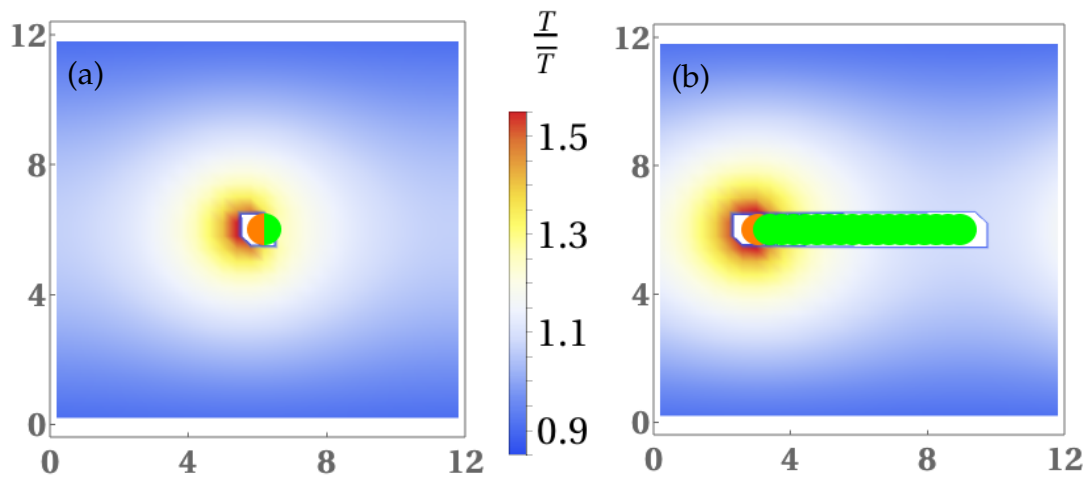


**Figure 6.3:** Temperature fields around pillars within similar microchannels. For comparison, analytical calculations of temperature field are also presented (with boundary conditions at walls and the center, while PBCs are neglected). (a)  $W/d = 1$ , cylindrical Janus like pillars, (b)  $W/d = 8$ , elongated pillars, the background is color coded as in Fig. 6.3(a).

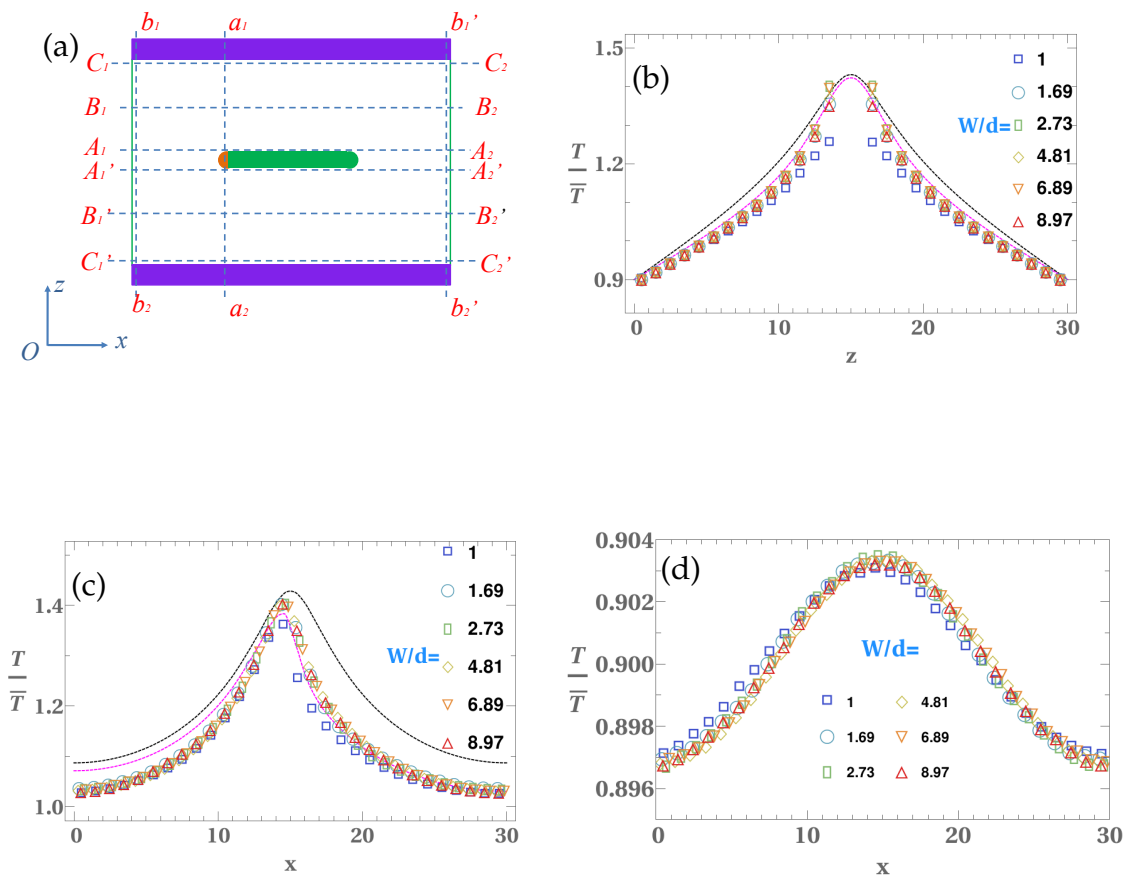


**Figure 6.4:** Temperature profiles along different axes for different  $W/d$ : (a) Locations of different axes in the device. (b)  $a_1 - a_2$  axis, (c)  $A_1 - A_2$  axis, (d)  $C_1 - C_2$  axis. The dashed lines denote the theoretical calculations. The black one represent full circular heated, and the magenta one is the half heated.

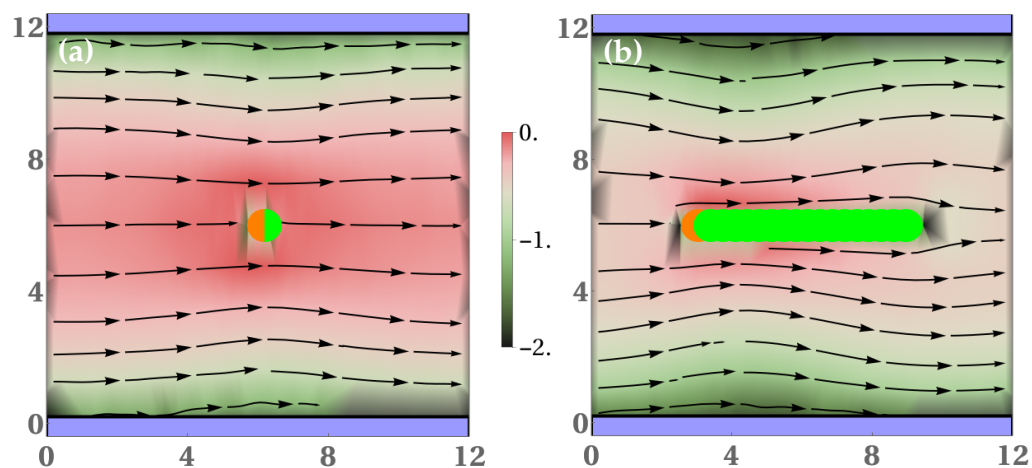


**Figure 6.5:** Maps of flow stream lines for pillars with different aspect ratios (corresponding to Fig. 6.3). Background color coding is prescribed in Chapter 2 Sec. 2.5. (a)  $W/d = 1$ , namely cylindrical pillars, (b)  $W/d = 6.889$ .

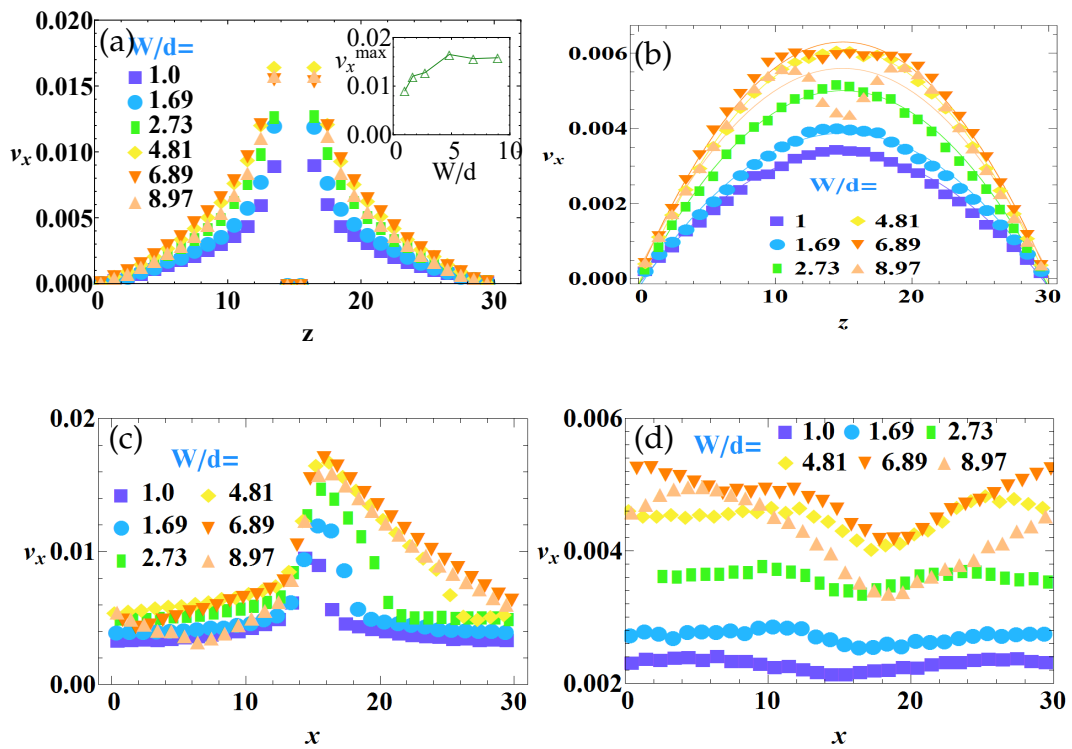


**Figure 6.6:** Flow velocity profiles  $v_x$  along different axes for different aspect ratios. (a) Flow velocity profile at  $a_1 - a_2$  ( $y - z$ ) axis where bead is heated; the inset illustrates the corresponding  $v_x^{max}$  as a function of  $W/d$ . (b) Flow velocity profile at  $b_1 - b_2$  cross section, the solid lines correspond to parabolic fit, the same below. (c) Flow velocity profile at  $A_1 - A_2$  cross section close to pillar surface. (d) Flow velocity profile at  $B_1 - B_2$  cross section. For convenience, observation window is shifted to keep heated patch at the middle for (c) and (d).

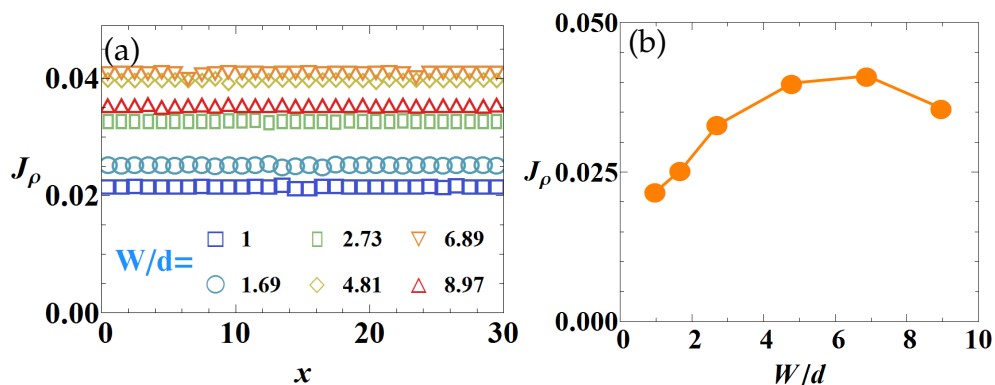


**Figure 6.7:** (a) Flow flux density  $J_\rho$  at  $y - z$  cross section as a function of channel position  $x$ . (b) The  $W/d$  dependence of  $\bar{J}_\rho$  (we omit the bar symbol in the following).

This investigation shows that local heated thermophoretic mechanism is appealing for fluid pumping. Although the local flow velocity is intricate, the flow far away from the pillar is Poiseuille-like. This may inspire the precise controlling of fluid pumping as an alternative approach to generate capillary flow. In the following section, the effects of the channel dimensions are discussed.

### 6.3.2 Channel geometrical effects

#### The role of channel width

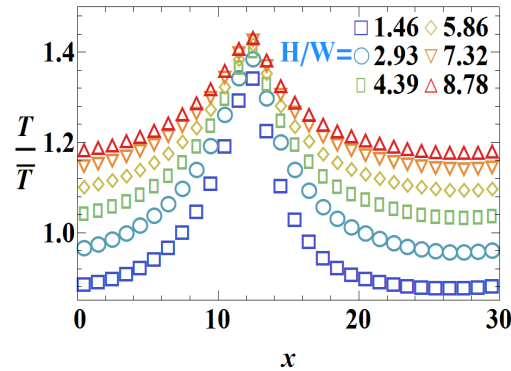


**Figure 6.8:** Temperature profiles for different channel width  $H$  in axis  $A_1 - A_2$ .

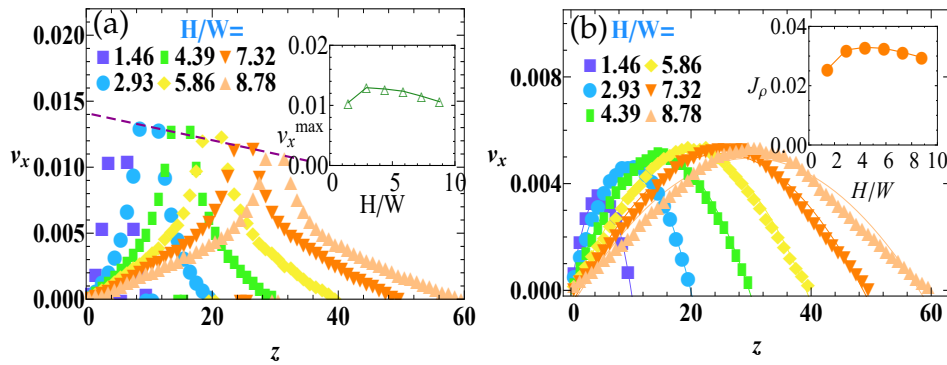


**Figure 6.9:** Flow velocities profiles and flux with different channel width  $H$ . (a) Velocity profile in axis  $a_1 - a_2$ . Dash line indicates the decay of the velocity peak. The inset illustrates the  $v_x^{max}$  as a function of  $H$ . (b) Velocity profiles at axis  $A_1 - A_2$ , the inset shows the flux density  $J_\rho$  as a function of  $H$ .

By fixing  $W/d = 2.73$ , we study the channel width dependence of the induced flux density. The thermophoretic force, determines the flow flux, and associated with the local temperature gradient along the solid pillar axis. Hence, we firstly compare the temperature profile along  $A_1 - A_2$  axis for different channel width (Fig. 6.8). The temperature gradient for narrower channel is stronger, what is influenced by the thermostating at the walls where  $T_w = 0.9$ . Thus we expect the larger flow velocity close to pillars for narrower channel. This can be seen in Fig. 6.9(a) and its inset, where the flow close to solid pillar ( $v_{x,max}$ ) decays as  $H$  increases (except for  $H = 10a$ ). Interestingly, as shown in Fig. 6.9(b), when the fluid is far away from the solid pillar, the maximums of  $v_x$  in the parabolic profiles are roughly the same for different  $H$ . The aforementioned *Poiseuille flow* approximation (Eq. (2.7) and (2.8)), where  $v_{max} \propto H^2$  seems not explain the channel width dependence of the velocity profiles as shown in Fig. 6.9. Increasing the channel width also decreases the overall  $J_\rho$  what very accurately balances with the velocity increase. The inset in Fig. 6.9(b) shows an almost constant value of flux density for different values of  $H$ . As shown in Fig. 6.9(b), the flow is also differed little with different  $H$ . Therefore, we detected  $J_\rho$  roughly constant for different  $H$  (Fig. 6.9(b) inset).

### Dependence of the obstacle interseparation

To study how the inter-pillar distance  $D$  influences the pumping, we plot the temperature profile for different values of  $D$  in Fig. 6.10. The shape of the curves shown in Fig. 6.10 indicates that within finite distance to heated part of pillars, the temperatures are almost the same. Therefore, the magnitudes of  $v_x$  close to hot area (namely  $v_x^{max}$ ) of the pillars in the inset of Fig. 6.11(a) are very close. When pillars are very close (with smaller values of  $D$ ), the average thermophoretic (thermoosmotic) force per unit volume of fluid is larger, thus the flow profile in the middle of two neighboring pillars is enhanced, as shown in Fig. 6.11(b). However, in the case of  $D/W = 1.46$  the flow profile exhibits double peaks. Moreover, when  $D$  gets larger, the flow velocity at the position with distance of  $D$  to the pillar gets weaker for larger  $D$ . This is because of the longer ranged decay of hydrodynamics with larger  $D$ . As shown in the inset of Fig. 6.11(b), the  $J_\rho$  linearly decays as increasing of  $D$ , what can be understood since the obstacle density decreases linearly. This tendency doesn't hold for  $D/W = 1.46$ , since the adjacent obstacles are

almost contact, in which case the flow along the channel would be symmetric and the average  $J_\rho$  is zero.

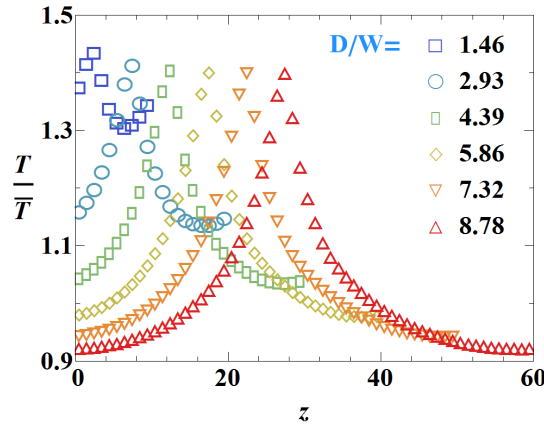


**Figure 6.10:** Temperature profiles in  $A_1 - A_2$  axes for different  $D$ .

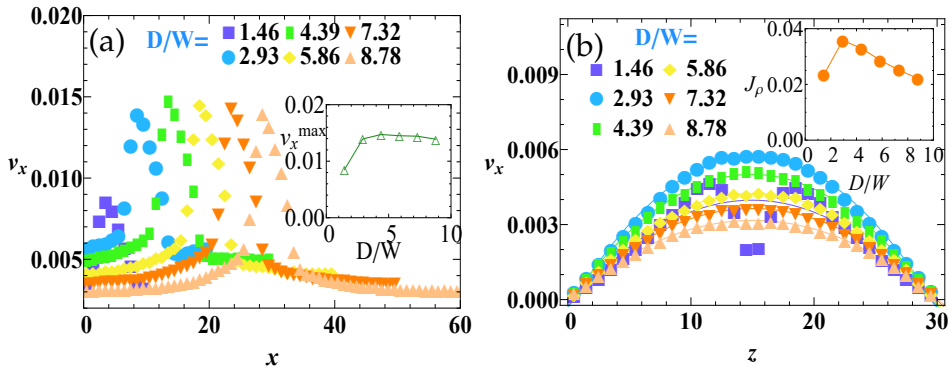


**Figure 6.11:** The inter-pillar separation  $D$  dependencies of flow velocity profiles and flux densities. (a) Velocity profiles at axis  $a_1 - a_2$ , the inset indicates  $v_x^{max}$  as a function of  $D$ . (b) Velocity profiles in axis  $b_1 - b_2$ , the inset shows  $J_\rho$  as a function of  $D$ .

### 6.3.3 Comparison with other thermophoretic micropumps

Here we provide a comparative discussion of three types of thermophoretic micropumps recently have been developed: the ratchet pump (RP) [47], the anisotropic pump (AP) (Chapter 5) and the partially heated pump (PP) presented in this chapter. Therefore, it is constructive to address the comparisons of the potential and versatility between them.

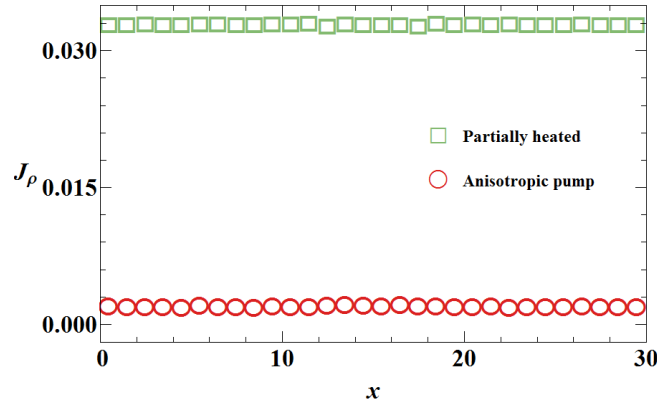


**Figure 6.12:** Flow flux density of two types of micropumps as a function of channel positions.

### Pumping capability

The most straightforward approach is to compare the pumping capability, or the flow flux density  $J_\rho$  in the same environment. As an initial comparison between AP and PP, we fix  $\Delta T = T_h - T_c = 0.6k_B T$ , the interaction potential parameter  $n = 3$  and the rugosity parameter  $l/d = 0.4$ . Surprisingly, as illustrated in Fig. 6.12, the  $J_\rho$  of partially heated pump is one order of magnitude larger than the anisotropic phoretic pump. The reason can be explained from two aspects. One is that partially heating approach in PP establishes non-linear temperature gradient and much stronger local gradient at pillar-solvent interfaces close to heated part. This implies that partially heating renders significant phoretic thrust on fluid close to the coated area. While in AP, the external gradient is always constant in the whole solvent everywhere. The energy cost for establishing temperature gradient in the solely solvent area doesn't contribute to osmotic flow. The other reason is that the pumping of AP is dominated by the parameter  $\chi_T = \alpha_{T,\perp} - \alpha_{T,\parallel}$  (Chapter 5), which is quite small compared with the overall  $\alpha_T$  values. This effect leads to large portion of energy is consumed at the orthogonal direction of channel. In contrast to that is the partially heated pump with total thermophoretic forces along the channel which is much more profitable for fluid pumping.

This primary comparison encourages us to make a fair comparison between these three micropumps. As noticed in all our simulation results, the flux density is majorly determined by the effective thermal diffusion factors, i.e.  $\chi_T$  for ATP and  $\hat{\alpha}_T$  for PP. To a large extent, the channel geometrical parameters, such as channel width  $H$  (an effective height of the sawteeth in RP [47] should be considered) and interseparation  $D$ , only modify the flux density up

to 50%. Since different approaches to fluid pumping lead to various strength of local temperature gradient, especially in ref. [47] the fluid parameters are different from what we used in this thesis, drastic but reasonable approximations are made to make a proper comparison. Namely we approximate that the flow flux density is proportional to the effective thermal diffusion factor  $\hat{\alpha}_T$ , the reciprocal of viscosity  $1/\eta$ , fluid density  $\rho$  and temperature difference  $\Delta T$ , but rarely dependent on  $H$  and  $D$ . Additionally, the obstacle parameters (potential, bead diameter and  $l/d$ ) are the same in three types of pumps. Only differed by obstacle length  $W$ , which is linearly related to  $\hat{\alpha}_T$ . With these considerations, we obtain the expression of the flux,

$$J_\rho \approx \frac{\rho}{\gamma_{eff}} \hat{\alpha}_T k_B |\nabla_{eff} T|, \quad (6.2)$$

where  $\hat{\alpha}_T$  is the effective thermal diffusion factor,  $\gamma_{eff}$  the effective friction factor per unit length of obstacle (ratchet wall), which depends on the viscosity  $\eta$  of the fluid. Albeit the temperature gradient in different devices are applied differently, here we assume them all various linearly along the obstacle. Hereby  $\nabla_{eff} T = \Delta_{eff} T/H = (T_h - T_c)/H$ . Thus the comparison of pumping capability between RP, AP and HP devices is made by displaying the normalized flux density  $J_\rho^* = (J_\rho \cdot \eta)/(\rho \cdot W \cdot |\nabla_{eff} T|)$  with different channel geometrical parameters, as depicted in Table 6.1. Indeed, for the same type of micropump, the pumping capability is minorly dependent on the channel geometrical parameters. However, the pumping capability of PP seems to be an order of magnitude higher than both the RP and AP, while RP and AP are roughly the same (One should notice that the simulations in ref. [47] are performed in  $2D$ , such that an enhancement of around 5 times of  $J_\rho^*$  in  $3D$  should be taken into account).

Laser illumination [41, 137], with endowment of accurate temporal and spatial control of temperature and flows, can be applied on all three micropumps. For example, when the pumped flow is only required at one part of microfluidic devices or a specific period of time, the precise manipulation on laser irradiation would be of great benefit [47]. An alternative approach is employing heat reservoirs at the boundary walls of the microchannel [104, 151]. Contact heating might not be readily achieved in PP device, as the coated obstacles are placed in the middle of the channel. But this can be easily realized in the other two micropumps. This contact heating might have practical advantages like for built is devices, but an interesting additional

advantage of this approach is that those existing residual temperature differences in nano- or microscale, can be harnessed into flow motion. On the other hand, the heat sources at microscale such as microelectronic chips, also can be cooled down by boundary heating. Distinguished from the other two micropumps which may require coating techniques, AP can directly be realized by boundary heating.

RP				AP			PP		
$H$	$D$	$J_\rho^*$	$J_\rho^{3D*}$	$H$	$D$	$J_\rho^*$	$H$	$D$	$J_\rho^*$
15	31	0.00395	0.01973	20	20	0.00748	10	30	0.05441
20	31	0.00639	0.03168	30	20	0.00941	20	30	0.13617
30	31	0.00728	0.0364	20	30	0.0958	30	30	0.2098
50	31	0.01061	0.05307	30	30	0.01235	40	30	0.2767
90	31	0.01167	0.05835	40	30	0.01412	50	30	0.33152
20	10	0.001	0.00501	50	30	0.01692	60	30	0.37633
20	20	0.00614	0.03068	60	30	0.01451	30	10	0.14979
20	62	0.00438	0.02191	30	40	0.01197	30	20	0.22783
				30	50	0.01206	30	40	0.18247
				30	65	0.00942	30	50	0.16013
				30	75	0.00975	30	60	0.14079
				30	120	0.00612			

**Table 6.1:** Pumping capability of three types of micropumps. The pumping capability parameter from left to right shows the values of RP (ratched pump), AP (anisotropic pump) and PP (partially heated pump) with different channel geometrical parameters. The data of RP are taken from ref. [47],  $J_\rho^{3D*}$  considers the approximated correction in  $3D$ .

### Comparison of microfluidic pumping to physical parameters

To provide an estimation of physical units of the microchannels and fluxes investigated here is not trivial since it is not possible to match all related dimensionless numbers at the same time. A first possibility is to match the geometry of our model micropump with a microfluidic pump with channel width  $H = 15\mu m$  leads to the physical length  $a = 0.5\mu m$  of a collision cell (the most representative value of  $H$  is  $30a$ ), and the bead radius  $\sigma \simeq 0.6\mu m$ . We consider the density of bead is similar with water, then the mass of spherical bead can be evaluated  $M \simeq 9 \times 10^{-16} kg$ . The mass of a fluid particle in our simulation is considered as  $m = M$ . Thermal energy is  $k_B T \simeq 4.114 pNm$  at  $T = 300K$ . This leads the velocity unit in MPC is

$\sqrt{k_B T/m} \simeq 2 \times 10^3 \mu m/s$ . Therefore the flow velocities in all the simulations ranges from  $0.5 \mu m/s$  to  $10 \mu m/s$ . Likewise, the employed temperature gradient is  $5 \sim 10 K/\mu m$  in all the simulations, which is comparable to experimental set up around  $1 K/\mu m$  [41].

Another relevant fact is that in our simulations, the thermal diffusion factor, or Soret coefficient and viscosity are all underestimated compared with  $\alpha_T$  in real material such as carboxyl-modified polystyrene bead. Taking all these factors into account, the pumping flow velocity of a micropump could be around  $20 \sim 400 \mu m/s$  [47], which is very competitive for microfluidic pumping.

## 6.4 Summary

In this Chapter, we analyze the performance of a self-thermophoretic micropump inspired by synthetic technology for Janus particles. We characterized the temperature field and flow patterns in different circumstances with various aspect ratio, channel width and separation distance. Although this pumping architecture is similar to several studies on spherical shaped obstacles [60, 83, 150], our research has focused on the microfluid capability of the geometry and it has been extended to elongated shaped and characterized systematically. The features are summarized as follows:

The temperature field is radial-like but modified by the thermostats at channel walls. Interestingly, the temperature field is rarely influenced by pillar length. Since the pillars always have finite length and the non coated part endures temperature gradient, when the pillar is aligned to the channel direction which is the optimal orientation for fluid pumping. The gradient at positions far away from the heated part is negligible, such that to obtain an optional pumping ability, the pillar should be designed adequate long to serve larger thermophoretic force, but not too long to induce friction that hampers the fluid flow. The flow profile far away from the pillar is parabolic, which ensembles the capillary flow in micro- and nano-scales. This parabolic flow is equivalent as applying external pressure gradient, but due to surface forcing of phoresis, the present micropump can become much more precise and efficient on quantitative fluid pumping [47].

The optimal pumping of fluid is found at  $W/d = 7$  ( $H = D = 12d$ ), when  $W/d > 7$ , larger friction will decrease the pumping capability. Moreover,

with the combination of thermostats at walls and coated or heated part of pillars, and no-slip boundary walls, for the range of channel width we observed, the flux density varies little. However, due to decaying of the flow at long-ranged distance, larger separation distance also lows the pumping capability.

Compared with other two previous micropumps based on thermophoretic mechanism, partially heated micropump provides higher pumping capability. Due to the optimized orientation of the pillars and higher local temperature gradient at the phoretic part of pillars, stronger thermophoretic forces are generated and pump larger flow flux. Technically, compared to boundary heating approach, the coating and laser illumination protocols might not be easily achieved.

In all, this microdevice provides high pumping capability and also can be generalized into other phoretic mechanisms.

## Chapter 7

# Thermophoretic orientation of heterodimers

### Synopsis

*This Chapter studies how dimers composed of two non-identical monomers behave in temperature gradients. Due to the different thermophoretic forces on individual monomers, heterodimers are subjected to a net phoretic torque, and therefore to an alignment in the presence of a gradient of temperature. Firstly, we provide a theoretical description of the alignment based on linear response theory. Our simulation results nicely agree with theory in the case of weak thermophoretic torque. Non-linear behavior is observed in the case of large phoretic torque. Furthermore, the effect of size asymmetry, and the how the alignment modifies isotropic thermophoretic force are discussed. Finally, a concentrated solution of heterodimers confined in a slit and driven by thermophoresis is studied. The concentration and orientation as a function of the distance to the aggregation wall are investigated. The hydrodynamic attraction between dimers induced by thermophoretic flow fields, is shown to be amplified close to the wall, which enhances the packing of colloids. At low dimer density cases, the hedgehog-like cluster with horizontal sweeping and rhythmic cluster are observed.*

## 7.1 Introduction

Besides of formerly discussed the thermal mass transport effect, recent molecular dynamics simulations have shown that, thermal gradients can also trigger a preferential orientation in diatomic fluids (the “thermomolecular orientation” effect) [109–111]. However, attempts to investigate similar effects in

colloidal systems have not yet been performed. As stated by Lee [111], theoretical approach in the framework of local-equilibrium is only valid in the case of molecular mixtures in which the two components have similar sizes. In colloidal suspensions, the solute and the solvent particle sizes are separated several orders of magnitude. The colloid-fluid interaction range is also much thinner than the colloid radius. Within this framework, the underlying physics is dominated by hydrodynamics.

This chapter discusses the *thermophoretic orientation* (alignment) of heterodimers. We describe how the torque exerted by the external gradient inhibits rotational diffusion and favors the orientation with an external thermal gradient.

## 7.2 Alignment

### 7.2.1 Linear response theory

A schematic representation of a general heterodimer is shown in Fig. 7.1. A heterodimer embedded in a liquid is composed by two monomers with non-identical thermophoretic properties. Monomers  $A$  and  $B$  are connected by a rigid bond of length  $L_D$ . Monomer  $A$  ( $B$ ) is subjected to thermophoretic force  $\mathbf{F}_{T,A}$  ( $\mathbf{F}_{T,B}$ ) under temperature gradient  $\nabla T$ . These forces are related to their own thermophoretic properties by Eq. (1.14). Because of the different thermophoretic responses of two monomers, an orientational dependent thermophoretic torque  $\Psi_T$  (Eq. (7.1)) is exerted on the dimer what results in the dimer alignment. The thermophoretic inhomogeneity of the composition in the dimer results in  $\Psi_T$ , reads,

$$\begin{aligned} \Psi_T &= \frac{L_D}{2} \hat{\mathbf{u}} \times (\mathbf{F}_{T,B} - \mathbf{F}_{T,A}) = \\ &= -\frac{L_D}{2} \hat{\mathbf{u}} \times (\alpha_{T,B} - \alpha_{T,A}) k_B \nabla T, \end{aligned} \quad (7.1)$$

where  $\alpha_{T,i}$  the thermal diffusion factor of monomer  $i$  ( $i = A, B$ ) (which can be measured in experiments. In our simulation model, those values also can be analytically estimated by the recipes in Appendix A), and  $\hat{\mathbf{u}}$  the unit orientation vector along  $\overrightarrow{AB} = L_D \hat{\mathbf{u}}$ . The factor  $(\alpha_{T,B} - \alpha_{T,A}) = \chi_H$  is viewed as thermophoretic heterogeneity of the dimer.

As discussed previously, the translational Brownian motion is not coupled with rotational Brownian motion of rod-like colloid (Chapter 1). Thus, the

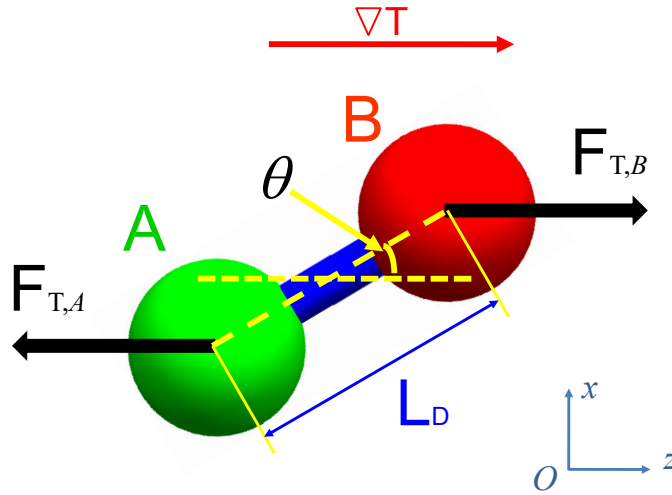


**Figure 7.1:** Schematic representation of a heterodimer in temperature gradient.

problem of thermal orientation is reduced to the rotational Brownian motion, supplemented with thermophoresis. Accordingly, the Langevin equation for the rotational motion in temperature gradient can be written as,

$$\frac{dJ}{dt} = -\gamma_r \Omega + \Psi_{th}(t) - \Psi_T(t), \quad (7.2)$$

with  $\Omega$  the angular velocity and  $J$  the angular momentum. For a particle with momentum of inertia  $I_d$ ,  $J$  is expressed as

$$J = I_d \cdot \Omega. \quad (7.3)$$

In Eq. (7.2)  $\gamma_r$  is the rotational friction coefficient,  $\Psi_{th}(t)$  denotes the fluctuation torque comes from thermal noise (also termed as *Brownian torque*),  $\Psi_T(t)$  the thermophoretic torque of the dimer in the presence of temperature gradient.

The time scale of colloidal thermophoretic behavior is beyond *Brownian time scale*  $\tau_D$  (Chapter 1 Section 1.2.1) [17, 20], such that the colloid dynamics is overdamped, namely the inertial forces can be neglected and Eq. (7.2) is rewritten as,

$$\gamma_r \Omega + \Psi_T(t) = \Psi_{th}(t). \quad (7.4)$$

Within the overdamped limit, the fluctuating Brownian torque can be evaluated in terms of the probability distribution function (*pdf*)  $p(\hat{\mathbf{u}}, t)$  [152],

$$\Psi_{th}(t) = -k_B T \hat{\mathcal{R}} \ln p(\mathbf{r}, \hat{\mathbf{u}}, t). \quad (7.5)$$

where  $\hat{\mathcal{R}}$  is the *orientational operator* defined as,

$$\hat{\mathcal{R}}(\dots) = \hat{\mathbf{u}} \times \nabla_{\hat{\mathbf{u}}}(\dots), \quad (7.6)$$

here  $\nabla_{\hat{\mathbf{u}}}$  is the gradient operator with respect to the Cartesian coordinates  $\hat{u}_x$ ,  $\hat{u}_y$  and  $\hat{u}_z$ ,

$$\nabla_{\hat{\mathbf{u}}} = \left( \frac{\partial}{\partial \hat{u}_x}, \frac{\partial}{\partial \hat{u}_y}, \frac{\partial}{\partial \hat{u}_z} \right). \quad (7.7)$$

The logarithm of  $p$  in the expression of  $\Psi_{th}$  in Eq. (7.5) relates to its entropic nature, which drives the system towards equilibrium. Eq. (7.4) reveals the torque free nature in the overdamped limit. Substitution of Eq. (7.5) into (7.4) results in,

$$\Omega = \beta D_r [-k_B T \hat{\mathcal{R}} \ln p(\hat{\mathbf{u}}, t) + \Psi_T(t)], \quad (7.8)$$

with  $\beta = 1/k_B T$  and  $D_r = k_B T / \gamma_r$  the rotational diffusion of heterodimer in thermal equilibrium. As discussed in Chapter 4,  $D_r$  is almost independent on external thermal gradient. Therefore, the extended single particle *Smoluchowski equation* for rotational motion [17] is written as,

$$\frac{\partial}{\partial t} p(\hat{\mathbf{u}}, t) = D_r \hat{\mathcal{R}} \cdot [\hat{\mathcal{R}} p(\hat{\mathbf{u}}, t) - \beta \Psi_T(t) p(\hat{\mathbf{u}}, t)], \quad (7.9)$$

We consider a constant (or oscillating) temperature gradient as a linear perturbation. The probability distribution function is then written as,

$$p(\hat{\mathbf{u}}, t) = p_0 + \nabla T p_1(\hat{\mathbf{u}}, t), \quad (7.10)$$

where  $p_0$  is the pdf in the absence of temperature gradient, and  $p_1$  the temperature gradient induced perturbation of the pdf. Note that  $p_0$  is a normalizing constant,

$$p_0 = \frac{1}{4\pi}. \quad (7.11)$$

In the absence of  $\nabla T$  the colloid undergoes purely *rotational Brownian motion*, such that the expectation of orientation is zero, i.e.  $\langle \hat{u}_x(t) \rangle = \langle \hat{u}_y(t) \rangle = \langle \hat{u}_z(t) \rangle = 0$ . In the presence of temperature gradient, however, alignment (i.e. thermophoretic orientation) of the heterodimer will be triggered by temperature gradient and the intrinsic particle asymmetry. Thus, we introduce an order parameter to quantify alignment: the average of the  $z$  component of the orientation vector of the dimer  $\langle \hat{u}_z \rangle$ , which is equivalent to  $\langle \cos \theta \rangle$  (with  $\theta$  is the polar angle between gradient axis and the orientation vector  $\hat{\mathbf{u}}$ ) as shown in Fig. 7.1. Note that here we follow the same convention as with

the standard spherical coordinates such that  $\theta \in [0, \pi]$  and conditions with symmetric opposite orientations in  $x$  would be described by the same angle  $\theta$ . Since  $\langle \hat{\mathbf{u}} \rangle = \oint d\hat{\mathbf{u}} p(\hat{\mathbf{u}}, t) \hat{\mathbf{u}}$ , multiplying both sides of Eq. (7.9) with  $\hat{\mathbf{u}}$  and integrating over all orientations, the equation to describe the time evolution of  $\hat{\mathbf{u}}$  is obtained as,

$$\begin{aligned} \frac{d\langle \hat{\mathbf{u}} \rangle(t)}{dt} &= D_r \oint d\hat{\mathbf{u}} \hat{\mathbf{u}} \hat{\mathcal{R}} \cdot [\hat{\mathcal{R}} p(\hat{\mathbf{u}}, t) - \beta \Psi_T(t) p(\hat{\mathbf{u}}, t)] \\ &= D_r \oint d\hat{\mathbf{u}} p(\hat{\mathbf{u}}, t) [\hat{\mathcal{R}}^2 \hat{\mathbf{u}} - \beta \frac{L_D}{2} \chi_H k_B (\hat{\mathbf{u}} \times \nabla T) \cdot \hat{\mathcal{R}} \hat{\mathbf{u}}] \end{aligned} \quad (7.12)$$

where partial integrations have been performed in the second equality. As explained in appendix of the lecture notes B1 [152],  $\hat{\mathcal{R}}^2 \hat{\mathbf{u}} = -2\hat{\mathcal{R}} \hat{\mathbf{u}}$  and  $(\hat{\mathbf{u}} \times \nabla T) \cdot \hat{\mathcal{R}} \hat{\mathbf{u}} = (\hat{\mathbf{I}} - \hat{\mathbf{u}} \hat{\mathbf{u}}) \cdot \nabla T$ , with what Eq. (7.12) can be rewritten as,

$$\frac{d\langle \hat{\mathbf{u}} \rangle(t)}{dt} = -D_r [2\langle \hat{\mathbf{u}} \rangle(t) - \beta \frac{L_D}{2} \chi_H k_B (\hat{\mathbf{I}} - \hat{\mathbf{u}} \hat{\mathbf{u}}(t)) \cdot \nabla T]. \quad (7.13)$$

Considering the linear perturbation of temperature gradient,  $\langle \hat{\mathbf{u}} \rangle(t)$  can be evaluated with respect to the pdf  $p_0$  and disregarding higher order terms in the linear expansion (7.10), which gives  $\langle \hat{\mathbf{u}} \hat{\mathbf{u}} \rangle(t) = (1/3) \hat{\mathbf{I}}$ . Note that only the component of  $\hat{\mathbf{u}}$  along the gradient is nonzero, i.e.  $\hat{u}_x = \hat{u}_y = 0$ . The equation of the expectation value of the  $\hat{u}_z$  yields,

$$\frac{d\langle \hat{u}_z \rangle(t)}{dt} = -D_r [2\langle \hat{u}_z \rangle(t) - \frac{1}{3} \beta L_D \chi_H k_B |\nabla T|]. \quad (7.14)$$

Now this is an ordinary differential equation. At the stationary state, Eq. (7.14) is independent on time, thus the solution is,

$$\langle \hat{u}_z \rangle = \frac{\beta L_D}{6} \cdot \zeta \cdot \chi_H k_B |\nabla T|, \quad (7.15)$$

here the parameter  $\zeta \in (0, 1]$  is introduced to consider the additional surface correction when the (colloid-solvent) interaction area of two monomers is overlapped. For simplicity, as also the monomers are not allowed to overlap in the following simulations (at most perfectly touch), we simplify  $\zeta = 1$ . Interestingly, this formula is very similar to the alignment suggested by Lee [111], who derived  $\langle \hat{u}_z \rangle = \langle \cos \theta_z \rangle$  from a local equilibrium perspective by assuming the probability distribution function obeys Boltzmann weight of surface energy.

Note that the theoretical prediction via Eq. (7.15) solely considers thermophoretic

forces act on the two individual beads as point forces. This assumption ignores the local effects of thermophoretic forces and the anisotropy induced by the non-spherical geometry.

Although we will not investigate here the case of the temperature varies sinusoidally, it is interesting to briefly consider it here. A sinusoidal temperature results in a sinusoidal temperature gradient, which can be expressed as

$$\nabla T = \cos(\omega t) \nabla T_0, \quad (7.16)$$

the solution of Eq. (7.14) in this case can be expanded to,

$$\langle \hat{u}_z \rangle (t) = \frac{1}{3} \frac{\beta D_r}{(2D_r)^2 + \omega^2} L_D \zeta \cdot \chi_H k_B [2D_r \cos(\omega t) + \omega \sin(\omega t)] |\nabla T|, \quad (7.17)$$

where  $\omega$  is the frequency of oscillatory temperature, a constant temperature gradient is the case when  $\omega = 0$ .

**The sign of the alignment:** As indicated in Fig. 7.1, the orientation of the unit vector defined from the center of monomer  $A$  to monomer  $B$ . In this case, the sign of the alignment depends on how  $\hat{u}$  is chosen initially. For simplicity, we define the alignment with some additional considerations to unify the sign of  $\langle \hat{u} \rangle$ : Imagine the heterodimer aligns with  $\nabla T$  due to thermophoresis without Brownian motion, we denote the monomer at the warm side (with respect to the center of the colloid) as  $B$ , then the orientation vector is marked as  $\overrightarrow{AB} = L_D \hat{u}$ . In such a way,  $\langle \hat{u}_z \rangle$  will be no less than 0 and such that easier to compare with different dimers. This definition holds in most of the following content, except in the case of dimers with size asymmetry which will be redefined.

**Visualization of the probability distribution function:** Note that the *pdf* interprets how the tip of the orientation unit vector  $\hat{u}$  distributes on the surface of the unit sphere. Given that the *pdf* here is cylindrically symmetric along the gradient axis, in what follows, the *pdf* is represented by the probability distribution function in a plane crosses the gradient axis.

### 7.2.2 Simulation vs. linear response theory

The alignment of two types of heterodimers is explored by considering a fixed bead-bead distance  $L_D = 4a$ . The first type with  $a48 - r6$  potential, contains a thermophilic bead at one side and a thermophobic one at the other side, such that both  $\mathbf{F}_{T,A}$  and  $\mathbf{F}_{T,B}$  contribute positively to the torque (Eq. (7.1)). The *pdf* in this case is shown in Fig. 7.2 (a) under different temperature gradients is relatively large ( $p > 0.5$ ), and peaks at  $\theta = 0$  (the singular peak is due to the poor statistics at the axis direction). Likewise, the  $r12 - r6$  type with both thermophilic beads rotate oppositely and result in a smaller thermophoretic torque (Eq. (7.1)) ( $\chi_H$  is smaller than the  $a48 - r6$  dimer). The corresponding *pdf* in different  $\nabla T$  in Fig. 7.2(b) is clearly much smaller than for the  $a48 - r6$  potential. With Fig. 7.2(a) and Fig. 7.2(b), we calculate the alignment order parameter  $\langle \hat{u}_z \rangle = \langle \cos \theta \rangle$  as a function of  $\nabla T$  and depicted in Fig. 7.2(c). The alignment for both heterodimers increases with increasing  $\nabla T$ , what is intuitive since  $\Psi_T$  grows monotonously with  $\nabla T$ .

Moreover, for the  $r12 - r6$  dimer,  $\Psi_T$  is relatively small and can be treated as external linear perturbation (which was the assumption of the theoretical derivation in the previous section), therefore we observed the nice agreement between the simulation data and linear response theory (green data in Fig. 7.2(c)). Note that in spite of the error of estimating  $\alpha_{T,A}$  and  $\alpha_{T,B}$  from their obtained colloidal values the prediction for the  $r6 - r12$  potential is quantitatively correct. That is though not the case for the  $a48 - r6$  potential where the linear slope is underestimated by the same approximation. However, this weak perturbation assumption breaks down for larger  $\Psi_T$  such as  $a48 - r6$  dimer (blue data in Fig. 7.2(c)) at  $\nabla T > 0.008$ . We observe a non-linear behavior of the alignment at larger gradient and  $\Psi_T$ . Thus the theoretical solution requires higher order of modification in Eq. (7.10).

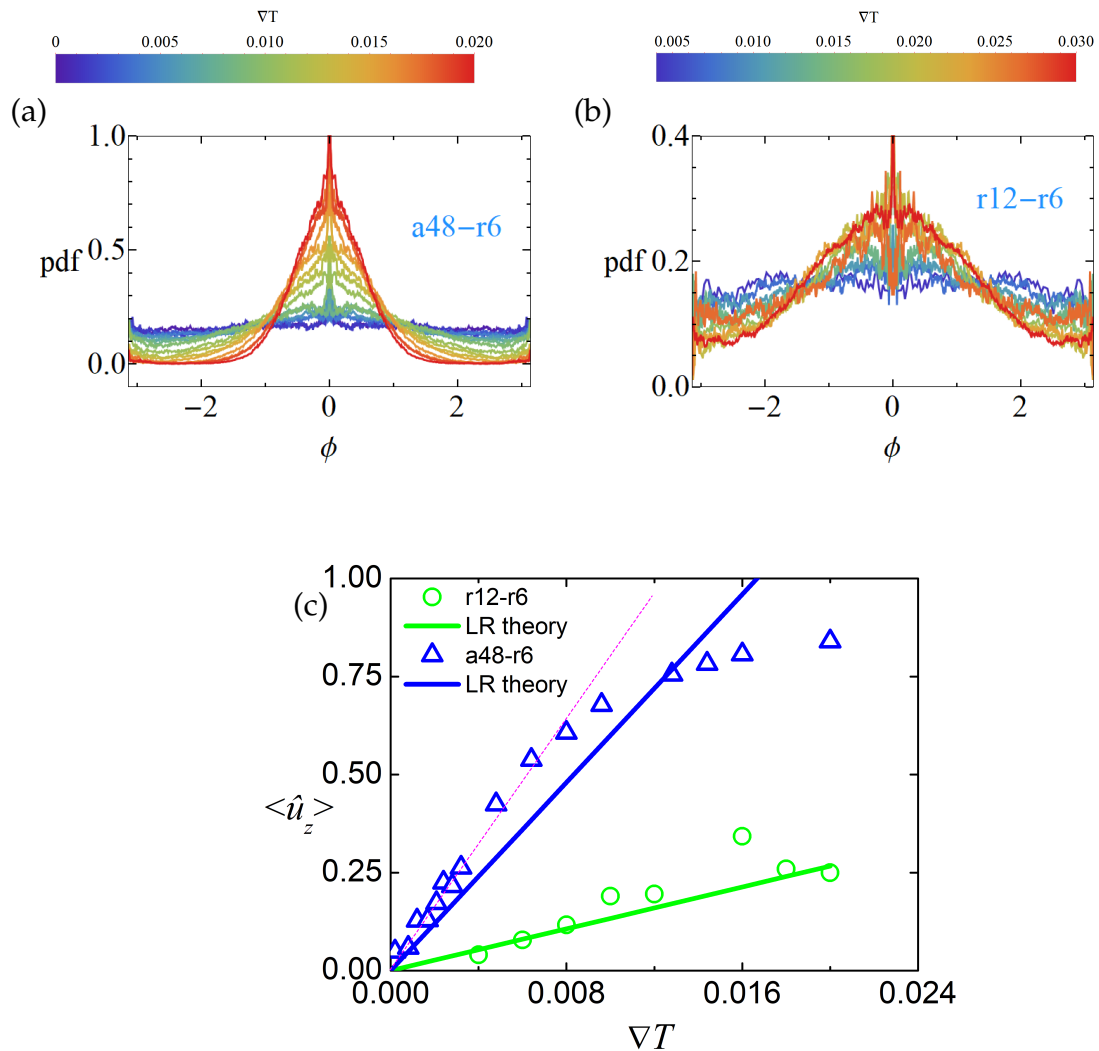


**Figure 7.2:** The alignment of heterodimers in different temperature gradients. (a) The pdf of heterodimer with  $a48 - r6$  potential in different temperature gradients. (b) Similar curves, but with  $r12 - r6$  potential. (c) The alignment  $u_z$  as a function of  $\nabla T$ . Symbols correspond to simulation results and solid lines to the prediction of the linear response theory in Eq. (7.15). The magenta dash line indicates the linear region in the simulation data of  $a48 - r6$  dimer.

## 7.3 Size ratio effect

To evaluate the thermophoretic orientation of dimers composed of two monomers made of the same material and different sizes, it is necessary to know what is the dependence of the thermophoretic factor  $\alpha_T$  on the bead size (see Eq. (7.1) and Eq. (7.15)) which is yet under debate in both molecular mixture and colloidal dispersions. The scaling of the  $S_T$  with particle diameter has shown to be both linear or quadratic, various by molecular species or colloid-solvent interactions [24, 26, 94, 111, 153]. Similarly, the interaction details influence size dependence in coarse-graining simulation study. The scaling law of the size dependence of the thermal diffusion factor are not the same if different types of potential are applied. (i) With conventional Lenard-Jones potential, has shown  $\alpha_T \propto R^3$  [59]; (ii) if displaced Lenard-Jones potential employed,  $\alpha_T \propto R^2$  (2.5).

In this section, we initialize the orientation of the dimer along the gradient, and encode the initial position of the monomer at the cold area as  $A$ , the other one as  $B$ . We discuss the size ratio dependence based on the parameter  $\mathfrak{R}_r = R_B/R_A$  and bond length  $L_D$ .

*Simulations:* we mainly performed two types of simulations and the results are shown in Fig. 7.3 (a): **A**) Fixing  $R_A$  and  $\delta = L_D - (R_A + R_B) = 0.8$  but varying  $R_B$  in a  $r6 - r6$  heterodimer (blue circles). **B**) Fixing  $L_D$  and  $\delta = 0$  (two beads are just in contact with each other) but varying  $\mathfrak{R}_r = R_B/R_A$ . We examined three kinds of heterodimers. The  $r6 - r6$  dimers with  $L_D = 4$  (upper solid triangles),  $r6 - r6$  dimers with  $L_D = 6$  (lower solid triangles), and the  $a48 - a48$  dimers with  $L_D = 4$  (diamond symbols). According to the data of  $r6 - r6$  dimer with  $\delta = 0.8$  and  $R_A = 2$  fixed, the tendency of size ratio effect is qualitatively captured by Eq. (7.15) which is indicated by the cyan curve, as we expected. The sign change of alignment occurs where the  $\mathfrak{R}_r$  changes from smaller to larger than 1. The deviation between theory and simulation results in Fig. 7.3 (a) due to the theoretical approximation since the theory where the thermophoretic force has been considered as point force. Then the accuracy of the geometry (size) is lost.

In the **B**) type simulation, the alignment  $\langle \hat{u}_z \rangle$  increases as increasing of  $\mathfrak{R}_r = R_B/R_A$  in all three kinds of dimers. Compared with “ $(r6 - r6, 4)$ ” dimers, “ $(r6 - r6, 6)$ ” dimers induce stronger thermophoretic torque  $\Psi_T$  at a fixed size ratio. This means the effect of size asymmetry on the alignment of the dimer is more pronounced in the cases of dimers with larger size. Namely instead

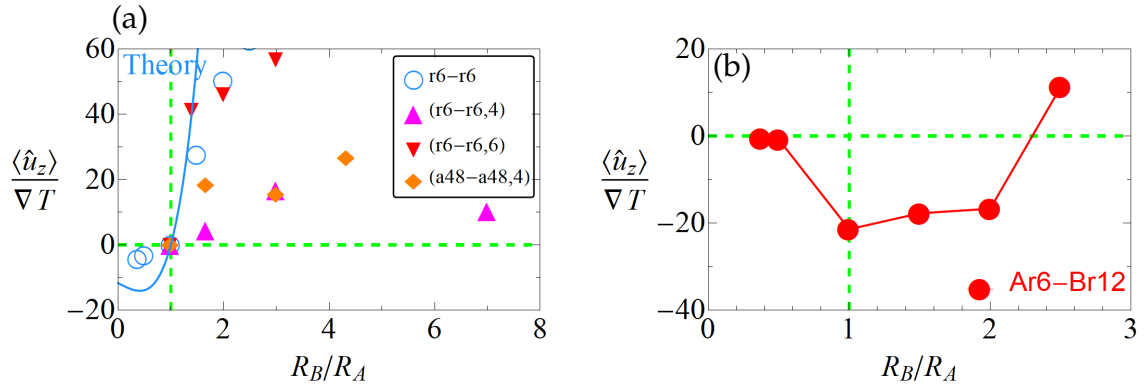


**Figure 7.3:** Size ratio dependence of thermophoretic orientation under temperature gradient. (a)  $\langle u_z \rangle$  is depicted as a function of  $\mathfrak{R}_r$ . Symbols correspond to simulation results; the solid line refers analytical evaluation via Eq. (7.15). The label “(r6-r6, 4)” denotes  $r6 - r6$  dimers with fixed bond length. The rest are similar to “(r6 - r6, 4)”. The convention of the sign of the alignment 7.2.1 is applied on the cases of fixed bond length. (b)  $\langle u_z \rangle$  as a function of  $\mathfrak{R}_r$  when dimers with fixed nearest surface distance 0.8, and  $r12 - r6$  type potential applied at  $\nabla T = 0.0125$ .

of large size asymmetry, large colloids are of significant importance to obtain strong thermophoretic orientation. Interestingly, we observed that the magnitude of alignment in  $(r6 - r6, 4)$  dimers is close to the what in  $(a48 - a48, 4)$ , albeit the former dimers are thermophilic and the latter are thermophobic. This might be due to their similar colloid-solvent interaction range and sizes.

A similar discussion could have also been performed with case (ii) namely the colloids interacting with the fluid via displaced Lennard-Jones (dLJ) potential. The size ratio dependence is expected to behave akin to the results in Ref. [111]. In which the thermophoretic orientation of size differentiated diatomic, non-polar molecular mixture has been exploited.

If the potential type of individual beads are differentiated as for example  $r6 - r12$  type potential, the size dependence is significantly different. Essentially because the two effects (size and composition) will have opposite or additive effects. As indicated in Fig. 7.3(b), the alignment exhibits non-zero peak value at  $\mathfrak{R}_r = 1$  rather than zero but with a large negative value, since the  $r6$  bead has stronger thermophoretic force. Besides this,  $\langle u_z \rangle$  increases after  $\mathfrak{R}_r$  is above one, and results in a positive sign. As the thermophoretic force on  $r12$  bead becomes significant enough to reverse the preferred orientation. On the other hand, according to the data we obtained, the orientation effect is indistinguishable when  $\mathfrak{R}_r < 1$ , as the Brownian motion of the dimer

dominates over the thermophoretic torque  $\Psi_T$  for such small structures.

## 7.4 Isotropic thermal diffusion factor of heterorod

A heterodimer or heterorod not only shows preferred orientation in temperature gradient, also exhibits a gradient dependence of isotropic thermal diffusion factor  $\alpha_{T,iso}$ . Different from a rod composed with identical segments (beads) as discussed in Chapter 4, a heterorod which comprises two types of monomers, induces alignment which will modify the isotropic thermal diffusion factor of the freely rotating heterorod in Eq. (4.6). The estimation is that the alignment,  $\langle \hat{u}_z \rangle$ , linearly contributes to the weight of  $\alpha_{T,\parallel}$ . Note that in the case that  $\langle \hat{u}_z \rangle = 1$  (fully aligned) leads to  $\alpha_{T,iso} = \alpha_{T,\parallel}$ . Thus the expression of  $\alpha_{T,iso}$  can be approximated by,

$$\alpha_{T,iso} = \frac{2 - 2|\langle \hat{u}_z \rangle|}{3} \alpha_{T,\perp} + \frac{1 + 2|\langle \hat{u}_z \rangle|}{3} \alpha_{T,\parallel}, \quad (7.18)$$

as  $|\langle u_z \rangle|$  is linearly related to  $\nabla T$ ,  $\alpha_{T,iso}$  is proportional to  $\nabla T$ . Eq. (7.18) indicates that if  $|\alpha_{T,\perp}| > |\alpha_{T,\parallel}|$ , then  $\alpha_{T,iso}$  would be underestimated by using Eq. (4.6) in Chapter 4.

As an example depicted by the cartoon in Fig. 7.4, a heterorod is composed of two  $r6$  beads at one side and two  $r12$  beads at the other. Beads with equal radius  $R = 2$ , and separated by inter-distance of 4.8. We measure the corresponding thermophoretic forces  $\mathbf{F}_{T,\perp}$  (black),  $\mathbf{F}_{T,\parallel}$  (red) and  $\mathbf{F}_{T,iso}^{sim}$  (olive) for fixed and freely rotating heterorods under different temperature gradients. Interestingly, after considering the modification of alignment effect in Eq. (7.18), the temperature gradient dependence is readily captured, as the values  $\mathbf{F}_{T,iso}$  obtained by Eq. (7.18) (magenta solid line) overlap the measured  $\mathbf{F}_{T,iso}^{sim}$ . This shows that the thermophoretic force of a (hetero)rod is the linear combination of two orthogonal thermal diffusion factors with preferred orientation consideration. Note that in Fig. 7.4 we are still within the linear response regime where the orientation is not so large, such that the linear combination works nicely. Further simulations with other potentials or larger  $\nabla T$  will show this effect more clearly. In the nonlinear regime, we expect the values of  $\mathbf{F}_{T,iso}^{sim}$  will be much closer to  $\mathbf{F}_{T,\parallel}$ .

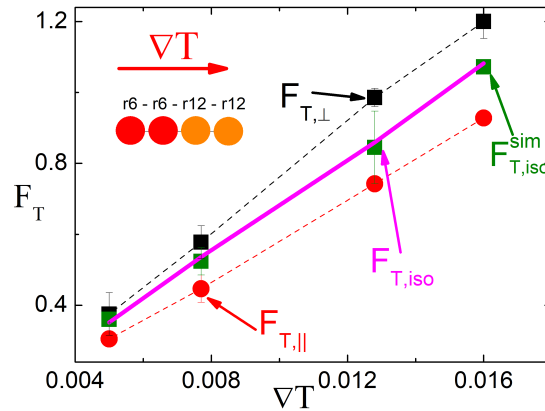


**Figure 7.4:** Thermophoretic forces of a heterorod as a function of temperature gradient. The solid symbols connected with dashed lines refer to measured thermophoretic forces of heterorod perpendicular ( $F_{T,\perp}$ , black), parallel ( $F_{T,\parallel}$ , red) and freely rotating ( $F_{T,iso}^{sim}$ , olive) in different temperature gradients. The magenta symbolized data are obtained by using Eq. (7.18).

## 7.5 Phoretic motion of heterodimeric dispersions in confinement

Previous sections based on heterodimers are discussed in the infinite dilute limit. In which no interactions between them are considered (except for the PBCs induced long-ranged hydrodynamic interactions). When the concentration increases, dimer-dimer interactions play a vital role. The collective behavior of asymmetric colloidal particles driven by thermophoresis is of fundamental interest. In this section we investigate how the heterodimers accumulate and align near confining walls at different concentration and temperature gradients. Special interest will be devoted to elucidate how the hydrodynamic interactions between colloids influence their dynamic behavior.

An interesting parallelism in this case can be found with a system of sedimenting colloids, such that we here summarize the so-called *Sedimentation-Diffusion Equilibrium* [17]. Colloids in gravitational field and in confinement are driven to approach and accumulate at the container wall. This results in a concentration gradient of the colloids in the opposite direction of the driven force. At the stationary state, the flux of sedimentation cancels the flux from the (Fickian) diffusion. Usually, a concentrated liquid-like phase is formed

close to the aggregation wall; whilst the colloids far away from the wall have more degrees of freedom to diffuse to the gas-like phase. As previously mentioned in Chapter 3, phoretic force is always treated as an analogy to the body forces, albeit it is governed by local hydrodynamics stress. An interesting question that we can ask is what if this sedimentation process is replaced by thermophoretic driven? Especially, *Sedimentation-Diffusion Equilibrium* has also been recently applied as an approach to achieve self-assembly [154]. Another interesting factor is that one can expect hydrodynamic flow field of phoretic particles might play a role on sedimentation equilibrium. Several work reported that phoretic colloids accumulated at walls can induce strong hydrodynamic interaction to form phoretic colloidal crystal [80, 90, 155]. Therefore, it is constructive to probe the dynamics of thermally driven heterodimeric suspensions in the similar container. As discussed above, heterodimers or heterorods, exhibit rich translational and orientational dynamical behaviors, might be suitable candidates of building blocks for colloidal self-assembly.

We take the interactions between heterodimers (prescribed in Chapter 2) into account. The container is considered as a slit with walls perpendicular to it. Temperature gradient is perpendicularly applied to the walls. The heterodimers will be accumulated at the hot or cold container wall depending on the net phoretic drift of the dimer. Besides the translational motion, the thermophoretically induced orientation of the heterodimer will also affect the colloidal structure formation. In particular, in two dimensional configuration, the mutual alignment effect is strongly pronounced when dimers or rods are approaching each other.

### 7.5.1 Concentration and orientation order

We start with many heterodimers confined in a quasi-two dimensional box with an applied temperature gradient. As indicated in Fig. 7.5(a), 150 number of  $a48 - r6$  heterodimers (the  $r6$  bead is colored with red, and the  $a48$  bead with green, their radius  $R_A = R_B = 1.25$ ) are initially distributed at the nodes of triangular lattice, with random orientation in  $x - z$  plane. We constrain the particles in a slit with cuboid simulation box (the blue frame in Fig. 7.5) size of  $(L_x, L_y, L_z) = (100, 10, 150)$ . A strong, repulsive potential ( $r6$  with  $\sigma = 0.5L_y$ , formulation as prescribed in Chapter 2) are symmetrically applied at walls parallelly to the  $y$  axis, such that the heterodimers are only allowed

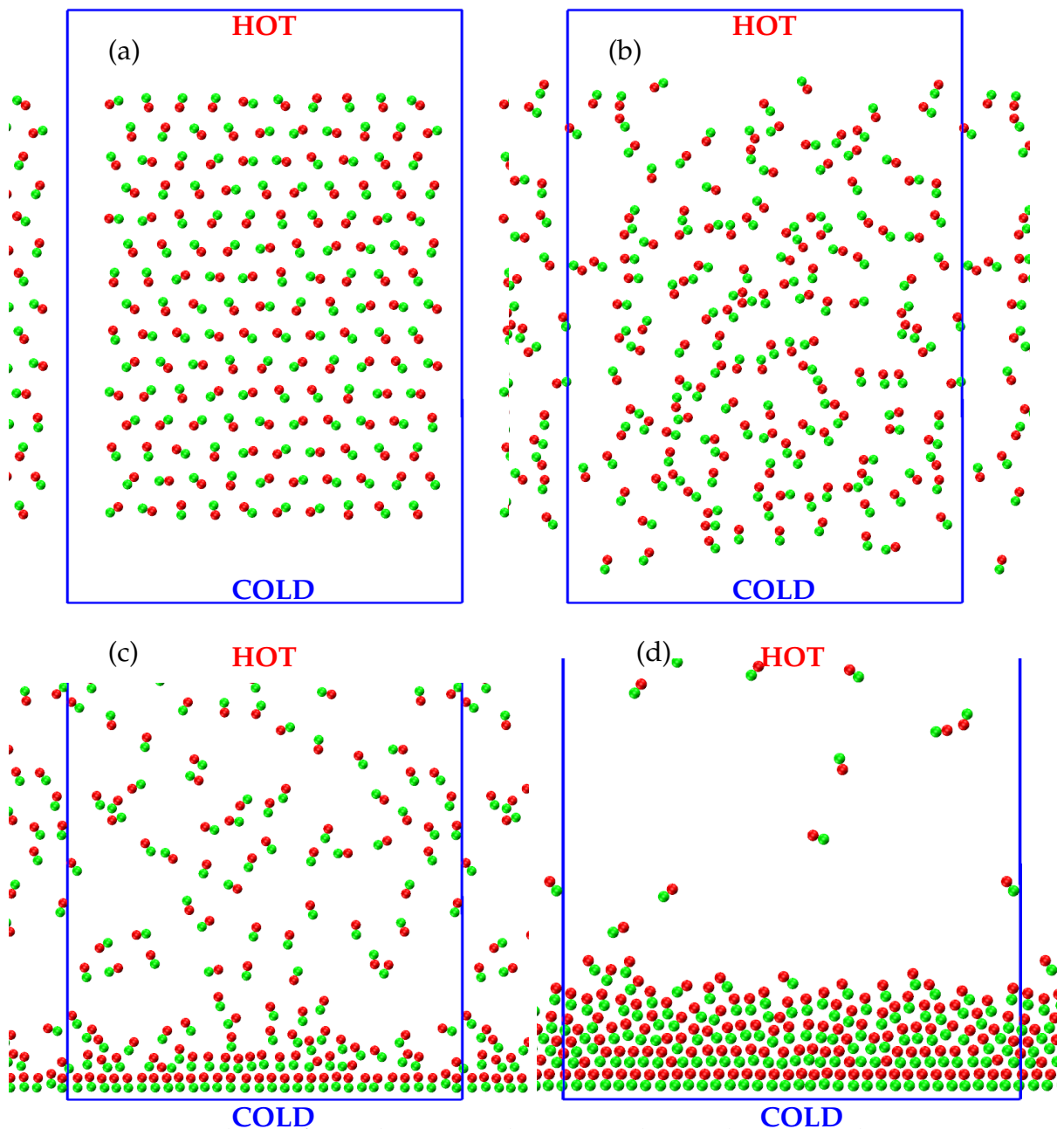


**Figure 7.5:** Snapshots of simulations with  $a48 - r6$  heterodimers, with volume fraction  $\phi \approx 25.5\%$  and  $\nabla T \approx 0.0107$ . The blue contour indicates the simulation box. PBCs are applied along left-right direction. Here and in what follows, the direction of the external temperature gradient is indicated by "COLD" and "HOT". (a) 150 heterodimers are initially distributed at the triangular lattice sites, with random orientation in  $x - z$  plane. (b) At  $t = 2000$ . (c) At  $t = 25000$ . (d) At  $t = 100000$ , heterodimers are separated into gas and crystal-like phases with an orientation order.

to move in the  $x - z$  plane at  $y = 0.5L_y$ . Along the gradient axis, the colloids are confined between the hot ( $z = 150$ ) and cold ( $z = 0$ ) walls with symmetric shifted repulsive potential ( $(\Delta 2, r6)$  potential, as prescribed in Chapter 2). The MPC solvent particles are confined between the walls along both the gradient and the  $y$  axes by the realization of bounce back rule, what ensures no-slip boundary conditions. Purely repulsive  $r6$  potential between colloids is used with  $\sigma = R_{cc} = 2.25R$ . The larger colloid-colloid interaction radius  $R_{cc}$  is considered to avoid artificial depletion interactions and resolve lubrication forces, which are intrinsic in the MPC algorithm [78]. Note that this separation is still small to preserve the importance of hydrodynamic interactions.

Fig. 7.5(b) shows a snapshot at  $t = 2000$ , the particles driven by phoretic forces towards the cold wall ( $z = 0$ ) with some alignment along the gradient axis. This reveals that the onset of the aligning and the drifting motion happen simultaneously. This is a reasonable fact since both effects are originated from thermophoretic forces on different monomers. Fig. 7.5(c) at  $t = 25000$  shows that some dimers reach the cold wall keeping a significant alignment; the first layer of the dimers forms an ordered crystal-like structure. Not just the ordered position is formed in this layer, the strong orientation is also built with  $a48$  beads face the wall. We checked the time-averaged orientations relax faster than the concentrations reach the steady states. *This is because the concentration steady state is strongly influenced by the spatial distance between two walls.* The simulation results in Fig. 7.5(d) show the steady state of both orientation and concentration. In this particular case, heterodimers form a crystal-like structure with an orientation order. This layered structure constitutes smectic-A liquid-crystalline phase. According to the flow field data of a heterodimer pair, the near wall phoretically induced flow field can also induce attraction and therefore to enhance the crystallization.

We further investigate the system under different temperature gradients. Quantitatively, both concentration and orientation decay for increasing separation to the cold wall, as shown in Fig7.6. Interestingly, as the local orientation order has relaxed into steady state, and an exponentially decay of the orientation is observed in Fig. 7.6 (b). The concentration profile of different temperature gradients also obeys exponentially decay, except for the case  $\nabla T = 0.0107$ . Note that the concentration of heterodimers very close to the wall at  $\nabla T = 0.0040, 0.0053, 0.0067$  and  $0.0080$ , has not reached the stationary state (in  $nabla T = 0.0107$  is at the stationary state), this will be further

discussed in Sec. 7.5.3. Hence a concentration drop at those positions is observed. These exponential concentration and orientation profiles, is reminiscent of *Sedimentation-Diffusion Equilibrium* [17]. Since the solution of the *pdf* in the Smoluchowski equation is also exponential.

Following the theoretical derivation in sedimentation, one can construct the Smoluchowski equation in our heterorod system. The assumption is that the thermophoretic forces act on the beads are treated as point forces, the same as what applied in Section 7.2.1. Hydrodynamic interactions between heterodimers or heterorods are neglected. As the volume fraction is very low in most simulations, which is lower than  $d/l$  where the isotropic-nematic phase transition can happen, the those hetero-colloids are very far apart. Moreover, when the potential interactions between colloids play a role, the accurate description based on slip flow of thermophoresis seems to be unnecessary. Therefore, treating the phoretic force on the bead as point loading should be reasonable. However, the fact that thermophoretic forces and thermal fluctuations of these heterodimers are temperature dependent should be bear in mind. To solve this, one need the interaction potential in non-spherical particle systems is not trivial. One possible way is connecting with density function theory approach as described in Ref. [156].

More interestingly, it seems that the non-exponential concentration profile signals a transition from nematic phase to smectic phase in the system.

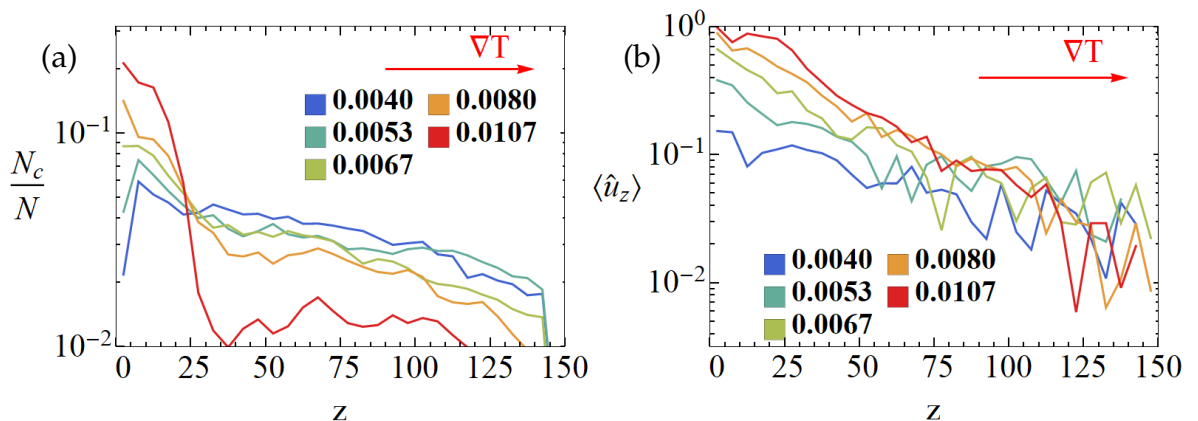


**Figure 7.6:** (a) The concentration and (b) the orientation order parameter a function of distance to the aggregation (cold) wall.

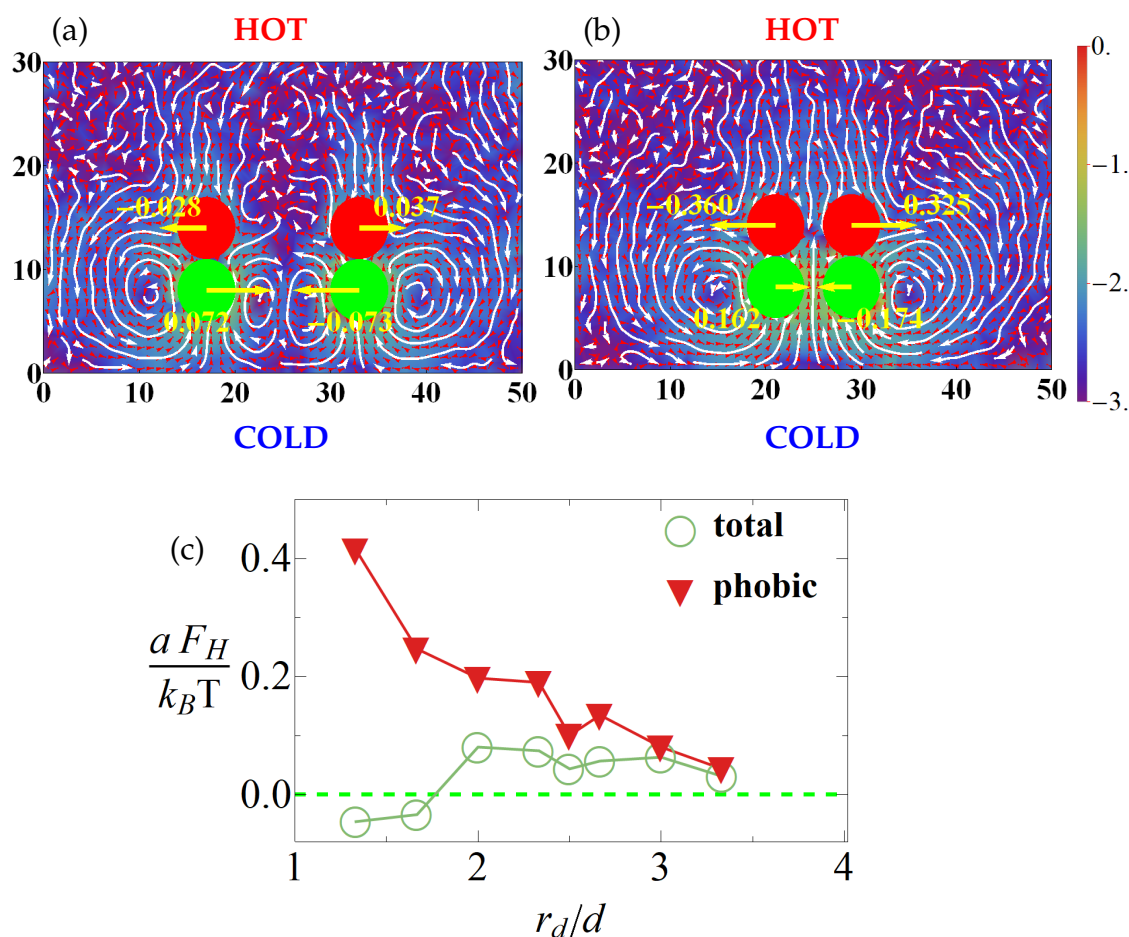


**Figure 7.7:** The flow fields of (a)  $a48 - r6$  dimer pairs with separation distance  $5.3R$ , and (b)  $a48 - r6$  dimer pairs with separation distance  $2.6R$ . Yellow arrows indicate the direction and the numbers the value of the measured forces perpendicular to the gradient, on each individual bead. Background color coding is prescribed in Chapter 2 Sec. 2.5. (c) The hydrodynamic interaction  $F_H$  of dimer (green open symbol line) and phobic monomer (red solid symbol line) as a function of dimer-pair distance  $r_d$ . Note that the bead radius  $R = 3$ , so a qualitative comparison of this data with the simulation of collective behaviors can be made.

### 7.5.2 Confirming the effects of hydrodynamic interaction

When phoretic beads stay against the wall, the phoretic flow field (Fig. 7.7 (a) and Fig. 7.7 (b)) of the phobic beads (green) can induce attraction which is long-ranged, specially in comparison with steric interaction which will enhance the structure close to the wall. Keeping two  $a48 - r6$  dimers aligned along the gradient direction at different separation distances  $r_d$ , with phobic ( $a48$ ) bead facing the cold wall to a distance of 5, we measure first the velocity field and the corresponding stream lines as indicated in Fig. 7.7 (a) and Fig. 7.7 (b) where certain inter-particle attraction can be inferred. To be more precise we also measure the force that each individual bead experiences as well as the total force on the dimer. The hydrodynamic force as a function of  $r_d$  between two dimers and two phobic beads is shown in Fig. 7.7 (c), which is almost the same order of the thermal energy  $k_B T$  (as the hydrodynamic interaction length scale is the order of a cell size  $a$ ). Especially, when two phobic beads are close to each other near the cold wall, strong hydrodynamic attraction is observed. This attractive force can lead to the aggregation of colloids close to the wall and enhance the stability of the colloidal structure [80, 90, 155]. The philic beads (red) create repulsion then lead to a net hydrodynamic torque on the dimer. However, the hydrodynamic torque is one order of magnitude smaller than the phoretic torque  $\Psi_T$  such that can be neglected. Therefore the lateral attraction is strong and play a vital role for heterocolloids aggregation.

### 7.5.3 Relaxation time of position and orientation

According to the second snapshot in Fig. 7.5, when dimers are driven by net phoretic forces towards the cold wall (due to the stronger thermophilic force), the thermophoretic torque aligns them simultaneously to the gradient axis. As the spatial movement for aligning is much smaller than the dimers travel towards the wall, the steady state of orientation is much faster than density arrangement. Indeed, the concentration and orientation relaxation can be investigated by the temporal average process, as indicated in Fig. 7.8. The concentration at positions very close to the cold wall with various of temperature gradients is not fully relaxed in the performed simulations, especially for  $\nabla T = 0.0040$  close to the aggregation wall. However, the orientation has relaxed even with  $\nabla T = 0.0040$  at different positions. Therefore we still observed the nice exponentially decay of orientation order at the steady state.

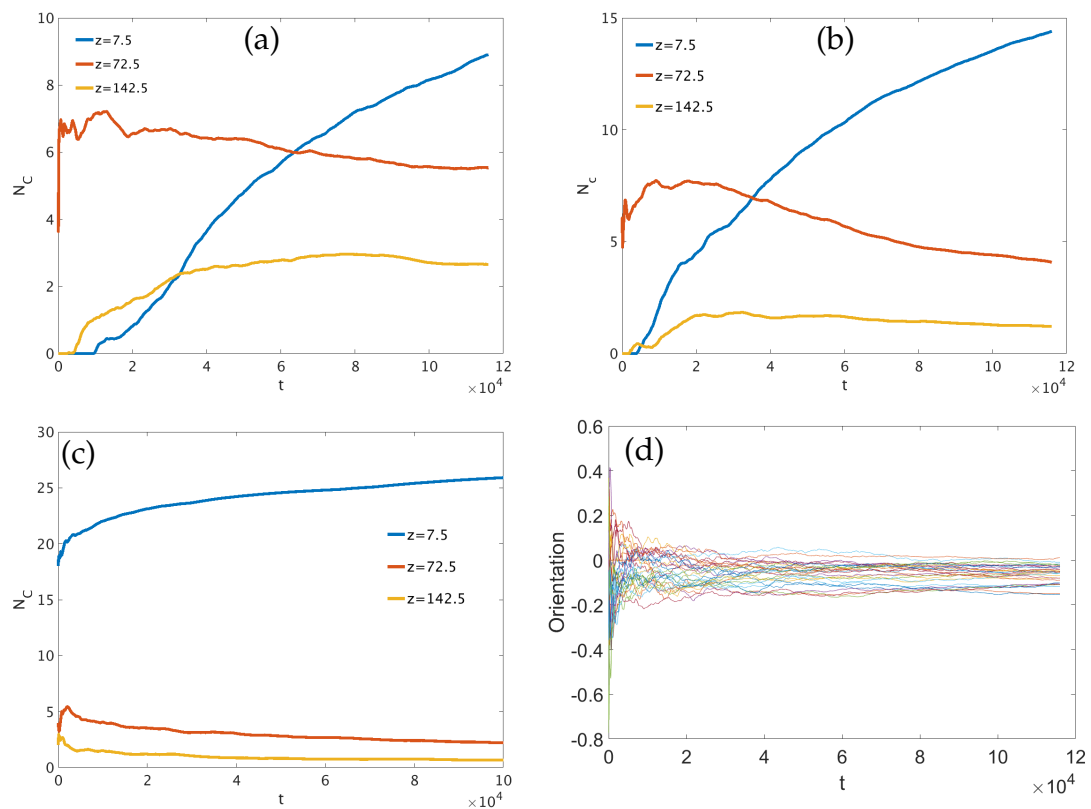


**Figure 7.8:** Temporal average of concentration and orientation at different gradients. (a) Concentration at the cold wall (first slab  $z = 7.5$ ), the middle of the container ( $z = 72.5$ ), and the hot wall ( $z = 145.5$ ) with  $\nabla T = 0.0040$ . (b) Concentration at the same positions with  $\nabla T = 0.0080$  (c)  $\nabla T = 0.0107$  (d) The local temporal average of orientation  $\langle \hat{u}_z \rangle$  at different positions with  $\nabla T = 0.0040$ .

### 7.5.4 Aggregation for different dimer densities

To further confirm the role of hydrodynamic attraction, as well as investigate how the dimer density dependence of the aggregation, we study the collective behavior of the same systems only differed by the number of heterodimers. The dynamic behaviors of heterocolloids are different in different systems. The hydrodynamic interaction seems to *enhance* the aggregation, since the colloid-colloid interaction is purely repulsive. Here we show and explain the dynamic cluster formation in three different densities. The snapshots and associated director fields are shown below.

Fig. 7.9 shows the case in which 10 dimers reach the bottom of the container with a clear homeotropic alignment in the system, and seems to gather together due to hydrodynamic attraction close to the wall.

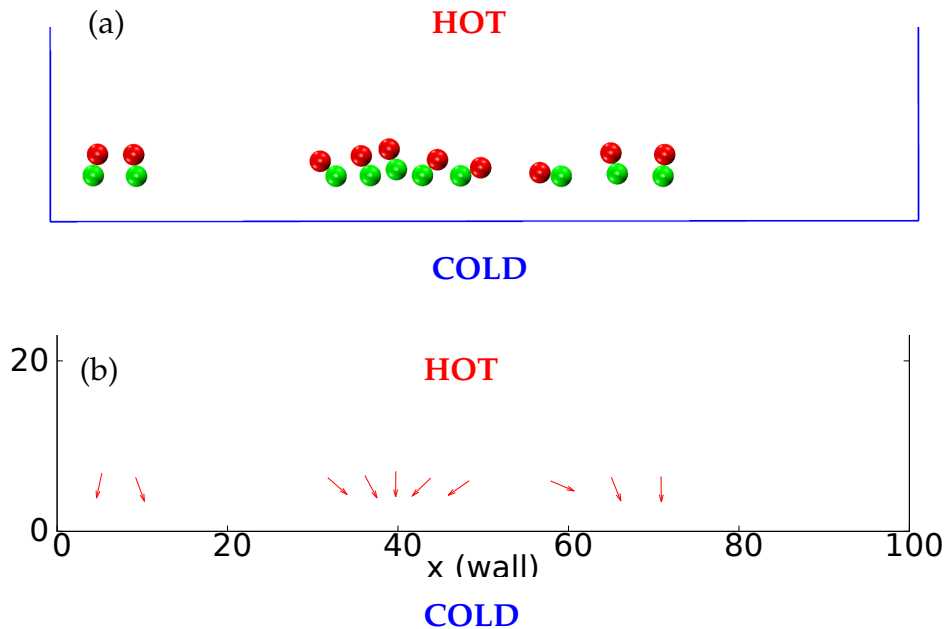


**Figure 7.9:** (a) Snapshot of 10 heterodimers aggregate at the wall. (b) The corresponding director field.

*Hedgehog-like cluster with near-wall sweeping* (Fig. 7.10): 20 dimers are driven by thermophoretic forces towards the cold wall. Part of the colloidal particles were stopped by the wall earlier than the others. The homeotropic order is found in most of the near wall heterodimers which is similar to the scenario in Fig. 7.9 (a). Then a small group of heterodimer complex is formed with successively sweeping as a whole along the wall due to anisotropic thermophoretic driving force. This near-wall sweeping can take up the speed of other near wall dimers. More heterodimers are picked up and join into the cluster. Some of the particles drift to the wall until they reach the near-wall

cluster such that a hedgehog-like cluster is formed [156], especially the orientation order is also established due to thermophoretic torque in the heterodimers. This self-assembled cluster is also stable (with overall sweeping), which can be understood by the aforementioned hydrodynamic attraction between phobic beads close to the wall. Interestingly, this *Hedgehog-like cluster*, which is formed by passive colloids under external fields in our simulations, has also been observed in active systems without sweeping movement [156].

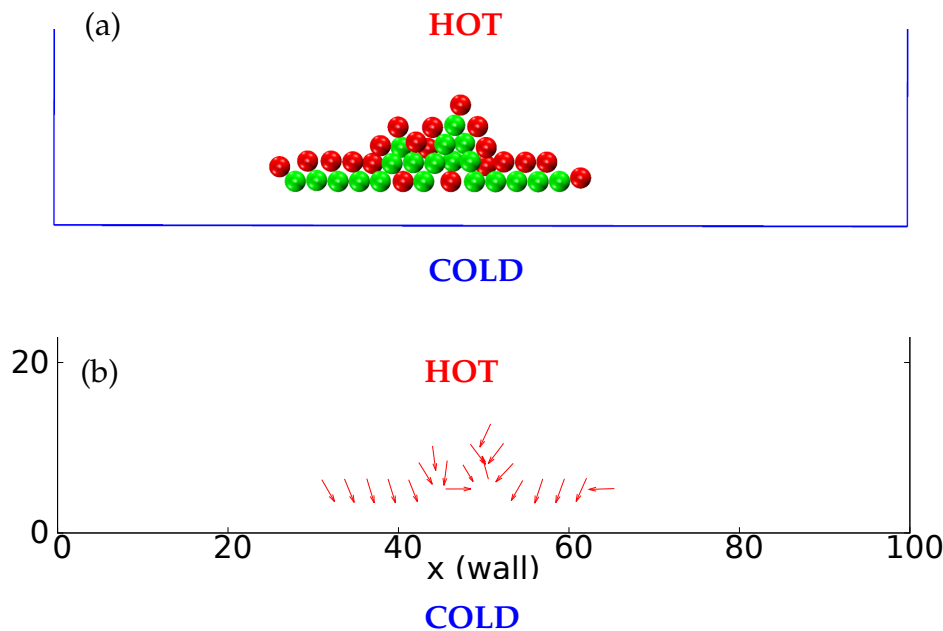


**Figure 7.10:** (a) Snapshot of 20 heterodimers aggregate at the wall. (b) The corresponding director field.

*Rhythmic cluster formation* (Fig. 7.11): When the dimer density is higher (50 dimers in the simulation box with the same size as before), the clustering formation becomes unstable and exhibits a clustering instability. At this dimer density, an early stage cluster is formed and also generates some mechanical instabilities. Because the heterodimers are not perfectly aligned and packed as the situation in Fig. 7.5 near the wall. This instability leads to the rolling of part of the cluster (Fig. 7.11 (a) or Fig. 7.11 (b)). This sub-cluster has weaker hydrodynamic attraction since it is further away from the wall, such that a small fluctuation is able to detach it from the wall and dissolve into gas-like phase (Fig. 7.11 (c) or Fig. 7.11 (d)). These particles will be driven to the wall and the process start again. Therefore,

the phenomena of the cluster formation is rhythmic in time, i.e. a typical frequency is expected to be identified, which is associated with the cluster formation and release [157].

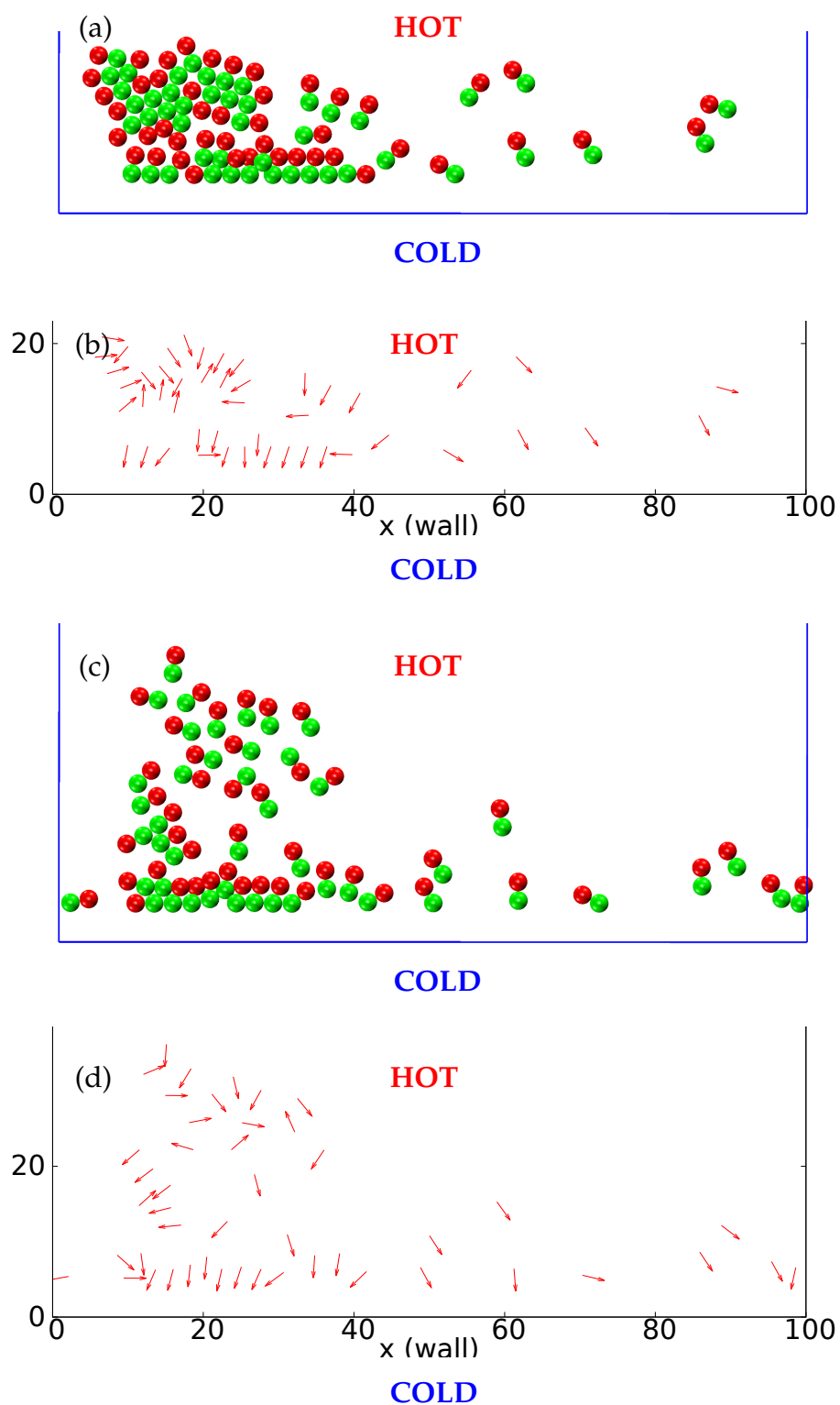


**Figure 7.11:** (a) Snapshot of 50 heterodimers aggregate near the wall at  $t = 121250$  units of time; (b) the corresponding director field. (c) Snapshot at  $t = 122741$  units of time; (d) the corresponding director field.

## 7.6 Conclusions and outlook

On basis of rotational Brownian motion, supplemented with thermophoresis, a theoretical expression of the alignment of a heterodimer in temperature gradient is derived. A linear relation between the alignment and external temperature gradient can be predicted. This expression is clearly consistent with the theoretical work about molecular thermal diffusion by Lee [111] in the framework of local equilibrium approach. Moreover, this linear dependence of alignment also agrees with the simulation study of Römer et.al. [109] in the case of non-polar diatomic fluids.

Interestingly, our simulation study reveals that temperature gradient, combined with thermophoretic heterogeneity influence the thermophoretic orientation strongly. More specifically, the theoretical prediction holds for the case at weak temperature gradient, or the thermophoretic heterogeneity is small. On the contrary, this prediction breaks down when the thermophoretic heterogeneity is strong. In this case the alignment can easily get saturated even at small gradient. The reason is that our derivation is based on linear response theory, namely the probability distribution function is slightly perturbed and proportional to applied temperature gradient.

We further investigated the size ratio dependence of the alignment in the heterodimer. Our simulation study qualitatively captures this tendency. Additionally, instead of large size asymmetry, thermophoretic orientation prefers large monomer size with the same size asymmetry. However, combined with interfacial interaction asymmetry, the alignment evolves non-monotonically when size asymmetry changes. Compared with the heterodimer contains solely size asymmetry, the sign changing scenario of the alignment appears at an asymmetric size case. As our analytical prediction includes thermophoretic effect as point force and omits the fact of its local forcing mechanism, this might leads to inaccurate calculation of the thermophoretic torque. We suggest that a precise way is integrating the local pressure gradient induced torque of the heterodimer under a bi-spherical coordinate system [87].

The isotropic thermal diffusion factor of a *heterorod* shows a temperature gradient dependence. This is intuitive because a freely rotating heterorod exhibits thermal orientation. The isotropic thermal diffusion factor of a heterorod should account for the enhanced weight of thermal diffusion factor along the gradient direction, which is proportional the applied temperature gradient.

Finally, we investigated concentrated systems of hetero-dimers confined in a slit between walls, and driven by thermophoresis. The particle distribution at the steady state is reminiscent of well-known *Sedimentation-Diffusion Equilibrium* phenomenon. As the concentration and orientation of heterocolloids as functions of the distance far away to the aggregation walls, both obey exponential decay, together exhibit smectic liquid-crystalline phase. However, according to the flow field data we obtained, we speculate that the hydrodynamic attraction effects of phoretic heterodimeric colloids close to the walls enhances crystallization.

The investigation of thermally driven colloids towards wall opens several possibilities for future explorations. These thermophoretic heterocolloids exhibit rich phase behaviors at different temperature gradients and concentrations. We can perform more intensive simulation study to construct the phase diagram, in different *wall temperatures, temperature gradients* and *colloid densities*. By the research so far, we have observed nematic and smectic phases, hedgehog-like cluster and rhythmic cluster. Thermophoretic heterocolloids, are therefore novel building blocks for self-assembled structures have promising potential to practical applications.

## Chapter 8

# Epilogue

*“Le vrai point d’honneur [d’un scientifique] n’est pas d’être toujours dans le vrai. Il est d’oser, de proposer des idées neuves, et ensuite de les vérifier.”*

Pierre-Gilles de Gennes

### 8.1 Synopsis

In this thesis, we have studied the thermophoretic responses of asymmetric particles, and their resulting net flows in microchannels. These asymmetries can be geometric such as shape, length, and even surface roughness; and also can be compositional i.e the particle can be made of different materials which have disparate thermophoretic properties.

As an essential step, we have shown in Chapter 3, using simulations of MPC-MD methods and continuum theory, that the physics of thermophoresis of spherical colloids, i.e. the local pressure gradient and the resultant slip flow at the colloid-liquid boundary layer, can be correctly captured by simulations. As a parallel numerical model of diffusiophoresis, our model for thermophoresis describes similar hydrodynamics and driving forces in the framework of phoresis in general. We have discussed the finite system size effects under two types of boundary conditions, both offer similar enhancement on the measurement of thermal diffusion factor.

Then we moved to rod-like colloids. The elongated geometry induced anisotropic thermophoresis is readily captured in terms of linear decomposition approach. We extended this interpretation that colloids with arbitrary geometry, the thermophoretic response can be characterized by three orthogonal thermal diffusion factors. More importantly, our investigations highlighted that the

geometrical details can significantly influence this anisotropic effect, which results in thermophoretic force for rod align the gradient axis can be larger or smaller than the rod perpendicular to it. To quantitatively describe the anisotropic thermophoresis, we proposed the *thermal anisotropy factor* which is the difference between the two orthogonal thermal diffusion factor of the rod. From the application point of view, this quantification offers an interesting tunability of anisotropic thermophoresis.

As a step further, we have studied the dimer model contains two parts with different thermophoretic properties. Especially we have focused on the thermophoretic torque induced orientation order. In the infinite dilute region, we observed the alignment is linearly dependent on the applied temperature gradient, despite the thermophoretic properties of two different monomers. The size ratio seems to play a less significant role than the inherent individual particle size on the alignment. Our simulation studies on the hetero-colloids confined in a slit between walls, and driven by thermophoresis, is reminiscent of well-know *Sedimentation-Diffusion Equilibrium* phenomenon. Since the concentration and orientation of hetero-colloids as functions of the distance to the accumulation walls, both obey exponentially decay. However, our simulations also emphasized that the hydrodynamic attraction effects of phoretic colloids close to the walls can enhance crystallization.

Now turning to application part, we proposed two schemes of micropumps with spatial symmetry breaking in the middle of the microchannels. In piratical, one can design and exchange the material of the obstacles without modifications of the channel walls. Based on the study of anisotropic thermophoresis, we designed micropumps with elongated obstacles tilted to gradient but placed in the middle of the microchannel. We have shown that this novel phoretic pump provides sinusoidal-like effective flow lines. Besides the dependence of channel width, to gain the optimized net flow flux, we also observed that the obstacles can be fixed in different positions in the middle of the channel. More interestingly, as the phoretic response of the fluid, the flux density in this micropump can be perfectly captured by the anisotropic thermophoresis of obstacles. We have observed that the magnitudes and the direction of the resultant flux density closely depend on interfacial properties of elongated obstacles such as aspect ratio, surface rugosity and *thermophilic* or *thermophobic* properties, and is linearly related to thermal anisotropy factor.

Finally, we studied the fluid pumping of Janus-particle-like obstacles in the

middle of microchannels. The local temperature gradient is generated due to the higher heat adsorption at the metal part of the obstacles, with the technique of laser illumination. We revealed that the resulting far-field flow resembles the external pressure gradient induced Poiseuille flow. The net flow flux strongly relies on the obstacle length rather than the channel width. In comparison with other micropumps such as the former anisotropic thermophoretic pump, and ratcheted wall pump, this partially heated phoretic pump has higher pumping capability due to the higher local temperature gradient.

## 8.2 Outlook

We outline two main possible directions of future research for this thesis.

**Thermal fluctuations in non-equilibrium Thermodynamics:** From fundamental point of view, the study of thermophoresis in asymmetric colloids is of significant importance for non-equilibrium thermodynamics. One possible study is that how the Fluctuation-dissipation theorem (FDT) is modified in the presence of temperature gradient. Meanwhile, the resultant fluctuation acts on asymmetric colloid is of interest to exploit.

**Colloidal self-assembly:** Why do we study the mechanicals and hydrodynamics of colloids with different types of asymmetry in temperature gradient? On one hand, as already has been addressed in the beginning of the thesis, it is a step further to study and underpin the fundamental physics of thermophoresis, the mechanism obtained is very useful. On the other hand, novel phoretic behaviors can be used to form self-assembled colloidal structures. External gradient induces phoretic thrust on colloids and interact with other individuals via hydrodynamics, is promising route for fabrication of nanostructures. The potential use of phoresis developed spontaneous self-organisation of colloid provides versatile tunability of the effective interactions between the colloidal particles. One promising approach is first study the individual building blocks under temperature gradient. According to the observations in this thesis, the colloids with geometrical and/or compositional asymmetries show an unusual thermophoretic behavior. As suitable candidates for colloidal self-assembly, these phoretic building blocks can be

tuned to form colloidal crystal, liquid crystal or disordered structures. One interesting feature for this kind of self-assembly is that the interaction between building blocks are dependent on both colloidal collision and long ranged hydrodynamics. The hydrodynamic interaction can be treated as effective colloid-colloid potential interaction. As presented in the Chapter 7, the building blocks hetrocolloids are used to form different types of colloidal structures. Specifically, combining with confinement, asymmetric building blocks with different composition form closed anisotropic crystal structure close to the wall; far away from the wall, the thermophoretic hydrodynamics mediated interaction and movement between building blocks are weaker, resulting a less ordered structure. Consequently, these heterodimeric building blocks are attracted to the walls and with a orientation order. The space between individuals and their orientation orders can be tuned by external gradient and colloid-solvent interactions, as their thermophoretic responses.

## Appendix A

# Analytical calculation for thermophoretic force

In Chapter 3, we analytically calculated the slip flow velocity, the local pressure gradient for MPC-MD model. This can be used to evaluate the thermophoretic force in different ways. The following solutions can be applied to evaluate the thermal diffusion factor of spherical bead (from Chapter 4 to 7).

### A.1 The slip flow solution

Substituting Eq.(3.17) into Eq.(3.7), we found that the slip velocity  $v_s(z)$  in MPC fluid is expressed as,

$$v_s(z) = -\frac{1}{\eta} \frac{P_\infty}{k_B T^2(z)} \frac{\partial T}{\partial z} \int_0^{R+\delta} \left\{ U(x) \exp \left[ -\frac{U(x)}{k_B T(z)} \right] x \right\} dx. \quad (\text{A.1})$$

Here the ideal gas equation of the state is applied. Note Eq.(A.1) is also valid for spherical colloid by replacing the notation  $z$  with  $\tau$  (the tangential direction). A theoretical estimation of  $\mathbf{F}_T = -4\pi\eta R(2/3)v_B$ , where  $v_B$  is the maximum of the slip velocity of colloid in external temperature gradient.

## A.2 Local pressure gradient solution

The flow is barely induced by tangential pressure gradient. Therefore the resulting thermophoretic force can be computed by integrating the local pressure gradient around a colloid.

$$\mathbf{F}_T = -\frac{2\pi P_\infty \nabla T}{k_B} \int_0^\pi \sin^3 \theta d\theta \int_0^{R+\delta} \left\{ n^2 \frac{U(n)}{(\bar{T} + n \cos \theta \nabla T)^2} \exp \left[ -\frac{U(n)}{k_B(\bar{T} + n \cos \theta \nabla T)} \right] \right\} dn, \quad (\text{A.2})$$

where  $\bar{T}$  is the temperature at colloid center. In Eq.(A.2) spherical coordinate is applied,  $\theta$  is the polar angle.

## A.3 Force balance solution: summing all the potential interacting forces

Different from the former two approaches, the thermophoretic force can be obtained by summing all of the central interacting forces (i.e.  $-\partial U(n)/\partial n$ ) along gradient direction. This is due to the force balance condition, namely how much external force we should apply on colloid in temperature gradient to fix the position.

$$\begin{aligned} \mathbf{F}_T &= \int_0^{R+\delta} n^2 dn \int_0^\pi \sin \theta d\theta \int_0^{2\pi} \rho(n, \theta) \frac{\partial U(n)}{\partial n} \cos \theta d\phi \\ &= \frac{2\pi P_\infty}{k_B} \int_0^\pi \sin \theta \cos \theta d\theta \int_0^{R+\delta} \left\{ n^2 \frac{1}{\bar{T} + n \cos \theta \nabla T} \exp \left[ -\frac{U(n)}{k_B(\bar{T} + n \cos \theta \nabla T)} \right] \frac{\partial U(n)}{\partial n} \right\} dn, \end{aligned} \quad (\text{A.3})$$

Similarly, the spherical coordinate is applied. The prefactor  $\cos \theta$  in the first line of Eq. (A.3) indicates the force is projected along the gradient direction. Due to the asymmetric density distribution, the unbalanced central forces come into the thermophoretic calculation. This is different from the two previous approaches.

## Appendix B

# Analytical flow field for different boundary conditions

This appendix services as the detailed analytical calculation for finite size effect correction in Chapter 3. Based on Eq. (3.13), the solutions to analytically construct the thermophoretic flow field with different boundary conditions has been presented. Recalling the boundary conditions result in an additional friction force on the measurement of phoretic force, this methods provide a way to calculate the *effective friction*  $F_T^\gamma$ . In this way, the finite size effects factor  $\lambda$  in Eq.(3.21) for different boundary conditions is quantified by analytical calculation.

### B.1 Thermophoretic flow field of fixed colloid confined between walls

The first boundary condition we considered is colloid confined between walls in the center.

The flow field of fixed colloid is a combination of a Stokeslet and a source dipole. Colloids pump the fluid forward (opposite from  $\mathbf{F}_T$ ) but bounces back when it hits the wall and act on the central colloid. Meanwhile, the cooperation with other images perpendicular to the gradient leads to convection flow pattern in Ref.[60] and Fig.3.12(a).

Fig. B.1(b) indicates the schematic diagram of analytical calculation of flow pattern via including effects from walls (applying constant back flow assumption) and periodic boundary conditions along other two( $x$  and  $y$ ) directions.

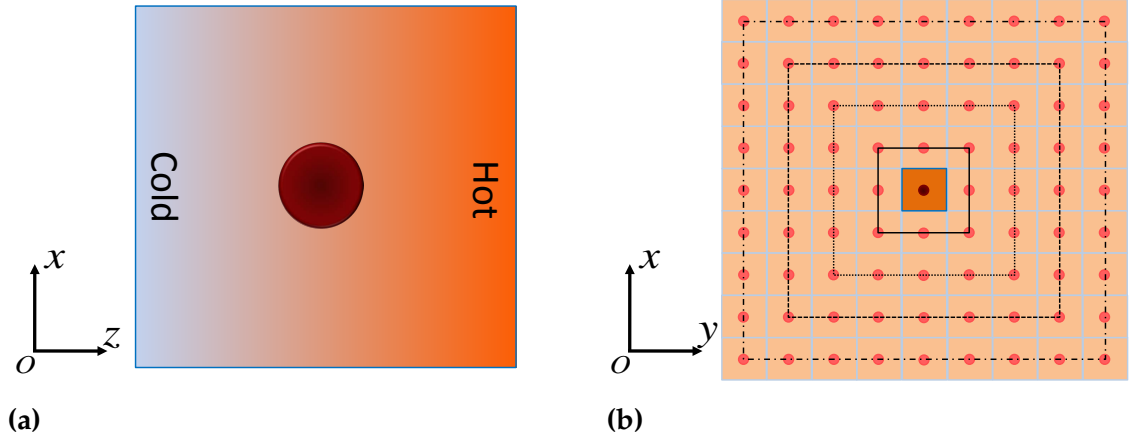


**Figure B.1:** (a) Model consideration for measurement of thermophoretic force: colloid is fixed in the center of simulation box, temperature gradient is applied in  $z$ -direction with walls (were not visualized). (b) Schematic representation of calculation route for flow field considering periodic boundary conditions ( $x - y$  directions are considered).

To characterize  $F_T^\gamma$  to thermophoresis, the calculation procedure is considered as follows: the first part comes from the thermophoretic flow at the walls bouncing back (constant back flow assumption) without changing the magnitudes, in which contributions from all images and center box are counted; the second part is the thermophoretic flow excited by other images whose directions are the same as the thermophoretic flow which decrease the measured net force. Specifically,  $F_T^\gamma(\mathbf{r})$  is the sum of the hydrodynamic interactions from the back flow of the colloid itself as well as its periodic images, and the thermophoretic flow of periodic images (which is opposite from the back flow direction). Hence the effective friction is represented by,

$$F_T^\gamma(\mathbf{r}) = 4\pi\eta R(\mathbf{v}_b^{center}(\mathbf{r}) + \mathbf{v}_b^{img}(\mathbf{r}) - \mathbf{v}_c^{img}(\mathbf{r})). \quad (\text{B.1})$$

Fig.B.2(a) indicates the flow interactions between images and walls is long ranged, which doesn't vanish crossing simulation boxes. This long range hydrodynamic interaction due to Stokes term in eqn.(3.23) which is well known. In contrast, the second source dipole term decays  $\frac{1}{R^3}$  which dominates near-field flow and is thereby short ranged. Fig.3.14(b) renders the corresponding averaged  $z$  component of effective friction velocity calculated analytically. Basing on the calculation outlined in Fig. B.2(b), we examined the value of effective flow velocity converges as the number of layers of images goes to 10. In this way, we make sure 10 layers of images (total number is

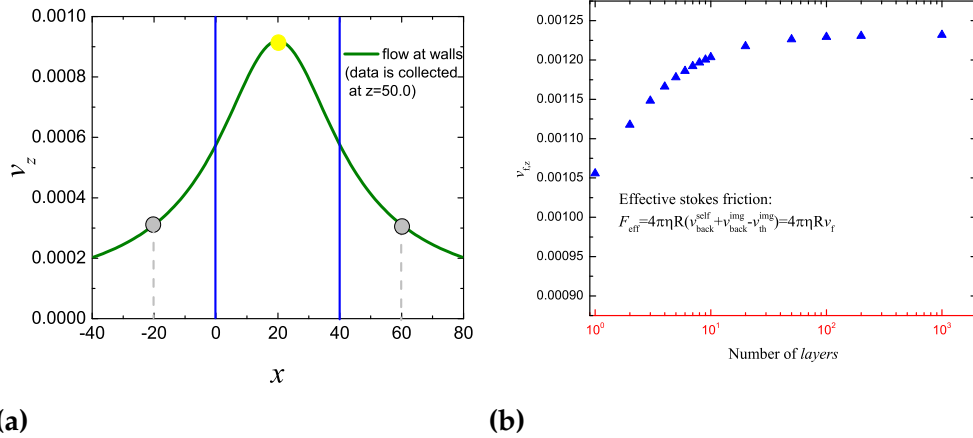


**Figure B.2:** (a) Analytical calculation of  $z$  component of flow along  $x$  axis at walls without considering walls' effect. Blue solid lines distinguish the center box boundaries along  $x$  or  $y$  direction, the gray dash lines mark the two nearest images, spheres are the representations of colloids. (b) Convergence of average flow velocity acting on fixed colloid is calculated by averaging all of the fluid velocities in the colloid domain; the effective friction is therefore obtained by Stokes law.

$(2 \times 10 + 1)^2 = 441$ ) is sufficient to consider the effect of all the images. Then we apply the previously mentioned back flow assumption to obtain the enhanced part of thermophoretic force.

Using the same protocol as in simulations in reference [58], we vary the cubic box size into different values and measure the thermal diffusion factors by considering the effective friction contribution. Comparing the results with simulation data, we found a nice agreement between these two by applying the empirical linear fitting. It is important to note that the strongly depends on the error of the simulation results, thus the changing of potential type, radius of colloids leads to different  $\lambda$ . Therefore the numerical errors may lead to deviations from theoretical results (always are larger).

The comparison between simulation and analytical calculation reveals consistency of constant considerations of back flow assumption and periodic boundary conditions. And the characterization parameter  $\lambda \approx 1.0$  manifests the correctness of Stokes flow approximation.

## B.2 Thermophoretic flow field of fixed colloid in open PBCs

In open PBCs as illustrated in Fig.3.13. The corresponding effective friction is calculated analytically as follows: we focus on one colloid target in a half simulation box, and consider the hydrodynamics induced by twin colloid and infinite number of images; i.e. calculating the average flow velocity at positions where colloid covers. Latter, repeating the procedure as in previous subsection, we evaluate the thermal diffusion factor characterization factor analytically. The results denotes that  $\lambda \approx 1.0$  which confirms the FSEs in full PBCs is the same as in boundary conditions with walls.

Numerically, the calculation is different from what we applied on boundary conditions with walls. Since the influence from images not only along  $x$  and  $y$  directions, but also along  $z$  direction where the temperature gradient applied. We perform the Discretized Fourier Transformation. As depicted in Fig. When looking at the flow field in Fourier  $k$  space, the theoretical calculation is a continuous integration over all  $k$ ; in numerical simulation, the theory doesn't serve the continuous form since periodic boundary conditions applied. In this case, we adopt a discrete Fourier transformation in space. Meanwhile, the source dipole term ( $\sim r^{-3}$ ) decays much faster than

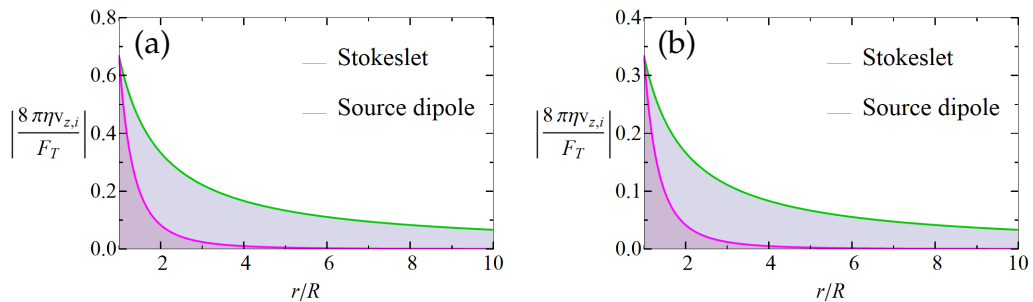


**Figure B.3:** (a) Stokes term (green) and source dipole term (magenta) in Eq.(3.13) decay as a function of the distance to the colloid center along ( $\parallel$ ) the gradient axis. (b) Stokes term (green) and source dipole term (magenta) in Eq.(3.13) decay as a function of the distance to the colloid center perpendicular ( $\perp$ ) to the gradient axis.

the Stokeslet term ( $\sim r^{-1}$ ) in Fig.B.3, such that the far field flow, intimately related to finite size effects, is dominated by the Stokeslet. Thereby the Fourier transformation is only applied on the Stokes (point force) term. In this particular full PBCs simulations, the DFT is applied on the force dipole.

The system is considered in a primary box with size of  $(L_x, L_y, 2L_z) = (40, 40, 100)$ . The two Stokes terms are associated with two thermophoretic forces oppositely, located at  $\mathbf{r}_1 = (0.5L_x, 0.5L_y, 0.5L_z)$  and  $\mathbf{r}_2 = (0.5L_x, 0.5L_y, 1.5L_z)$ , respectively. The resulting flow field is described by

$$\mathbf{v}(r) = O(\mathbf{r} - \mathbf{r}_1) \cdot \mathbf{F}_T + O(\mathbf{r} - \mathbf{r}_2) \cdot (-\mathbf{F}_T), \quad (\text{B.2})$$

with the Oseen tensor

$$O(\mathbf{r}) = \frac{1}{8\pi\eta r} (\mathbf{I} + \hat{\mathbf{r}}\hat{\mathbf{r}}), \quad (\text{B.3})$$

the notations are the same as in Eq.(3.13). To compute the flow field in a cuboid box with PBCs, we consider the Oseen tensor in Fourier space ( $k$ -space)[99]

$$\tilde{O}(\mathbf{k}) = \frac{1}{\eta k^2} (\mathbf{I} - \hat{\mathbf{k}}\hat{\mathbf{k}}), \quad (\text{B.4})$$

here  $\mathbf{k} = (k_1, k_2, k_3)$  the wave number vector. The flow field in  $k$ -space is formulated as

$$\tilde{\mathbf{v}}(r) = \tilde{O}(\mathbf{k})\tilde{\mathbf{F}}_T(\mathbf{k}) + \tilde{O}(\mathbf{k})(-\tilde{\mathbf{F}}_T(\mathbf{k})), \quad (\text{B.5})$$

here the Fourier transformation is also applied on the point force, which gives  $\tilde{\mathbf{F}}_T(\mathbf{k}) = \frac{1}{V} \int \mathbf{F}_T \delta(\mathbf{x} - \mathbf{r}_j) \exp(-i\mathbf{k} \cdot \mathbf{x}) d^3\mathbf{x} = \frac{1}{V} \mathbf{F}_T \exp(-i\mathbf{k} \cdot \mathbf{r}_j)$ ,  $j = 1, 2$ .

The flow field with PBCs is therefore obtained by inverting Fourier transformation, yields,

$$\mathbf{v}'(\mathbf{r}) = \sum_{\mathbf{k} \neq 0} \tilde{\mathbf{v}}(\mathbf{k}) e^{i\mathbf{k} \cdot \mathbf{r}}, \quad (\text{B.6})$$

with the corresponding three components of  $k$  multiples of  $2\pi/L_x, 2\pi/L_y, 2\pi/2L_z$ , respectively. The calculation of  $\mathbf{F}_T^\gamma$  on the left side colloid is the sum of the hydrodynamic interactions from the right side colloid as well as its periodic images, and the periodic images of the left side colloid. Which is given by

$$\mathbf{F}_T^\gamma(\mathbf{r}) = 4\pi\eta R(\mathbf{v}^{right}(\mathbf{r}) + \mathbf{v}^{right,img}(\mathbf{r}) + \mathbf{v}^{left,img}(\mathbf{r})). \quad (\text{B.7})$$



## Appendix C

# Further discussion on the rugosity dependence of $\alpha_T$

The model of rod is sort of “shish-kebab” like which is a series of soft spherical beads connected with rigid bonds. We formally mentioned that the rugosity is tuned by adjusting overlapping of beads. This model counts for the geometrical effects of interfacial properties which have been shown to be the dominant mechanism of unusual anisotropic thermophoresis. To compensate the explanation about rugosity dependence of  $\alpha_{T,\parallel}$  in Chapter 4, we discuss the geometrical effect in detail in the following text. Furthermore, we discuss the influences of the model such as employed attractive/repulsive interaction, interaction range, effective potential differed by the overlapping of neighboring beads, which subtly modify the anisotropy of thermophoresis.

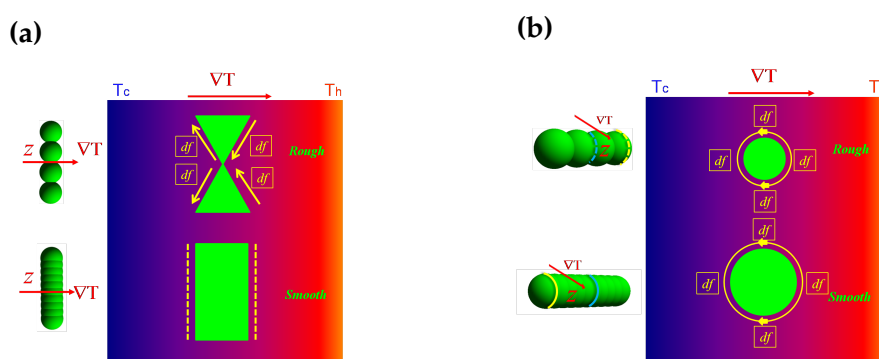


**Figure C.1:** Schematic diagrams of thermophoretic surface forces (yellow arrows) with rods aligned perpendicularly to  $\nabla T$ . (a) View of surfaces of cross sections along long axis; (b) View of surfaces of cross sections perpendicular to long axis.

## C.1 Geometric effects on $\alpha_{T,\perp}$ and $\alpha_{T,\parallel}$

### C.1.1 The perpendicular factor $\alpha_{T,\perp}$

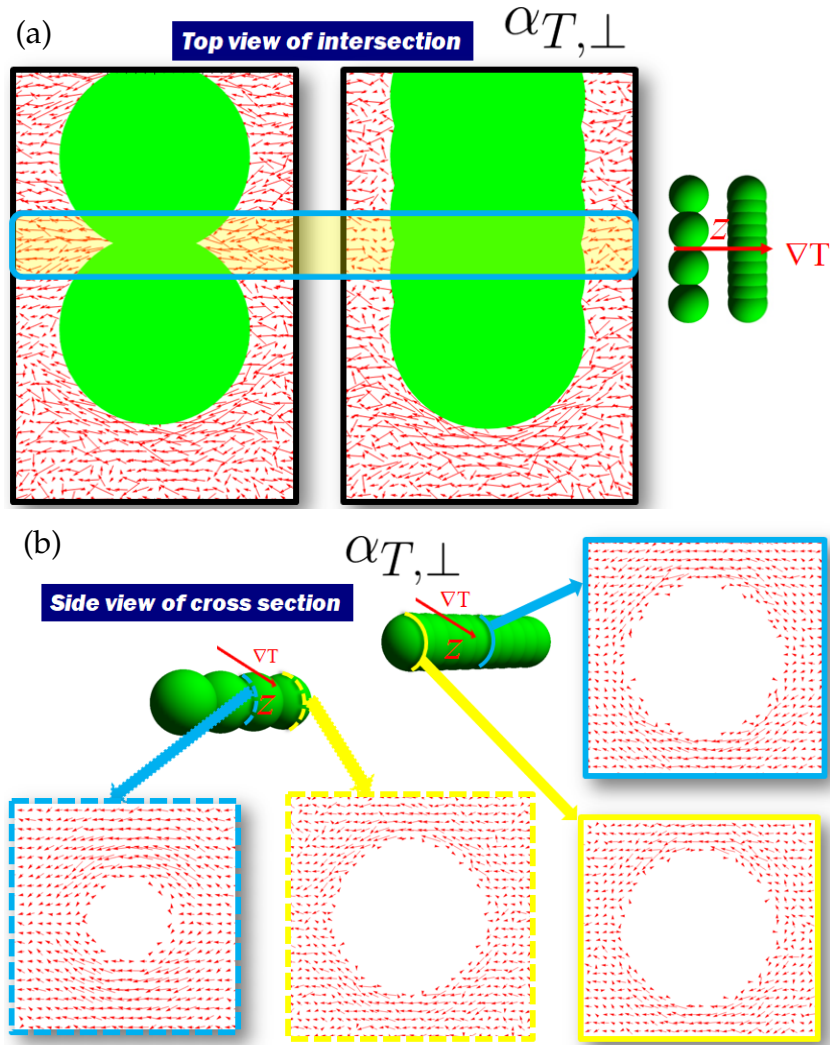


**Figure C.2:** The flow velocity fields of rod perpendicular to  $\nabla T$  in different cross sections. (a) The view of the flow velocity in a cross section along the long axis and gradient axis of the rod. (b) The view of the flow velocity in cross sections at different positions and perpendicular to the long axis of the rod.

Since the rod ends are identical for both rough and smooth ones, only the intermediate surfaces differentiate their contributions to  $F_T$  for the rod aligned perpendicularly to  $\nabla T$ . Here are two scenarios about geometrical effects summarized in the following.

*Scenario one:* When cross sections are taken parallel to the long axis of rods, the immersed surfaces of rough (double triangular shape) and (perfectly)

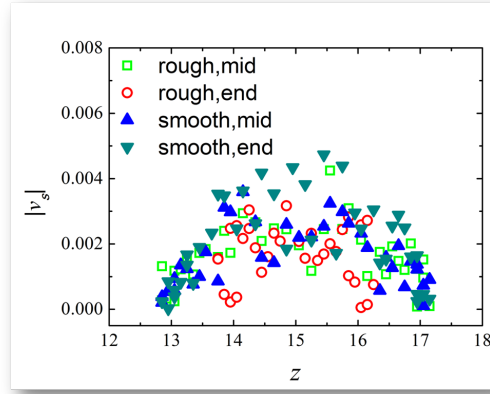


**Figure C.3:** The magnitudes of the *averaged* slip flow in different cross sections perpendicular to the long axis of the rod, in this case the rod is placed perpendicular to  $\nabla T$ .

smooth (rectangular shape) rods are indicated in Fig.C.1(a). Apparently, the indentation area of rough rod feels the temperature gradient and undergoes surfaces forces (depicted with yellow arrows). In contrast, no local gradient at the perfectly smooth surfaces. Hence,  $\mathbf{F}_{Rough}^{cross,\parallel} > \mathbf{F}_{Smooth}^{cross,\parallel}$ . Here  $\mathbf{F}_{Rough}^{cross,\parallel}$  and  $\mathbf{F}_{Smooth}^{cross,\parallel}$  denote aforementioned thermophoretic force contributions.

*Scenario two:* When the cross sections are perpendicular to the long axis in Fig.C.1(b), the contribution to  $F_{T,\parallel}$  of surface forces in the rough rod case is less than the smooth one due to less surface close to indented area.

This leads to  $\mathbf{F}_{Rough}^{cross,\perp} < \mathbf{F}_{Smooth}^{cross,\perp}$ . The competition between these two effects result in  $\alpha_{T,\perp}$  undetermined.

Moreover, the resultant flows around the rod surface in Fig.C.2 also support the above arguments. Fig.C.3 shows the magnitudes of the averaged tangential flow for different cross sections are similar.

### C.1.2 The parallel factor $\alpha_{T,\parallel}$

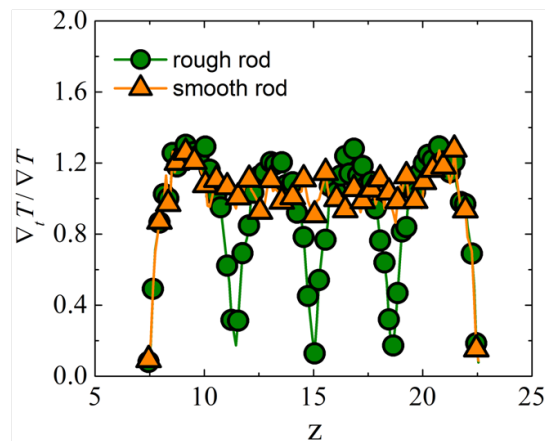


**Figure C.4:** The local temperature gradient along the long axis of the rough and smooth rods which align to  $\nabla T$  (as indicated in the carton in Fig.C.5(a)).

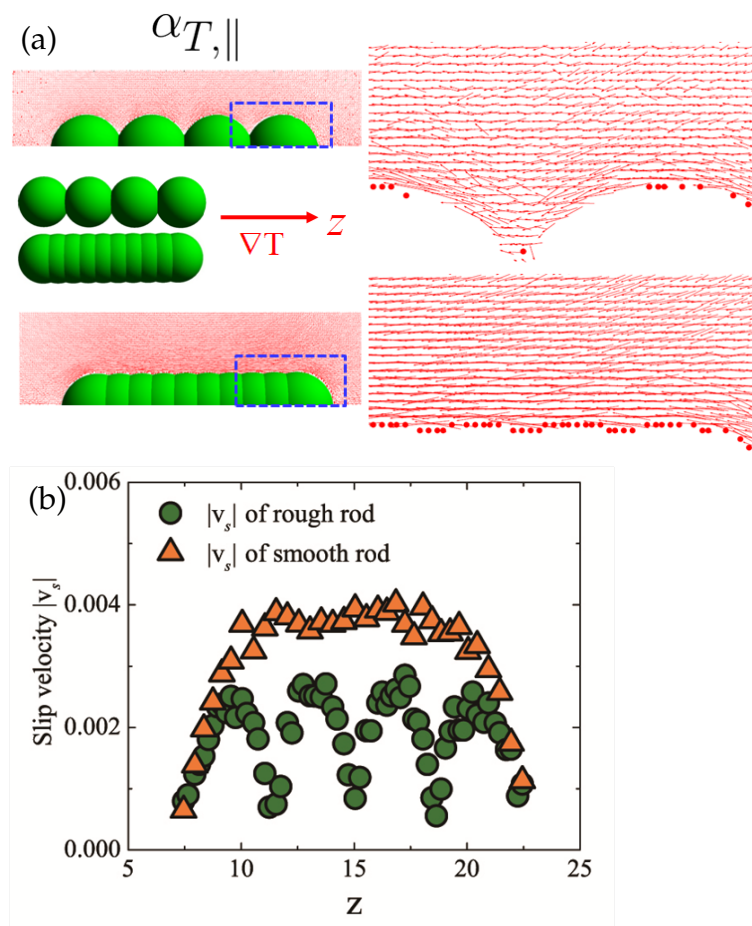


**Figure C.5:** The flow velocity fields of rod parallel to  $\nabla T$  with different rugosities. (a) The flow velocity field. (b) The comparison of the magnitudes of *averaged* slip velocities between rods with different rugosities.

## C.2 Non-geometric effects on $\alpha_{T,\perp}$ and $\alpha_{T,\parallel}$

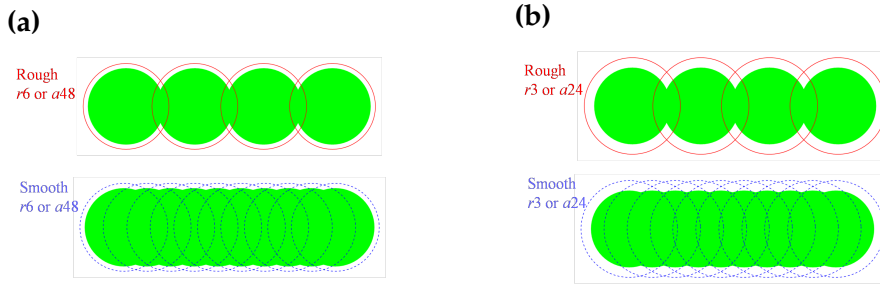


**Figure C.6:** Schematic representations of overlapping interacting area of rough and smooth rods with different potentials. (a)  $r6$  or  $a48$  potentials result in solvent particles at indentation interact 2 neighboring beads; (b) while  $r3$  or  $a24$  potentials lead to ONE solvent particle may interacts with 2 or 3 beads.

**Overlapping of beads and types of potential.** Interestingly, the rugosity dependence of  $r6$  and  $r3$  (or  $a48$  and  $a24$ ) behave similarly with respect to their corresponding single bead thermal diffusion factor  $\alpha_T^o$ . This means that the enhanced thermophoretic forces (compared with spherical colloids) don't rely on the interaction stiffness  $n$  of solo repulsive or attractive potentials. However, the difference between repulsive and attractive potentials are apparent. This is the consequence of the nature of attractive and repulsive potential combined with the overlapping of bead-solvent interaction (the finite range of the solvent-bead interactions results in overlapping potential area which is illustrated in FigC.6), although the overlapping effects on rough rods is very weak and also shown in the data Chapter 4. Generally, overlapping of beads strengthens the rigidity of the (effective) repulsive potential and deepens the well of the attractive (effective) potential in the vicinity of indentation area. When the rod is aligned along the gradient, solvent particles located at the overlapping indentation area contribute oppositely to  $F_{T,\parallel}$ . This explains the data of repulsive potentials are above attractive potentials. Likewise, the perpendicular thermophoretic force decreases with the rugosity in the attractive case, while changes slightly in the repulsive case. It is important to note that this explanation relies on the argument that  $F_T$  is positively correlated to number of particles within bead-solvent interaction range and potential barely deforms the temperature field.

As it has been found that thermophoresis is sensitive to minor modifications of interfacial properties [21, 26], our investigations on rugosity dependence

of rods also enrich the diversity of thermophoretic properties. Nevertheless, we mainly emphasize the geometrical effects rather than homogenizing the effective surface potential in the model of rods. Because in experiments, the interaction at indentation area might be different from what at non-indentation area. The further detailed experimental studies on interfacial factors of rod such as repulsive or attractive potentials might be of interest and importance in theory and application.

# Bibliography

- [1] C.L. Blanc. *Huai-nan Tzu: Philosophical Synthesis in Early Han Thought : the Idea of Resonance (kan-ying) with a Translation and Analysis of Chapter Six*. Hong Kong University Press, 1985.
- [2] David I Perrett et al. "Symmetry and Human Facial Attractiveness". In: *Evolution and Human Behavior* 20.5 (1999), pp. 295–307.
- [3] Anthony C Little, Coren L Apicella, and Frank W Marlowe. "Preferences for symmetry in human faces in two cultures: data from the UK and the Hadza, an isolated group of hunter-gatherers". In: *Proceedings of the Royal Society of London B: Biological Sciences* 274.1629 (2007), pp. 3113–3117.
- [4] Magnus Enquist, Anthony Arak, et al. "Symmetry, beauty and evolution". In: *Nature* 372.6502 (1994), pp. 169–172.
- [5] Keith A Olive, Particle Data Group, et al. "Review of particle physics". In: *Chinese physics C* 38.9 (2014), p. 090001.
- [6] Rong Li and Bruce Bowerman. "Symmetry breaking in biology". In: *Cold Spring Harbor perspectives in biology* 2.3 (2010), a003475.
- [7] 2017. URL: <https://images.google.de/> (visited on 08/18/2017).
- [8] Mohammad Reza Domiri Ganji. *Nasir-Al-Mulk Mosque in Shiraz*. 2017. URL: <http://gravity.ir/nasir-al-mulk-mosque-in-shiraz/> (visited on 04/22/2016).
- [9] Leo Radzihovsky. "Critical Soft Matter". In: (2015).
- [10] G. Gompper et al. "Multi-Particle Collision Dynamics: A Particle-Based Mesoscale Simulation Approach to the Hydrodynamics of Complex Fluids". English. In: *Advanced Computer Simulation Approaches for Soft Matter Sciences III*. Ed. by Christian Holm and Kurt Kremer. Vol. 221. Advances in Polymer Science. Springer Berlin Heidelberg, 2009, pp. 1–87.
- [11] Andreas Walther and Axel H. E. Müller. "Janus Particles: Synthesis, Self-Assembly, Physical Properties, and Applications". In: *Chemical Reviews* 113.7 (2013). PMID: 23557169, pp. 5194–5261.

- [12] Jasper van der Gucht and Cécile Sykes. "Physical model of cellular symmetry breaking". In: *Cold Spring Harbor perspectives in biology* 1.1 (2009), a001909.
- [13] Doreen Niether et al. "Accumulation of formamide in hydrothermal pores to form prebiotic nucleobases". In: *Proceedings of the National Academy of Sciences* 113.16 (2016), pp. 4272–4277.
- [14] Philipp Baaske et al. "Extreme accumulation of nucleotides in simulated hydrothermal pore systems". In: *Proceedings of the National Academy of Sciences* 104.22 (2007), pp. 9346–9351.
- [15] Kohki Okabe et al. "Intracellular temperature mapping with a fluorescent polymeric thermometer and fluorescence lifetime imaging microscopy". In: *Nature communications* 3 (2012), p. 705.
- [16] Don S. Lemons and Anthony Gythiel. "Paul Langevin's 1908 paper "On the Theory of Brownian Motion" ["Sur la théorie du mouvement brownien," C. R. Acad. Sci. (Paris) 146, 530–533 (1908)]". In: *American Journal of Physics* 65.11 (1997), pp. 1079–1081.
- [17] J.K.G. Dhont. *An Introduction to Dynamics of Colloids*. Studies in Interface Science. Elsevier Science, 1996.
- [18] M Ripoll et al. "Low-Reynolds-number hydrodynamics of complex fluids by multi-particle-collision dynamics". In: *EPL (Europhysics Letters)* 68.1 (2004), p. 106.
- [19] M. Ripoll et al. "Dynamic regimes of fluids simulated by multiparticle-collision dynamics". In: *Phys. Rev. E* 72 (1 2005), p. 016701.
- [20] Thomas Franosch et al. "Resonances arising from hydrodynamic memory in Brownian motion-The colour of thermal noise". In: *arXiv preprint arXiv:1106.6161* (2011).
- [21] Simone Wiegand. "Thermal diffusion in liquid mixtures and polymer solutions". In: *J. Phys.: Condensed Matter* 16.10 (2004), R357.
- [22] C. Ludwig et al. *Diffusion zwischen ungleich erwärmten Orten gleich zusammengesetzter Lösung*. Aus der K.K. Hof- und Staatsdruckerei, in Commission bei W. Braumüller, Buchhändler des K.K. Hofes und der K. Akademie der Wissenschaften, 1856.
- [23] J Clerk Maxwell. "On stresses in rarified gases arising from inequalities of temperature". In: *Philosophical Transactions of the royal society of London* 170 (1879), pp. 231–256.
- [24] R Piazza and A Parola. "Thermophoresis in colloidal suspensions". In: *J. Phys.: Condensed Matter* 20.15 (2008), p. 153102.

- [25] Paul S. Epstein. "Zur Theorie des Radiometers". In: *Zeitschrift für Physik* 54.7 (1929), pp. 537–563.
- [26] Alois Würger. "Thermal non-equilibrium transport in colloids". In: *Rep. Prog. Phys.* 73.12 (2010), p. 126601.
- [27] Alois Würger. "Thermophoresis in Colloidal Suspensions Driven by Marangoni Forces". In: *Phys. Rev. Lett.* 98 (13 2007), p. 138301.
- [28] Abhijit Guha and Subho Samanta. "Effect of thermophoresis and its mathematical models on the transport and deposition of aerosol particles in natural convective flow on vertical and horizontal plates". In: *Journal of Aerosol Science* 77 (2014), pp. 85–101.
- [29] F. Zheng. "Thermophoresis of spherical and non-spherical particles: a review of theories and experiments". In: *Advances in Colloid and Interface Science* 97.1 (2002), pp. 255–278.
- [30] Huan J Keh and Chang L Ou. "Thermophoresis of aerosol spheroids". In: *Aerosol science and technology* 38.7 (2004), pp. 675–684.
- [31] Mingcheng Yang and Marisol Ripoll. "Driving forces and polymer hydrodynamics in the Soret effect". In: *Journal of Physics: Condensed Matter* 24.19 (2012), p. 195101.
- [32] Jan K. G. Dhont. "Thermodiffusion of interacting colloids. I. A statistical thermodynamics approach". In: *The Journal of Chemical Physics* 120.3 (2004), pp. 1632–1641.
- [33] Jan K. G. Dhont. "Thermodiffusion of interacting colloids. II. A microscopic approach". In: *The Journal of Chemical Physics* 120.3 (2004), pp. 1642–1653.
- [34] Jerome Burelbach et al. "A Unified Description of Colloidal Thermophoresis". In: *arXiv preprint arXiv:1708.02195* (2017).
- [35] LD Landau and EM Lifshitz. "Fluid mechanics, 1959". In: *Editions de Moscou* (1967).
- [36] John Chipman. "THE SORET EFFECT". In: *Journal of the American Chemical Society* 48.10 (1926), pp. 2577–2589.
- [37] Robert S. Mulliken. "THE SEPARATION OF ISOTOPES BY THERMAL AND PRESSURE DIFFUSION". In: *Journal of the American Chemical Society* 44.5 (1922), pp. 1033–1051.
- [38] R Clark Jones and WH Furry. "The separation of isotopes by thermal diffusion". In: *Reviews of Modern Physics* 18.2 (1946), p. 151.
- [39] J Calvin Giddings. "Field-flow fractionation: analysis of macromolecular, colloidal, and particulate materials". In: *Science* 260.5113 (1993), pp. 1456–1465.

- [40] Fathi A. Messaud et al. "An overview on field-flow fractionation techniques and their applications in the separation and characterization of polymers". In: *Progress in Polymer Science* 34.4 (2009), pp. 351–368.
- [41] Hong-Ren Jiang, Natsuhiko Yoshinaga, and Masaki Sano. "Active Motion of a Janus Particle by Self-Thermophoresis in a Defocused Laser Beam". In: *Phys. Rev. Lett.* 105 (26 2010), p. 268302.
- [42] Ramin Golestanian. "Collective Behavior of Thermally Active Colloids". In: *Phys. Rev. Lett.* 108 (3 2012), p. 038303.
- [43] Mingcheng Yang and Marisol Ripoll. "Simulations of thermophoretic nanoswimmers". In: *Phys. Rev. E* 84 (6 2011), p. 061401.
- [44] Martin Wagner and Marisol Ripoll. "Hydrodynamic front-like swarming of phoretically active dimeric colloids". In: *EPL (Europhysics Letters)* 119.6 (2017), p. 66007.
- [45] Mingcheng Yang, Marisol Ripoll, and Ke Chen. "Catalytic microrotor driven by geometrical asymmetry". In: *The Journal of Chemical Physics* 142.5 (2015), p. 054902.
- [46] Mingcheng Yang et al. "A microscale thermophoretic turbine driven by external diffusive heat flux". In: *Nanoscale* 6 (22 2014), pp. 13550–13554.
- [47] Mingcheng Yang and Marisol Ripoll. "Thermoosmotic microfluidics". In: *Soft matter* 12.41 (2016), pp. 8564–8573.
- [48] Anatoly Malevanets and Raymond Kapral. "Mesoscopic model for solvent dynamics". In: *J. Chem. Phys.* 110.17, 8605 (1999), pp. 8605–8613.
- [49] Raymond Kapral. "Multiparticle Collision Dynamics: Simulation of Complex Systems on Mesoscales". English. In: *Advances in Chemical Physics, Volume 140*. Ed. by Stuart A. Rice. Vol. 140. Advances in Polymer Science. John Wiley and Sons, Inc., 2008, pp. 89–146.
- [50] T. Ihle and D. M. Kroll. "Stochastic rotation dynamics: A Galilean-invariant mesoscopic model for fluid flow". In: *Phys. Rev. E* 63 (2 2001), p. 020201.
- [51] Mingcheng Yang et al. "Effect of angular momentum conservation on hydrodynamic simulations of colloids". In: *Phys. Rev. E* 92 (1 2015), p. 013301.
- [52] T. Ihle and D. M. Kroll. "Stochastic rotation dynamics. II. Transport coefficients, numerics, and long-time tails". In: *Phys. Rev. E* 67 (6 2003), p. 066706.

- [53] T. Ihle, E. Tüzel, and D. M. Kroll. “Resummed Green-Kubo relations for a fluctuating fluid-particle model”. In: *Phys. Rev. E* 70 (3 2004), p. 035701.
- [54] T. Ihle, E. Tüzel, and D. M. Kroll. “Equilibrium calculation of transport coefficients for a fluid-particle model”. In: *Phys. Rev. E* 72 (4 2005), p. 046707.
- [55] E. Tüzel, T. Ihle, and D. M. Kroll. “Dynamic correlations in stochastic rotation dynamics”. In: *Phys. Rev. E* 74 (5 2006), p. 056702.
- [56] C. M. Pooley and J. M. Yeomans. “Kinetic Theory Derivation of the Transport Coefficients of Stochastic Rotation Dynamics”. In: *The Journal of Physical Chemistry B* 109.14 (2005). PMID: 16851730, pp. 6505–6513.
- [57] Daniel Lüsebrink and Marisol Ripoll. “Temperature inhomogeneities simulated with multiparticle-collision dynamics”. In: *J. Chem. Phys.* 136.8 (2012), p. 084106.
- [58] Daniel Lüsebrink, Mingcheng Yang, and Marisol Ripoll. “Thermophoresis of colloids by mesoscale simulations”. In: *J. Phys.: Condensed Matter* 24.28 (2012), p. 284132.
- [59] Daniel Lüsebrink. “Colloidal Suspensions in Temperature Gradients with Mesoscopic Simulations”. PhD thesis. Universität zu Köln, 2011.
- [60] Mingcheng Yang and Marisol Ripoll. “Thermophoretically induced flow field around a colloidal particle”. In: *Soft Matter* 9 (18 2013), pp. 4661–4671.
- [61] Daniel Lüsebrink and Marisol Ripoll. “Collective thermodiffusion of colloidal suspensions”. In: *The Journal of Chemical Physics* 137.19 (2012), p. 194904.
- [62] Mingcheng Yang, Adam Wysocki, and Marisol Ripoll. “Hydrodynamic simulations of self-phoretic microswimmers”. In: *Soft Matter* 10 (33 2014), pp. 6208–6218.
- [63] JT Padding et al. “Stick boundary conditions and rotational velocity auto-correlation functions for colloidal particles in a coarse-grained representation of the solvent”. In: *Journal of Physics: Condensed Matter* 17.45 (2005), S3393.
- [64] Mario Theers et al. “From local to hydrodynamic friction in Brownian motion: A multiparticle collision dynamics simulation study”. In: *Phys. Rev. E* 93 (3 2016), p. 032604.

- [65] Mu-Jie Huang, Jeremy Schofield, and Raymond Kapral. "A microscopic model for chemically-powered Janus motors". In: *Soft Matter* 12 (25 2016), pp. 5581–5589.
- [66] Mike P Allen and Dominic J Tildesley. *Computer simulation of liquids*. Oxford university press, 1989.
- [67] Mie Gustav. "Zur kinetischen Theorie der einatomigen Körper". In: *Annalen der Physik* 316.8 (), pp. 657–697.
- [68] Taro Kihara. "Virial Coefficients and Models of Molecules in Gases". In: *Rev. Mod. Phys.* 25 (4 1953), pp. 831–843.
- [69] GA Vliegenthart, JFM Lodge, and HNW Lekkerkerker. "Strong weak and metastable liquids structural and dynamical aspects of the liquid state". In: *Physica A: Statistical Mechanics and its Applications* 263.1-4 (1999), pp. 378–388.
- [70] "On the determination of molecular fields.—I. From the variation of the viscosity of a gas with temperature". In: *Proceedings of the Royal Society of London A: Mathematical, Physical and Engineering Sciences* 106.738 (1924), pp. 441–462.
- [71] John D. Weeks, David Chandler, and Hans C. Andersen. "Role of Repulsive Forces in Determining the Equilibrium Structure of Simple Liquids". In: *The Journal of Chemical Physics* 54.12 (1971), pp. 5237–5247.
- [72] Luis F. Rull et al. "Brownian motion in an isothermal-isobaric bath: Mass and size dependence". In: *Phys. Rev. A* 40 (10 1989), pp. 5856–5859.
- [73] María J. Nuevo, Juan J. Morales, and David M. Heyes. "Self-diffusion coefficients and shear viscosity of model nanocolloidal dispersions by molecular dynamics simulation". In: *Phys. Rev. E* 58 (5 1998), pp. 5845–5854.
- [74] Tyler Shendruk. "Theoretical and Computational Studies of Hydrodynamics-based Separation of Particles and Polymers in Microfluidic Channels". PhD thesis. Université d'Ottawa/University of Ottawa, 2014.
- [75] A. Lamura et al. "Multi-particle collision dynamics: Flow around a circular and a square cylinder". In: *EPL (Europhysics Letters)* 56.3 (2001), p. 319.
- [76] Frederick Gittes and Christoph F. Schmidt. "Chapter 8 Signals and Noise in Micromechanical Measurements". In: ed. by Michael P. Sheetz. Vol. 55. *Methods in Cell Biology*. Academic Press, 1997, pp. 129–156.

- [77] Adam Wysocki et al. "Multi-particle collision dynamics simulations of sedimenting colloidal dispersions in confinement". In: *Faraday discussions* 144 (2010), pp. 245–252.
- [78] J. T. Padding and A. A. Louis. "Hydrodynamic interactions and Brownian forces in colloidal suspensions: Coarse-graining over time and length scales". In: *Phys. Rev. E* 74 (3 2006), p. 031402.
- [79] Laurent Helden, Ralf Eichhorn, and Clemens Bechinger. "Direct measurement of thermophoretic forces". In: *Soft Matter* 11 (12 2015), pp. 2379–2386.
- [80] R. Di Leonardo, F. Ianni, and G. Ruocco. "Colloidal Attraction Induced by a Temperature Gradient". In: *Langmuir* 25.8 (2009). PMID: 19265405, pp. 4247–4250.
- [81] John L. Anderson. "Colloid Transport by Interfacial Forces". In: *Annu. Rev. Fluid Mech.* 21 (1989), pp. 61–99.
- [82] Gunnar Rückner and Raymond Kapral. "Chemically Powered Nanodimers". In: *Phys. Rev. Lett.* 98 (15 2007), p. 150603.
- [83] Dmitry A. Fedosov, Ankush Sengupta, and Gerhard Gompper. "Effect of fluid-colloid interactions on the mobility of a thermophoretic microswimmer in non-ideal fluids". In: *Soft Matter* 11 (33 2015), pp. 6703–6715.
- [84] Fengchang Yang et al. "Self-diffusiophoresis of Janus catalytic micro-motors in confined geometries". In: *Langmuir* 32.22 (2016), pp. 5580–5592.
- [85] Audrey Hammack, Yeng-Long Chen, and Jennifer Kreft Pearce. "Role of dissolved salts in thermophoresis of DNA: Lattice-Boltzmann-based simulations". In: *Phys. Rev. E* 83 (3 2011), p. 031915.
- [86] Peter H. Colberg et al. "Chemistry in Motion: Tiny Synthetic Motors". In: *Acc. Chem. Res.* 47.12 (2014). PMID: 25357202, pp. 3504–3511.
- [87] Shang Yik Reigh and Raymond Kapral. "Catalytic dimer nanomotors: continuum theory and microscopic dynamics". In: *Soft Matter* 11 (16 2015), pp. 3149–3158.
- [88] Mu-Jie Huang, Jeremy Schofield, and Raymond Kapral. "A microscopic model for chemically-powered Janus motors". In: *Soft Matter* 12.25 (2016), pp. 5581–5589.
- [89] Mingcheng Yang et al. "A microscale turbine driven by diffusive mass flux". In: *Lab Chip* 15 (19 2015), pp. 3912–3917.
- [90] Franz M. Weinert and Dieter Braun. "Observation of Slip Flow in Thermophoresis". In: *Phys. Rev. Lett.* 101 (16 2008), p. 168301.

- [91] Zbigniew Idziaszek and Paul S. Julienne. “Universal Rate Constants for Reactive Collisions of Ultracold Molecules”. In: *Phys. Rev. Lett.* 104 (11 2010), p. 113202.
- [92] Raman Ganti, Yawei Liu, and Daan Frenkel. “Molecular Simulation of Thermo-osmotic Slip”. In: *Phys. Rev. Lett.* 119 (3 2017), p. 038002.
- [93] Jinglei Hu et al. “Modelling the mechanics and hydrodynamics of swimming *E. coli*”. In: *Soft Matter* 11 (40 2015), pp. 7867–7876.
- [94] Dirk Reith and Florian Müller-Plathe. “On the nature of thermal diffusion in binary Lennard-Jones liquids”. In: *The Journal of Chemical Physics* 112.5 (2000), pp. 2436–2443.
- [95] C. Debuschewitz and W. Köhler. “Molecular Origin of Thermal Diffusion in *Benzene + Cyclohexane* Mixtures”. In: *Phys. Rev. Lett.* 87 (5 2001), p. 055901.
- [96] Guillaume Galliéro et al. “Thermal diffusion sensitivity to the molecular parameters of a binary equimolar mixture, a non-equilibrium molecular dynamics approach”. In: *Fluid Phase Equilibria* 208.1 (2003), pp. 171–188.
- [97] Pablo Blanco et al. “Thermal Diffusion of a Stiff Rod-Like Mutant Y21M fd-Virus”. In: *Biomacromolecules* 12.5 (2011). PMID: 21438519, pp. 1602–1609.
- [98] Zilin Wang et al. “Thermophoresis of charged colloidal rods”. In: *Soft Matter* 9 (36 2013), pp. 8697–8704.
- [99] M. Doi and S.F. Edwards. *The Theory of Polymer Dynamics*. International series of monographs on physics. Clarendon Press, 1988.
- [100] Pedro Garcia-Ybarra and Daniel E. Rosner. “Thermophoretic properties of nonspherical particles and large molecules”. In: *AIChE Journal* 35.1 (1989), pp. 139–147.
- [101] Kassem Ghorayeb, Abbas Firoozabadi, Toshiyuki Anraku, et al. “Interpretation of the unusual fluid distribution in the Yufutsu gas-condensate field”. In: *SPE journal* 8.02 (2003), pp. 114–123.
- [102] Philipp Baaske et al. “Extreme accumulation of nucleotides in simulated hydrothermal pore systems”. In: *Proceedings of the National Academy of Sciences* 104.22 (2007), pp. 9346–9351.
- [103] Moran Jerabek-Willemsen et al. “MicroScale Thermophoresis: Interaction analysis and beyond”. In: *Journal of Molecular Structure* 1077 (2014), pp. 101–113.
- [104] Daniele Vigolo et al. “Thermophoresis: microfluidics characterization and separation”. In: *Soft Matter* 6.15 (2010), pp. 3489–3493.

- [105] Alberto Parola and Roberto Piazza. “A microscopic approach to thermophoresis in colloidal suspensions”. In: *Journal of Physics: Condensed Matter* 17.45 (2005), S3639.
- [106] Mingcheng Yang and Marisol Ripoll. “Drift velocity in non-isothermal inhomogeneous systems”. In: *The Journal of chemical physics* 136.20 (2012), p. 204508.
- [107] Hong-Ren Jiang et al. “Manipulation of Colloids by a Nonequilibrium Depletion Force in a Temperature Gradient”. In: *Phys. Rev. Lett.* 102 (20 2009), p. 208301.
- [108] T. Ihle and D. M. Kroll. “Stochastic rotation dynamics. II. Transport coefficients, numerics, and long-time tails”. In: *Phys. Rev. E* 67 (6 2003), p. 066706.
- [109] Frank Römer et al. “Thermomolecular Orientation of Nonpolar Fluids”. In: *Phys. Rev. Lett.* 108 (10 2012), p. 105901.
- [110] Christopher D. Daub, Per-Olof Astrand, and Fernando Bresme. “Thermomolecular orientation effects in fluids of dipolar dumbbells”. In: *Phys. Chem. Chem. Phys.* 16 (40 2014), pp. 22097–22106.
- [111] Alpha A. Lee. “Microscopic mechanism of thermomolecular orientation and polarization”. In: *Soft Matter* 12 (42 2016), pp. 8661–8665.
- [112] Marco Braibanti, Daniele Vigolo, and Roberto Piazza. “Does Thermophoretic Mobility Depend on Particle Size?” In: *Phys. Rev. Lett.* 100 (10 2008), p. 108303.
- [113] Stefan Dühr and Dieter Braun. “Why molecules move along a temperature gradient”. In: *Proceedings of the National Academy of Sciences* 103.52 (2006), pp. 19678–19682.
- [114] Maren Reichl et al. “Understanding the similarity in thermophoresis between single- and double-stranded DNA or RNA”. In: *Phys. Rev. E* 91 (6 2015), p. 062709.
- [115] Zihan Tan, Mingcheng Yang, and Marisol Ripoll. “Microfluidic pump driven by anisotropic thermophoresis”. In: *preprint* (2017).
- [116] Ignacio A. Martinez et al. “Colloidal heat engines: a review”. In: *Soft Matter* 13 (1 2017), pp. 22–36.
- [117] George M. Whitesides. “The origins and the future of microfluidics”. In: *Nature* 442.7101 (2006), pp. 368–373.
- [118] Todd M. Squires and Stephen R. Quake. “Microfluidics: Fluid physics at the nanoliter scale”. In: *Rev. Mod. Phys.* 77 (3 2005), pp. 977–1026.

- [119] Howard A Stone, Abraham D Stroock, and Armand Ajdari. "Engineering flows in small devices: microfluidics toward a lab-on-a-chip". In: *Annu. Rev. Fluid Mech.* 36 (2004), pp. 381–411.
- [120] Anton A Darhuber and Sandra M Troian. "Principles of microfluidic actuation by modulation of surface stresses". In: *Annu. Rev. Fluid Mech.* 37 (2005), pp. 425–455.
- [121] Sébastien Michelin and Eric Lauga. "Efficiency optimization and symmetry-breaking in a model of ciliary locomotion". In: *Physics of Fluids* 22.11 (2010), p. 111901.
- [122] Natan Osterman and Andrej Vilfan. "Finding the ciliary beating pattern with optimal efficiency". In: *Proceedings of the National Academy of Sciences* 108.38 (2011), pp. 15727–15732.
- [123] Jens Elgeti and Gerhard Gompper. "Emergence of metachronal waves in cilia arrays". In: *Proceedings of the National Academy of Sciences* 110.12 (2013), pp. 4470–4475.
- [124] Sebastien Michelin et al. "Geometric pumping in autophoretic channels". In: *Soft Matter* 11 (29 2015), pp. 5804–5811.
- [125] Mingren Shen et al. "Chemically driven fluid transport in long microchannels". In: *The Journal of Chemical Physics* 145.12 (2016), p. 124119.
- [126] Chong Liu and Zhigang Li. "Molecular Dynamics Simulation of Composite Nanochannels as Nanopumps Driven by Symmetric Temperature Gradients". In: *Phys. Rev. Lett.* 105 (17 2010), p. 174501.
- [127] Walter F. Paxton et al. "Catalytic Nanomotors: Autonomous Movement of Striped Nanorods". In: *Journal of the American Chemical Society* 126.41 (2004). PMID: 15479099, pp. 13424–13431.
- [128] Ziane Izri et al. "Self-Propulsion of Pure Water Droplets by Spontaneous Marangoni-Stress-Driven Motion". In: *Phys. Rev. Lett.* 113 (24 2014), p. 248302.
- [129] Sébastien Michelin, Eric Lauga, and Denis Bartolo. "Spontaneous autophoretic motion of isotropic particles". In: *Physics of Fluids* 25.6 (2013), p. 061701.
- [130] Sébastien Michelin and Eric Lauga. "Geometric tuning of self-propulsion for Janus catalytic particles". In: *Scientific Reports* 7 (2017).
- [131] Abraham D. Stroock et al. "Fluidic Ratchet Based on Marangoni-Bénard Convection". In: *Langmuir* 19.10 (2003), pp. 4358–4362.
- [132] Alexander A. Donkov et al. "Momentum and mass fluxes in a gas confined between periodically structured surfaces at different temperatures". In: *Phys. Rev. E* 84 (1 2011), p. 016304.

- [133] Steffen Hardt, Sudarshan Tiwari, and Tobias Baier. “Thermally driven flows between a Leidenfrost solid and a ratchet surface”. In: *Phys. Rev. E* 87 (6 2013), p. 063015.
- [134] Alois Würger. “Leidenfrost Gas Ratchets Driven by Thermal Creep”. In: *Phys. Rev. Lett.* 107 (16 2011), p. 164502.
- [135] R Di Leonardo et al. “Bacterial ratchet motors”. In: *Proceedings of the National Academy of Sciences* 107.21 (2010), pp. 9541–9545.
- [136] Mingcheng Yang and Marisol Ripoll. “A self-propelled thermophoretic microgear”. In: *Soft Matter* 10.7 (2014), pp. 1006–1011.
- [137] Claudio Maggi et al. “Micromotors with asymmetric shape that efficiently convert light into work by thermocapillary effects”. In: *Nature communications* 6 (2015).
- [138] Chien-Cheng Huang, Gerhard Gompper, and Roland G. Winkler. “Hydrodynamic correlations in multiparticle collision dynamics fluids”. In: *Phys. Rev. E* 86 (5 2012), p. 056711.
- [139] Zihan Tan, Mingcheng Yang, and Marisol Ripoll. “Anisotropic thermophoresis”. In: *Soft Matter* (2017), pp. –.
- [140] Jeffrey M. Catchmark, Shyamala Subramanian, and Ayusman Sen. “Directed Rotational Motion of Microscale Objects Using Interfacial Tension Gradients Continually Generated via Catalytic Reactions”. In: *Small* 1.2 (2005), pp. 202–206.
- [141] Alvaro Marin et al. “Three-Dimensional Phenomena in Microbubble Acoustic Streaming”. In: *Phys. Rev. Applied* 3 (4 2015), p. 041001.
- [142] Bhargav Rallabandi et al. “Three-dimensional streaming flow in confined geometries”. In: *Journal of Fluid Mechanics* 777 (2015), 408–429.
- [143] Robin H. Liu et al. “Bubble-induced acoustic micromixing”. In: *Lab Chip* 2 (3 2002), pp. 151–157.
- [144] Kyoko Namura, Kaoru Nakajima, and Motofumi Suzuki. “Quasi-stokeslet induced by thermoplasmonic Marangoni effect around a water vapor microbubble”. In: *Scientific Reports* 7 (2017), p. 45776.
- [145] Walter F. Paxton et al. “Catalytic Nanomotors: Autonomous Movement of Striped Nanorods”. In: *Journal of the American Chemical Society* 126.41 (2004). PMID: 15479099, pp. 13424–13431.
- [146] Thomas Bickel, Guillermo Zecua, and Alois Würger. “Polarization of active Janus particles”. In: *Phys. Rev. E* 89 (5 2014), p. 050303.
- [147] Francesco Sciortino, Achille Giacometti, and Giorgio Pastore. “Phase Diagram of Janus Particles”. In: *Phys. Rev. Lett.* 103 (23 2009), p. 237801.

- [148] Alexander Herms et al. "Concept, synthesis, and structural characterization of DNA origami based self-thermophoretic nanoswimmers". In: *physica status solidi (a)* 214.9 (2017). 1600957, 1600957–n/a.
- [149] Andreas P. Bregulla and Frank Cichos. *Polarization of thermophoretic swimmers in external temperature fields*. 2016.
- [150] Thomas Bickel, Arghya Majee, and Alois Würger. "Flow pattern in the vicinity of self-propelling hot Janus particles". In: *Phys. Rev. E* 88 (1 2013), p. 012301.
- [151] Franz M. Weinert et al. "Microscale Fluid Flow Induced by Thermo-viscous Expansion Along a Traveling Wave". In: *Phys. Rev. Lett.* 100 (16 2008), p. 164501.
- [152] Jan K. G. Dhont et al., eds. *Functional Soft Matter - Lecture Notes of the 46<sup>th</sup> IFF Spring School 2015*. Vol. 94. Jülich: Forschungszentrum Jülich GmbH Zentralbibliothek, Verlag, 2015.
- [153] Patrice Bordat, Dirk Reith, and Florian Müller-Plathe. "The influence of interaction details on the thermal diffusion in binary Lennard-Jones liquids". In: *The Journal of Chemical Physics* 115.19 (2001), pp. 8978–8982.
- [154] Henriette E. Bakker et al. "Phase diagram of binary colloidal rod-sphere mixtures from a 3D real-space analysis of sedimentation-diffusion equilibria". In: *Soft Matter* 12 (45 2016), pp. 9238–9245.
- [155] Julien Morthomas and Alois Würger. "Hydrodynamic attraction of immobile particles due to interfacial forces". In: *Phys. Rev. E* 81 (5 2010), p. 051405.
- [156] H. H. Wensink and H. Löwen. "Aggregation of self-propelled colloidal rods near confining walls". In: *Phys. Rev. E* 78 (3 2008), p. 031409.
- [157] H. H. Wensink and H. Löwen. "Rhythmic Cluster Generation in Strongly Driven Colloidal Dispersions". In: *Phys. Rev. Lett.* 97 (3 2006), p. 038303.

# Eigenhändigkeitserklärung

Ich versichere, dass ich die von mir vorgelegte Dissertation selbständig angefertigt, die benutzten Quellen und Hilfsmittel vollständig angegeben und die Stellen der Arbeit – einschließlich Tabellen, Karten und Abbildungen – , die anderen Werken im Wortlaut oder dem Sinn nach entnommen sind, in jedem Einzelfall als Entlehnung kenntlich gemacht habe; dass diese Dissertation noch keiner anderen Fakultät oder Universität zur Prüfung vorgelegen hat; dass sie – abgesehen von unten angegebenen Teilpublikationen – noch nicht veröffentlicht worden ist, sowie, dass ich eine solche Veröffentlichung vor Abschluss des Promotionsverfahrens nicht vornehmen werde.

Die Bestimmungen der Promotionsordnung sind mir bekannt. Die von mir vorgelegte Dissertation ist von Prof. Dr. Gerhard Gompper und Dr. Marisol Ripoll betreut worden.

---

(Ort, Datum)

---

(Unterschrift)

## Teilpublikation

- Zihan Tan, Mingcheng Yang and Marisol Ripoll. *“Anisotropic thermophoresis”*, Soft Matter, 2017,13, 7283-7291.
- Marisol Ripoll, Zihan Tan and Mingcheng Yang. *“Vorrichtung und Verfahren zur Umwandlung von Wärme, chemischer Energie oder elektrischer Energie in Bewegungsenergie sowie Verwendung der Vorrichtung”*, German patent application (NO. 10 2017003455.9).



# Zihan Tan

---

## Curriculum Vitae

### Academic Qualification

**Ph.D. Theoretical Physics**, *Institut für Theoretische Physik, Universität zu Köln, Köln, Germany.*  
2014- Present

**M.E. Engineering Mechanics**, *Dept. of Modern Mechanics, University of Science and Technology of China (USTC), Hefei, China.*  
2010- 2013

**B.E. Safety Engineering**, *School of Resources and Safety Engineering, Central South University (CSU), Changsha, China.*  
2006- 2010

### Publications

#### • Publications in Europe

**Zihan TAN**, Mingcheng YANG and Marisol RIPOLL. "Anisotropic thermophoresis", *Soft Matter*, 2017, 13, 7283-7291. ([paper online](#))

**Zihan TAN**, Mingcheng YANG and Marisol RIPOLL. "Vorrichtung und Verfahren zur Umwandlung von Wärme, chemischer Energie oder elektrischer Energie in Bewegungsenergie sowie Verwendung der Vorrichtung", [German patent application\(NO. 10 2017003455.9\)](#).

**Zihan TAN**, Mingcheng YANG and Marisol RIPOLL. "Microfluidic pump driven by anisotropic thermophoresis", in preparation.

**Zihan TAN**, Marisol RIPOLL. "Aggregation of thermally driven hetero-colloidal systems near walls", in preparation.

#### • Publications in China ([list online](#))

### Selected Presentations

**Feb. 2018** Flowing Matter 2018: **Oral presentation** 'Microphoretic pumps with mid-channel obstacles', Lisbon, Portugal.

**Jan. 2017** Flowing Matter 2017: **Oral presentation** 'Anisotropic thermophoresis', Porto, Portugal. ([slides online](#))

**Jun. 2016** 7th Summer School Complex Motion in Fluids: **Oral presentation**, Twente, Netherlands.

**May./Jun. 2016** 12th International Meeting on Thermodiffusion: **Oral presentation**, Madrid, Spain.

### Teaching Experiences

**2015, 2016, 2017** Guided the Lab Tour Section ("Computing Fluids: Mesoscale Hydrodynamics Simulations"), 46-48th IFF Spring School, Forschungszentrum Jülich, Germany

**Undergraduate teaching assistant:** Course instructor

**2011- 2012** Undergraduate course "Foundation of Stress Waves".